Exploring the super-orbital periodic behaviour of X-ray Binaries

Marissa Mimi Kotze

Submitted for examination: 7 February 2012
Corrected: 13 August 2012

Thesis Presented for the Degree of
DOCTOR OF PHILOSOPHY
in the Department of Astronomy
UNIVERSITY OF CAPE TOWN

Supervisors: Prof. P. A. Charles and Prof. B. Warner

Abstract

Name: **Marissa Mimi Kotze**

Title: **Exploring the Super-orbital Periodic Behaviour of X-ray Binaries**

Date: **7 February 2012**

Quasi-periodic super-orbital modulations are an established feature of several luminous X-ray binaries. The mechanisms that have been proposed to be responsible for such modulations include irradiation-driven warping/tilting and tidally-induced precession of the accretion disc, jet precession and the modulation of the mass-transfer rate due to an accretion disc instability or the effects of a third body.

A time-dependent period analysis technique (Dynamic Power Spectra) was employed to systematically investigate the long-term X-ray lightcurves from the All Sky Monitor (ASM) on the Rossi X-ray Timing Explorer (RXTE), which now span ~ 15 years. This analysis of X-ray binaries where super-orbital modulations had been reported demonstrated that the long-term behaviour of the majority of sources shows unstable/erratic and/or intermittent variations, which can also be a function of the X-ray spectral state. These are interpreted in terms of theoretical predictions of the stability of X-ray irradiated discs, along with other mechanisms that have been proposed or are likely to be responsible. The complex super-orbital behaviour likely results from a combination of mechanisms, which presents an enormous challenge for future theoretical modelling of mass transfer in interacting binaries and the structure of accretion discs.

The systematic analysis of the RXTE ASM archival data also allowed the serendipitous discovery of very long-term, large-amplitude, quasi-periodic modulations in some low-mass X-ray binaries, on much longer time-scales than any previously reported super-orbital periodicities. It is proposed that such very long-term modulations are likely due to variations in the mass-transfer rate from the donor as a consequence of its solar-like magnetic cycles.

Summary

An accretion disc forms as material is transferred from a donor star (secondary) onto a compact object (primary), such as a white dwarf (WD), neutron star (NS) or black hole (BH). X-ray binaries (XRBs) contain NS or BH primaries, while Cataclysmic Variables (CVs) contain WD primaries. Accretion discs are also present in other astronomical environments, such as Active Galactic Nuclei (AGN) and proto-planetary discs. However, their properties are best studied in the accretion-powered binaries, such as CVs and XRBs (Chapter 1 & 2).

Quasi-periodic or aperiodic super-orbital variations have been reported for several XRBs. However, a time-dependent period analysis (Chapter 3) is necessary in order to determine the behaviour of those modulations over the long term and although such an approach is computationally intensive, it has now become possible using desktop technology.

Accretion disc properties are considered to be responsible for a large fraction of the observed super-orbital modulations (Chapter 4). Mechanisms proposed to affect the geometry of the accretion disc, include irradiation-driven warping/tilting of the inner disc and tidal distortion of the outer disc due to interaction with the donor. Precession of such a disc modulates the flux, as the absorption of radiation from the central source varies. The accretion disc instability, as the result of a change in the mass-transfer rate in the disc, leads to transient outbursts whose recurrence causes quasi-periodic super-orbital modulations.

The publicly available archival X-ray lightcurves from the All Sky Monitor (ASM) on the Rossi X-ray Timing Explorer (RXTE), now span ~ 15 years. They represent comprehensive coverage of 585 X-ray sources, of which many are XRBs, allowing the systematic investigation and comparison of their long-term behaviour (Chapter 5 & Appendix A).

The primary goal of this work was the time-dependent period analysis of 25 XRBs with published super-orbital variations, that have been associated with warped/tilted and/or tidally precessing accretion discs at some stage. Mechanisms that have been proposed or that may be responsible for their variations, were investigated and sources were classified accordingly. These results have been published in Kotze & Charles (2012), of which an extensively expanded version is presented in Chapter 6. Very few sources display sustained steady or steadily evolving super-orbital modulations. The long-term behaviour of the majority of the sources are rather unstable/erratic and/or intermittent and can also be a function of the X-ray spectral state. Consequently traditional period analysis techniques may fail to identify them, while a time-dependent method was successful in doing so.

The systematic analysis of the RXTE ASM archival data, allowed the serendipitous discovery of very long-term, large-amplitude, quasi-periodic modulations in some low-mass XRBs (LMXBs) on much longer time-scales than any previously reported super-orbital periods. The results were published in Kotze & Charles (2010) and have been updated, expanded and included in Chapter 7. Such very long-term modulations, due to variations in the mass-transfer rate from the donor as a consequence of its solar-like magnetic cycles, have been observed in CVs. In LMXBs, Atoll sources displayed much larger amplitude modulations than Z sources over these time-scales, probably because Z sources are Eddington limited and hence unable to respond as readily as Atoll sources to such fluctuations in the mass-transfer rate from the donor.

RXTE ASM data archives contain a wealth of information for XRBs since its energy range is particularly suited to their study - the majority of significantly detected ASM sources (contained in Appendix B) are XRBs. Long observational baselines are required to probe the long-term behaviour of XRBs and while archival data are available for a large number of previous X-ray missions, many sources that were significantly detected by RXTE ASM were only marginally detected by other missions. Future missions (such as ASTROSAT) plan to extend the ~ 15 year RXTE ASM datasets, but it is unfortunate that RXTE shut down (January 2012) before a replacement mission could be launched.

Several publications were produced during the course of postgraduate studies. These do not only include the publication of the major results from this work, but also several co-authored papers and a paper produced from work which started during the BSc (Hons).

List of refereed first author papers:

- "Discovery of long-term superorbital periodicities in the pseudo-transient LMXBs: IGRJ17098-3628 and EXO0748-676"
  Kotze M. M., Charles P. A., Crause L. A., 2009, MNRAS, 395, 1579
- "Very long-term X-ray variations in LMXBs: solar cycle-like variations in the donor?"
  Kotze M. M., Charles P. A., 2010, MNRAS, 402, L16
- "Characterizing X-ray binary long-term variability"
  Kotze M. M., Charles P. A., 2012, MNRAS, 420, 1575

List of co-authored papers:

- "Long-Term Optical/X-ray Variability of CVs, LMXBs and BeX Sources"
  Charles P., Kotze M., Rajoelimanana A., 2010, AIPC, 1314, 303 (major contribution)
- "PySALT: the SALT science pipeline"
  Crawford S. M., et al., 2010, SPIE, 7737 (testing of SALT data reduction package)
- "Possible detection of two giant extrasolar planets orbiting the eclipsing polar UZ Fornacis"
  Potter S. B., et al., 2011, MNRAS, 416, 2202 (minor contribution)

Acknowledgements

Firstly, I want to thank Phil Charles for his exquisite patience and infectious enthusiasm about all aspects of the work. I also greatly appreciate being encouraged (and funded) to attend international conferences and publish my work in MNRAS. In particular, I appreciate having been enabled to attend the Instituto de Astrofísica de Canarias (IAC) Winter school on accretion discs in the Canary Islands and also the Wideband X-ray Astronomy meeting, hosted by the Inter-University Centre for Astronomy and Astrophysics (IUCAA) in India. I look forward to our ongoing collaboration.

Secondly, I wish to thank Brian Warner for his encouraging words, approachability and willingness to play a more active role in my supervision after Phil returned to Southampton. I particularly appreciate the nights at the telescopes in Sutherland, where I was not only instructed in the art of high-speed photometry, but was also privy to high quality music, coffee and very educational and interesting conversations.

The archival X-ray data used in this work were provided by the ASM/RXTE teams at the Massachusetts Institute of Technology (MIT) and at the RXTE Science Operations Facility and Guest Observer Facility at NASA's Goddard Space Flight Center (GSFC). Starlink's PERIOD package was used to produce all periodograms and window functions. All scripts to automate the analysis process were written in PYTHON, BASH and PERL. Alan Levine's FORTRAN programs were used to obtain the white noise estimates for the significance test and bin the dwell-by-dwell data. REDFIT was used for red noise modelling. Kosma von Maltitz and Wendy Williams provided the LaTeX template, on behalf of the UCT Astronomy department, which allows students to adhere to the departmental format requirements.

Being based at the South African Astronomical Observatory (SAAO), exposed me to many astronomers and other staff members, allowing a very natural integration into the South African astronomical research community. There, I have been given ample opportunity to gain observing experience by using a variety of CCDs and telescopes. Many current and future international collaborations involve optical observations using the SAAO's Sutherland facilities, particularly the Southern African Large Telescope (SALT). I wish to thank Darragh O'Donoghue and David Buckley for their willingness to be involved in my future development. I trust our future endeavours with SALT will be rewarded with success, however I want to thank the SALT astronomers in particular for their efforts to date with the coordinated observations with X-ray satellites.

I wish to thank Patrick Woudt at UCT for teaching me the ins and outs of photometry on the 1.9 meter telescope in Sutherland during one of his observing runs. I also want to thank him for allowing me to attend the AM Cvn and ThunderKAT workshops, which were both hosted by UCT.

With regards to opportunities to gain observing experience, I wish to particularly thank Remon Cornelisse at the IAC, who funded 10 days of observing on the Mercator telescope at the Observatorio del Roque de los Muchachos on La Palma. I greatly appreciate being given the opportunity to observe at such a renowned international facility.

I would like to thank Alan Levine for his comments and suggestions on a draft version of my very first paper (Kotze et al. 2009). I thank Guillaume Dubus for his comments on our most recent paper (Kotze & Charles 2012) and for pointing out the erroneous super-orbital period associated with Sco X-1 in Ogilvie & Dubus (2001). I also wish to thank Will Clarkson for his detailed comments and suggestions on our most recent paper.

Funding for all postgraduate education and research was directly or indirectly provided by the South African National Research Foundation (NRF) and the Department of Science and Technology (DST). All postgraduate coursework was completed as part of the National Astrophysics and Space Science Program (NASSP), hosted at UCT. I wish to thank the NASSP steering committee for giving me the opportunity to study Astronomy at the post-graduate level and the lecturers and researchers involved for the educational experience they provided. The primary goal of NASSP is the rapid production of (South) African students with PhDs and in my view they have put everything in place necessary to equip students to do just that. However, it's up to the students to fully engage with the program, motivate themselves accordingly and it's the responsibility of dissatisfied/disgruntled individuals to become part of the solution by making constructive suggestions toward appropriate corrective action. From the perspective of a student representative, I wish to commend Patricia Whitelock in particular for being accommodating and decisive with regard to the latter.

I am also very grateful for being given the opportunity to be involved in the organization of International Astronomical Union (IAU) conferences that were hosted by SAAO, such as: Communicating Astronomy to the Public (CAP2010) and the 2nd Middle-East and Africa Regional IAU Meeting (MEARIM II). Being on the L.O.C. for the latter certainly educated me in the proper ways in which to approach such an enterprise.

On a more personal note, I want to thank my husband for his continued and unwavering support. And finally, I wish to dedicate this work in memory of my father, who fostered my interest in mathematics and encouraged me to continually engage in studies that apply it.

Plagiarism Declaration

I, Marissa M. Kotze, know the meaning of plagiarism and declare that all of the work in the document, save for that which is properly acknowledged, is my own.

Contents

List of Figures

List of Tables

Chapter 1

Introduction

The scene is set herein, introducing the nomenclature from "Compact stellar X-ray sources", an extensive review of X-ray binaries, edited by Lewin & van der Klis (2006). The history and background contained in "Exploring the X-ray Universe" (Seward & Charles 2010), instilled a renewed sense of appreciation for the efforts of the early pioneers in this field. Additional relevant references are nevertheless included where specific concepts are introduced.

1.1 X-rays

The first Nobel prize in physics was awarded to Wilhelm Röntgen, the German scientist who discovered X-rays in 1895. Since this invisible form of radiation passes through most solid objects, it allowed him to create an image of the flesh and bone in his wife's hand on a photographic plate behind it, wherein her gold ring appeared impenetrable. This pioneering work illustrated that X-ray attenuation is determined by the atomic number (Z) of the element it encounters, since it passes easily through low Z elements (organic matter) but is increasingly absorbed by higher Z elements (heavy metals).

We now know that X-rays form part of the electromagnetic (EM) spectrum, and as such represent a particular energy range for photons. The EM spectrum ranges from low energy (radio waves) to high energy (γ-rays) radiation. These photon energies (E) correspond directly to the wavelengths (λ) or frequencies (ν) at which we can observe them.

X-ray energy is measured in kilo-electron volts (keV), implying a 1000 volt potential is required to produce 1 keV radiation through the acceleration of an electron beam. This is approximately 1000 times higher than the energy of optical photons. Consequently, they are invisible in the optical regime and require X-ray detectors to study them, because the wavelengths at which they are visible lie in the X-ray regime.

X-rays are further categorized as hard ($\sim 10-100$ keV) and soft ($\sim 1-10$ keV) according to their ability to pass through hard and soft objects respectively. Hard X-rays have higher E photons and can pass through higher Z elements than soft X-rays. High Z elements have higher absorption coefficients (μ) than low Z elements.

Fewer interactions between X-ray photons and atoms allow the radiation to pass through a material with greater ease. The thickness of a material therefore also plays a role, as thicker materials allow more interactions and therefore more absorption or deflection of photons. In this manner the Earth's atmosphere shields us from extraterrestrial X-rays, as its layers attenuate the radiation. Actually, it absorbs a very large portion of the EM spectrum, particularly the radiation with energies higher than those of optical photons.

1.1.1 Absorption

Radiation interacts with matter and can be scattered or absorbed. Both of these mechanisms cause photons to be diverted from their original path and as such, reduce the amount of radiation reaching the observer. They are collectively referred to as extinction.

In astronomy, absorption between source and observer depends on the number of atoms in a 1 cm^2 column (N_H) and their photoelectric cross section (σ), as a measure of thickness and absorption coefficient respectively. The absorption factor is then written as $e^{-\sigma N_H}$.

Dust extinction by the interstellar medium (ISM), is dependent on the source location with respect to the gas and dust in our Galaxy. The extinction is therefore expected to be very high in the direction of the Galactic centre or Galactic plane, while significantly lower in directions out of the plane.

1.2 X-ray Emission

Since the energies of X-ray photons are 1000 times higher than optical ones, such high energy release could not be reconciled with the physical mechanisms responsible for radiation in the optical regime. There are 4 dominant astrophysical mechanisms that produce X-rays. Each of these have their own spectral signature, making high-resolution broad-band spectra an invaluable diagnostic tool in discerning the emission processes within a source. Only a brief description of each is given here, since the main focus of this work is on the long-term variations in the total X-ray flux over time (X-ray lightcurves), irrespective of the contributing mechanisms.

1.2.1 Blackbody Radiation

A perfect absorber is black and since a surface must absorb and emit radiation, a black body is therefore also a perfect emitter. Blackbody radiation is a continuum spectrum which peaks at an energy that increases with temperature (T). Hot stars radiate higher energy photons so that they appear bluer than cooler stars, which appear redder. Stars therefore radiate as blackbodies with surface $T \sim 2500 - 40000$ K (from red dwarfs to O-type supergiants) producing photons in the optical range. However, a neutron star with surface $T > 10^6$ K will emit blackbody radiation in the X-ray regime.

1.2.2 Thermal Emission

Hot tenuous gas becomes ionized above $T \sim 10^5$ K and can be of such low density that it becomes transparent to its own radiation, allowing thermal energy to be shared easily as particles with opposing charges (electrons and ions) interact, radiating braking radiation or bremsstrahlung. The Maxwellian distribution describes the electron velocities (v) in thermal equilibrium, whereby the average energy of all particles is determined by their T. Electrons move faster at higher T and will release higher energy photons as they suffer these trajectory changes when passing positive ions.

1.2.3 Synchrotron Radiation

Electrons moving at relativistic speeds ($v \sim c$, c is the speed of light) at angles across magnetic fields, emit high-energy photons (X-rays) as their velocity vectors are changed and they are accelerated. The energy of emitted photons will depend on the strength (B) of the magnetic field ($\overrightarrow{B}$) and the energy of the electrons. Since electron energies are described by a power law, the resultant observed spectrum is a power law over a large energy range. Circular polarization of radiation may occur if the $\overrightarrow{B}$ is aligned along the line of sight of the observer and provides direct observational evidence of synchrotron radiation.

1.2.4 Inverse Compton Scattering

Ultra-relativistic electrons can produce X-rays if they collide with photons. The Cosmic Microwave Background (CMB) photons have very low energy and are found everywhere in space. They can be up-scattered to X-ray energies if ultra-relativistic electrons transfer energy to them during collisions. This process accounts for large energy losses suffered by relativistic particles during their journey over the vast distances that separate galaxies.

1.3 X-ray Astronomy

Since optical astronomy could initially be performed with the naked eye, it was the first field to be expanded with the development of instruments and detectors to allow the detailed study of visible astronomical objects. Radio astronomy was the next field to be developed, since it too could be conducted from ground based observatories. With the shielding effects of the Earth's atmosphere, the study of high energy radiation could only begin in the early 1960s, after US Naval Research Laboratory (NRL) rockets propelled instruments above it. As such, X-ray astronomy is a relatively young field and our Sun was the first astronomical source studied.

The first extrasolar X-ray source, Sco X-1 in the constellation Scorpius, was a serendipitous discovery by a group from American Science & Engineering (AS&E) in 1962, while attempting to detect X-rays from the Moon (Giacconi et al. 1962). While extremely bright in the X-ray, Sco X-1 is a comparatively unassuming 12th magnitude source in the optical

(Sandage et al. 1966). Later that year two fainter X-ray sources were also discovered by the AS&E group and the NRL group confirmed that one was the Crab supernova remnant (SNR) in the Crab Nebula. In 2002, Riccardo Giacconi was awarded the Nobel prize in physics for his pioneering efforts which led to the discovery of cosmic X-ray sources.

An ensuing plethora of balloons and rockets carried X-ray detectors high enough into the atmosphere to allow identification of yet more X-ray sources, most of which were designated by prefix GX (Galactic bulge and plane X-ray sources) followed by their galactic latitude and longitude. These short duration efforts were eventually surpassed by satellites (Bradt et al. 1992) that could survey the sky from eccentric equatorial orbits that allowed them largely to avoid the Van Allen radiation belts, while still staying safely tucked inside the protection that the Earth's magnetosphere provides against the solar wind.

1.3.1 Detectors

Photons are detected through their interaction with matter and their energies determine the type of interaction. X-ray photons in the energy range $\sim 0.1 - 10$ keV (soft X-rays) are absorbed by atoms via the photoelectric effect, which causes atoms to eject photoelectrons with energy equal to that of the absorbed photon minus the binding energy of the electron. Compton scattering occurs for X-ray photons with energies above 10 keV (hard X-rays) if they scatter from individual electrons in atoms, transferring some of their energy to those electrons depending on their incidence angle. Photons with energies above 1.02 MeV (γ-rays) will transfer all their energy to electron-positron pairs that they produce via pair-production during interaction with atoms.

Proportional Counters

Chodil et al. (1967) describes a typical X-ray detector (Figure 1.1) or proportional counter, used since the early rocket-borne missions. Fast photoelectrons and Compton electrons create tracks of ionized material in the active or main counter volumes of science detectors, which are shielded behind collimators and X-ray transparent windows. The electrons are attracted toward an anode or central wire where an avalanche occurs due to further interactions with atoms, linearly amplifying the number of electron-ion pairs produced. The anode is maintained at a particular voltage for which the number of electrons collected by the anode is proportional to the energy of the incident X-ray photon. A pulse-height spectrum is produced by sorting the events from the output of the detector by size.

Regular proportional counters detect an electron cloud as a charge collected by the anode, but gas-scintillation proportional counters rather detect the optical flash (or scintillation) produced by the recombination of ionized atoms in the gas and thereby achieve higher resolving power in comparison. Proportional counters contain gas mixtures in their main counter volumes that detect photons with energy up to 20 keV effectively, but become transparent to higher energy photons. Scintillation counters contain crystals in their detector volumes and are able to detect photons with energies up to several MeV.

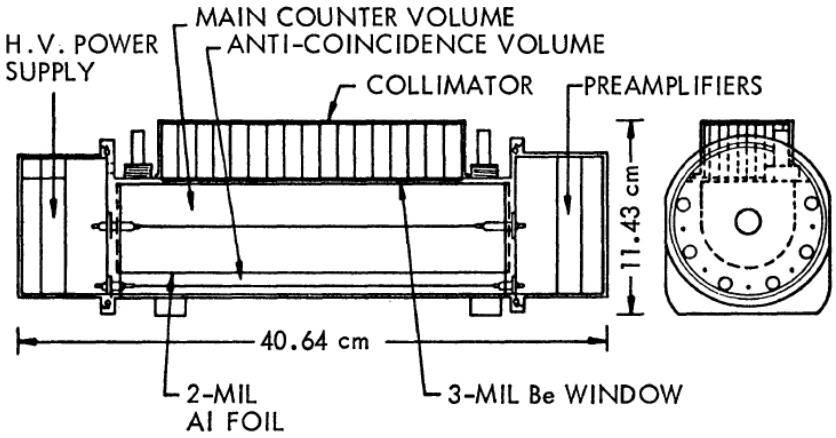

Figure 1.1: Cross-sectional view of a typical X-ray detector (Chodil et al. 1967).

Guard Counters

The study of X-ray emission from astronomical sources requires sensitive instruments that are able to detect the limited numbers of high energy photons and distinguish them from the substantial number of background events generated by cosmic rays and energetic ions in the solar wind. X-ray detectors are therefore surrounded by additional encased detectors, known as anti-coincidence chambers or guard counters, that only record higher energy particles. Cosmic ray events produce coincident events on the science detector and guard counters, allowing their identification and subsequent rejection.

1.3.2 Imaging Techniques

The anode of a position-sensitive proportional counter is made from a single wire of resistive material, so that the position of an event along its length can be determined from the relative size of the pulse measured at the two ends of the wire. Used at the focus of the telescope, this directly facilitates two-dimensional source localization as positive ions from such a localized avalanche travel to the cathode to deposit their charge close to location of the avalanche. The cathodes may be made of crossed resistive wire grids or resistive plates.

Other imaging or position-sensitive detectors include charge coupled devices (CCDs) used in optical astronomy and micro-channel plates (MCPs) that contain large numbers of channel electron multipliers that are fused together. Since X-rays pass through most solid materials they cannot be focused like optical light using refraction and reflection by lenses and mirrors at normal incidence. However, low energy X-rays with an incidence angle less than a degree may skip off a smooth reflective surface, so that sets of curved nested mirrors may direct X-rays toward a detector.

Slat or honeycomb collimators restrict the field of view for proportional counters, allowing one-dimensional localization of the sources per strip of sky scanned. Scanning modulation collimators scan at different orientations to allow determination of source locations in two dimensions (to within several arcminutes).

Coded Masks

Coded masks act like pinhole cameras with multiple, randomly distributed holes which allow localization of the spatial origin of X-rays, since each location above the mask produces its own unique footprint or shadow pattern on a position-sensitive detector (see Figure 1.2). They allow the observation of a larger field of view per pointing at moderate spatial resolution and have been used in imaging of high energy X-rays and γ-rays.

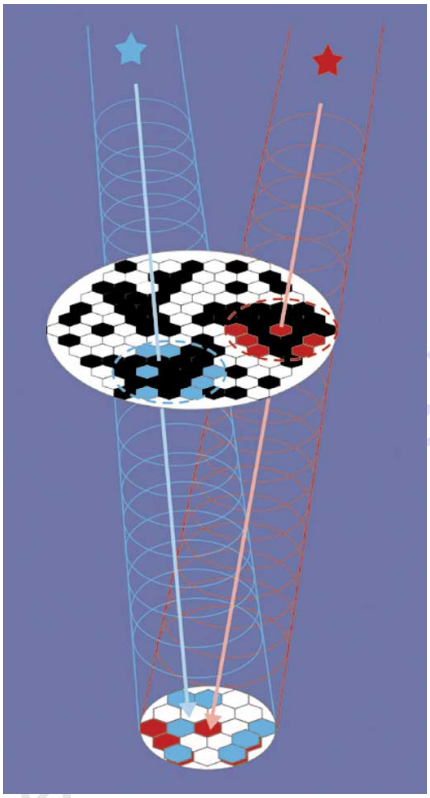

Figure 1.2: Coded Mask diagram.

1.3.3 Satellite Missions

X-ray sources, such as the sunlit atmosphere and the Sun itself, the solar wind and other regions with high concentration of charged particles, all interfere with the detection of astronomical X-ray sources. The Van Allen belts are ducts inside the Earth's magnetosphere that trap such charged particles and funnel them to the magnetic poles.

X-ray detectors are shut down whenever they pass through areas where there are high concentrations of charged particles, such as the South Atlantic Anomaly (SAA). For this reason most X-ray satellites avoid the Van Allen belts by following eccentric equatorial orbits inside the Earth's magnetosphere. Even though this offers protection from the solar wind, they are shut down during intense solar activity, when even the magnetosphere cannot protect them from the increased charged particle emissions from the Sun.

Information on past and current high energy missions is available online* (Gibb 2011), but they are listed here in Table 1.1 by launch date, for easy reference. A horizontal line indicates the division between past and current missions. Since γ-ray facilities cover the energy range above hard X-rays, they are included. Likewise, the extreme ultraviolet (UV) experiment covers the energy range just below the soft X-ray energies.

International collaborations ensured a large number of satellite missions, particularly during the 1970s. While the 1980s and 1990s saw a decline in their numbers, their average lifetimes increased, allowing several years of overlap between active missions.

Vela-5B was not intended for astronomical studies, but provided useful astronomical observations. Uhuru was the first of the National Aeronautics and Space Administration's (NASA) three Small Astronomical Satellites (SAS) and it added 339 new sources. The Astronomische Nederlandse Satelliet (ANS) was a collaboration between the US & Netherlands. NASA's High Energy Astronomy Observatory (HEAO) included three missions, of which the second (Einstein) added 5600 observations, allowing us to see the distribution of sources in other galaxies and the structure of SNRs. Copernicus or the Orbiting Astronomical Observatory 3 (OAO-3) was a collaborative effort between the US & UK. The Orbiting Solar Observatory (OSO) missions 7 and 8 also observed extrasolar X-ray sources. The European Space Agency (ESA) produced the COS-B γ-ray mission. Hakucho (swan in Japanese) was named for Cyg X-1 and was the first Japanese X-ray astronomy satellite, while Tenma (Pegasus in Japanese) was their second. The ESA's X-ray Observatory (EXOSAT) allowed 76 hours of continuous monitoring for most sources, thereby providing high quality lightcurves. The Röntgen/Roentgen Satellite (ROSAT) deep all-sky-survey produced catalogues with 18000 bright and 105000 faint sources. Shuttle borne missions included the Broad Band X-ray Telescope (BBXRT) and the Diffuse X-Ray Spectrometer (DXS), but were short-lived by satellite mission standards. NASA's Compton Gamma-Ray Observatory (CGRO) discovered the isotropic distribution of γ-ray bursts. NASA's Extreme Ultraviolet Explorer (EUVE) was the first mission dedicated to the extreme UV. Japan's Advanced Satellite for Cosmology and Astrophysics (ASCA) was the first to use CCDs in X-ray astronomy. BeppoSAX was a collaboration between the Netherlands & Italy. The High Energy Transient Explorer (HETE-2) was a collaboration between the US, Japan, France & Italy. A total of 26 past missions of varying lifetimes and energy ranges covered, contributed thousands of new high energy sources.

The Rossi X-ray Timing Explorer (RXTE), provides nanosecond accurate timing and all-sky monitoring. Chandra (a.k.a. AXAF, Advanced X-ray Astrophysics Facility) is dedicated to high quality X-ray imaging. The X-ray Multi-Mirror Mission (XMM-Newton) is capable of simultaneous optical and X-ray observations. The International Gamma-Ray Astrophysics Laboratory (INTEGRAL) is a high resolution γ-ray observatory. Swift is NASA's Gamma-ray Burster (GRB) multi-wavelength follow-up instrument. Japan's Suzaku (a mythological red bird) focuses on broadband spectroscopy. The Italian Space Agency's AGILE combines hard X-ray and γ-ray imaging. Fermi (formerly GLAST) is a highly sensitive γ-ray mission.

*http://heasarc.gsfc.nasa.gov/docs/heasarc/missions/

Table 1.1: High Energy Satellite Missions

Name	Lifetime	Energy Range	Purpose	Catalogue
Vela 5B	1969 - 1979	3 - 750 keV	all-sky	
Uhuru/SAS-1	1970 - 1973	2 - 20 keV	all-sky	2U, 3U, 4U
OSO-7	1971 - 1974	1 keV - 10 MeV	solar	1M
Copernicus/OAO-3	1972 - 1980	0.5 - 10 keV	X-ray	
SAS-2	1972 - 1973	20 Mev - 1 GeV	γ-ray	
ANS	1974 - 1977	1500 - 3300 Å	UV	
		0.1 - 30 keV	X-ray	
Ariel V	1974 - 1980	0.3 - 40 keV	all-sky	1A, 2A, 3A
SAS-3	1975 - 1979	0.1 - 60 keV	X-ray	
OSO-8	1975 - 1978	0.15 keV - 1 MeV	solar	
COS-B	1975 - 1982	2 keV - 5 GeV	γ-ray	
HEAO-1	1977 - 1979	0.2 keV - 10 MeV	all-sky	1H
Einstein/HEAO-2	1978 - 1981	0.2 - 20 keV	all-sky	1E, 1ES, 2E
Hakucho	1979 - 1985	0.1 - 100 keV	X-ray	
HEAO-3	1979 - 1981	50 keV - 10 MeV	γ-ray	H
Tenma	1983 - 1984	0.1 - 60 keV	Fe-spectra	
EXOSAT	1983 - 1986	0.05 - 50 keV	X-ray	EXO
Ginga	1987 - 1991	1 - 500 keV	all-sky	Ginga/GS
Granat	1989 - 1998	2 keV - 100 MeV	γ-ray	Granat/GRS
ROSAT	1990 - 1999	0.1 - 2.5 keV	all-sky	1RXS, RX J
		62 - 206 eV	UV	
BBXRT	Dec 1990	0.3 - 12 keV	shuttle	
CGRO	1991 - 2000	30 keV - 30 GeV	all-sky	GRO J
EUVE	1992 - 2001	70 - 760 Å	all-sky	EUVE J
ASCA	1993 - 2001	0.4 - 10 keV	broadband	AX J
DXS	Jan 1993	0.15 - 0.28 keV	shuttle	
BeppoSAX	1996 - 2002	0.1 - 300 keV	broadband	SAX J
HETE-2	2000 - 2006	0.5 - 400 keV	γ-ray	HETE J
RXTE	1995 -	2 - 250 keV	all-sky, timing	XTE J
Chandra	1999 -	0.1 - 10 keV	imaging	CXO J
XMM-Newton	1999 -	0.2 - 15 keV	imaging	XMM J
INTEGRAL	2002 -	3 keV - 10 MeV	imaging	IGR J
Swift	2004 -	0.2 - 150 keV	GRB follow-up	SWIFT J
Suzaku	2005 -	0.2 - 600 keV	broadband	SUZAKU J
AGILE	2007 -	18 - 60 keV	imaging	
		30 MeV - 50 GeV	X-ray	
Fermi/GLAST	2008 -	0.03 - 10 GeV	γ-ray	
MAXI	2009 -	2 - 16 keV	ISS all-sky	MAXI J

MAXI is an all-sky monitor on the International Space Station (ISS).

1.4 Astronomical X-ray Sources

Less than a decade after launching the first X-ray satellite, catalogued X-ray sources already numbered in the hundreds. Sources were no longer one of the three or four brightest X-ray sources in a particular constellation, and could no longer be afforded the luxury of being called by their constellation name and brightness rank, as Sco X-1 was. Newly discovered sources from satellite missions were therefore catalogued with source designations starting with a prefix indicating the mission, e.g. 4U for Uhuru's 4th catalogue (Forman et al. 1978). The rest of the name contains its coordinates in right ascension (RA) and declination (DEC), e.g. Sco X-1 is 4U 1617-15. Current missions are adding even more new sources, but they all fall into a few specific categories, which are briefly introduced hereafter.

1.4.1 Supernova Remnants

The Crab supernova remnant (SNR) is a bright X-ray source, containing a neutron star (NS) in an expanding shell of hot remnant material of the progenitor star, ejected during the supernova (SN) explosion ($T > 10^{11}$ K). The ejecta cools as it expands into the ISM at near-relativistic speeds ($v \sim 5 - 10\%$ of c) and X-rays are produced by thermal radiation from the shock-front as it propagates through the circumstellar material. In other SNRs, this is the main source of the observed X-ray luminosity (L_x).

However, the NS in the Crab SNR is a radio pulsar, a rapidly spinning NS with a strong $\overrightarrow{B}$ (Hewish et al. 1968, Gold 1968). The near-relativistic electrons in the pulsar wind nebula (PWN) that surrounds it, interact with the $\overrightarrow{B}$ to emit synchrotron radiation, contributing the majority of the $L_x \sim 10^{37}$ erg s^{-1} for the Crab.

1.4.2 Stellar Coronae

Most stellar coronae, even those of late-type stars like our Sun, are extremely high temperature ($T \sim 10^6$ K), low-density or tenuous regions filled with charged particles (ions and electrons) and are consequently sources of high-energy thermal radiation. The soft X-ray luminosities from stellar coronae range from $L_x \sim 10^{26} - 10^{33}$ erg s^{-1}, where the lower limit is applicable to our Sun.

1.4.3 Solar System Sources

The solar corona extends outward to become the solar wind and X-rays may be produced as it interacts with the atmospheres of planets. Auroral X-rays on Earth and Jupiter are the result of charged particles interacting with the atmosphere, as they are funnelled onto the auroral zones by the magnetic field lines. Solar X-rays are scattered from the Earth's atmosphere and the surface of the Moon. Comets also produce X-rays as their material interacts with solar wind particles.

1.4.4 Accretion-powered Binaries

The true nature of the bright astronomical X-ray sources largely remained a mystery until data from the Uhuru satellite revealed binary orbital periods in Cyg X-1 (Bolton 1972a, Webster & Murdin 1972) and Cen X-3. A rapidly spinning NS accounts for the 4.84 second pulsations in the X-ray flux of Cen X-3 (Giacconi et al. 1971), but the slight variations in those pulsations over a period of 2.09 days occur due to Doppler shift, as that NS orbits a supergiant optical counterpart (Schreier et al. 1972a). X-rays are produced as matter from the supergiant falls onto the surface of the NS and disappears for ~ 11 hours every orbit, as that accretion zone is eclipsed by the supergiant.

Most of the X-ray sources found in our Galactic bulge and plane are such systems, where a donor star (of mass M_2) transfers stellar material to a compact object (of mass M_1). They represent the brightest X-ray sources in our galaxy, up to $L_x \sim 10^{38}$ erg s^{-1}, which is comparable to that of the Crab SNR and $\sim 10^{11}$ times that of the solar corona.

Large accretion-powered binary populations have also been discovered in our neighbouring galaxies, a.k.a. the Local Group which includes the Milky Way, the Andromeda galaxy (M31), M33, the Small Magellanic Cloud (SMC) and the Large Magellanic Cloud (LMC). Though much more distant, the major advantage in studying those populations is the fact that they can all be considered to be at an equal distance from the observer.

Cataclysmic Variables

Warner (1995) presented an exhaustive review on the subject of Cataclysmic Variables (CVs), which contain white dwarf (WD) compact objects (surface $T \sim 30000$ K) and cool late-type donors. The majority of their radiation is in the optical regime, however extragalactic CVs include super-soft sources (SSS), with super-soft (< 1 keV) X-ray emission of $L_x \sim 10^{36}-10^{38}$ erg s^{-1} (Kahabka & van den Heuvel 1997). Since CVs have been studied extensively in the optical, decades before the discovery of X-ray binaries, much of the nomenclature pertaining to accretion-powered binaries originate from their study. See Figure 1.3, which illustrates the components of a CV.

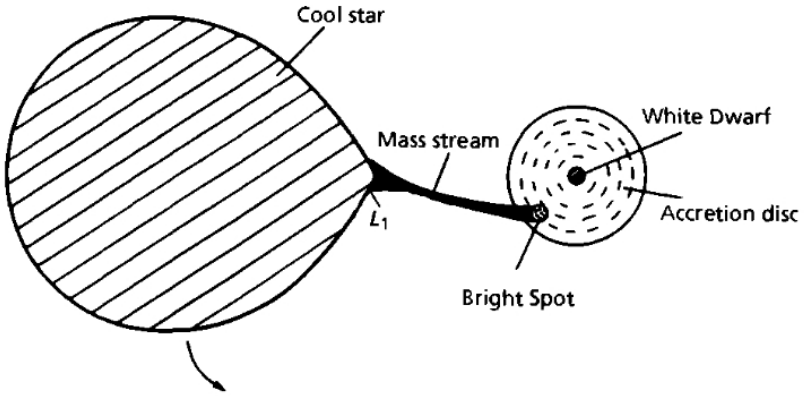

Figure 1.3: CV diagram (viewed from above) showing its major components (Warner 1995).

WDs, with masses of $< 1.4M_{\odot}$ and radii ~ 10000 km (comparable to that of the Earth), are extremely dense objects that create deep gravitational wells, into which matter would fall once captured by their gravitational influence. Electron degeneracy pressure supports them against further gravitational collapse and they represent the end product of stellar evolution of the majority of main sequence (MS) stars.

X-ray Binaries

Lewin & van der Klis (2006) edited an extensive review on the subject of X-ray binaries (XRBs), which contain NS or black hole (BH) compact objects. XRBs have either late-type main sequence stars or early-type giants/supergiants as donors and are further discussed in Chapter 2.

NSs may form as end products of the stellar evolution of sufficiently massive stars (Oppenheimer & Volkoff 1939). Above the Chandrasekhar limit ($1.4M_{\odot}$), electron degeneracy pressure fails to support a star against further gravitational collapse and it will collapse until neutron degeneracy pressure can support it.

NSs have masses of $\sim 1.4M_{\odot}$ squeezed into radii of $\sim 10 - 15$ km and represent even deeper gravitational wells than WDs do. BHs, with all their mass collapsed into singularities, can be considered infinitely deep gravitational wells and form if neutron degeneracy pressure fails to support a star against further collapse. Consequently, XRBs present an excellent opportunity to study NSs, the upper limit for NS masses (Section 2.3) and BHs.

X-ray Pulsars

Jocelyn Bell and Antony Hewish discovered the first radio pulsar (PSR) in 1967, by detecting pulsations of 1.337 seconds in data acquired during the testing of their newly constructed radio telescope. In Hewish et al. (1968) these pulsations were associated with oscillations of a WD/NS. However, Gold (1968) suggested that a NS with a strong $\overrightarrow{B}$ offers the only reasonable explanation for this pulsed radiation, that appears as though it was produced by a rotating beacon.

In XRBs, in-falling material is threaded onto these strong $\overrightarrow{B}$ lines once it reaches the magnetosphere of a NS (Ghosh & Lamb 1979a;b). These $\overrightarrow{B}$ lines funnel material toward the magnetic poles of the NS, where the in-falling material forms a hot X-ray producing shock. The X-ray emission is beamed in cones from there and the displacement of the magnetic and rotational axis from each other causes a lighthouse effect as the spinning NS causes these cones to sweep regularly over the observer's line of sight, thereby producing an X-ray PSR.

X-ray PSRs spin up as the result of accretion. Transferred material imparts angular momentum to them, which must be conserved, so they spin up. Brighter sources have faster spin-up rates, since more mass is transferred in those cases. Radio PSRs do not accrete material and tend to spin down, since they lose angular momentum as they emit a relativistic wind of particles powered by the rotating dipole.

1.4.5 Extragalactic Sources

X-ray sources outside our galaxy do not only include vast populations of accretion-powered binaries and SNRs in other galaxies, but also a variety of active galactic nuclei (AGN), lying at the hearts of galaxies that contain supermassive black holes (SMBHs). Depending on the viewing angle (Antonucci 1993, Urry & Padovani 1995), the AGN could appear as radio galaxies with narrow (NLRG) or broad (BLRG) emission lines, Blazars/BL Lac-objects, Quasars/quasi-stellar objects (QSOs), low-ionization nuclear emission region (LINER) galaxies, Seyfert 1 or Seyfert 2 galaxies. It is suggested that these SMBHs might be far more common than the numbers of AGN suggest, and that a galaxy becomes active if a star strays close enough to its SMBH to be ripped apart and accreted.

AGN account for many background X-ray sources when observing nearby galaxies and are supermassive versions of XRBs, which are called microquasars if they launch relativistic jets under conditions of extreme accretion (Chapter 2). Apart from sharing the jets that produce extended radio lobes as they impact the ISM, both quasars and microquasars contain discs of in-spiralling material that surround their BHs. See Figure 1.4 from Mirabel (2007).

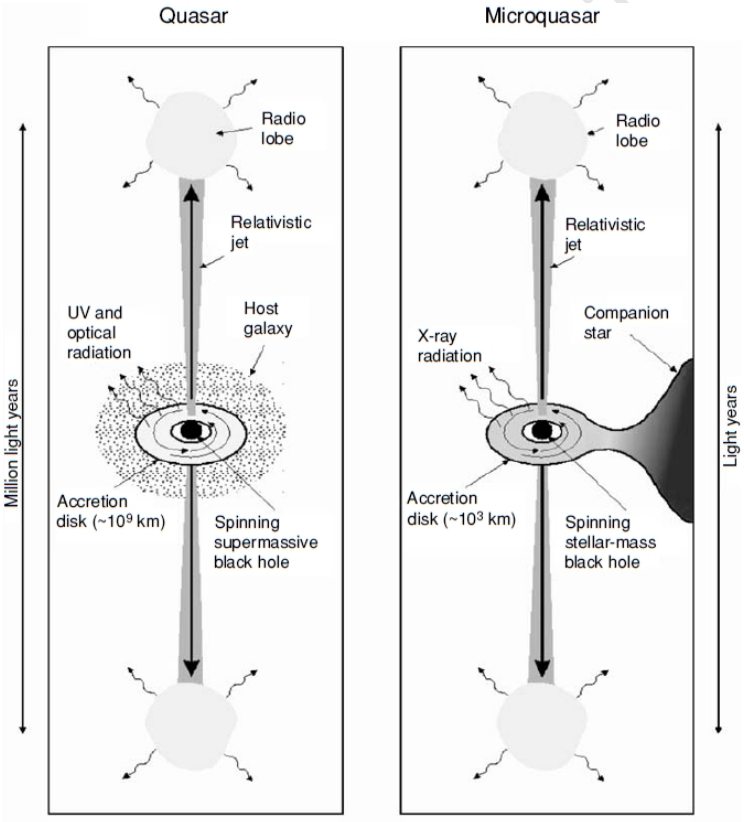

Figure 1.4: Quasar & Microquasar diagram (Mirabel 2007).

The hot gas ($T > 10^7$ K) between and around galaxies in clusters and groups is known as the intracluster medium (ICM). This strong source of diffuse X-ray emission (Mitchell et al. 1976), associated with dark matter, has been used to identify distant galaxy clusters.

1.5 Mass Transfer

Stars lose mass via radially out-flowing radiation-driven winds (Castor et al. 1975) at rates of $\sim 10^{-13} M_\odot$ yr^{-1} (late-type MS stars), $\sim 10^{-6} M_\odot$ yr^{-1} (early-type giants/supergiants) and up to $\sim 10^{-3} M_\odot$ yr^{-1} (Wolf-Rayet stars). Since these winds carry stellar material away from stars, it is an immediately obvious mechanism by which mass may be transferred in accretion-powered binaries. However, a far less intuitive but more efficient mechanism is introduced in this section together with some of the important consequences of mass transfer. The latter includes the formation of accretion discs and the emission of radiation during the accretion process. Frank et al. (2002), the standard reference for accretion in astrophysics, covers not only accretion-powered binaries but also AGN and protostellar systems. The review by King (2006) focuses on accretion in compact binaries.

1.5.1 Roche-lobe Overflow

Material can be transferred from a donor (of mass M_2) to a compact object (of mass M_1) by Roche-lobe overflow (RLO), the mass-transfer mechanism in CVs (Pringle & Wade 1985, Warner 1995). The Roche-equipotential surfaces are shown as contours in Figure 1.5, where the combined gravitational and centrifugal potentials are constant. Their shapes are determined by the mass ratio ($q = \frac{M_2}{M_1}$) and their scale by the binary separation distance (a) between the centres of mass of the stars. Forces balance at the inner Lagrangian point (L_1) and the equipotential that includes it defines the Roche lobes of the stars. RLO occurs once the donor fills its Roche lobe and takes place via the saddle-point at L_1, forming a ballistic accretion stream in which material travels faster than the speed of sound (c_s).

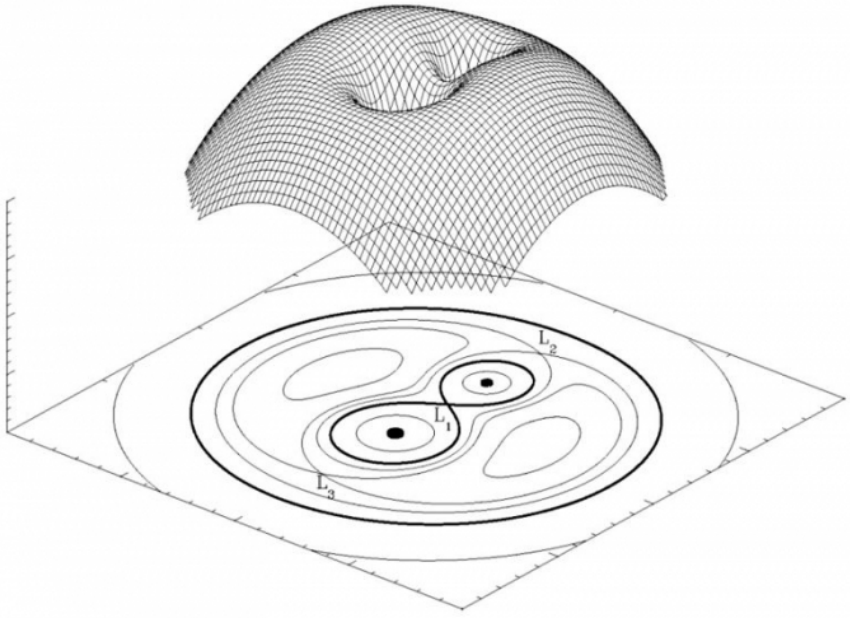

Figure 1.5: Roche geometry (van der Sluys 2006).

1.5.2 Accretion Discs

Shakura & Sunyaev (1973) described how transferred material, which has angular momentum, cannot be accreted onto the compact object directly but will lose angular momentum gradually as it spirals in toward it (Figure 1.6), forming a thin disc. The top figure shows RLO and the bottom one a stellar wind scenario. Viscosity in the disc causes material to heat up as it moves inward through the disc, giving the accretion disc a wide range of temperatures from inner disc to outer edge. Each disc annulus, at a temperature that increases radially inwards, is considered to be a blackbody.

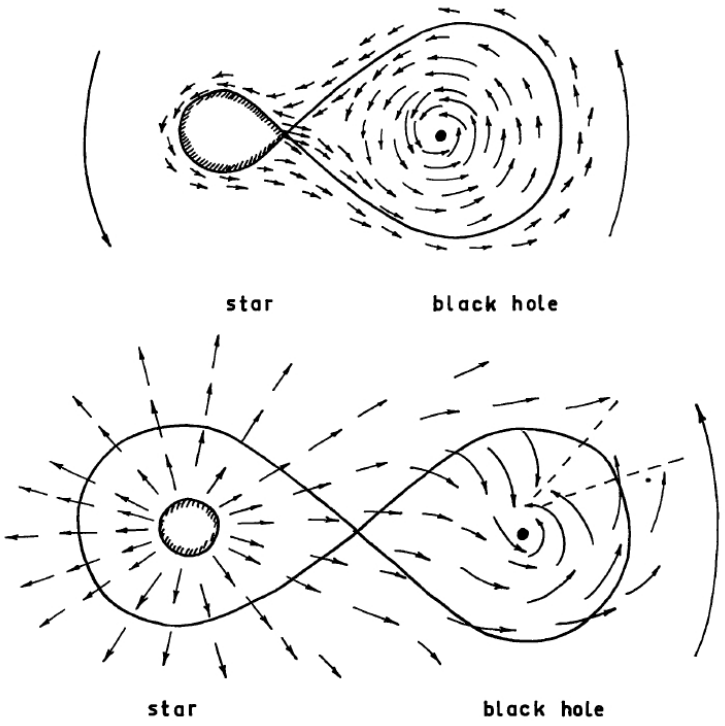

Figure 1.6: Accretion discs (top view) (Shakura & Sunyaev 1973).

Figure 1.7: Accretion disc (side view) (Shakura & Sunyaev 1973).

The accretion stream impacts the disc at the outer edge, producing a bright spot. The result is a bulge at the impact site and due to the in-spiralling of the material through the disc, the entire disc edge becomes flared in comparison to the rest of the disc.

The viscosity parameter (α), sound-speed (c_s) and vertical structure of the accretion disc (Equation 1.1) or scale height (H) define this viscosity as $\nu = \alpha c_s H$. These thin discs with flared edges are called Shakura-Sunyaev or α-discs (Figure 1.7), in which accretion of material at a particular radius (R) occurs on the viscous time-scale (τ_{visc}).

$$H \simeq \frac{c_s}{\sqrt{GM}} R^{\frac{3}{2}} \ll R \tag{1.1}$$

Pringle (1981) reviewed accretion in astrophysics while the nature of the viscosity, responsible for the angular momentum transport in accretion discs, was still mysterious. However, the magneto-rotational instability (MRI) proposed by Balbus & Hawley (1991) may provide the mechanism to account for the viscosity. According to the MRI a weak $\overrightarrow{B}$, threading a differentially-rotating accretion disc, is wound up by the shear in the disc. Angular momentum is transported outwards and magnetic reconnection allows for the dissipation of the $\overrightarrow{B}$, thereby limiting its growth. The τ_{visc} in dwarf novae (a sub-class of CVs) imply $\alpha \sim 0.1$ and numerical simulations of the MRI have sometimes yielded comparable values for α.

The circularization radius (R_{circ}) defines the radius at which transferred material would orbit a compact object (of mass M) if no angular momentum (J) was lost (Equation 1.2), where G is the gravitational constant. An accretion disc will form if R_{circ} exceeds the effective size of the compact object, which is the radius of a non-magnetic WD or NS, the radius of the last stable circular orbit for a BH and approximately the magnetospheric radius if its $\overrightarrow{B}$ is dynamically significant. Viscosity transports angular momentum to spread the ring at R_{circ} inwards into a disc.

$$R_{circ} = \frac{J^2}{GM} \tag{1.2}$$

In addition to the viscous time-scale (τ_{visc}) and thermal time-scale (τ_{th}), other relevant time-scales (τ) are represented in Equation 1.3. In this context, R is the outer-disc radius. The dynamical equilibrium and the vertical hydrostatic balance are restored on the dynamical time-scales τ_{dyn} and τ_z respectively. These imply that $\tau_{dyn} < \tau_{th} < \tau_{visc}$.

$$\tau_{visc} \sim \frac{R^2}{\nu} \quad , \quad \tau_{th} \sim \left(\frac{H}{R}\right)^2 \tau_{visc} \quad , \quad \tau_{dyn} \sim \sqrt{\frac{R^3}{GM}} \quad , \quad \tau_z \sim \frac{H}{c_s} = \tau_{dyn} \tag{1.3}$$

1.5.3 Accretion Power

It is the descent of transferred matter into deep gravitational wells that results in the radiation of X-rays. If a compact object with mass (M) and radius (R) accretes material at rate $\dot{M} \equiv \frac{dM}{dt}$, gravitational energy will be released as radiation of luminosity $L = GM\dot{M}/R$. For $M \sim 1M_{\odot}$, the observed $L_x \sim 10^{38}$ erg s^{-1} in XRBs would be released through accretion of $\dot{M} \sim 10^{-8} M_{\odot}$ yr^{-1}.

The total energy that matter possesses may be expressed by Einstein's formula $E = mc^2$. The luminosity produced, as a result of the accretion of mass $\dot{M}$, may be expressed as a fraction (η) of that energy (Equation 1.4). This allows the efficiency of the accretion process to be compared to other processes that also release energy.

$$L = \eta \dot{M} c^2 \ , \ \eta = \frac{GM}{Rc^2} \tag{1.4}$$

Higher values of η imply a more efficient release of energy and M/R is higher for more compact objects. For a WD $\eta \sim 0.001$, for a NS $\eta \sim 0.1$ and for a BH $\eta \sim 0.06 - 0.42$, while nuclear reactions have an efficiency of $\sim 0.001 - 0.01$ in comparison. Accretion of matter onto NSs or BHs is therefore an extremely efficient mechanism by which energy is released.

1.5.4 The Eddington Limit

The radiation from a star with luminosity L and radius R, creates radiation pressure ($\sigma_o L/4\pi R^2 c$) on an electron with Thompson cross-section σ_o. If L is large enough, it can overcome the gravitational force (GMm_p/R^2) of a compact object with mass M, for a proton of mass m_p. Assuming protons and electrons are electrostatically bound, accretion is spherically symmetric and the accreting plasma is pure Hydrogen, the luminosity where the radiation pressure becomes sufficiently large to prevent further accretion is known as the Eddington luminosity (L_{Edd}).

$$L_{Edd} = 1.3 \times 10^{38} \left(\frac{M}{M_\odot}\right) \quad \text{erg s}^{-1} \tag{1.5}$$

1.6 Periodic Variations

The detection of strictly periodic variability in Cen X-3, was instrumental in the interpretation of this bright X-ray source as an accretion-powered binary. There are at least two stable periodic signals that may be detected in these types of binaries (White et al. 1995).

1.6.1 Spin

Since the spin period (P_{spin}) indicates the rotation speed of an object, comparing it to the equatorial velocity ($v = 2\pi R/P_{spin}$) of the object gives an indication of its size. Radii (R) at which the centrifugal force (mv^2/R) experienced by mass (m) is less than the gravitational force (GMm/R^2) on it, is given by Equation 1.6, where G is the gravitational constant.

$$R < \left(\frac{GMP_{spin}^2}{4\pi^2}\right)^{\frac{1}{3}} \tag{1.6}$$

For $M = 1M_\odot$ and $P_{spin} = 1$ s this gives $R < 1500$ km, while radii are ~ 10000 km for a WD and $\sim 10 - 15$ km for a NS. Historically this calculation offered proof that the compact object in such a case must be a NS, rather than a WD (Giacconi et al. 1971).

Moreover, a rapidly spinning X-ray PSR will produce a periodic modulation in the X-ray flux as the collimated X-ray beam sweeps across the line of sight of the observer. The major importance of the detection of a very rapid spin period, is therefore the implication that the compact object must necessarily be an accreting PSR (i.e. a NS with large $\overrightarrow{B}$). Such pulsations will not be observed from a rapidly spinning BH, but only from a NS.

1.6.2 Orbit

Eclipsing systems allow for a direct measurement of the orbital period (P_{orb}) from the periodic modulation in their lightcurves and Doppler shifts produced as a radiation source moves around in an orbit, can be measured by shifts in spectral lines from their rest values. Kepler's third law allows us to calculate the binary separation (a in units of $R_\odot$), using the P_{orb} (in days) and total mass ($M_1 + M_2$ in units of $M_\odot$) of a binary system, by:

$$a = 4.2\,(M_1 + M_2)^{\frac{1}{3}}\,P_{orb}^{\frac{2}{3}} \tag{1.7}$$

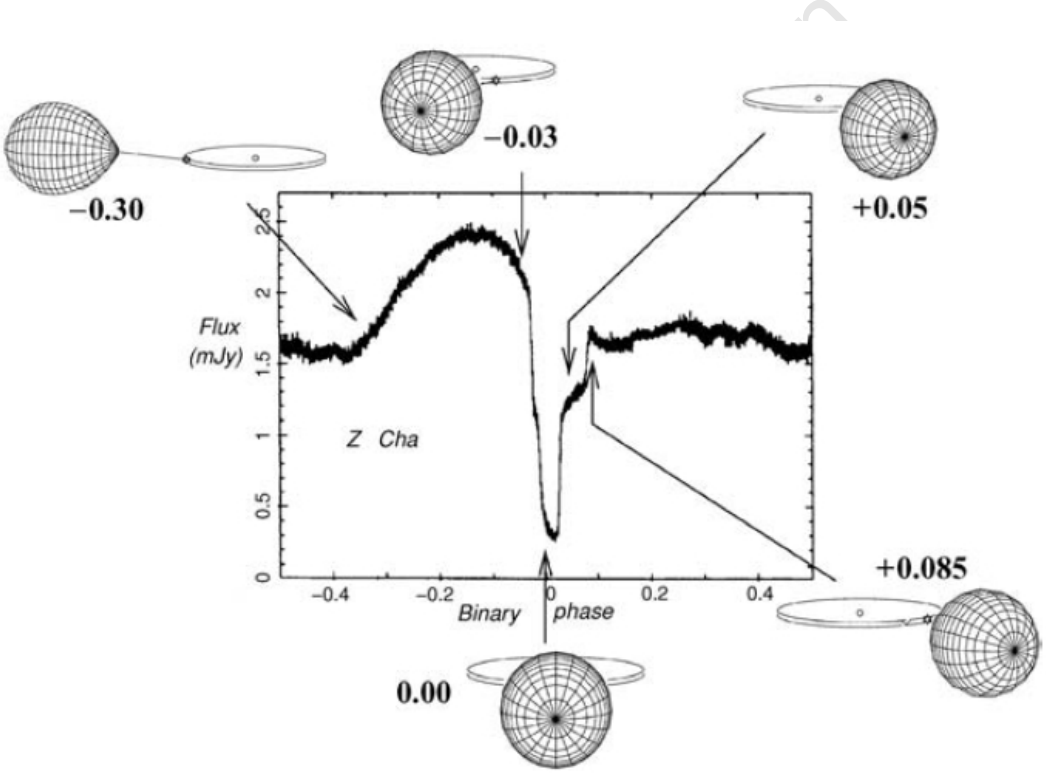

Figure 1.8: An eclipsing accretion-powered binary (Seward & Charles 2010).

Figure 1.8 was adapted by Seward & Charles (2010) from lecture notes by Tom Marsh. It shows a deep minimum in the flux at phase 0 in the optical lightcurve of Z Cha (a CV), produced by the eclipse of the WD and bright spot. The WD comes out of eclipse very rapidly (vertical increase) followed by the bright spot, which remains at the far side of the disc thereafter. Finally the bright spot moves back into full view at the front of the disc, producing the big maximum flux bump before phase 0.

1.7 Quasi-periodic Variations

Variations, over the entire range of time-scales, that are only semi-regular/semi-periodic are referred to as quasi-periodic (White et al. 1995). However, the term "quasi-periodic oscillations" (QPOs) generally refers to very high-frequency oscillations, observed on time-scales of $\sim$ Hz – kHz (van der Klis 2006). To avoid misunderstanding, longer term quasi-periodic behaviour is rather referred to as quasi-periodic modulations.

1.7.1 QPOs

The revised beat-frequency model (Lamb et al. 1985) suggested that unstable X-ray oscillations may be produced by the difference in frequency between the P_{orb} and the P_{spin} of NSs. Material accreted onto the compact object is not a uniform plasma, but is rather clumpy, containing blobs of varying sizes. Some QPOs are believed to be the result of clumps of matter falling through openings in the barrier that the rapidly spinning magnetosphere of the NS produces. These are situated over the magnetic poles of the NS and a short X-ray flash is produced when a clump of material falls through onto the NS surface. Source brightening implies a higher accretion rate, which is also expected to produce more frequent X-ray flashes as more clumps hit the NS surface, producing higher frequency QPOs. Consequently, QPOs change to higher frequencies as sources brighten, but disappear above a certain brightness. If the $\overrightarrow{B}$s in the NSs are weak, the accretion onto the magnetic poles occurs over much larger areas than in the case where NSs have large $\overrightarrow{B}$s. This has the effect of smearing out the spin related periodic signal, otherwise observable for X-ray PSRs. QPOs are therefore normally $\sim P_{spin}$ and $< P_{orb}$.

However, stable high-frequency QPOs have been observed in accretion-powered binaries where the compact objects are believed to be BHs. Such systems are without the influence of a $\overrightarrow{B}$ or direct radiation from the compact object (as applicable in NS systems). It may therefore be expected that they exhibit more stable high-frequency QPOs than those observed in NS systems.

1.7.2 Super-orbital Variations

Periodic or quasi-periodic (even aperiodic) variations with periods $P > P_{orb}$ are known as super-orbital modulations, associated with super-orbital time-scales/periods (P_{sup}). A variety of mechanisms have been proposed to account for such observed modulations in the X-ray lightcurves of XRBs, some with their own predictions about discernible characteristics (discussed in Chapter 4). A major aim of this thesis is to systematically characterize the behaviour of these observed super-orbital modulations, in an effort to distinguish between the mechanisms likely to be responsible for them.

The major results from this work include revealing the behaviour of long-term modulations over time, allowing comparison to the theoretical predictions of the mechanisms that have been proposed to account for their existence. Those results have been published in

Kotze & Charles (2012). A significantly expanded version thereof is included as Chapter 6, with conclusions presented in Chapter 8.

This work also led to the serendipitous discovery of very long-term modulations in some XRBs, which have been published in Kotze & Charles (2010). Updated results, including two additional years of data, are presented and discussed in Chapter 7. Conclusions have been included in Chapter 8.

Chapter 2

X-ray Binaries

X-ray binaries (XRBs) are the main theme of this work and are accretion-powered binary systems (Chapter 1), containing a donor star (of mass M_2) which transfers stellar material to a compact object (of mass M_1). Their particular nomenclature from Lewin & van der Klis (2006) and Seward & Charles (2010) is introduced here, but relevant basic references are included where appropriate. The compact object in an XRB, reviewed by Psaltis (2006), could be either a neutron star (NS) or a black hole (BH). While super-soft sources (SSS) are also accretion-powered binaries that are bright in X-rays, they are Cataclysmic Variables (CVs) with white dwarf (WD) compact objects (Kahabka & van der Heuvel 2006).

The classification of an XRB refers directly to the mass of its donor, as either high or low. Table 2.1 in Section 2.6 summarizes the major differences between these types, after they have been discussed in more detail in this chapter. Typically the total binary mass is $M_1 + M_2 \sim 2 - 40 M_\odot$ and orbital periods are $P_{orb} < 20$ days, down to as short as ~ 10 minutes. Consequently $a \sim 2R_2$ by using Kepler's third law, implying that the binary separation is comparable to the size of the donor star.

2.1 Low-Mass X-ray Binaries

The very first extrasolar X-ray source discovered, Sco X-1, belongs to the class of low-mass X-ray binaries (LMXBs). See Figure 2.1 for an illustration of such a system. P_{orb} ranges from tens of minutes to days and the mass donors are slightly evolved cool late-type stars ($M_2 < 1 M_\odot$), which are optically faint and difficult to detect. The mass-transfer mechanism in LMXBs is Roche-lobe overflow (RLO) and they are therefore similar to CVs in many aspects, with the only major difference being the type of compact objects they include. The rest of the morphology is essentially the same and consequently uses the same nomenclature. The major observational difference is that CVs (except SSS) are usually weak X-ray sources ($L_x < 10^{33}$ erg s^{-1}) and LMXBs are strong X-ray sources ($L_x > 10^{35}$ erg s^{-1}). At higher luminosities, and depending on spectral and temporal characteristics, the compact object may be considered a BH candidate (White & Marshall 1984).

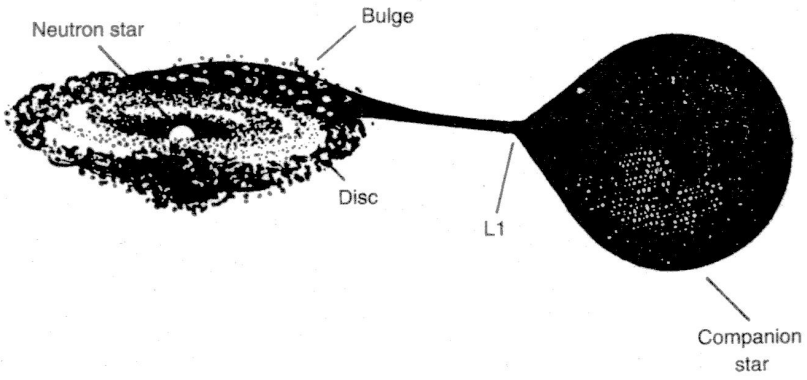

Figure 2.1: LMXB illustration. Credit: EXOSAT Observatory, ESA.

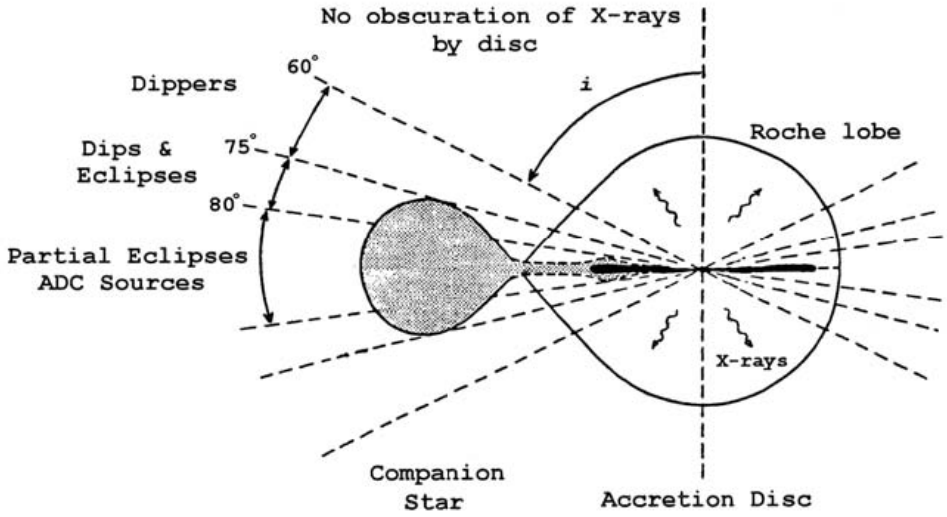

Figure 2.2: Schematic of inclination limitations (Seward & Charles 2010).

2.1.1 Inclination Limitations

P_{orb} is very difficult to detect from the X-ray lightcurves of LMXBs, due to the morphology of the systems. The accretion disc itself poses a problem in detecting the X-ray source in the inner disc, since the disc edge is thick enough to shield the central regions from edge-on observers. Therefore, only a narrow range of inclination angles (i) would allow a donor to eclipse an X-ray source, which needs to be visible over the disc edge, in order to produce the signature orbital modulation in the X-ray lightcurve (see Figure 2.2). Photometry of the faint optical counterparts, which are irradiated by the X-ray source, allowed the P_{orb} to be determined for many of these systems.

2.1.2 X-ray Dippers

If the donor is just larger than the projected disc edge and the observer is at a very particular inclination (see Figure 2.2), the X-ray source will only be eclipsed or partially eclipsed for a very small portion of the binary orbit. For example, in EXO 0748-676 the X-ray eclipses last ~ 8 minutes of the P_{orb} of 3.8 hours. These sources allow a unique opportunity to observe the variable vertical structure of the edge of the accretion disc itself (White & Swank 1982).

2.1.3 Accretion Disc Coronae

For a high i, closer to the orbital plane, the X-ray emitting inner disc region and compact object would permanently be hidden behind the disc edge. However, X-ray emission is observed in some of these sources, which must therefore originate from an extended region in the direction of the compact object. These X-rays are scattered toward the observer by an accretion disc corona (ADC), producing a weak X-ray source that is modulated as the structure of the edge of the accretion disc changes with viewing angle as the binary rotates over time (White & Holt 1982).

2.1.4 X-ray Bursters

Strohmayer & Bildsten (2006) reviewed bursts in LMXBs. There are two types of bursts under consideration when referring to X-ray bursters, namely type I and type II bursts.

Type I bursts last ~ 1 minute, reach maximum $L_x \sim 1.8 \times 10^{38}$ erg s^{-1} (which is $\sim L_{Edd}$ for a $1.4 M_{\odot}$ NS) and are characterized by a rapid rise, which is directly followed by a tail of fast (slow) decay at higher (lower) energies (Grindlay et al. 1976). It is believed to be the result of unstable thermonuclear burning of He on the surface of the NS (He flash), where transferred material first formed a layer of H, which steadily fused to form a He layer and actually contributed to the "steady" X-ray flux detected. The recurrence time-scale of bursts (~ 3 hours) is therefore linked to the mass-transfer rate ($\dot{M}$), since higher $\dot{M}$ would lead to more frequent X-ray bursts.

Type II bursts observed every ~ 10 seconds in the rapid burster MXB 1730-335 have a different origin (Lewin et al. 1993). Each burst depends on the preceding one, because larger bursts are followed by longer gaps, while small bursts rapidly follow one another. If a NS is surrounded by a strong enough $\overrightarrow{B}$, its magnetosphere can act like a gate that temporarily holds transferred material back. The combined pressure of material piling up behind it, eventually overcomes the magnetic support and the gate opens, allowing material to fall onto the NS surface and produce an X-ray burst. The gate closes immediately and transferred material starts building up behind the magnetospheric gate again. The size of the burst and the time to the next burst therefore both depend on the amount of material that passed through the gate. Thermonuclear induced X-ray bursts (type I) may also still occur in these cases and are therefore not excluded by the occurrence of type II bursts.

2.1.5 Atoll and Z Sources

Hasinger & van der Klis (1989) classified some LMXBs as Atoll or Z sources, based on the strong correlation between their X-ray timing properties and their spectral states. They studied the power spectra of a source as a function of its behaviour in the X-ray colour-colour diagram (e.g. Figure 2.3). In doing so, they identified a class of sources with Z-shaped colour-colour diagrams (called Z sources as a result) and another class with fragmented colour-colour diagrams (called Atoll sources). The latter may exhibit a banana-shaped branch together with several isolated islands. Figure 2.3 includes colour-colour diagrams of Z sources (left) and Atoll sources (right).

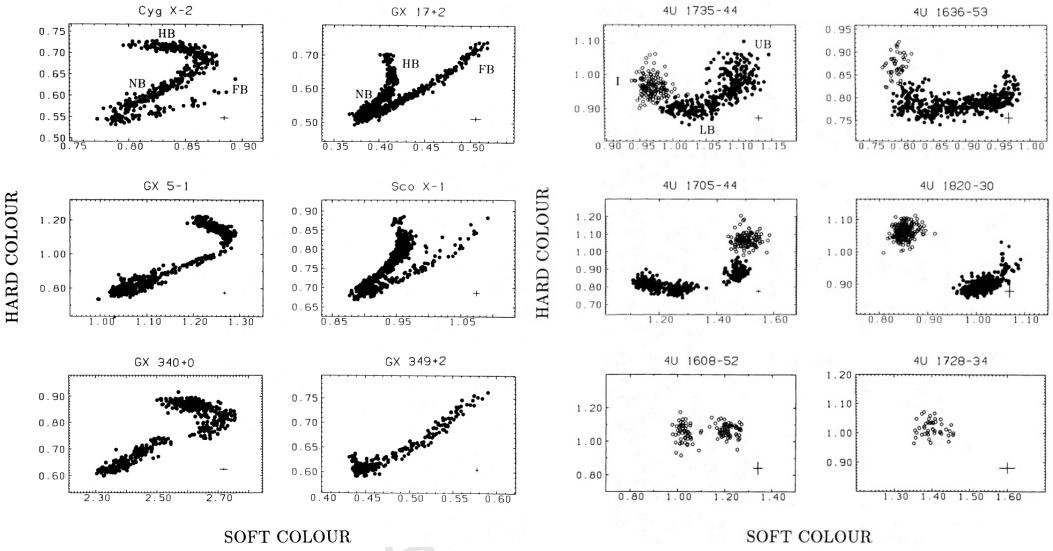

Figure 2.3: Colour-colour diagrams of Z and Atoll sources (Hasinger & van der Klis 1989).

The three branches of the Z-shape, indicated on Z source colour-colour diagrams, are the horizontal branch (HB), the normal branch (NB) and the flaring branch (FB). Each branch represents a different spectral state and each spectral state is characterized by specific X-ray timing properties, e.g. flux dependent high-frequency QPOs and low-frequency red noise are observed in the HB, but are weak or absent in the NB, and only high-frequency QPOs are present in the FB. The features, indicated on Atoll source colour-colour diagrams, are the upper banana (UB), lower banana (LB) and islands (I). Very low-frequency noise is observed in the banana branch, while high-frequency noise dominates during the island states.

Z sources have higher accretion rates and are more X-ray luminous as a result, while Atoll sources have much lower accretion rates and are fainter. Furthermore, they suggest that Z sources have NSs with stronger $\overrightarrow{B}$s than those in Atoll sources. As further products of this apparently different evolutionary history, evolved companions are only present in Z sources and P_{orb} are longer for Z sources and shorter for Atoll sources.

2.1.6 LMXB Evolution

Tauris & van der Heuvel (2006) reviewed the evolution of CVs and LMXBs, which evolve from detached close binaries wherein the more massive stars evolve more rapidly. The subsequent binary evolution, which ultimately leads to the formation of CVs and LMXBs, depends on the masses of the binary components (Patterson 1984). Once formed, their evolution is determined by their sustained high mass-transfer rates, which require the effective loss of angular momentum by magnetic braking of the donor and gravitational radiation.

The high stellar densities in globular clusters seem conducive to the formation of LMXBs (Hut et al. 1992, Pooley et al. 2003, Verbunt & Lewin 2006). There are two mechanisms under consideration whereby a single NS can acquire a companion in such a crowded environment. Firstly, the compact object can tidally distort a potential companion as it approaches (Fabian et al. 1975). Two unbound stars before their interaction will remain unbound afterwards unless energy is lost somehow. Raising tides provides the opportunity to do that. It is more likely to occur if the captured star is larger, e.g. a red giant. Secondly, the compact object can replace the lower mass star in a wide non-interacting binary, through triple-star interaction (Hills 1976). The first mechanism is believed to have a greater probability of success and it would therefore be the dominant LMXB formation mechanism in crowded environments (Verbunt & Hut 1987). If a NS and a red giant collide (expected 1 in 3 times), the latter is not disrupted but the NS ends up inside the red giant's outer layers or common envelope (CE). The NS will spiral in toward the red giant's He core and produce an enormous amount of X-ray radiation as it accretes vast amounts of material while doing so. However, radiation is scattered in the CE during this phase and the binary becomes highly obscured. It likely remains unobserved until it sheds the CE as a result of the propeller action created by the rapidly orbiting binary components. At the end of this phase the NS is left orbiting a He WD in an ultra-compact X-ray binary (UCB) with $P_{orb} \sim 10$ minutes. If a NS captures a MS star or sub-giant, the mass transfer will be unstable and subsequently the donor would eventually expand to engulf the NS. This presents the same situation and evolution as described in the case where a NS and red giant collides.

After the mass-transfer phase, the NS remains alone or in a detached binary. As one of the oldest population of stars, the NS has a weak $\overrightarrow{B}$ because of its decay over time. However, the accretion of material over long periods of time can transfer large amounts of angular momentum directly to the NS, spinning it up. Millisecond radio pulsars (MSPs) necessarily result from the described LMXB evolution, because such extreme mass transfer is required to spin them up sufficiently.

2.1.7 LMXB Population Distribution

Slowly evolving low-mass late-type stars form part of the older population of stars in our Galaxy. Consequently LMXBs are concentrated in and around our Galaxy's bulge region and close to the cores of its globular clusters. The size of the population of LMXBs in a galaxy can therefore be linked to its overall stellar population density (Gilfanov 2004).

2.2 High-Mass X-ray Binaries

High-mass early-type donor stars ($M_2 > 10M_\odot$) have strong stellar winds from which material can be accreted onto the compact object as it moves through this radially out-flowing stellar wind ($\dot{M}_w$). See Figure 2.4 for an illustration of such a system. Early-type stars are optically bright and consequently high-mass X-ray binary (HMXB) donors are easy to identify. P_{orb} ranges from several days to tens or even hundreds of days.

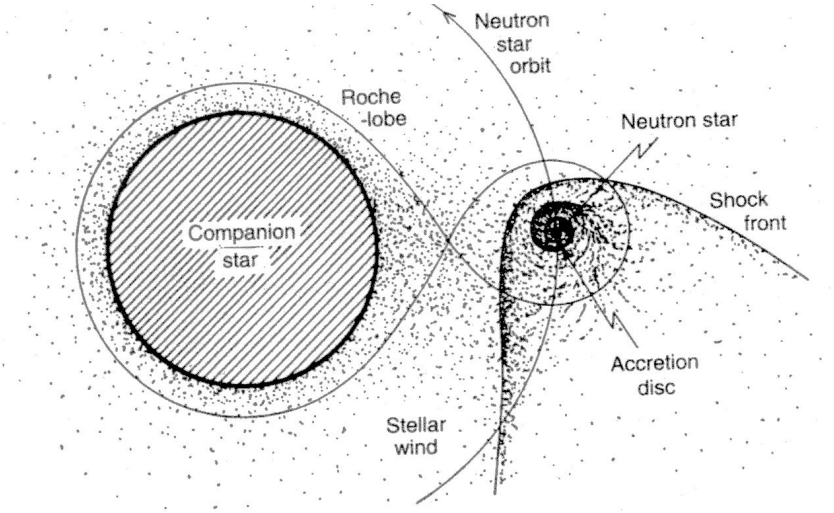

Figure 2.4: HMXB illustration. Credit: EXOSAT Observatory, ESA.

A stellar wind carries little angular momentum, therefore large accretion discs are unlikely to form in HMXBs. The Bondi-Hoyle equation calculates the fraction of the stellar wind that may be accreted, using the velocities of the wind (v_w) and compact object (v). Material will be accreted if the gravitational potential near M_1 exceeds its kinetic energy. The Bondi-Hoyle equation was first applied to HMXBs by Davidson & Ostriker (1973).

$$\frac{\dot{M}}{\dot{M}_w} = \left(\frac{M_1}{M_2}\right)^2 \frac{(v/v_w)^4}{[1+(v/v_w)^2]^{3/2}} \sim 10^{-3} - 10^{-5} \tag{2.1}$$

Therefore 0.1% of the typical $\dot{M}_w \sim 10^{-6} M_\odot$ yr^{-1} yields $\dot{M} \sim 10^{-9} M_\odot$ yr^{-1}, in comparison with the required $\dot{M} \sim 10^{-8} M_\odot$ yr^{-1} to achieve the observed $L_x \sim 10^{38}$ erg s^{-1}. Consequently $\dot{M}$ accounts for a significant portion, if not all, of the observed L_x.

X-ray pulsars (PSRs) are often found in HMXBs and allow the mass of the NS to be determined from observational parameters. The pulsar spin period shows a modulation on the orbital cycle in the X-rays, due to Doppler shifts, as it moves in a near-circular orbit around the donor star. Doppler shifts relating to the motion of the donor, can be observed in absorption lines at high spectral resolution in the optical, since the donors are usually bright in the optical. The majority of such mass determinations are consistent with the Chandrasekhar mass ($1.4M_\odot$), but there are a few systems that show evidence of NS masses greater than this as a relic of their formation mechanism.

HMXBs divide into two large groups. The first group contains early-type OB supergiants which have powerful outflows that evacuate the surrounding interstellar material (ISM), creating low density bubbles around them. However, some O or B type supergiants do not have winds of sufficient strength to provide the $\dot{M}$ required to account for the observed X-ray flux, in which case mass must also be transferred by overfilling their Roche lobes (i.e. RLO, as in LMXBs). The second group contains Be stars.

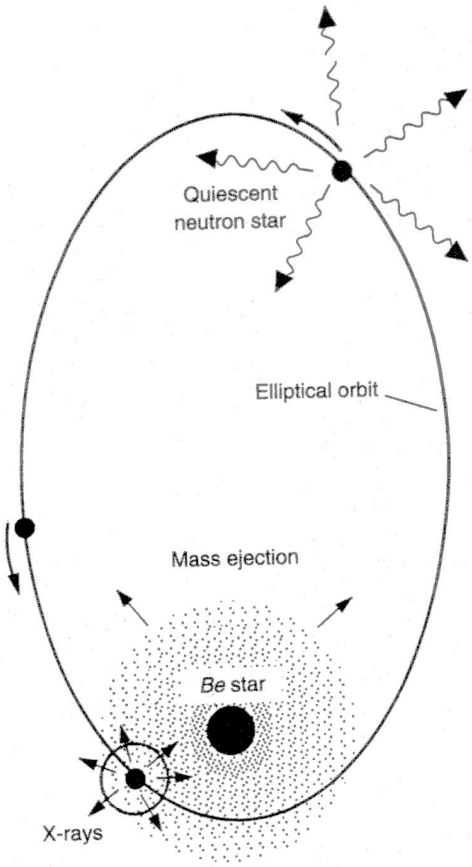

Figure 2.5: BeX diagram. Credit: Ed van den Heuvel.

2.2.1 Be X-ray Binaries

Early-type B stars with emission lines are called Be stars, of which some have been found in HMXBs with NS (mostly PSR) companions (Coe 2000). These systems are known as Be X-ray binaries (BeX), illustrated in Figure 2.5. Be stars are rapidly rotating stars and some rotate close to the break-up speed at their equators, which lowers surface gravity there. Extended equatorial discs may form as the result of an ejection mechanism (like non-radial stellar pulsations). Periastron passage of a NS in a highly eccentric binary orbit with a Be star, allows extreme accretion during its passage through this disc, producing an X-ray outburst.

2.2.2 HMXB Evolution

Tauris & van der Heuvel (2006) reviewed the evolution of HMXBs, which is determined by the stellar evolution of the donor. The evolutionary scenario for HMXBs is best explained with an example from computer model simulations. It starts with a pair of massive stars, in a binary with $P_{orb} \sim 100$ days with initial masses $\sim 8M_{\odot}$ and $\sim 14.4M_{\odot}$ respectively. The more massive star evolves faster and produces a growing He core through its normal H-burning phase. As it expands, due to increased energy generation in the core, it overfills its Roche lobe and H from its outer envelope is transferred to the less massive star.

Although this first mass-transfer phase took 13.3×10^6 years to commence, it takes only 50000 years to transfer $\sim 9M_{\odot}$ of material to the less massive star, increasing its mass to $\sim 17M_{\odot}$. All that remains of the initially more massive star, is a $\sim 3.5M_{\odot}$ He core. Because mass and angular momentum is assumed to be conserved, the binary orbit consequently expands to $P_{orb} \sim 400$ days.

The He star (Wolf-Rayet star) fuses He to Carbon (C) in its core, but in 2×10^6 years this fuel source runs out and it collapses catastrophically to explode as a supernova. This explosion causes the binary orbit to become highly eccentric, as the newly formed NS receives a kick that may be large enough to cause the binary to break up, as it does in many cases. If the binary survives, the period would have significantly increased to $P_{orb} \sim 5400$ days.

The $\sim 17M_{\odot}$ star evolves in exactly the same way and after approximately 10×10^6 years it expands. Since accretion of matter occurs from the donor's stellar wind during this initial phase, the binary is an HMXB. The donor's expansion eventually forms a CE that includes the NS, which spirals in toward the He core as a result of angular momentum losses suffered due to the viscosity of the CE. The orbit shrinks dramatically ($P_{orb} \sim$ few hours) as a result of this in-spiralling, while it also expels the CE over the course of 1×10^6 years. This is a phase of extreme mass transfer, which may initially lead to such exotic behaviour as the production of relativistic jets, as observed in the prototypical microquasar SS433 where $\dot{M} \sim 10^{-4} M_{\odot}$ yr^{-1}.

At this stage, the HMXB contains a He star $\sim 4M_{\odot}$ and NS $\sim 1.4M_{\odot}$, where He is transferred by RLO from the donor to the NS. The orbit shrinks further as the binary evolves to $P_{orb} \sim 1.5$ hours. The more massive star evolves further and explodes in a supernova, producing another NS, leaving a pair of NSs in an eccentric binary orbit with $P_{orb} \sim 8$ hours. Such young radio PSR pairs have been observed.

2.2.3 HMXB Population Distribution

HMXBs have short lifetimes, because massive early-type stars evolve rapidly, and are therefore found close to the stellar nurseries in which they were born. Consequently they are located in the spiral arms of our Galaxy and in our neighbouring irregular galaxies, the SMC and LMC. The size of the HMXB population of a galaxy is therefore closely linked to its star formation rate (Grimm et al. 2003).

2.3 Black Holes

McClintock & Remillard (2006) reviewed BH XRBs. The compact object in an accretion-powered binary is either a WD, NS or a BH. Additionally, it necessarily has to be either an XRB or SSS in order to produce the observed L_x. SSS have super-soft X-ray spectra that distinguish them from XRBs. White & Marshall (1984) suggested that X-ray transients with ultra-soft X-ray spectra in their HS states should be considered potential BH candidates.

There is a theoretical limitation of $\sim 1.4M_{\odot}$ for a WD mass, above which the equation of state (EOS) for the gas changes and the compact object must be a NS. There is also believed to be such an upper limit for NS masses, consequently predicting a maximum mass of just over $1.5M_{\odot}$ for one permissible EOS. However, the EOS may not be that relevant and theoretical predictions assuming only General Relativity (GR) and causality ($c_s < c$), suggest a maximum mass $\sim 3.2M_{\odot}$ for a non-spinning NS, which increases to $\sim 3.8M_{\odot}$ when allowing for rotation of the NS. Mass estimates from radial velocity measurements of radio PSRs, set the mass upper limit of a NS at $\sim 3M_{\odot}$. Though this latter agreement is encouraging, the upper limit for NS mass remains a topic of debate. One of the main difficulties is that the observational evidence relies on assumptions regarding the inclination angle (i) and more importantly the donor's mass (M_2), which is estimated according to its spectral type. The latter is based on masses associated with stars in non-interacting binaries of particular spectral types, while the donor would clearly have been affected by the fact that it transferred material from its outer layers, which is not being accounted for. There is general agreement that mass transfer leads to a star always displaying a spectral type that is too early for its actual mass. The maximum NS mass limit remains an important issue to resolve, since compact objects with masses above it are considered to be BH candidates (BHCs), covering a range of $\sim 3 - 15M_{\odot}$ in the Local Group.

Fortunately there are a few other observational X-ray characteristics that require the compact object to be a NS. Rapid pulsations associated with the spin of a compact object, require an X-ray PSR which is a rapidly rotating NS by definition. Type I and II bursts both require the compact object to be a NS. While non-accreting NSs can be observed as radio PSRs, it is impossible to observe non-accreting BHs since they are objects from which nothing can escape (not even light) and by the interpretation of GR, represent infinitely deep gravitational wells in space-time. However, XRBs give us an opportunity to study accreting stellar sized BHs, since they radiate X-rays from regions close to the Event Horizon.

The radius (R) from within which nothing can escape the BH, is the event horizon or Schwarzschild radius ($R_S = 2GM/c^2$), where the escape velocity is c. Transferred material in the accretion disc cannot orbit a BH closer than the innermost stable circular orbit (R_{ISCO}), which is expressed in terms of R_S. A maximally spinning or Kerr BH has an $R_{ISCO} = 0.5R_S$, while a non-spinning or Schwarzschild BH has an $R_{ISCO} = 3R_S$. If the inner edge of the accretion disc is closer to the event horizon, the material is hotter and its temperature can be determined by fitting a model spectrum to the observed X-ray spectrum. Such a fully relativistic model must assume a thin disc with blackbody emission.

2.4 Transients

There are three types of X-ray transients, namely the BeX sources which are HMXBs with hard X-ray spectra, the soft X-ray transients (SXTs) which are LMXBs with soft X-ray spectra and the supergiant fast X-ray transients (SFXTs) which appear and disappear in less than a day (Heise & in't Zand 2006). SXTs are also called X-ray novae (XRN) and are similar to regular LMXBs, except for the erratic mass transfer onto the compact object that is responsible for occasional outbursts interrupting long quiescent intervals that can last for several years or even decades. Outbursts rise to maximum in a few days but take months to decline. Only $\sim 25\%$ of these XRN are NS LMXBs, consequently the majority are BHCs.

XRN have characteristic X-ray spectra. For both BH and NS compact objects, the spectra include a thermal component which is associated with the accretion disc. This is a soft component which dominates at low frequencies. Additionally, BH XRN display a power-law component which can extend to high energies, while NS XRN also display a hard thermal component which is associated with the NS surface itself.

Historically, spectral states were labelled as high/low with respect to brightness and hard/soft with respect to spectral shape. Several XRN were observed to switch between these low-hard (LH) and high-soft (HS) states. However, the labelling was later deemed limited and a clearer classification of the states has been suggested in McClintock & Remillard (2006). Essentially they suggest 3 states, namely the Steep Power Law (SPL), the Thermal and the Hard states. The hard state is the old LH state and the thermal state is the old HS state. It is believed that the accretion disc reaches closer to the compact object during the higher thermal state, but that it is replaced with a hot tenuous medium during the hard and quiescent states (see Figure 2.6). Narayan & Yi (1994) referred to the latter as an advection-dominated accretion flow (ADAF).

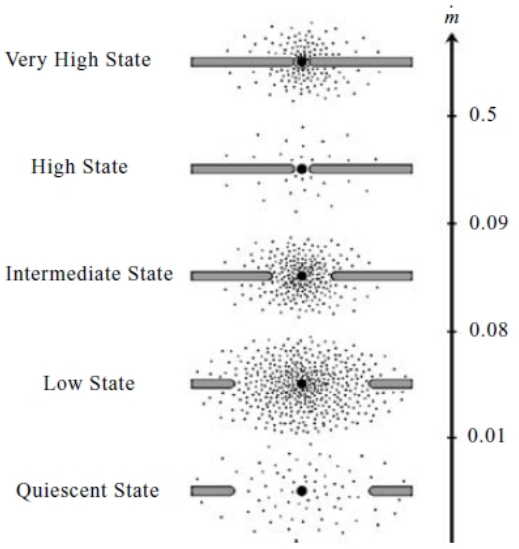

Figure 2.6: ADAF diagram. (Esin et al. 1997).

XRN may produce jets during state transitions, thereby forming microquasars, for which Figure 2.7 presents a unified model describing the disc-jet coupling (Fender et al. 2004, Fender 2006). QPOs with frequencies $\sim 0.001 - 40$ Hz have been observed during the SPL state of XRN (van der Klis et al. 1996, van der Klis 2006). These may be observable in both X-ray and optical wavelengths, in which case simultaneous observations at high time-resolution may produce time-lags between the periodic signals contained in the multi-wavelength data.

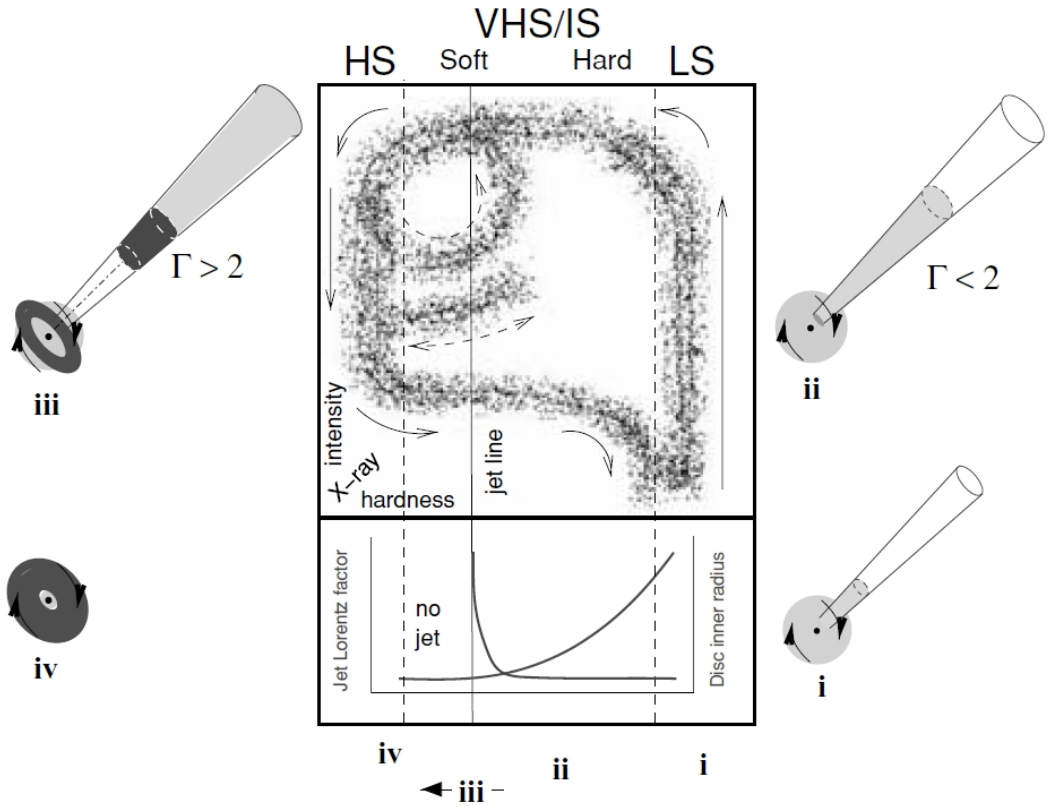

Figure 2.7: XRN jet formation diagram (Fender et al. 2004). LS represents the low-hard state, HS the high-soft state, VHS the very high state and IS the intermediate state. Jet speeds are indicated by their Lorentz factor (Γ) and the cartoons indicate the status of jets at different points in the bottom diagram, in which jet speed is plotted against hardness. The progression of an XRN through the different states is shown by arrows in the main panel.

2.5 Ultra-Luminous X-ray Sources

Extragalactic XRBs (Fabbiano & White 2006) include the ultra-luminous X-ray sources (ULXs), for which $L_x > 10^{39}$ erg s^{-1}. Although there are ~ 1 per galaxy, they are not galactic nuclei by definition and have larger numbers in starburst galaxies, which have more young O associations.

Since the L_{Edd} of a $1.4M_{\odot}$ NS is $\sim 1.8 \times 10^{38}$ erg s^{-1}, the higher L_x for ULXs imply either a compact object of $> 7M_{\odot}$, super-Eddington accretion or beamed emission (a jet). Super-Eddington accretion can occur if the position of the accretion and radiation zones are displaced from one another, so that the radiative pressure does not directly oppose the accretion. Whether or not these objects represent intermediate-mass black holes (IMBHs) is a topic of considerable controversy at the present time.

2.6 Summary

The major differences between LMXBs and HMXBs, as reviewed by Psaltis (2006), have been summarized in Table 2.1. The properties and evolution of stars are determined by their mass. Consequently, the differences between LMXBs and HMXBs are linked to the masses of their donors.

Table 2.1: Classification of X-ray binaries

Characteristic	**LMXB**	**HMXB**
Donor mass	$< 1M_{\odot}$	$> 10M_{\odot}$
Donor type	low-mass	high-mass
	cool	hot
	late-type	early-type
	evolved	young
	main sequence	giant/supergiant
Donor spectral type	K - M	O - B
Optical characteristics	faint	bright
	redder	bluer
Galactic distribution	old population	young population
	galactic bulge	spiral arms
	globular clusters	
Mass-transfer mechanism	RLO	strong stellar wind (and RLO)
P_{orb}	tens of minutes to days	days to hundreds of days
Orbits	near circular	eccentric
Lifetimes	$\sim 10^7 - 10^9$ years	$\sim 10^5 - 10^7$ years
Evolution driver	mass transfer	stellar evolution

Chapter 3

Identifying Periodic Behaviour

Due to their distance and size, X-ray binaries cannot be resolved since microarcsecond resolution would be required to resolve even the widest one in the Milky Way. Therefore they represent only point sources for observation. However, everything known about them to date originates from the study of their spectra and lightcurves. In particular, periodic behaviour is an important diagnostic in determining the astrophysical processes that may be involved.

3.1 Lightcurves

Pure X-ray time-series data or lightcurves contain primarily time stamps, with their detected flux levels and may also include error estimates for the latter. Flux levels are essentially count rates of photon detections and are therefore dependent on the detector and instrument used to detect them. Detectors are sensitive to particular photon energy ranges. Photon counting devices such as proportional counters and micro-channel plates tag the arrival time of each photon to produce photon lists, which require binning into appropriately sized time bins to form lightcurves. CCDs allow photon detections to be accumulated during the entire length of an exposure, subsequently producing a lightcurve directly. Whatever their format, lightcurves indicate the observed brightness for a source as a function of time. Figure 3.1 represents the $1.5 - 12$ keV lightcurve of SMC X-1, obtained by the All Sky Monitor (ASM) on board the Rossi X-ray Timing Explorer (RXTE). The one-day-average data were binned into 10-day bins for plotting purposes.

In some cases, such as the example shown here, variability is immediately apparent for a source when plotting its lightcurve over appropriate time and flux ranges. Quantification of the presence of any periodic signals requires fitting the time-series data with an appropriate function to determine an accurate period to associate with the periodic behaviour, by employing any of the statistical techniques described in Wall & Jenkins (2003). Those relevant to the work here will now be briefly introduced and applied to the example lightcurve to illustrate their efficiency in identifying known periodic signals contained therein.

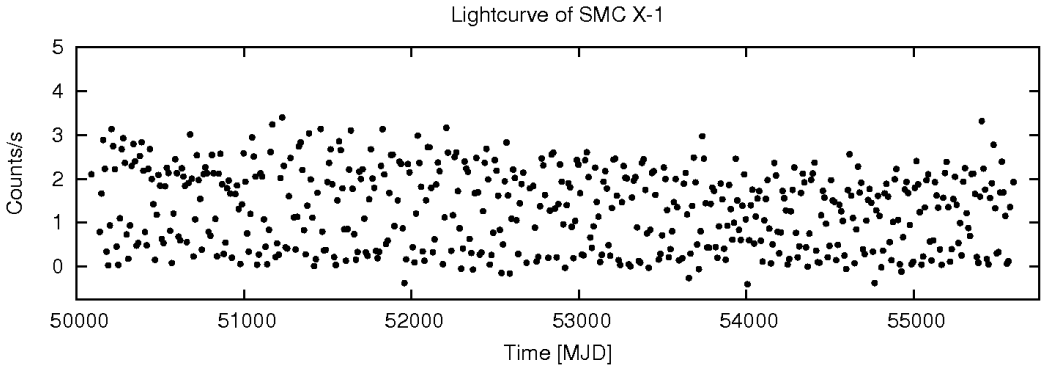

Figure 3.1: RXTE ASM lightcurve of SMC X-1

3.2 Fourier Series

In the 1800s, the French mathematician Joseph Fourier proposed that any time series of data could be represented by a combination of sines and cosines. The Fourier series of a function $f(x)$ is given by Equation 3.1, wherein a_0, a_n and b_n are given by Equations 3.2, 3.3 and 3.4 respectively. Noise will spread over all frequencies in a Fourier series and periodic signals contained in the time-series data, will be concentrated in terms with higher amplitudes, thereby transforming a time series into a frequency series.

$$f(x) = \frac{1}{2}a_0 + \sum_{n=1}^{\infty} a_n \cos(nx) + \sum_{n=1}^{\infty} b_n \sin(nx) \tag{3.1}$$

$$a_0 = \frac{1}{\pi}\int_{-\pi}^{\pi} f(x)dx \tag{3.2}$$

$$a_n = \frac{1}{\pi}\int_{-\pi}^{\pi} f(x)\cos(nx)dx \tag{3.3}$$

$$b_n = \frac{1}{\pi}\int_{-\pi}^{\pi} f(x)\sin(nx)dx \tag{3.4}$$

Even a square wave can be approximated by a Fourier series. Figure 3.2 illustrates how the fit (solid line) improves progressively as Fourier terms (dashed lines) with higher frequencies are added.

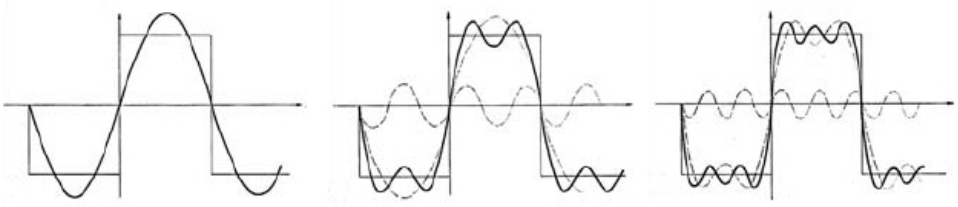

Figure 3.2: Fourier series approximation for a square wave

3.3 Discrete Fourier Transform

Evenly sampled data (at equal time intervals of Δ) can be represented by the discrete Fourier transform (DFT), which is defined by Equation 3.5 for a discrete function $f(t)$. Therein $f_k \equiv f(t_k)$ where $f(t) \rightarrow f(t_k)$ for $t_k \equiv k\Delta$.

$$F_n = \sum_{k=0}^{N-1} f_k e^{-\frac{2\pi i}{N} kn} \quad , \quad k = 0, 1, ..., N-1 \tag{3.5}$$

Autocorrelation provides a measure of the repeatability of a pattern embedded in time-series data. Therefore periodic signals have high autocorrelation coefficients. The power spectrum is the Fourier-transformed autocorrelation function, via the Wiener-Khinchine theorem. It yields frequencies with their associated powers (amplitude squared) that indicate their significance relative to one another. Peaks that rise significantly above the rest, are more significant and the peak with the highest power represents the dominant period contained in the time-series data for the frequency range considered. Narrow (broadened) peaks indicate strict periodic (quasi-periodic) behaviour.

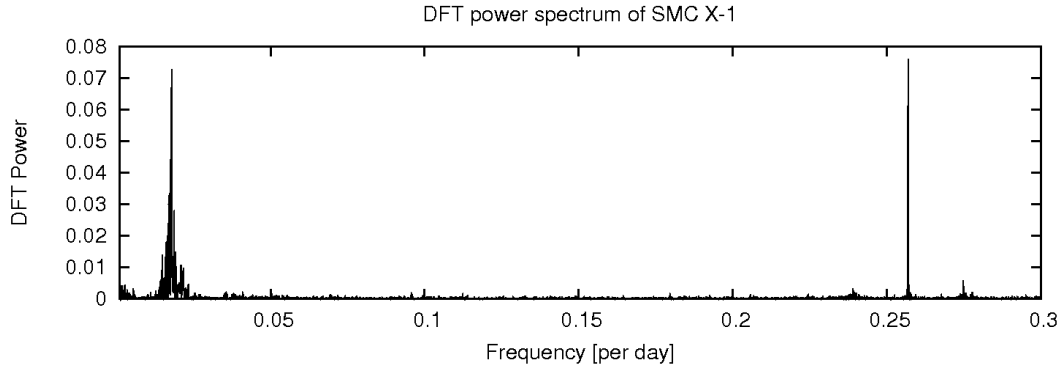

Figure 3.3: DFT power spectrum of SMC X-1

The DFT power spectrum for the one-day-average lightcurve of SMC X-1 is presented in Figure 3.3. The data were evenly sampled with very few gaps, making the DFT method appropriate for constructing a power spectrum. It shows a significant sharp/narrow peak at frequency ~ 0.257 per day and another significant broadened peak at frequency ~ 0.018 per day, representing the P_{orb} of 3.89 days (Schreier et al. 1972a) and $P_{sup} \sim 50 - 70$ days (Wen et al. 2006) of SMC X-1 respectively. The influence of the latter is also detected as beat periods (P_{beat}) at frequencies ~ 0.239 and ~ 0.275 per day, which surround the orbital period's peak according to Equation 3.6.

$$\frac{1}{P_{beat}} = \frac{1}{P_{orb}} \pm \frac{1}{P_{sup}} \tag{3.6}$$

3.4 Window Functions

Spectral leakages occur due to the sampling pattern of the data and may introduce false periodic signals in the power spectrum. Window functions are constructed by Fourier analysis of the time-series data, where the detections have all been set to unity. By removing the variations in the detection levels, the Fourier analysis can identify only the periodic signals associated with the sampling. Apparently significant source-related periodic signals are obviously not associated with such periods. Therefore, coincidence of a periodic signal in the power spectrum with a significant peak in the window function typically excludes it, although it is always worth examining such circumstances carefully.

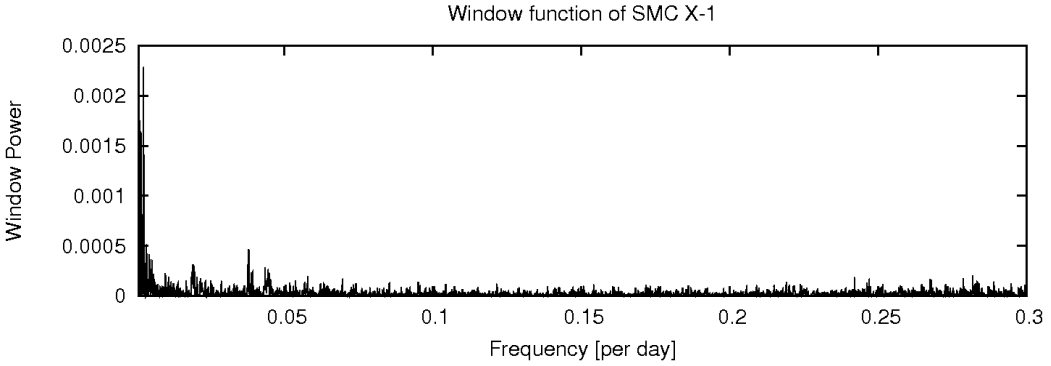

Figure 3.4: Window function of SMC X-1

The window function of SMC X-1 (Figure 3.4) contains peaks at the low frequency end as a result of poorer sampling of long periods. However, there are no features in the window function that coincide with the significant peaks in the power spectrum (Figure 3.3).

3.5 White Noise

White noise is independent of frequency and its level can be determined by generating thousands of random datasets by Monte Carlo simulation, assuming a white noise distribution and using the same time values, mean and standard deviation as those of the time-series data. Power spectra are then used to determine the maximum power in each such dataset, and the subsequent distribution of powers yields a probability distribution function. The cumulative probability of occurrence of a given power level can be considered as defining the false alarm probability (FAP), the opposite of the confidence level. These FAPs reflect the probability that a randomly generated white noise dominated lightcurve, with similar properties to that under consideration, produced periodic signals with certain powers. Significant periodicity at a particular confidence level therefore requires that a peak in the power spectrum exceeds the white noise level. Figure 3.5 indicates the white noise level of SMC X-1 (green line) associated with the 99% confidence level, usually adopted as the minimum for considering a signal to be genuine.

3.6 Red Noise

Red noise, as its name suggests, is dependent on frequency and tends to increase toward lower frequencies due to poorer sampling thereof or particular physical processes occurring in the source under consideration. Consequently, red noise becomes more important to consider when determining long-term periods. Modelling of red noise is performed in a similar manner as is employed for white noise, except that a red noise distribution is assumed. REDFIT (Mudelsee & Schulz 2008), developed for modelling red noise in paleoclimatic time series, yields power values associated with the 99% confidence level at different frequencies assuming a first-order autoregressive process (appropriate for uneven sampling) for the red noise distribution. In Figure 3.5 the red noise of SMC X-1 (red line) clearly increases toward lower frequencies, starting below the white noise at high frequencies but rising to almost double the white noise level at low frequencies.

3.7 Lomb-Scargle Normalized Periodogram

Unevenly sampled data are better treated with the Lomb-Scargle (L-S) analysis method (Lomb 1976, Scargle 1989), whereby time-series data are weighted per point rather than time interval, as in the case of the DFT. It also calculates its own FAP for a power peak, which is essentially the probability that other peaks may exceed it, making it dependent on the number of independent frequencies considered. FAPs theoretically negate the need to test against the white noise level. However, a more conservative approach would still rather formally test peaks against noise levels. Figure 3.5 contains the L-S normalized periodogram of SMC X-1, with the white noise and red noise estimates at a 99% confidence level.

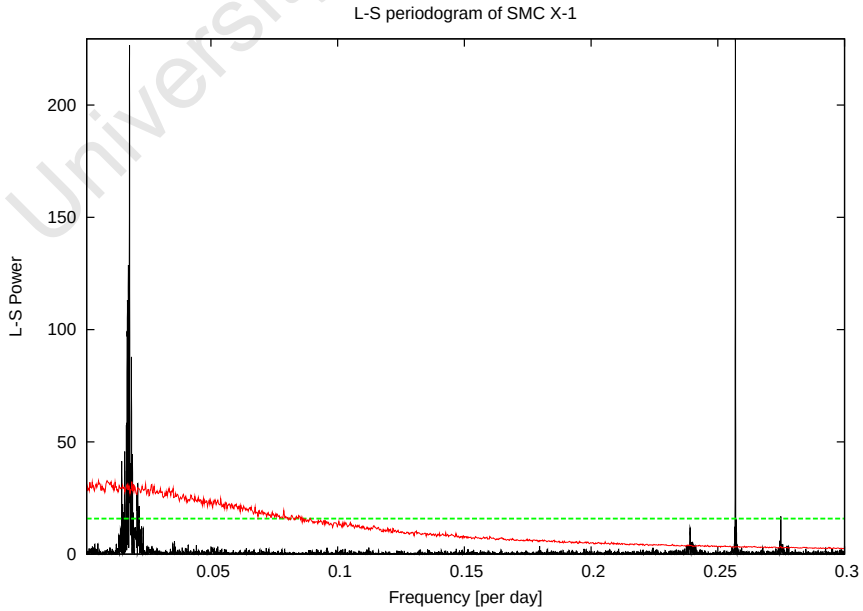

Figure 3.5: L-S normalized periodogram of SMC X-1

3.8 Folded Lightcurves

Lightcurves can be phased by splitting their data into equal sections of period length from an ephemeris, which is subtracted from each time value before dividing it by the period. Disregarding the integer value, phased data are then folded by averaging all these datasets into an appropriate number of bins over the phase [0,1]. While this can be performed for any period, it will obviously yield the best result when the data are phase folded on an appropriate significant period contained in the time-series data, minimizing the scatter and producing a smooth modulation if the period is truly periodic. The folded lightcurves are usually plotted over two cycles to make the shape of the modulations clearer (Figure 3.6).

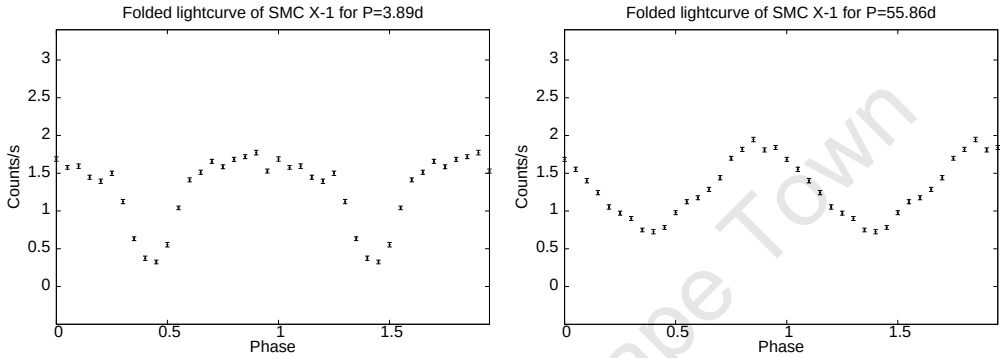

Figure 3.6: Folded lightcurves of SMC X-1

3.9 Phase Dispersion Minimization

In the phase dispersion minimization (PDM) method (Stellingwerf 1978), the lightcurve is phase folded on each period and the variance is calculated in each phase bin and summed. The periods for which the summed variances are minimized, are considered more significant. The major advantages of this method (as with Epoch-folding) are its independence from the shape of the variations (e.g. it is more sensitive than L-S to non-sinusoidal variations) and the fact that it deals much better with unevenly sampled data than DFTs do.

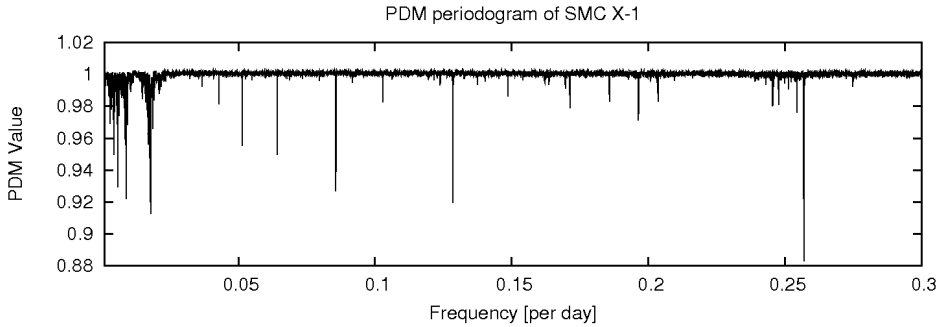

Figure 3.7: PDM periodogram of SMC X-1

3.10 Validating Periodic Behaviour

In order to determine the validity of any period which has been detected by employing one of these temporal analysis techniques, a number of tests are required. These are:

- use another technique to confirm it (L-S and PDM are good tests for one another)
- the window function should not contain any significant features at its position
- its peak must exceed the white noise level
- its peak should exceed the red noise level

By combining the L-S, PDM, window function, white and red noise levels in Figure 3.8, all these tests can immediately be confirmed. All plots cover the same frequency domain and for ease of interpretation, the plots were rather made on a log scale with the equivalent periods on the horizontal axis.

The two significant periods are clearly detected in the L-S and the PDM, while the latter also identifies aliases thereof. Harmonics are integer multiples of the frequencies associated with significant periods, with progressively lower powers. However, the aliases identified in the PDM rather occur at $\frac{1}{2}, \frac{1}{3}, \frac{1}{4}, \ldots$ times the frequencies of the most significant periods.

There are no significant features in the window function at the location of these periods in the periodograms. The dominant peaks in the L-S are well above the white noise level (dashed green line) and the red noise level (solid red line).

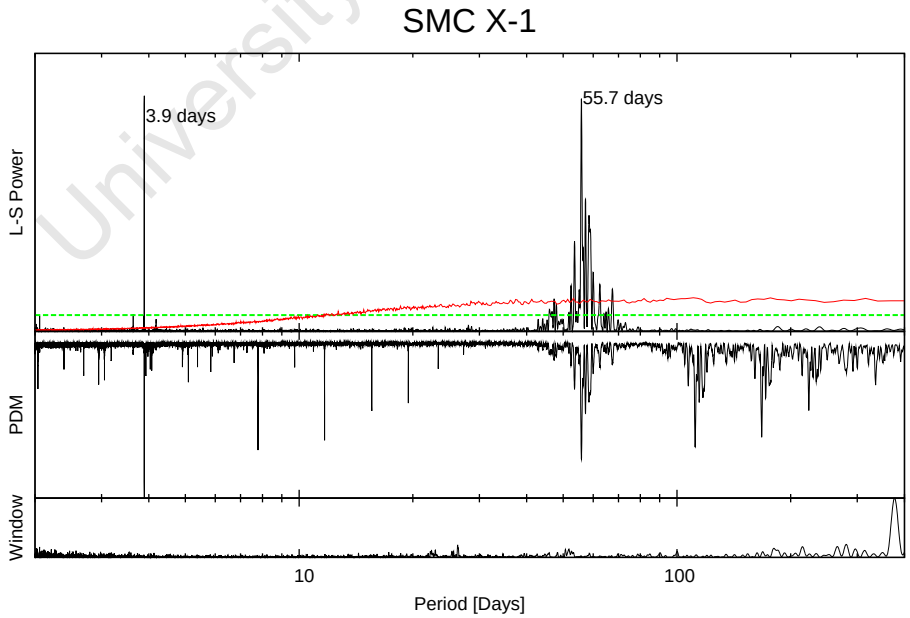

Figure 3.8: Plot of L-S, PDM, window function, white and red noise for SMC X-1

Schwarzenberg-Czerny (1991) advised that estimated errors in the derived periods should be obtained by measuring the width and heights of peaks in a periodogram. This may be accomplished by fitting a Gaussian to the peak in the periodogram to determine the scatter (standard deviation) around the derived period (average). Periods derived by applying different methods (e.g. L-S and PDM) falling within 3× each other's error estimates, may therefore be considered to be the same period.

3.11 Time-dependent Period Analysis

Periods are normally identified using the entire available datasets. While this allows distinction between periodic and quasi-periodic behaviour, it has limitations when dealing with varying (quasi-periodic and aperiodic) signals.

3.11.1 Windowing

Lightcurves may be split into data windows of sufficient size to allow period analysis to detect the maximum period considered. Larger window sizes cause the smearing out of variability in the periodic signal as they average out small variations, but have the advantage of enhancing sustained and stable periodic signals. However, variable or intermittent periodic signals may be completely damped out if windows are too large. Consequently, the signal whose period is itself varying with time (evolving periodic signal) shows much stronger detection in a time-dependent period analysis (Figure 3.9) than the steady signal, while their detection strengths were comparable in the periodograms considering the entire dataset (Figure 3.8). This clearly illustrates that a weaker persistent periodic signal is amplified when considering the entire dataset, while a stronger evolving one becomes damped thereby, as its power is spread over more frequencies.

Sliding windows allow consecutive datasets to overlap, such that they move in steps in the time domain that are smaller than the window sizes. This approach provides improved resolution in the time domain and allows for a degree of smoothing of the resulting data presentation.

3.11.2 Mapping 3D Data onto 2D Plots

Density maps allow the 2D representation of 3D data. Therein, the frequency range is plotted along the horizontal/x-axis and time along the vertical/y-axis, while the power is plotted in the line-of-sight/z-axis. The density scale bar indicates the powers associated with each point in the frequency-time (x-y) domain, with stronger detections being darker.

3.11.3 Dynamic Power Spectra

The dynamic power spectrum (DPS) method employed by Clarkson et al. (2003a) has the advantage of clearly illustrating whether periodic signals are intermittent/sustained and whether they are stable/evolving. It requires the datasets to be split up into windows, for which periodograms are produced. The results of all the periodograms for a source are plotted together in a density map, using the power for each frequency, plotted at every window's midpoint along the time axis. Figure 3.9 (left) shows that the low frequency signal is evolving, which resulted in a broadened peak in the periodograms for the entire dataset. In contrast, the high frequency signal is steady, which in turn resulted in a sharp peak in the periodograms for the entire dataset. The beat frequencies show less evolution, because they result from both the steady high and evolving low frequency signal.

3.11.4 Dynamic Window Functions

To ensure that the features contained in the DPS are not artificially induced by the sampling or windowing employed, a 3D spectral window function can be constructed in the same way the DPS produced a 3D periodogram. These results can also be plotted in a density map, similar to the way the DPS information was plotted in a density map. The resulting dynamic window function (DWF) can then be compared to the DPS. Significant features contained in the DPS that are repeated in the DWF, may be artificial and therefore not necessarily the result of source variability.

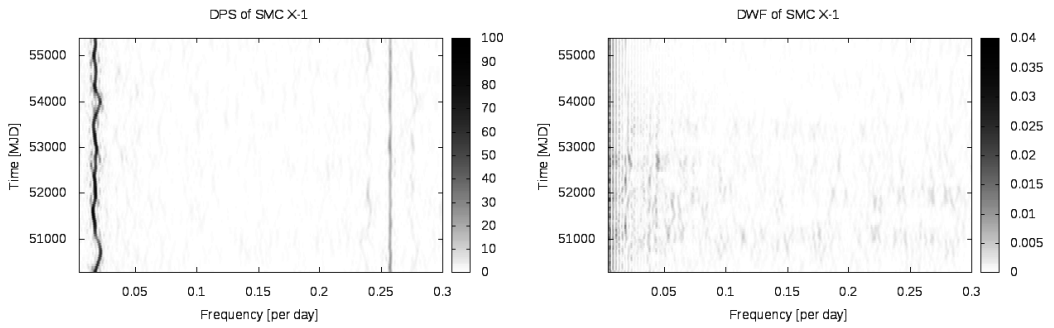

Figure 3.9: DPS (left) and DWF (right) of SMC X-1

The DWF (Figure 3.9 (right)) shows faint signals in the low frequency end as a result of poorer sampling of long periods. However, it contains no significant features at the same locations as those in the DPS (Figure 3.9 (left)).

3.12 Weighting Schemes

Weighting schemes are used to enhance the sensitivity of the period analysis techniques and are normally applied to the data before employing a period analysis method.

3.12.1 Simple Weighting Scheme

Corbet (2003) suggested a simple weighting scheme to boost periodic signals contained in data with large variability in the statistical quality of data points (non-uniform error bars). Weighted data points (y_i/σ_i^2) are produced by weighting the flux count rates (y_i) by their error bars (σ_i). However, it is not appropriate if the intrinsic scatter in the data points is large with respect to their error bars (e.g. variable bright sources).

3.12.2 Modified Weighting Scheme

The modified weighting scheme (Corbet et al. 2007) takes the variance due to source variability (V_S) into account. Its modified weighting factors $1/[(f\sigma_i)^2+V_S]$, are to be multiplied with their respective flux count rates y_i.

$$V_S = \frac{1}{N-1}\sum_{i=1}^{N}(\overline{y}-y_i)^2 - \frac{1}{N}\sum_{i=1}^{N}(f\sigma_i)^2 \tag{3.7}$$

Therein, $\overline{y}$ is the mean flux count rate for a source and N is the number of data points. The correction factor (f) is the scaling factor required to produce a $\chi^2 = 1$, when a constant value is fitted to the data of constant sources (e.g. SNRs and Galaxy Clusters). If $V_S < 0$, it is set to 0. The performance of any technique is measured by its success in identifying true periodicities that other methods are unable to detect. Corbet et al. (2007) determined that their modified weighting scheme performs better than their previous simple weighting scheme or L-S weighting methods, for all sources except the faintest ones.

3.12.3 Window Weighted

The window function will be convolved with the power spectrum, so the true periodic signals may be recovered by de-convolving the observed power spectrum with the window function. Levine et al. (2011) proposed a method to boost weak periodic signals at the very high frequency end (applicable to short P_{orb} or QPOs) by reducing the effects imposed by the window function. In addition to using the simple weighting scheme suggested by Corbet (2003), binning of data points is employed and a further weighting factor ($\frac{1}{W_i}$) is applied to determine the weighted-average intensity (d_i) in the i-th time bin, containing n_i measurements with source intensities s_j and errors σ_j (for $j = 1, ..., n_i$). Since the window function sets detections to unity, $W_i = \sum_{j=1}^{n_i}\frac{1}{\sigma_j^2}$.

$$d_i = \frac{1}{W_i}\sum_{j=1}^{n_i}\frac{s_j}{\sigma_j^2} \tag{3.8}$$

3.13 Characterizing Periodic Behaviour

The example presented in the previous sections of this chapter, clearly illustrates that quasi-periodic signals may evolve/vary over time. It is the primary focus of this work to characterize such quasi-periodic and aperiodic signals using the DPS method, which is a time-dependent period analysis method.

In order to do so, the possible presence of periodic behaviour in a source must first be investigated by using sensitive methods that are capable of detecting weak periodic signals, such as L-S periodograms. Thereafter, it should be validated by applying all the rigorous tests discussed previously. Exceeding approximate white noise levels is considered the first and most important of the tests to pass, after which a source is considered worthy of further analysis. The PDM and window functions are then produced, in addition to which the white and red noise levels are properly modelled.

The ensuing tests allow identification of all significant periods over a particular frequency range, contained in a time-series dataset. The advantage of considering sources with previously published period(s), is that the DPS analysis can be performed directly to characterize the behaviour of those periods, without requiring the rigorous tests necessary when claiming newly discovered periodicities.

All the techniques described herein have been successfully employed in period analysis of a variety of astronomical sources. Starlink's PERIOD package has been used by astronomers since the early 1990s and allows computation of DFT power spectra, PDM and L-S normalized periodograms, window functions and phase-folded lightcurves.

Once a source has been confirmed as periodic over a particular frequency range, the DPS method can be employed and its results can be plotted with additional panels which contain useful information. Subsequently the two plots in Figure 3.10 contain the DPS in their main panels, the lightcurves in their top panels and the L-S periodograms over their entire dataset (with its white noise level indicated by a vertical line) in the left panels.

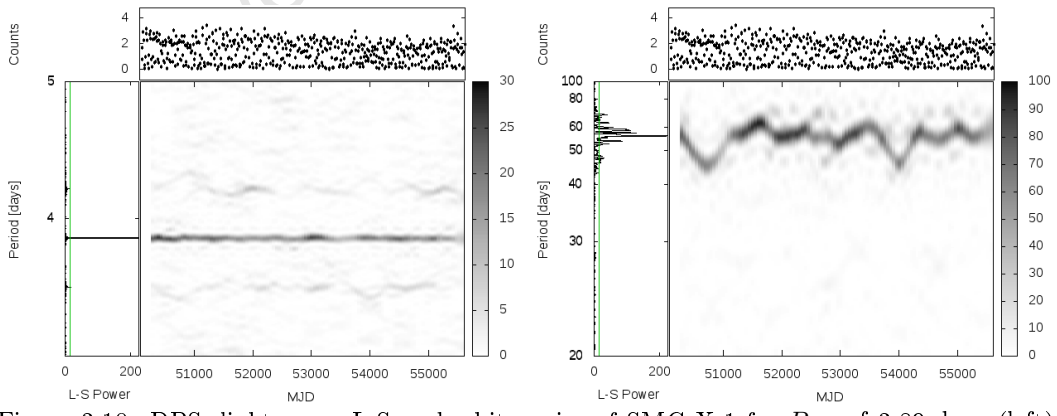

Figure 3.10: DPS, lightcurve, L-S and white noise of SMC X-1 for P_{orb} of 3.89 days (left) and $P_{sup} \sim 40 - 70$ days (right).

The P_{orb} of 3.89 days in Figure 3.10 (left) is clearly very stable, as is expected from strictly periodic behaviour such as orbital periods. However, the P_{sup} of 55.86 days in Figure 3.10 (right) is part of a steadily evolving periodic signal between $\sim$ 40 and $\sim$ 70 days, which constitutes quasi-periodic behaviour.

Chapter 4

Super-orbital Behaviour

From the beginning of satellite X-ray astronomy, long-term monitoring of the most luminous Galactic X-ray binaries revealed modulations that were quasi-periodic on time-scales substantially longer than their well-established orbital periods (P_{orb}). These included results from missions such as Ariel V's All Sky Monitor (e.g. Kaluzienski et al. (1976)) and Vela 5B (e.g. Priedhorsky & Terrell (1983b; 1984b)). Her X-1, with its 35 day on/off cycle (which appears remarkably stable, at $\sim 20 \times P_{orb}$) exhibits the prototypical super-orbital period (Petterson 1977). Periodic or quasi-periodic variations with periods $P > P_{orb}$ are generally referred to as *super-orbital* modulations, which are associated with super-orbital time-scales/periods (P_{sup}).

Such super-orbital variations are seen to occur on time-scales of tens to hundreds of days and are mostly believed to be related to the properties of the accretion disc, but have occasionally been linked to variations in the donor. Many such quasi-periodicities have been determined for a number of sources, using archival data from later X-ray satellite missions such as CGRO's BATSE (e.g. Robinson et al. (1997)), RXTE's All Sky Monitor (ASM; e.g. Wen et al. (2006)) and Swift's Burst Alert Telescope (e.g. Farrell et al. (2009)).

This work focuses on characterizing the behaviour of long-term and very long-term super-orbital modulations detected in the X-ray lightcurves of XRBs, which has recently been reviewed and summarized in Charles et al. (2008; 2010). They will be discussed in more detail, in the context of the observed behaviour of their P_{sup} over time or their newly determined P_{sup}, in the applicable chapters devoted to the observed long-term (Chapter 6) and very long-term (Chapter 7) behaviour in XRBs respectively.

4.1 Long-term Variations

In this context, long-term variations refer to $P_{sup} < 1$ year. A number of mechanisms have been proposed to account for modulations on this time-scale, which may also apply to slightly longer time-scales. Some of these mechanisms produce stable variations, while others produce modulations that are quasi-periodic at best and often unstable.

4.1.1 Tidally-induced Disc Precession

Whitehurst & King (1991) described how tidal interactions with the donor may excite resonances in the accretion disc, causing it to precess and produce quasi-periodic variations in the lightcurve. Essentially the disc becomes elliptical, expanding beyond its critical radius while remaining within its Roche-lobe radius, so that disc precession is effectively the result of changes in the orientation of this elliptical accretion disc with respect to the donor. Tidal disc precession depends on the mass ratio ($q = \frac{M_2}{M_1}$) and will only occur if $q < 0.25 - 0.33$, producing so-called "superhumps", which have been detected in the SU UMa sub-class of CVs (Warner 1995) and the soft X-ray transients or SXTs (O'Donoghue & Charles 1996).

4.1.2 Radiation-induced Disc Warping/Tilting

Petterson (1977) proposed a mechanism to account for the $P_{sup} \sim 35$ days in Her X-1, which was further developed by Wijers & Pringle (1999) and Ogilvie & Dubus (2001), OD01 hereafter. Thereby, accretion discs may develop a warp (see Figure 4.1) in response to the intense radiation from the central X-ray source, allowing the discs to become tilted in extreme cases. The instability of accretion discs to radiation-induced warping depends heavily on the viscosity parameter (α) and slightly less on the accretion efficiency (ϵ).

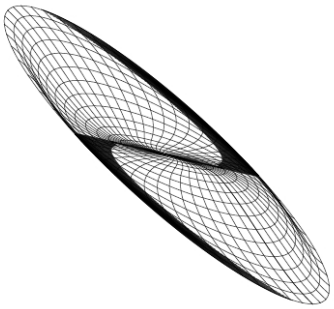

Figure 4.1: Radiation-induced warped accretion disc (Ogilvie & Dubus 2001).

These warped/tilted discs could produce quasi-periodic variations in the lightcurves, due to partial obscuration of the central X-ray source (Clarkson et al. 2003a). It is expected that chaotic or unstable warping may result in quasi-periodic super-orbital variations, while precession of stable/sustained warps should result in steady super-orbital modulations.

Tidal torque was ignored in OD01 and they assumed $\alpha = 0.3$ and $\epsilon = 0.1$, which are considered reasonable for persistent NS X-ray binaries in general. Stability against radiation-induced warps was considered for different values for the mass input radius (r_{add}), with boundary values set by the circularization radius (r_c) and the outer disc radius (r_o). Figure 4.2 (from OD01) summarizes their result for XRBs as functions of their mass ratio (q) and binary separation (r_b), calculated by Equation 4.1.

$$r_b \left[\frac{GM_1}{c^2}\right] = 1.98 \times 10^6 \left(\frac{P_{orb}\ [\mathrm{d}]}{M_1\ [M_\odot]}\right)^{\frac{2}{3}} (1+q)^{\frac{1}{3}} \tag{4.1}$$

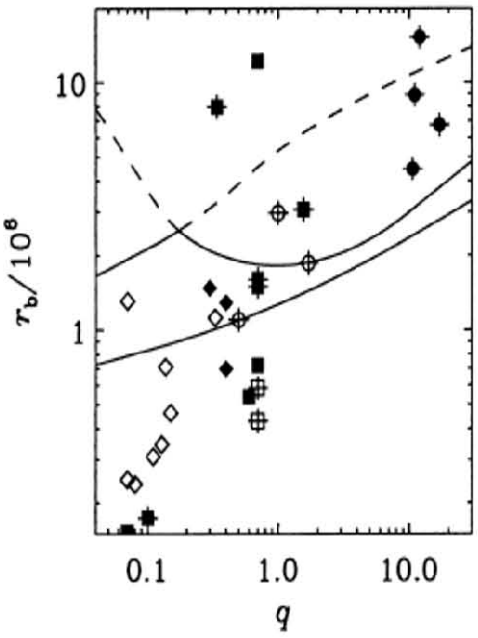

Figure 4.2: OD01 accretion disc stability to radiation-driven warping in XRBs, as functions of q and r_b $[\frac{GM_1}{c^2}]$. HMXBs are shown as circles, SXTs as diamonds and other LMXBs as squares, with open/closed symbols for BHCs/NSs. Crosses indicate systems with known super-orbital behaviour. The upper two lines (solid & dashed) correspond to the first two bending modes for $r_{add} = r_c$ (mode 0 starts higher than mode 1). Sustained stable warps are only possible close to those solid curves, while warps become increasingly variable/unstable toward the dashed curves and above them. The so-called "instability zone" lies between these solid and dashed curves. The bottom solid line corresponds to mode 1 for $r_{add} = r_o$, below which discs are unlikely to experience radiation-driven warping, but they may still be subject to the separate effect of tidally-induced disc precession if $q < 0.25 - 0.33$. The area between the bottom and top solid lines is considered an "intermediate instability zone" where a disc may display warping cycles as the disc alternates between warped and flat.

By their own insistence, the OD01 analysis remains an approximation only and a more accurate approach would have to include tidal precession due to interactions with the donor. Different values for α and ϵ would also produce different results and since all systems are not expected to have the same values, each system should be analysed individually. Nevertheless it remains the best analytical guestimate, predicting that the occurrence of a steady P_{sup} as the result of radiation-induced warping of the accretion disc, should be rare in LMXBs with $P_{orb} < 1$ day.

Recent Smooth Particle Hydrodynamics (SPH) simulations by Foulkes et al. (2010) easily produced warps in the systems they considered, as their "disc continuously flexes in response to the changing orientation of the Roche potential". They suggest that the SPH simulations should reflect the complexities involved in an irradiated accretion disc more accurately than an analytical approach could. Contrary to OD01, they conclude that irradiation-driven warping should be very common in LMXBs, producing long-term P_{sup}.

Producing warps in an accretion disc therefore appears to be easy, but sustaining it for a prolonged period may not be such an easy matter. Lodato & Price (2010) used SPH simulations to consider the diffuse propagation of warps in viscous thin discs, where they determined the diffusion coefficient to be $\sim 1/\alpha$ for small amplitude warps and $\alpha < 0.1$, but in general found that higher viscosity leads to slower diffusion and lower viscosity to faster diffusion. They claim to find remarkable agreement with the analytic theory for linear and non-linear warps, with respect to the warp diffusion coefficient and the precession rate from their recent simulations.

4.1.3 X-ray State Changes

Mass accretion (at rate $\dot{M}$) in X-ray novae is far more efficient during the HS or thermal state than during the LH state, causing occasional outbursts to interrupt long quiescent intervals (Chapter 2). However, modulation of $\dot{M}$ through the accretion disc may result in occasional state transitions in the X-ray spectra of some persistent sources (e.g. Cyg X-1) where $\dot{M}$ is believed to be intermediate between the HS and LH states (King et al. 1997). Their observed P_{sup} may reflect the time-scales on which those transitions occur.

Dubus (2003) reviewed the solutions for radiatively efficient (high $\dot{M}$) and low radiative efficiency accretion flows (LRAF; low $\dot{M}$), applicable to geometrically thin, optically thick accretion discs and geometrically thick, optically thin accretion discs respectively. Pringle (1981) presented a standard model for thin discs, based on his own earlier work and that of Shakura & Sunyaev (1973), where the steady state is defined as a geometrically thin, optically thick accretion disc which is cooled by radiating efficiently. Such thin discs may become thermally unstable if the material is optically thin or viscously unstable if density perturbations become amplified instead of being smoothed out by accretion.

The Shapiro-Lightman-Eardley model (SLE) suggests that hot protons are cooled by Coulomb interactions with cooler electrons and are heated by viscous dissipation (Shapiro et al. 1976). Sufficient cooling will stabilize the disc back into the cool thin disc, but further heating causes the SLE flow to evaporate into a two temperature advection-dominated (Narayan & Yi 1994, Abramowicz et al. 1995) accretion flow (ADAF), which cools by advection and represents the steady state solution of the LRAF optically thin case. The steady state for the optically thick LRAF case is referred to as a slim disc, which also cools by advection and is radiation pressure dominated.

The transitions between steady solutions form the basis of the disc instability model or DIM (Bath & Pringle 1982, Lasota 2001), which predicts periodic enhanced mass accretion that are observed as dwarf novae outbursts in some CVs (diagram on the left in Figure 4.3). Disc column density is defined as $\Sigma = 2\rho_0 H$, where ρ_0 is the mean density and H is the vertical scale height of the accretion disc.

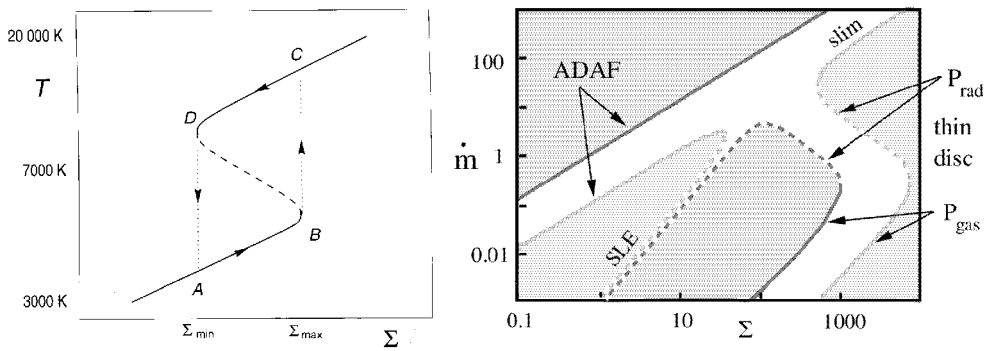

Figure 4.3: The DIM for CVs (left) is represented by the S-curve on a plot of Σ versus $\dot{M}$ and/or T (Hellier 2001), which describes a thermal limit cycle ($A \rightarrow B \rightarrow C \rightarrow D \rightarrow A$) for dwarf novae outbursts produced by their accretion discs as they transition between stable solutions (solid curves). But, for the DIM to be applicable for XRBs (right) it must include irradiation and the inner disc should be replaced by ADAF in quiescence, producing a more complex Σ versus $\dot{M}$ plot (Dubus 2003).

4.1.4 Precessing Relativistic Jets

Margon (1984) showed that the microquasar SS433 displays shifts in some of its optical emission lines (Figure 4.4). The Doppler shift in the observed wavelength (λ) of a spectral line from its rest value (λ_0) is defined by $z = (\lambda - \lambda_0)/\lambda_0 = \frac{v}{c}\cos\theta$, where v is the speed of the material, c is the speed of light and θ is the angle with respect to the observer's line-of-sight. However, for material moving at relativistic speeds ($v \sim c$) the relativistic Doppler shift includes time dilation, defined by the Lorentz factor: $\Gamma = (1 - \frac{v^2}{c^2})^{-\frac{1}{2}}$.

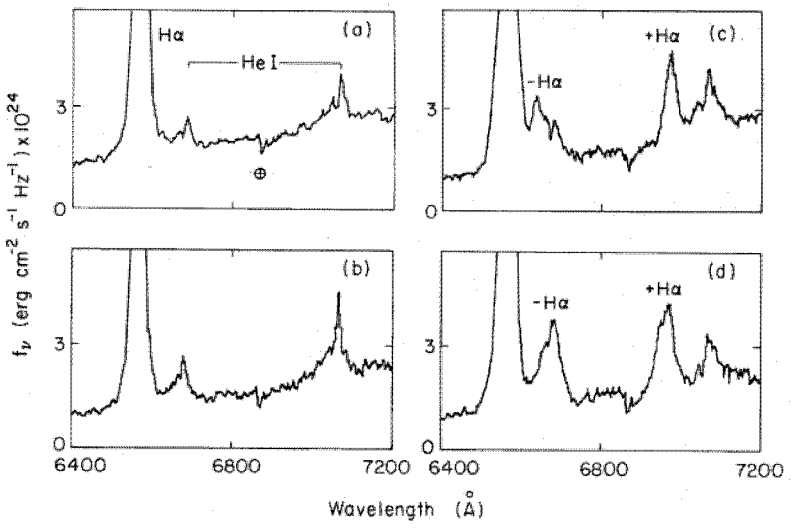

Figure 4.4: Doppler-shifted optical spectral lines of SS433 (Margon 1984).

$$\lambda = \lambda_0 \Gamma (1 + \frac{v}{c}\cos\theta) \tag{4.2}$$

The relativistic Doppler shift therefore contains a time varying component that changes due to direction of motion, but it also includes a time dilation factor or transverse Doppler shift that is independent of direction (Seward & Charles 2010). Margon (1984) plotted the calculated z values for their observations over ~ 3 years (Figure 4.5), clearly showing two components in the observed shifts. The transverse Doppler shift allowed determination of $v \sim 0.26c$.

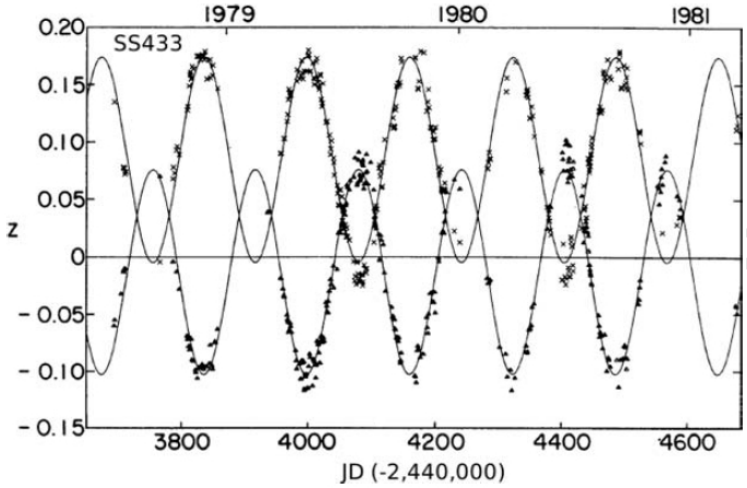

Figure 4.5: Doppler shift variations for SS433 over time (Margon 1984).

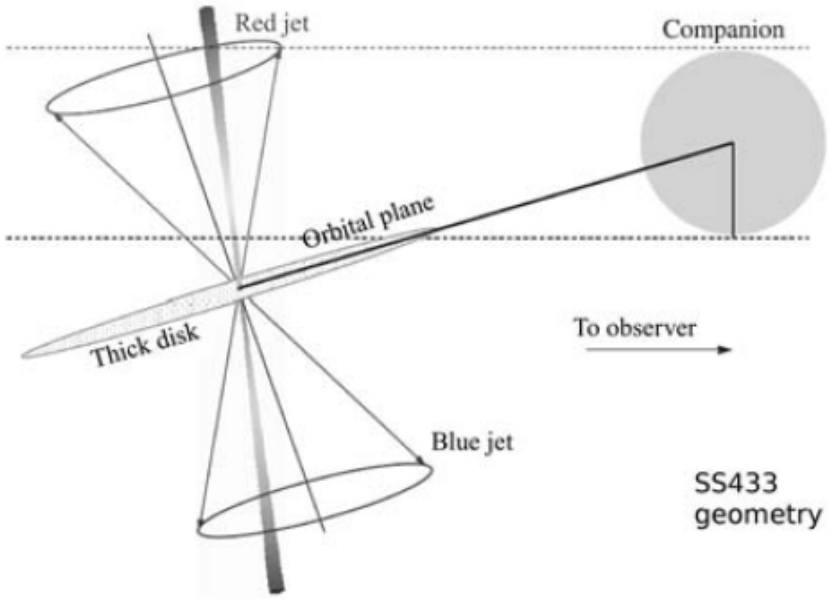

Figure 4.6: Microquasar diagram proposed to explain the geometry of SS433 (Seward & Charles 2010). Two relativistic jets are orientated in opposite directions and precess around their shared rotational axis. Since the latter is not perpendicular to the orbital plane, but rather set at an angle thereto, the precessing jets perform a corkscrew motion.

The kinematic model illustrated in Figure 4.6 suggests that two relativistic jets, orientated in opposite directions, produce the stable $P_{sup} \sim 162$ day cycle in SS433 as they precess around a shared rotational axis (Seward & Charles 2010). The jets and this corkscrew motion have also been directly observed with the Very Long Baseline Array (VLBA) at radio wavelengths (Figure 4.7), since they produce emission at those wavelengths as they interact with the ISM (Mioduszewski & Rupen 2006).

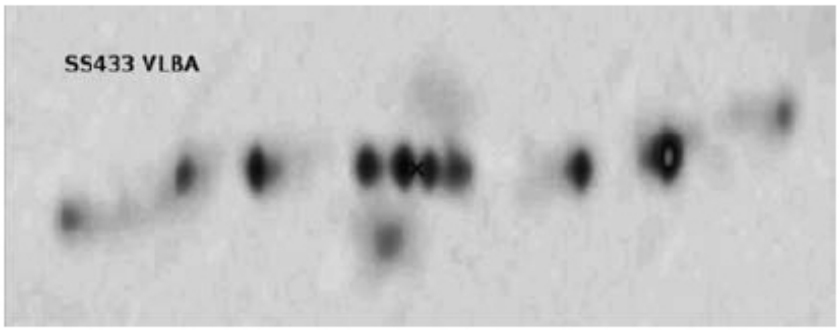

Figure 4.7: VLBA image of precessing jets in SS433 (Mioduszewski & Rupen 2006).

4.1.5 Third Body

Many LMXBs are found in very crowded stellar environments (e.g. globular clusters), where interactions may lead to the creation of stable triple systems. A stable $P_{sup} \sim 172$ days has been observed in 4U 1820-303, which Chou & Grindlay (2001) suggested is the effect of a third body on the $\dot{M}$ in the system. They investigated variations in the $P_{orb} \sim 11$ minutes, by determining the period derivative ($\frac{\dot{P}}{P}$) using historical X-ray data, which they found to deviate from the prediction for the standard scenario, wherein an evolved donor transfers material via RLO to a compact object. Their results are consistent with the effects of a third body with a $P_{orb} \sim 1.1$ days around this otherwise ultra compact X-ray binary (UCB). Since the Roche-lobe radius is proportional to the binary separation of the UCB components, the eccentricity the third body induces in it will affect $\dot{M}$, causing a beat effect between the orbital period of the UCB (P_{inner}) and the period of this third body around it (P_{outer}). The $\frac{\dot{P}}{P}$ they determined was deemed consistent with a $P_{sup} \sim 172$ days, produced as a result of this effect.

4.1.6 Be X-ray Binaries

BeX systems display variations at both the X-ray & optical wavelengths. As discussed earlier, the former is linked to the P_{orb} of a PSR in an eccentric orbit around a Be star, producing X-ray outbursts as the PSR accretes material while moving through the Be star's circumstellar disc. However, the $P_{sup} \sim 200 - 3000$ days in the optical are believed to be linked to the time-scale on which the Be star's equatorial disc expands and contracts, likely also causing variations in the amplitude of the X-ray outbursts (Rajoelimanana et al. 2011).

4.2 Very Long-term Variations

Very long-term variations refer to $P_{sup} \sim$ several years to decades. The mechanism that has been proposed to account for modulations on this time-scale, applies primarily only to it.

4.2.1 Donor Magnetic Cycles

According to Applegate & Patterson (1987), the $\overrightarrow{B}$ of the donor may play a role in the modulation of $\dot{M}$ on the very long-term in a RLO accretion-powered binary, such as a CV or LMXB. They suggested that a donor's $\overrightarrow{B}$ causes variations in its oblateness by affecting its magnetic quadrupole, which in turn affects the Roche lobe and consequently the $\dot{M}$. Richman et al. (1994) reported on the observational evidence of these effects in CVs by determining their $\frac{\dot{P}}{P}$. However, very long-term modulations observed in the X-ray lightcurves of several LMXBs, likely present direct observational evidence of such effects in the RLO X-ray binaries (Kotze & Charles 2010). An entire chapter will be devoted to those results, along with a follow-up with updated results which include additional data.

Chapter 5

RXTE ASM Archival Data

5.1 RXTE

X-ray observations of XRBs are performed by high-energy satellites. The Rossi X-ray Timing Explorer (RXTE) was designed with timing on all time-scales as its goal. Short time-scales require a large collecting area and long time-scales require the ability to scan the whole sky rapidly and regularly. RXTE contains several instruments on board, including the Proportional Counter Array (PCA) and the High Energy X-ray Timing Experiment (HEXTE), which are sensitive to the $2-60$ keV and $15-250$ keV energy ranges respectively (Gibb 2011). Apart from scheduled observations with PCA & HEXTE, the RXTE scans the Galactic bulge and plane continuously, making use of a separate dedicated All Sky Monitor (ASM) instrument that operates in the energy range $1.5-12$ keV (Levine et al. 1996).

5.2 ASM

The ASM instrument and data products are described in detail by Levine et al. (1996), from which a summary of the most relevant information has been included in this section. The Massachusetts Institute of Technology (MIT) has operated the ASM on board the RXTE since early 1996, monitoring the X-ray sky by using three rotating Scanning Shadow Cameras (SSCs). An illustration of the main components of the ASM is provided in Figure 5.1.

5.2.1 Detectors

The SSCs are mounted on a motorized drive assembly, allowing their rotation ("scanning") in order to access different areas on the sky. They all use proportional counters that view the sky through coded masks ("shadow cameras"), allowing the determination of source strengths and positions. Each position-sensitive proportional counter (PSPC) is sensitive to $1.5-12$ keV X-rays and each SSC has on-axis effective areas of 10 cm^2 (at 2 keV), 30 cm^2 (at 5 keV) and 23 cm^2 (at 10 keV).

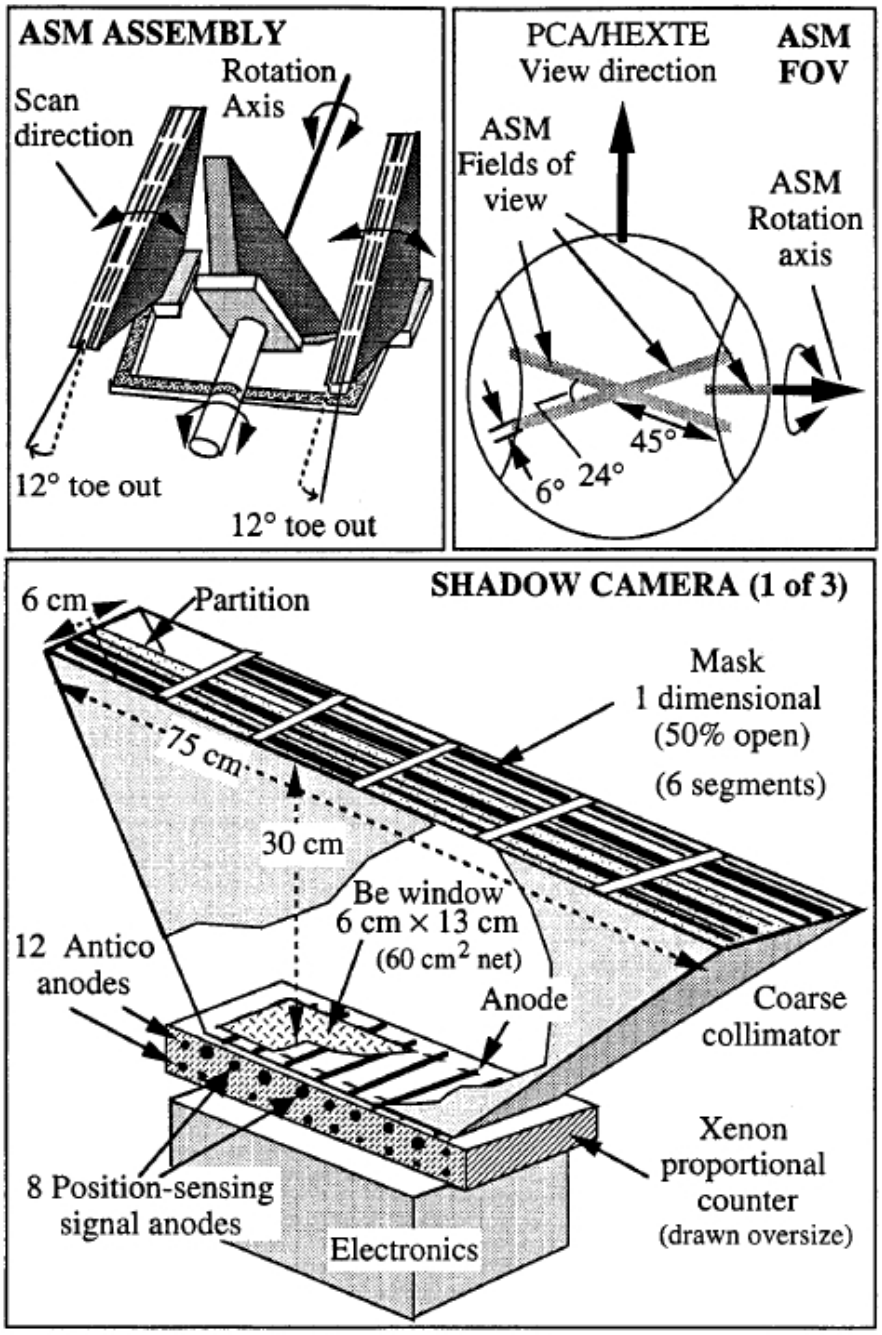

Figure 5.1: Schematic diagrams of the RXTE ASM (Levine et al. 1996). The relative orientation of the 3 SSCs on the ASM assembly is shown (top left). The field of view (FoV) of SSC1 and SSC2 are tilted by $-12°$ and $+12°$ relative to the ASM rotation axis, while the FoV of SSC3 is parallel to it (top right). The viewing direction of the other RXTE instruments (PCA and HEXTE) are also indicated. The bottom schematic diagram shows the major components of each SSC (discussed in the text hereafter).

Coded Mask

Each coded mask consists of a thin aluminium sheet, subdivided into 12 (6×2) subsections, each containing $\sim$ 15 open and $\sim$ 16 closed 1×110 mm slit elements which have been arranged in a pseudo-random pattern. The volume between the mask and the PSPC is split by a partition, so that each half has a FoV $\sim 6^\circ \times 90^\circ$ of the sky through 6×1 subsections of the coded mask.

Proportional Counter

A gas mixture of 95% xenon and 5% CO_2 under 1.2 atm pressure is used to absorb X-rays. Each PSPC contains 8 resistive carbon-coated quartz fibre anodes. The ends of each of these are connected to an electronic measurement chain, so that a detection of an X-ray photon in the vicinity of an anode allows the calculation of both its energy and its position. The resistive coating turns the anode wire into an R-C chain that acts to effectively divide the signal received at each end in a way that indicates the position at which the X-ray arrived.

False positives due to energetic particles, carried to Earth by the solar wind, are identified as events that are also detected by any of 12 metal anodes contained in each PSPC as guard counters. These are very important in the operation of proportional counters as the intrinsic X-ray signal is usually much smaller than the number of background particle events.

Shielding

Each SSC is equipped with an 8 μm aluminized plastic thermal shield and a 50 μm beryllium window through which photons must penetrate to reach the PSPC. The properties of the window select the energies to which the detector will be sensitive. SSC2 and SSC3 are also shielded from leaks by a 2 μm polyimide coating on the inside of their beryllium windows.

Event Analysers

Event data are compressed within two event analysers (EAs). The first EA bins counts according to position into histograms for three energy bands, accumulating these position histograms over a 90 second "dwell", separately for each SSC. During a dwell the SSCs are fixed with respect to the sky, as the ASM rotation drive remains inactive and the satellite is maintained at fixed attitude. The second EA produces X-ray and background count rates and pulse-height spectra. Since the ASM duty cycle is determined by the orientation of the PCA & HEXTE for scheduled observations, ASM sources are sampled $\sim 5 - 10$ times per day in a stochastic pattern.

5.2.2 Solar Constraints

Proximity of sources to the Sun may cause annual gaps in the data if their solar angular separation is $<30^\circ$. These gaps may induce false periodicities in the data, which will present themselves as coincident peaks in the window functions and power spectra.

5.2.3 Data Analysis

Source intensities are only determined for sources that are listed as active in the ASM master catalogue, which include all X-ray sources with accurate positions (uncertainty $< 3'$) that have past X-ray flux measurements of > 3 mCrab in the energy range $2-10$ keV. Transient sources may lie below the ASM detection threshold during quiescence and may only be detected during outbursts.

A linear least squares fit of position histograms (either dwell-by-dwell or SSC-by-SSC) with model shadow patterns for each active source in the FoV yields source intensities and uncertainties based on photon counting statistics. Fits are then repeated, successively removing sources with fitted source intensities below two standard deviations until the fits yield no more sources with such low detections. Thereby negative fitted source intensities are eliminated and problems of source confusion in crowded fields are reduced. Fitted intensities and uncertainties are saved from the last solution for which they were listed. The fitting process is then repeated again, adjusting the SSC pointing direction by increments, since the latter is not sufficiently accurately calibrated. Source intensities and uncertainties are saved for the fit that minimizes the reduced χ^2 value.

Residuals of the fits are cross-correlated to identify sources that are not contained in the active master catalogue. If the location of the source, using the intersection of error boxes from multiple dwells and SSCs, corresponds to an inactive listing in the master catalogue, the listing is updated to active. Otherwise, a new active source is added to it.

Corrections are applied to the count rates from SSC2 & SSC3 to compensate for the absorption by the polyimide coating on their windows. Another correction is applied to compensate for the loss of effective collecting area for sources at large elevations in the FoV, using an empirically determined factor calculated from Crab observations. Together they normalize fitted intensities to the on-axis count rates in SSC1.

5.3 Data Archives

The ASM on board the RXTE has been operational for 15 years, with archival datasets compiled weekly and made publicly available on the ASM website* by the ASM/RXTE teams at MIT and at the RXTE Science Operations Facility (SOF) and Guest Observer Facility (GOF) at NASA's Goddard Space Flight Center (GSFC). These datasets allow study of the long-term behaviour of all 585 X-ray sources contained in the ASM catalogue. Data are available as dwell-by-dwell or one-day-averages in four energy bands, namely: the A-band ($1.5-3$ keV), B-band ($3-5$ keV), C-band ($5-12$ keV) and the sum of all energy bands or sum-band ($1.5-12$ keV). One-day-average data are the dwell-by-dwell data binned into 1-day bins.

*http://xte.mit.edu/ASMlc.html

5.4 Summary of Results

Tables A.1-A.13 contain a summary of the average flux analysis of the sum-band one-day-averages from 20 February 1996 (MJD 50133) to 12 February 2011 (MJD 55608), listed in ascending right ascension (RA). Sources are referred to by their ASM source names throughout this chapter and all the appendices. A source's ASM name is an abbreviated version of its catalogue name (e.g. scox1 for Sco X-1).

The averages of the fluxes ($\overline{y} = \frac{1}{N}\sum_{i=1}^{N} y_i$) and estimated flux errors ($\overline{\sigma} = \frac{1}{N}\sum_{i=1}^{N} \sigma_i$) were determined for each source, using data points for which $|y_i| > |\sigma_i|$. For sources with fluxes below the detector threshold, the background subtraction results in negative flux values. Therefore weak X-ray sources may have average fluxes < 1 counts s^{-1}.

In a Gaussian distribution (with standard deviation σ and average μ) 99.7% of measured values are expected to lie within $\mu \pm 3\sigma$, but only 68.3% within $\mu \pm 1\sigma$. However, if σ is purely interpreted as the error in the measurements and μ as their average, then the detection level may be defined by $n = \overline{y}/\overline{\sigma}$. The latter is commonly referred to as an $n\sigma$ detection.

Sources with $> 3\sigma$ detection and an average flux > 0.5 counts s^{-1} were considered significantly detected. Sources for which detections were not significant or for which too few data points were available, were considered marginal. Subsequently, sources were assigned to a category according to the following criteria:

- 520 "marginal" (if $< 3\sigma$ detection or average flux < 0.5 counts s^{-1})
- 8 "transient" (if outbursts, exceeding the average flux by $> 500\%$, occurred)
- 5 "recurring" (if multiple outbursts occurred)
- 52 "persistent" (if $> 3\sigma$ detection, average flux > 0.5 counts s^{-1} and not transient)

The SIMBAD astronomical database of the Centre de Données astronomiques de Strasbourg or CDS (2011) provides fundamental catalogue classifications for astronomical sources. These SIMBAD types were extracted from their SIMBAD website* via url queries. While this was successful for the vast majority of the sources, there were some for which the SIMBAD types could not be determined. Subsequently, the Liu et al. (2007) classifications were used where possible. For sources that were still undetermined, the Astronomer's Telegrams† (Atel) were searched for classifications of the objects subsequent to their discovery, in which case the number of the Atel is included as a footnote to the table. ASM source names prefixed with 'bl' are BL Lac-type AGNs and those containing '.cg.' are clusters of galaxies. Some of the SIMBAD types were abbreviated as follows: high-mass X-ray binary (HMXB), low-mass X-ray binary (LMXB), cataclysmic variable (CV), active galactic nuclei (AGN) and supernova remnant (SNR).

*http://simbad.u-strasbg.fr/simbad/
†http://www.astronomerstelegram.org/

5.5 Significant Detections

There are 520 ASM sources in the "marginal" category. The 65 significantly detected sources contained in the RXTE ASM data, include the following object types:

- 45 Low-mass X-ray binaries (LMXBs)
- 12 High-mass X-ray binaries (HMXBs)
- 3 Supernova remnants (SNRs)
- 1 LINER-type AGN
- 1 BL Lac-type AGN
- 1 Seyfert 2 galaxy
- 1 Be star (therefore an HMXB)
- 1 Galactic centre transient (GC transient)

Therefore the significantly detected sources in the RXTE ASM are predominantly XRBs, accounting for 58 of the 65 sources. These archival datasets consequently present an unprecedented opportunity to analyse the long-term behaviour of XRBs, particularly since their observational baseline now stretches over an entire 15 years. Therefore, the sum-band one-day-average data over the entire observational baseline, for the significantly detected sources, were binned into 10-day bins and plotted on scales that allow examination of long-term flux modulations. Only data points for which the binned flux value exceeded the error therein were plotted in Figure B.1-B.11 (presented by ascending RA), with their SIMBAD object types included in square brackets.

These lightcurves clearly display a variety of flux behaviours over the observational baseline of ~ 15 years. There are flux variations visible on the short, medium and long term, with some sources showing very long-term modulations in their flux. The behaviour also varies within the LMXB and HMXB object types. Some sources show fairly steady flux, while others contain single or even multiple transient outbursts with durations and recurrence times ranging from short to very long time-scales.

Not all significantly detected sources can be considered persistent, since transient behaviour accounted for the detection of 13 sources, namely: v0332+53, x0535+262, x1543-475, xtej1550-564, x1608-522, x1630-472, groj1655-40, xtej1701-462, gx339-4, h1743-322, swiftj1753.5-0127, xtej1859+226 and aqlx1 (all of which are XRBs).

The remaining 52 significantly detected sources are considered to be persistent sources, which include 45 XRBs, the Galactic centre transient, 3 SNRs, a LINER-type AGN, a BL Lac-type AGN and a cluster of galaxies which includes a Seyfert 2 galaxy. Their variability (if any) may be revealed as periodic, quasi-periodic or aperiodic by applying period analysis techniques to their lightcurve data.

Visual inspection of the lightcurves revealed one of the most significant results produced by this work, namely the large amplitude, very long-term modulations exhibited by some XRBs: xper, cirx1, x1636-536, x1708-407, gx9+9, gx354-0, ks1731-260, x1735-444, gx3+1, x1746-370, gx9+1 and serx1. These results regarding the LMXBs have been published (Kotze & Charles 2010) and are presented in Chapter 7.

SNRs (particularly the Crab) are considered to be steady and are expected to remain steady. Therefore, the RXTE ASM team has been using them as calibration sources when performing their data reductions. The decline in the counts of the Crab at MJD $\sim$ 55500, indicates that the calibration parameters require adjustment (Levine, in private correspondence), but it should not affect the overall period analysis of the datasets. However, ASM coverage after MJD $\sim$ 55600 is no longer continuous, consequently this work excludes data after 12 February 2011 (MJD 55608).

5.6 Period Analysis

Considering only significantly detected sources (Section 5.5) may be too conservative since many sources with known periodic behaviour (orbital and super-orbital) were considered marginally detected. Periodic signals may be significantly detected in sources that are not considered significantly detected themselves, e.g. the following sources with known super-orbital periods: x1730-333, igrj17098-3626, x1916-053, exo0748-676, xtej1716-389, ss433, x0114+650, lmcx4, grs1747-312 and ms1603.6+2600. With the exception of the very last one listed, these sources all have detection $> 1\sigma$ and average flux > 0.5 counts s^{-1}. Consequently a systematic period analysis intending to include all the aforementioned sources, will have to consider all 166 sources for which the detection $> 1\sigma$ and average flux > 0.5 counts s^{-1}.

Alternatively, all 585 sources in the ASM catalogue can be considered, with the obvious advantage of including sources with even lower detections. But it has the equally clear disadvantage of complicating the computations and analysis by including more than 3$\times$ as many sources. However, such an approach may assist in identifying periodic behaviour that has not yet been reported, making it an attractive endeavour. A systematic approach applied to all sources may also aid in the detection of systematic effects that are not source related and if it proves reliable in the detection of known periodic behaviour, it gains credibility for its ability to detect new periodic behaviour.

In order to apply a systematic approach to 65 or 585 sources, automation of the period analysis process was necessary, which may be applied to all sources, once it has been proven to be effective on the smaller sample. Consequently, the period analysis techniques discussed in Chapter 3, were automated using a combination of shell scripts in LINUX* and PYTHON†, while utilizing GNUPLOT‡ for the visualization of the results. The Starlink PERIOD§ package was employed to obtain L-S, PDM and window functions.

*https://www.linux.com/
†http://www.python.org/
‡http://www.gnuplot.info/
§http://star-www.rl.ac.uk/docs/sun167.htx/sun167.html

5.6.1 Own Constructed One-day-averages

The one-day-average data provided by the RXTE ASM team contain all dwell-by-dwell data binned into 1-day bins, allowing for bins to be constructed from data points that do not necessarily meet all stringent requirements in determining the reliability of a data point. Since it involves binning the data without the filtering prescribed by the ASM team on their own website*, it may introduce false signals that are a result of factors other than the variability of the sources themselves. However, a preliminary period analysis may be conducted on the ASM one-day-average data, to determine which sources show potential variability. Consequently, a full investigation should include a detailed variability analysis conducted on the dwell-by-dwell data re-binned into 1-day bins, using Alan Levine's FORTRAN code for binning, after applying two sets of filters using PERL† scripts. Together these sets of filters eliminate unreliable data points from inclusion in the binning process so that the one-day-averages constructed in this manner represent data that could be considered reliable for the sources. The first set of filters are those officially prescribed by the RXTE ASM team for constructing your own one-day-averages from dwell-by-dwell data (Levine et al. 1996):

- $\chi^2_\nu < 8$ for scox1, otherwise $\chi^2_\nu < 1.5$ (reject results from poor fits)
- number of sources in the FoV < 16 (avoid exceptionally crowded fields)
- Earth angle $> 75^\circ$ (avoid sources close or behind the Earth's limb)
- exposure time > 30 seconds (entry into high background regions cuts exposures short)
- long-axis angle: $-41.5^\circ < \theta < 46^\circ$ (avoid edges, since $\theta = 110^\circ$ for the full FoV)
- short-axis angle: $-5^\circ < \phi < 5^\circ$ (avoid edges, since $\phi = 12^\circ$ for the full FoV)

The second set of filters were compiled from recommendations by individuals that have been working on ASM data analysis for many years, such as Alan Levine and Ron Remillard. Those additional filters that should be applied to yield the most reliable dataset, are:

- background counts < 10 (avoid high background values)
- hardness ratio: $-5 < \frac{B+C}{A} < 5$ (avoid unreliable detections in individual bands)
- flux error < 3 counts s^{-1} (avoid large errors)
- Scanning Shadow Camera (SSC) > 1 (SSC1 may suffer from secular gain increases‡)
- number of data points per bin > 1 (require more than one dwell value per day)

The application of all the aforementioned constraints may lead to a considerable data loss. Therefore, the measure by which each own constructed one-day-average dataset manages to cover the observational baseline needs to be considered (see Table 5.1).

*http://xte.mit.edu/ASMlc.html
†http://www.perl.org/
‡Levine et al. (2011)

Table 5.1: Summary of potentially periodic, significantly detected ASM sources

ASM name	**SIMBAD type**	**Average flux(error)** [counts s^{-1}]	**Category**	**Detection significance**	**Coverage**
smcx1	HMXB	1.7(4)	persistent	4.2σ	71%
ngc1275.cg	Seyfert 2 galaxy	2.6(4)	persistent	5.9σ	70%
xper	HMXB	1.6(4)	persistent	4.2σ	68%
crab	SNR	75.1(9)	persistent	82.5σ	70%
lmcx3	HMXB	1.7(4)	persistent	4.6σ	80%
x0614+091	LMXB	3.3(4)	persistent	7.8σ	71%
velax1	HMXB	4.1(4)	persistent	9.9σ	64%
mkn421	BL Lac-type	1.4(4)	persistent	3.5σ	70%
cenx3	HMXB	4.5(5)	persistent	9.8σ	59%
gx301-2	HMXB	2.0(4)	persistent	4.6σ	60%
m87	LINER-type	1.5(5)	persistent	3.1σ	62%
cirx1	LMXB	45.8(8)	persistent	59.5σ	66%
scox1	LMXB	890(6)	persistent	142.6σ	69%
x1624-490	LMXB	3.5(6)	persistent	6.1σ	52%
x1636-536	LMXB	9.1(6)	persistent	15.4σ	66%
gx340+0	LMXB	28.9(8)	persistent	35.2σ	34%
herx1	LMXB	1.6(3)	persistent	4.8σ	79%
x1700-377	HMXB	4.5(7)	persistent	6.3σ	43%
x1702-429	LMXB	3.2(7)	persistent	4.9σ	54%
x1705-440	LMXB	11.8(7)	persistent	16.4σ	53%
x1708-407	LMXB	2.2(6)	persistent	3.4σ	47%
x1724-307	LMXB	2.1(7)	persistent	3.2σ	18%
gx9+9	LMXB	19.5(8)	persistent	23.2σ	64%
gx354-0	LMXB	6.7(7)	persistent	9.9σ	41%
ks1731-260	LMXB	5(1)	persistent	5.4σ	16%
x1735-444	LMXB	12.8(7)	persistent	18.3σ	60%
gctr_diffuse	GC transient	5(1)	persistent	3.6σ	3%
gx3+1	LMXB	22(1)	persistent	20.5σ	28%
x1746-370	LMXB	2.5(6)	persistent	3.9σ	40%
gx5-1	LMXB	70(1)	persistent	56.4σ	45%
gx9+1	LMXB	38(1)	persistent	39.6σ	60%
gx13+1	LMXB	22.5(8)	persistent	27.4σ	62%
x1820-303	LMXB	21.0(9)	persistent	24.7σ	40%
gs1826-238	LMXB	3.0(7)	persistent	4.2σ	38%
serx1	LMXB	15.8(5)	persistent	29.3σ	74%
grs1915+105	LMXB	54.5(8)	persistent	72.7σ	66%
cygx1	HMXB	31.2(5)	persistent	61.2σ	83%
x1957+115	LMXB	2.4(4)	persistent	5.8σ	74%
exo2030+375**	HMXB	1.3(4)	transient	3.5σ	78%
cygx3	HMXB	12.4(4)	persistent	30.2σ	72%
cygx2	LMXB	37.6(6)	persistent	67.1σ	85%
casa	SNR	5.0(3)	persistent	14.6σ	90%

Error applies to the last digit of the flux.
** Minus transient outburst

5.6.2 Persistent Sources

When considering periodic behaviour, it is customary to exclude transient sources, however exo2030+375 remained persistent even after removing its outburst. The 52 persistent sources that were significantly detected ($> 3\sigma$), represent the sources for which period analysis techniques should reveal any periodic behaviour most reliably. Among them are several sources with known periodic behaviour, with which these results may be compared. Period analysis of their ASM one-day-average datasets indicated possible periodic behaviour (peaks $>$ white noise) over the range $2-1000$ days in 42 sources. The remaining 10 sources revealed no significant periodic behaviour, and are: tychosnr, lmcx2, lmcx1, x1254-690, x1543-624, x1556-605, gx349+2, gx17+2, x1822-000 and x1822-371.

Table 5.1 contains SIMBAD types, detection levels and the % of the baseline covered by own constructed one-day-averages for the 42 potentially periodic sources. In the majority of the sources the coverage is $> 33\%$, leaving only gctr_diffuse, ks1731-260, x1724-307 and gx3+1 with very low coverages of 3%, 16%, 18% and 28% respectively. Sources with better coverage should lead to a more accurate determination of periods contained in the data. The major advantage of own constructed one-day-averages is naturally the improvement in quality of each available data point.

Corbet et al. (2007) suggested using a modified weighting scheme, which may be applied to datasets to improve the sensitivity of period analysis techniques. Consequently, applying it to the own constructed one-day-average data should result in the most reliable dataset, which should have the greatest probability of eliminating periods induced by inclusion of unreliable data points when using unfiltered ASM one-day-averages. Unfortunately, severe spectral leakages due to the exclusion of such a large portion of the data points, have the negative effect of introducing spurious periodic signals when using this approach. But, the potentially significant periods determined from the ASM one-day-averages that are coincident with those from the own constructed one-day-averages, constitute the most reliably determined significant periodic signals for a source. To facilitate this, all the significant periodic signals (peaks $>$ white noise) in the period range were extracted and their periods and estimated errors were determined, subsequently allowing all periods to be identified that fall within $3\times$ each other's error estimates, for the results of the two datasets respectively. This approach immediately eliminated the following 12 sources from being potentially periodic over the range $2-1000$ days: ngc1275.cg, xper, x1624-490, gx340+0, x1708-407, x1724-307, gx9+9, x1735-444, gctr_diffuse, x1746-370, gs1826-238 and casa.

Furthermore, periods that are coincident with peaks in the window functions, are the result of spectral leakage and are therefore not source related. These are particularly prevalent around ~ 365 days or ~ 183 days due to the annual cycle. Sources that appear to have been considered periodic only due to these effects were: crab, m87 and ks1731-260.

Consequently, none of the SNRs (crab, casa & tychosnr) remain as potentially periodic, which is to be expected since they are considered intrinsically steady sources. The Galactic centre transient (gctr_diffuse), the LINER-type AGN (m87) and the cluster of galaxies (ngc1275.cg) have also been eliminated as potentially periodic sources in our context.

Therefore, only 27 sources remain as potentially periodic out of 65 significantly detected ($> 3\sigma$) sources, all of which are XRBs with the exception of mkn421 (a BL Lac-type AGN). Their combined plots for the period analysis over the entire observational baseline (L-S, PDM, window and noise) and the time-dependent period analysis (including the DPS, lightcurve and L-S) are presented in Appendix C.

Table 5.2: Summary of known periods < 1 year confirmed for significant sources

Source	P_{orb} [days]	P_{sup} [days]	**Harmonics**
smcx1	3.89 $^{[S]}$	$46 - 68$ $^{[W]}$	
velax1	8.97 $^{[L1]}$		4.48 (1st)
cenx3	2.09 $^{[L1]}$		
gx301-2	41.49 $^{[L1]}$		20.73 (1st), 13.83 (2nd)
cirx1	16.55 $^{[L2]}$		
herx1		34.95 $^{[W]}$	17.48 (1st)
x1700-377	3.41 $^{[L1]}$		
x1820-303		169.2 $^{[W]}$	84.25 (1st)
exo2030+375	46.13 $^{[L1]}$		
cygx2		$37 - 85$ $^{[W]}$	

$^{[L1]}$ Liu et al. (2006), $^{[L2]}$ Liu et al. (2007) and references in aforementioned, $^{[S]}$ Schreier et al. (1972a), $^{[W]}$ Wen et al. (2006) and references therein

Table 5.2 contains the periods identified in these sources that correspond to known (super-)orbital periods. However, there were additional potential periods identified, such as $P_{sup} \sim 59$ days for x0614+091, together with a $P_{sup} \sim 188$ days (linked to spectral leakage), of which the former is not a harmonic. However, its spectrum is noisy since neither peak is $> 10\times$ the average power or significantly above the white noise. Other sources with such noisy spectra are gx354-0, scox1, x1702-429, gx5-1, gx9+1, gx13+1 and serx1. The weak detections (L-S power $< 2\times$ white noise) in x0614+091, scox1, x1702-429, gx354-0, gx5-1, gx13+1 and serx1 all appear to be produced by intermittent aperiodic signals.

In cirx1, two significant peaks at $P_{sup} \sim 342$ & $P_{sup} \sim 389$ days are rather close to 365 days. These appear to be beat periods associated with the (bi)annual cycle and the very long-term modulation in its lightcurve. The $P_{sup} \sim 179$ & ~ 337 days in x1636-536, $P_{sup} \sim 314$ & ~ 441 days in gx3+1 and $P_{sup} \sim 333$ & ~ 408 days in gx9+1 also result from this effect. Sources exhibiting very long-term behaviour are discussed in Chapter 7.

Both smcx1 and cygx2 display P_{sup} over a range of periods. Other sources exhibit similar behaviour that may be directly linked to the time-scale of the lightcurve features themselves. They are: lmcx3, mkn421, cenx3, x1705-440, grs1915+105, cygx1, x1957+115 and cygx3. In those cases the DPS reveal complex periodic behaviour, such as multiple intermittent and/or variable periodic signals. These include sources with known super-orbital behaviour, such as: smcx1, lmcx3, cenx3, cygx1, x1957+115 and cygx2. Sources with previously reported super-orbital behaviour and the interpretation of their time-dependent period analysis, are discussed in detail in Chapter 6.

The analysis employed to identify periodic behaviour successfully detected most of the known periods (considered in Chapter 6), which were among the 65 significantly detected sources. The exceptions are the $P_{sup} \sim 8$ days for lmcx2 (Figure 6.19) which was optically detected, $P_{sup} \sim 46$ days for x1636-536 and $P_{sup} \sim 38$ days for ks1731-260. Both the latter are quasi-persistent transients with intermittent periodic signals. Additional periodic signals detected in the analysis all appear to have their origin in the source behaviour itself, except those that were coincident with peaks in the window function.

5.6.3 All ASM sources

The primary focus of this work is the characterization of long-term periodic behaviour in XRBs with known P_{sup}, which is discussed in Chapter 6. However, the development of the systematic approach applied in the previous section allowed the search for similar long-term periodic behaviour in XRBs that may have gone unnoticed or have been ignored thus far.

The initial period analysis on the one-day-averages of all 585 ASM sources identified 165 sources with potential periodic behaviour over the range $2 - 1000$ days, using an average white noise estimate of 15 (L-S power units). The latter value was based on the average white noise estimates determined for the 65 significantly detected sources, which were all > 15. Individual white noise estimates for all 165 potentially periodic ASM sources were also > 15 and the subsequent test of all peaks against the individually determined white noise estimates yielded 149 sources exhibiting possible periodicities.

Potentially significant periods determined from the ASM one-day-averages are required to be coincident with those from the own constructed one-day-averages. The previous section has proven this to be a reliable test to eliminate spurious periodicities. There were only 83 sources for which at least one period occurred in both datasets and they are listed in Tables 5.3 & 5.4 with their SIMBAD types, detection levels and coverage achieved by the own constructed one-day-averages.

XRBs with known super-orbital behaviour are discussed in detail in Chapter 6 and sources exhibiting very long-term behaviour are discussed in Chapter 7. These 83 potentially periodic sources include most XRBs with known super-orbital behaviour (Chapter 6), which were indicated by suffixing their source names with * in Tables 5.3 & 5.4 and the rest of the section. However, ms1603.6+2600 (Figure 6.20) has an optically identified P_{sup} which is not detected in the ASM one-day-averages. Intermittent quasi-periodic signals in igrj17098-3628 (Figure 6.17) were only detected in the high state. Although quasi-periodic signals in grs1747-312 (Figure 6.13) were significantly detected in the ASM one-day-averages, they were not detected in the own constructed one-day-averages. No significant periodic signals were detected in the ASM one-day-averages for x1916-053 (Figure 6.25).

All 40 sources in the marginal category are therefore additional to those considered in the previous section, which only included significantly detected sources. They include 33 XRBs (16 HMXBs, 15 LMXBs and 2 uncategorized XRBs) and 7 other sources: xtej1837+037 and swiftj1842.5-1124 (X-ray sources), cena (Seyfert 2 galaxy), mkn501 (BL Lac-type AGN), amher (CV), bl2005-489 (BL Lac-type AGN) and mr2251-178 (Seyfert 1 galaxy).

Table 5.3: Summary of potentially periodic ASM sources (RA: 00-17)

ASM name	**SIMBAD type**	**Average flux(error)** [counts s^{-1}]	**Category**	**Detection significance**	**Coverage**
smcx1*	HMXB	1.7(4)	persistent	4.2σ	71%
x0114+650*	HMXB	0.5(3)	**marginal**	1.7σ	86%
x0115+634	HMXB	1.0(4)	**marginal**	2.9σ	72%
v0332+53	HMXB	1.5(4)	transient	4.0σ	76%
x0512-401	LMXB	0.7(3)	**marginal**	2.0σ	77%
lmcx4*	HMXB	0.6(4)	**marginal**	1.7σ	75%
crab	SNR	75.1(9)	persistent	82.5σ	70%
x0535+262	Be star	1.8(5)	recurring	3.8σ	64%
lmcx3*	HMXB	1.7(4)	persistent	4.6σ	80%
x0614+091	LMXB	3.3(4)	persistent	7.8σ	71%
x0656-072	HMXB	0.8(4)	**marginal**	1.8σ	69%
x0726-260	HMXB	0.2(4)	**marginal**	0.6σ	75%
exo0748-676*	LMXB	0.8(3)	**marginal**	2.3σ	77%
velax1	HMXB	4.1(4)	persistent	9.9σ	64%
mkn421	BL Lac-type	1.4(4)	persistent	3.5σ	70%
xtej1118+480	LMXB	0.3(4)	**marginal**	0.8σ	71%
cenx3*	HMXB	4.5(5)	persistent	9.8σ	59%
gx301-2	HMXB	2.0(4)	persistent	4.6σ	60%
m87	LINER-type	1.5(5)	persistent	3.1σ	62%
cena	Seyfert 2	1.0(4)	**marginal**	2.4σ	67%
cirx1	LMXB	45.8(8)	persistent	59.5σ	66%
x1538-522	HMXB	1.1(5)	**marginal**	2.3σ	62%
xtej1550-564	LMXB	9.7(6)	transient	15.2σ	55%
x1608-522	LMXB	4.9(6)	recurring	8.9σ	60%
scox1*	LMXB	890(6)	persistent	142.6σ	69%
x1630-472	LMXB	7.4(6)	transient	11.5σ	52%
x1636-536*	LMXB	9.1(6)	persistent	15.4σ	66%
xtej1650-500	LMXB	1.1(7)	**marginal**	1.5σ	49%
mkn501	BL Lac-type	0.6(3)	**marginal**	1.9σ	81%
groj1655-40	LMXB	30.8(8)	recurring	36.7σ	41%
herx1*	LMXB	1.6(3)	persistent	4.8σ	79%
x1657-415	HMXB	1.3(6)	**marginal**	2.0σ	46%
xtej1701-462	LMXB	5.8(8)	transient	7.2σ	41%
x1658-298	LMXB	0.9(7)	**marginal**	1.2σ	25%
gx339-4*	LMXB	9.7(7)	recurring	14.2σ	58%
x1700-377	HMXB	4.5(7)	persistent	6.3σ	43%
x1702-429	LMXB	3.2(7)	persistent	4.9σ	54%
x1704+240	LMXB	0.5(4)	**marginal**	1.3σ	76%
x1705-440	LMXB	11.8(7)	persistent	16.4σ	53%
xtej1716-389*	HMXB	1.4(7)	**marginal**	2.1σ	39%
gx354-0*	LMXB	6.7(7)	persistent	9.9σ	41%
x1730-333*	LMXB	2.0(7)	**marginal**	3.0σ	39%
ks1731-260*	LMXB	5(1)	persistent	5.4σ	16%
x1735-444	LMXB	12.8(7)	persistent	18.3σ	60%
h1743-322	LMXB	4.5(8)	transient	5.5σ	14%

Table 5.4: Summary of potentially periodic ASM sources (RA: 17-24)

ASM name	**SIMBAD type**	**Average flux(error)** [counts s^{-1}]	**Category**	**Detection significance**	**Coverage**
gx3+1	LMXB	22(1)	persistent	20.5σ	28%
exo1745-248	LMXB	1(1)	**marginal**	1.3σ	17%
x1745-203	LMXB	1.0(9)	**marginal**	1.1σ	38%
sl1746-331	LMXB	1.2(8)	**marginal**	1.5σ	18%
swiftj1753.5-0127	LMXB	1.5(5)	transient	3.2σ	66%
gx5-1	LMXB	70(1)	persistent	56.4σ	45%
gx9+1	LMXB	38(1)	persistent	39.6σ	60%
x1803-245	LMXB	1(1)	**marginal**	1.5σ	27%
gx13+1	LMXB	22.5(8)	persistent	27.4σ	62%
amher	CV	0.3(3)	**marginal**	1.2σ	86%
xtej1818-245	LMXB?	1.0(9)	**marginal**	1.1σ	27%
x1820-303*	LMXB	21.0(9)	persistent	24.7σ	40%
xtej1837+037	X-ray source	0.3(5)	**marginal**	0.6σ	66%
serx1	LMXB	15.8(5)	persistent	29.3σ	74%
swiftj1842.5-1124	X-ray source	0.6(6)	**marginal**	1.1σ	50%
xtej1855-026	HMXB	0.5(5)	**marginal**	1.0σ	55%
xtej1856+053	LMXB	0.7(5)	**marginal**	1.3σ	56%
xtej1859+226	LMXB	1.2(4)	transient	3.2σ	75%
x1901+031	HMXB	0.8(5)	**marginal**	1.6σ	63%
x1907+097*	HMXB	1.0(5)	**marginal**	1.9σ	55%
aqlx1	LMXB	3.4(5)	recurring	6.8σ	67%
ss433*	HMXB	0.7(4)	**marginal**	1.8σ	68%
grs1915+105	LMXB	54.5(8)	persistent	72.7σ	66%
x1942+274	X-ray binary	0.6(4)	**marginal**	1.7σ	74%
ks1947+300	HMXB	0.6(4)	**marginal**	1.8σ	75%
x1953+319	HMXB	0.9(4)	**marginal**	2.5σ	76%
cygx1*	HMXB	31.2(5)	persistent	61.2σ	83%
x1957+115*	LMXB	2.4(4)	persistent	5.8σ	74%
bl2005-489	BL Lac-type	0.4(5)	**marginal**	0.8σ	66%
xtej2012+381	LMXB	0.7(4)	**marginal**	1.7σ	74%
exo2030+375**	HMXB	1.3(4)	transient	3.5σ	78%
cygx3	HMXB	12.4(4)	persistent	30.2σ	72%
saxj2103.5+4545	HMXB	0.5(3)	**marginal**	1.5σ	78%
xtej2123-058	LMXB	0.3(6)	**marginal**	0.5σ	61%
x2127+119	X-ray binary	1.1(4)	**marginal**	2.7σ	71%
cygx2*	LMXB	37.6(6)	persistent	67.1σ	85%
x2206+543	HMXB	0.6(3)	**marginal**	2.0σ	85%
mr2251-178	Seyfert 1	0.4(5)	**marginal**	0.9σ	64%

** Minus transient outburst

Annual gaps in the data are responsible for the detection of the only significant periodicities in mr2251-178 and cena, since they are also coincident with window peaks. Both xtej1837+037 and swiftj1842.5-1124 are transients, so are the uncategorized XRBs: x1942+274 and x2127+119. In fact, some of the HMXBs are also transients: x0115+634, x0656-072, x1901+031 and ks1947+300. LMXB transients are: xtej1118+480, xtej1650-500, exo1745-248, x1745-203, sl1746-331, x1803-245, xtej1818-245, xtej1856+053, xtej2012+381 and xtej2123-058.

The remaining 20 sources are all potentially periodic. The HMXBs included among them are: x0114+650*, lmcx4*, x0726-260, x1538-522, x1657-415, xtej1716-389*, xtej1855-026, x1907+097*, ss433*, x1953+319, saxj2103.5+4545 and x2206+543. The LMXBs are: x0512-401, exo0748-676*, x1658-298, x1704+240 and x1730-333*. Their results are presented in Appendix C. The transient source x1942+274 was also included therein, since a change in its outburst recurrence time is clear in its period analysis. Table 5.5 contains the periods identified in these sources that correspond to known (super-)orbital periods.

Table 5.5: Summary of known periods < 1 year confirmed for marginal sources

Source	P_{orb} [days]	P_{sup} [days]	**Harmonics**
x0114+650*	11.6 [L1]	31 [W]	
lmcx4*		30 [W]	
x0726-260	34.6 [L1]		
x1538-522	3.7 [L1]		
x1657-415	10.5 [L1]		
xtej1716-389*		99 [W]	
xtej1855-026	6.1 [L1]		
x1907+097*	8.4 [L1]		4.2 (1st)
x1942+274		80 [L1]	
ss433*		162 [W]	

[L1] Liu et al. (2006), [L2] Liu et al. (2007), [W] Wen et al. (2006) and references in all the aforementioned

Several sources exhibit behaviour that may be directly linked to the time-scale of the lightcurve features themselves. They are: x0512-401, mkn501, x1658-298, x1704+240, x1730-333* (variable outburst recurrence times), amher, x1942+274 (outburst recurrence), x1953+319, bl2005-489, saxj2103.5+4545 and x2206+543. Sources with noisy power spectra produced by intermittent aperiodic signals, include exo0748-676*.

The DPS detects the intermittent quasi-periodic signals in x1636-536* (Figure 6.22) and ks1731-260* (Figure 6.18), which are discussed in Chapter 6. It may therefore be useful as a detection method in future, not only as a tool for the characterization of periodic behaviour.

Clearly periods may be determined successfully for sources that are only marginally detected themselves ($< 3\sigma$), but they are all $> 0.5\sigma$. A 1σ detection implies a $\sim 32\%$ probability of the detection occurring by chance, while a 3σ detection reduces this to $< 1\%$. However, even if a source is only weakly detected, a periodic modulation in that weak signal may rise significantly above the noise if the observational baseline is of sufficient length.

Considering that periods have only been determined for sources in the marginal category that have detection significance $> 0.5\sigma$, we may recategorize those $< 0.5\sigma$ as 'negligible'. The intention in calculating the average flux using data points for which $|y_i| > |\sigma_i|$, was to exclude unreliable data points from the calculations. However, since each measurement is automatically background subtracted for a coded mask instrument, flux measurements of a faint source are normally distributed around zero. Exclusion of points for which the error estimate exceeds the absolute flux value, will ignore values that are $\sim$0 and will lead to an overestimation of the average flux, an underestimation of the average estimated error and consequently an overestimation of the significance of detection for faint sources. A further 15 sources (among them are Her X-1 and v0332+53) can be considered only marginally detected if all data points are used in the calculation of average flux and average errors. If these parameters are ever included in a future publication, I will update them to include all data points.

Levine et al. (2011) presented results from their analysis of $\sim$ 14 years of RXTE ASM data. They extended the Wen et al. (2006) search, which detected 41 periodicities and 5 potential quasi-periodicities in XRBs using $\sim$ 8.5 years of RXTE ASM data. By employing new strategies and using the longer observational baseline they improved the search sensitivity and added 18 newly detected orbital periods for XRBs. Their new strategy involved using the window weighting scheme (Chapter 3) which led to a substantial increase in sensitivity for periods < 1 day. Wen et al. (2006) and Levine et al. (2011) are the most comprehensive searches conducted to date for periods from hours to years on the RXTE ASM data.

The super-orbital periodicities contained in Wen et al. (2006) were almost all identified by the analysis method employed herein. The only exception is grs1747-312 (Figure 6.13), for which the own constructed one-day-averages did not achieve sufficient coverage to allow the detection of the evolving quasi-periodic signals. Since the method requires the periodic signal to be present in both ASM and own constructed one-day-averages, grs1747-312 was not considered periodic even though the quasi-periodic signal was significantly detected in the ASM one-day-average data.

The analysis presented here did not identify any new super-orbital behaviour in sources with no previously known super-orbital behaviour. However, additional periodicities were found in several of the sources with known super-orbital behaviour, as a result of their complex super-orbital behaviour (Chapter 6).

Chapter 6

Characterizing Known Behaviour

The aim of the results presented here and published in Kotze & Charles (2012), is to provide a clearer picture of the super-orbital behaviour of XRBs which have been associated with the precession of warped and/or tilted accretion discs. The primary goal is the characterization of long-term behaviour ($P_{sup} < 1$ year) in these XRBs using Dynamic Power Spectra (DPS), described in Chapter 3.

Clarkson et al. (2003a) presented DPS results for Cyg X-2, Her X-1, LMC X-4 and SMC X-1, which are all NS systems with known P_{sup} for which independent observational evidence supported the association of their observed P_{sup} with warped and/or tilted precessing accretion discs. A systematic approach which includes all the XRBs with known P_{sup}, has not yet been attempted and since the approach here is to consider the vast majority of such sources, it requires greater emphasis on other mechanisms that may be responsible for the previously reported P_{sup}, discussed in Chapter 4. However, the availability of the OD01 (Ogilvie & Dubus 2001) stability predictions for accretion discs against radiation-driven warping/tilting, makes it an obvious first choice against which to test the observed behaviour. Thereafter, Whitehurst & King (1991) tidal disc precession and other mechanisms will be considered where appropriate.

6.1 Sources with Known P_{sup}

The 9 HMXBs and 16 LMXBs with known $P_{sup} < 1$ year are listed in Tables 6.1 & 6.2 respectively, together with their previously published P_{sup}, P_{orb}, $q = \frac{M_2}{M_1}$ and r_b. Values for the latter two parameters were taken from OD01, with values in square brackets indicating their best approximations. The positions of the sources (if known) are shown on an adapted plot (Figure 6.1) of radiation-induced disc instability zones (Figure 4.2) with respect to q and r_b (in units of $\left[\frac{GM_1}{c^2}\right]$). The tables also include the source types in the Liu et al. (2006; 2007) catalogue papers, for which abbreviations were added as footnotes in the tables. Although every effort was made to include as many sources as possible, there may be previously published results/sources that are not represented here.

Table 6.1: HMXBs with known $P_{sup} < 1$ year

Source	P_{sup} [days]	P_{orb} [days]	q $[\frac{M_2}{M_1}]$	$r_b/10^6$ $[\frac{GM_1}{c^2}]$	**Types**
Cen X-3	120-165 [1], 140 [2]	2.09 [3]	17.0	6.7	P,E,C
Cyg X-1	150 [4], 326 [5], 290 [6]	5.6 [7]	1.7	1.9	U,R
LMC X-3	99 [8], 100-500 [9]	1.70 [10]	0.5	1.1	
LMC X-4	30 [11]	1.41 [12]	10.6	4.5	
SMC X-1	50-70 [13]	3.89 [14]	11.0	8.9	
SS433	162 [15]	13.10 [16]	[1.0]	[3.0]	
X0114+650	31 [17]	11.6 [18]			P,C?
X1907+097	42 [19]	8.38 [20]	12.0	15.3	P,T,C
XTE J1716-389	99 [21]				

[1] Priedhorsky & Terrell (1983b), [2] Ogilvie & Dubus (2001), [3] Schreier et al. (1972b), [4] Özdemir & Demircan (2001), [5] Rico (2008), [6] Lachowicz et al. (2006), [7] Bolton (1972a), [8] Cowley et al. (1991), [9] Wen et al. (2006), [10] Cowley et al. (1983), [11] Lang et al. (1981), [12] Chevalier & Ilovaisky (1977), [13] Clarkson et al. (2003b), [14] Schreier et al. (1972a), [15] Margon (1984), [16] Crampton et al. (1980), [17] Farrell et al. (2004), [18] Crampton et al. (1985), [19] Priedhorsky & Terrell (1984b), [20] Marshall & Ricketts (1980), [21] Cornelisse et al. (2006),

C: cyclotron resonance scattering feature in X-ray spectrum, E: eclipsing or partially eclipsing XRB,
P: X-ray PSR, R: radio loud XRB, T: transient XRB, U: ultra-soft X-ray spectrum, associated with BHCs

Table 6.2: LMXBs with known $P_{sup} < 1$ year

Source	P_{sup} [days]	P_{orb} [days]	q $[\frac{M_2}{M_1}]$	$r_b/10^6$ $[\frac{GM_1}{c^2}]$	**Types**
Cyg X-2	60-90 [1]	9.844 [2]	0.34	8.0	B,Z,R
EXO 0748-676	181 [3]	0.158 [4]			T,B,D,E
GRS 1747-312	147 [5]	0.515 [6]			T,G,B,D,E
GX 339-4	190-240 [7]	1.755 [8]	[0.7]	[0.6]	T,U,M,R
GX 354-0	63 or 72 [9]	0.007 [10]			B,A,R
Her X-1	33-37 [11]	1.700 [12]	1.56	3.1	P,D,E
IGR J17098-3628	163 [3]				T,R?
KS 1731-260	38 [13]				T,B
LMC X-2	10 [14]	0.34 [15]			Z
MS 1603.6+2600	5 [16]	0.077 [17]			B
Sco X-1	2.6 [18]	0.788 [19],[20]	[0.7]	1.6	Z,M,R
X1636-536	46 [21]	0.158 [22]	[0.6]	0.5	B,A
X1730-333	217 [23]				T
X1820-303	171 [24]	0.008 [25]	[0.1]	0.1	G,B,A,R
X1916-053	5 [26] & 199 [27]	0.035 [28],[29]	[0.1]	0.2	B,A,D
X1957+115	117, 235 & 352 [30]	0.390 [31]	[0.7]	[0.4]	U

[1] Clarkson et al. (2003a), [2] Cowley et al. (1979), [3] Kotze et al. (2009), [4] Parmar et al. (1986), [5] Wen et al. (2006), [6] in't Zand et al. (2000), [7] Kong et al. (2002), [8] Hynes et al. (2003), [9] Kong et al. (1998), [10] Galloway et al. (2010), [11] Leahy & Igna (2010), [12] Tananbaum et al. (1972b), [13] Revnivtsev & Sunyaev (2003), [14] Cornelisse et al. (2007b), [15] Motch et al. (1985), [16] Hakala et al. (2009), [17] Morris et al. (1990), [18] Kudryavtsev et al. (1989) [19] Cowley & Crampton (1975), [20] Gottlieb et al. (1975), [21] Shih et al. (2005), [22] Pedersen et al. (1981), [23] Guerriero et al. (1999), [24] Chou & Grindlay (2001), [25] Stella et al. (1987), [26] Homer et al. (2001), [27] Priedhorsky & Terrell (1984b), [28] Walter et al. (1982), [29] White & Swank (1982), [30] Nowak & Wilms (1999), [31] Thorstensen (1987),

A: known Atoll source, B: X-ray burst source, C: cyclotron resonance scattering feature in X-ray spectrum,
D: "dipping" LMXB, E: eclipsing or partially eclipsing XRB, G: globular-cluster XRB, M: microquasar,
P: X-ray PSR, R: radio loud XRB, T: transient XRB, U: ultra-soft X-ray spectrum, associated with BHCs,
Z: Z-type source

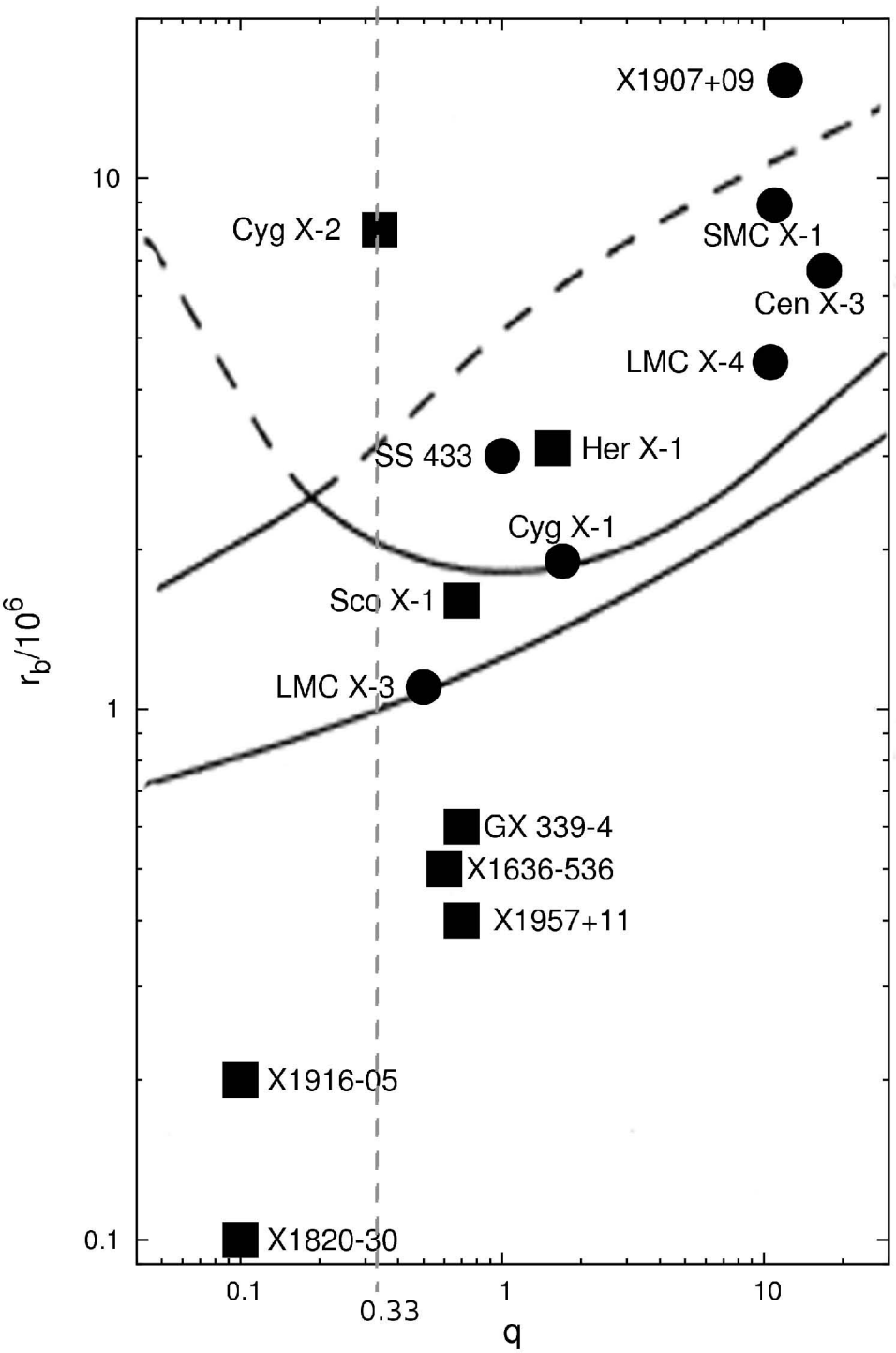

Figure 6.1: Accretion disc stability to radiation-driven warping in XRBs, as functions of q and r_b (in units of $\left[\frac{GM_1}{c^2}\right]$), adapted from OD01 to include only XRBs with known P_{sup}. Squares indicate LMXBs and circles HMXBs. The vertical dashed line indicates the $q \sim 0.33$ boundary (Whitehurst & King 1991, Murray et al. 2000), to the left of which XRBs are susceptible to tidal disc precession.

6.2 Time-dependent Period Analysis

RXTE ASM one-day-average data from 20 February 1996 to 12 February 2011 (MJD 55608) for the sum-band were used, providing 15 year lightcurves of unparalleled quality and sensitivity. As illustrated in Chapter 3, period analysis of entire datasets can provide the maximum sensitivity for steady low-level modulations, but has severe limitations when dealing with unstable or evolving periodic signals. Intermittent signals may be completely damped out. Evolving signals may cause multiple power peaks over considerably larger frequency ranges than expected for quasi-periodic modulations, which are generally represented by broadened peaks. As an added complication, these effects are aggravated with longer observational baselines. Since P_{sup} relating to accretion disc behaviour are expected to be quasi-periodic, unstable and may drift, our interest lies in characterising the behaviour of those periods over time.

6.2.1 Dynamic Power Spectra

The DPS requires datasets to be split into windows of sufficient length to allow detection of the maximum period considered. L-S periodograms (Lomb 1976, Scargle 1982; 1989) were produced for every such dataset. Those results were plotted in a density map, with the L-S power for each frequency plotted at each window's midpoint (in MJD) along the temporal axis. The frequency domain covered periods of minimum 2 days to a maximum comparable to the chosen window size for a source.

6.2.2 Windowing

Larger window sizes cause the smearing out of variability as they average out small variations, but have the advantage of enhancing weak but steady periodic signals. On the other hand, variable or intermittent periodic signals may therefore be completely washed out if windows are too large. Window sizes were initially chosen to be 400 days for all sources, providing coverage of $\sim 5-10$ periodic cycles in the range $\sim 40-80$ days, having the added advantage of being directly comparable to the Clarkson et al. (2003a) results for SMC X-1, LMC X-4, Her X-1 & Cyg X-2. It also allowed identification of longer potential periods, which could subsequently be investigated in more detail by choosing more appropriate window sizes to sample them properly. For $P_{sup} > 80$ days, windows of ~ 5 times the periods were used for the results presented here, and for $P_{sup} < 10$ days window lengths of 100 days. The sliding window approach was also employed, whereby consecutive datasets overlap such that they move in 50 days steps in the time domain. This approach provides adequate temporal resolution, whilst smoothing out the noise from otherwise independent windows.

6.2.3 Dynamic Window Function

To ensure that the features contained in the DPS are not artificially induced by the sampling or windowing employed, the spectral window function was determined for each dataset and

a density map was constructed with that information. To allow comparison, the resulting Dynamic Window Function (DWF) was plotted next to the DPS for each source.

6.2.4 Dwell-by-dwell Data

The DPS analysis was repeated for one-day-averages that were constructed from the sum-band dwell-by-dwell data, employing aggressive filtering of the data to eliminate unreliable data points, as described in Chapter 5. Those results are consistent with what is presented here. However, the data loss due to the more conservative approach leads to diminished temporal coverage and the features in the DPS are therefore clearer using the ASM one-day-averages. Prominent features contained therein were all repeated in own constructed one-day-averages, adding legitimacy to those features in the same way that the coincidence of peaks, when considering the complete datasets, facilitated identification of truly significant periods in Chapter 5.

6.2.5 Noise Levels

White noise levels were determined by generating 10^4 random datasets by Monte Carlo simulation. Therein a white noise distribution is assumed, using the time values, mean and standard deviation of each complete 15 year one-day-average dataset. L-S periodograms for each random dataset then yield periods associated with the maximum power in each. The subsequent distribution of powers constitute a cumulative probability distribution function, providing the false alarm probability associated with a particular power. The white noise level for a 99.9% confidence level is therefore the power associated with a false alarm probability of 0.1%. The white noise level for the dataset as a whole can be used as an estimate for its windows and also does not differ significantly between sources.

Farrell et al. (2009) determined the red noise levels for the RXTE ASM data of 5 of these sources by making use of REDFIT, which indicated that the red noise levels do not always exceed the white noise at the low frequencies. For Sco X-1 and X1916-053 the white noise levels were $\sim$ double those of the red noise, while Cyg X-2, X1636-536 & X1820-303 had red noise levels that rose to > 3 times the white noise levels at low frequencies $(0.001 - 0.01)$. Apart from differing significantly for each source, these modelled red noise levels are extremely dependent on the time domain covered by the dataset, as well as the weighting scheme applied to it, if any. Furthermore, red noise levels obtained for the dataset as a whole may therefore not be an appropriate estimate for its windows.

However, the aim here is to characterize the behaviour of previously reported periodic signals over time, not claim the discovery of new periodic behaviour. The latter would normally require rigorous testing against noise, while such requirements should be irrelevant in case of the former. While noise levels may serve as an accepted statistical measure for the significance of prominent periodic signals, the true measure of their significance lies in their persistence over time, which a time-dependent periodic analysis such as the DPS provides automatically.

6.3 Results

In an effort to allow easier interpretation of features in the DPS and how they translate to features contained in the lightcurves, they were plotted together with the lightcurve of each source. The lightcurves shown were re-binned into 10-day bins and plotted above the DPS, over the same temporal range (horizontal/x-axis). The density scale bar included in each plot indicates the power (line-of-sight/z-axis) associated with the periodogram, with stronger detections being darker. Furthermore, the L-S periodogram for the entire 15 year dataset was plotted to the left of the DPS for each source and over the same frequency range (vertical/y-axis). This allows immediate comparison of features in the DPS to the overall periodogram. Frequency labels were replaced by the equivalent period labels, to facilitate easier comparison with previously published P_{sup}, contained in Tables 6.1 & 6.2 and included in the caption of each source. In addition thereto, they are also clearly indicated on each plot with red ticks (for individual) and bars (for ranges) along the period/frequency-axis.

DPS and L-S plots were produced for frequencies appropriate to their reported P_{sup}. Including a wider range of frequencies around those periods allows a more complete picture of the temporal properties of each source. To allow comparability between sources, the size of the frequency range plotted was kept relatively constant at $\sim 0.02 - 0.03$ for all the plots, except that sources with $P_{sup} < 10$ days were plotted over a frequency range of 0.1. Only the plot for the $P_{sup} \sim 199$ days in X1916-053 (Figure 6.25) is included, since no evidence was found for the $P_{sup} \sim 5$ days.

The estimated white noise levels for all sources are plotted as lines/curves on the L-S plots of the sources as a guide. Prominent features in the L-S periodogram which are well above these estimated noise levels, can normally be considered significant, the situation for the majority of the sources considered here. For X1907+097, LMC X-2 and MS 1603.6+2600 (Figures 6.9, 6.19 & 6.20) no significant features were detected in the L-S or DPS.

The figures contained in this Chapter each feature the DPS on the left and DWF on the right for every source considered here. In each of the respective DPS or DWF figures, the different panels contain additional information for comparative purposes. Top panels contain the RXTE ASM lightcurves, left panels contain the L-S/window over the entire ~ 15 years dataset, while the main panels contain the actual DPS/DWF, wherein time and frequency are plotted on the x and y axes respectively. Scale bars to the right of each figure indicate DPS/DWF power, which is plotted on the z-axis. Note that the dominating DWF features are at $P > 100$ days, but excluding them from the plots accentuates the much lower level window powers for $P < 100$ days (generally ~ 10 times smaller). For KS 1731-260 (Figure 6.18) the DWF feature at ~ 50 days is not coincident with the DPS features.

Results were presented in a way that provides readers with sufficient information to reach their own conclusion regarding the variability properties of a source at a single glance. All relevant additional information, not contained in the plots themselves, was therefore included in the caption of each source. The sources are presented in the same order as their listing in Tables 6.1 & 6.2.

6.4 Discussion

X-ray sources are referred to by various names, all of which are available in SIMBAD* by CDS (2011). Primary source names are linked to their discovery, indicating their host constellations and X-ray brightness rank (e.g. Cen X-3 in Centaurus) or the prefix for the mission with which they were discovered (see Table 1.1), followed by their coordinates. Generalized designations contain either equatorial coordinates (e.g. X1119-603) or Galactic coordinates (e.g. GX 292+0), prefixed by X or GX (for Galactic bulge sources) respectively. The source may also be referred to by its optical counterpart's name (e.g. V779 Cen) or designation in the optical catalogues, e.g.: Henry Draper (HD), Hipparcos (HIP & HIC), Luminous Star (LS), Tycho (TYC), Smithsonian Astrophysical Observatory (SAO) and the 2Micron All-Sky Survey (2MASS). Furthermore, the designations for Cen X-3 in the various high-energy satellite missions include: 2U 1119-60, 3U 1118-60 and 4U 1119-603 (for Uhuru), H 1119-603 and 1H 1118-602 (for HEAO), 1ES 1119-60.3 and 2E 1119.0-6020 (for Einstein), 3A 1119-603 (for Ariel V), 1M 1119-603 (for OSO-7), SWIFT J1120.9-6037, INTEGRAL1 8 and GPS 1119-604 (for the Galactic plane survey).

The convention followed in this work, is to use the ASM source name which refers to Cen X-3 as cenx3, although these may be used interchangeably. However, the latter was used when discussing and presenting ASM results in Chapter 5 and the Appendices, while the former is used here and in the remaining Chapters.

These DPS results aim to provide the long awaited time-resolved analysis, that OD01 suggested would be required for aperiodic sources, as a basis for future investigations into super-orbital variations and the mechanisms believed to be responsible for producing them. In-depth analysis of each source and detailed discussion of the full implications of these results, go beyond the scope of this work where the focus is on whether the results from the DPS analysis suggest steady, evolving, persistent or unstable periods, and how they relate to previously published periods.

In the discussion of each source, the observed behaviour apparent from the DPS analysis is first compared with the OD01 predictions for stability of accretion discs against radiation-driven warping, since the OD01 process has a dependence on system parameters. The latter determines an XRB's location on Figure 6.1 and allows its feasibility, as the mechanism responsible for the P_{sup}, to be assessed. The impact of more recent estimates for the binary system parameters, is also considered. Sources for which other mechanisms may account for the P_{sup} are also compared to those predictions, where applicable. Such mechanisms (discussed in Chapter 4) include tidal disc precession for $q < 0.25 - 0.33$ (low q systems), precessing relativistic jets and $\dot{M}$ variations ($\Delta\dot{M}$) due to a third body, state changes or variations in the size of the equatorial disc surrounding a Be star donor. $\dot{M}$ variations that are not the result of any of the aforementioned mechanisms, may also occur and result in very long-term modulations of the X-ray flux (discussed in Chapter 7).

*http://simbad.u-strasbg.fr/simbad/

6.4.1 HMXBs

Cen X-3

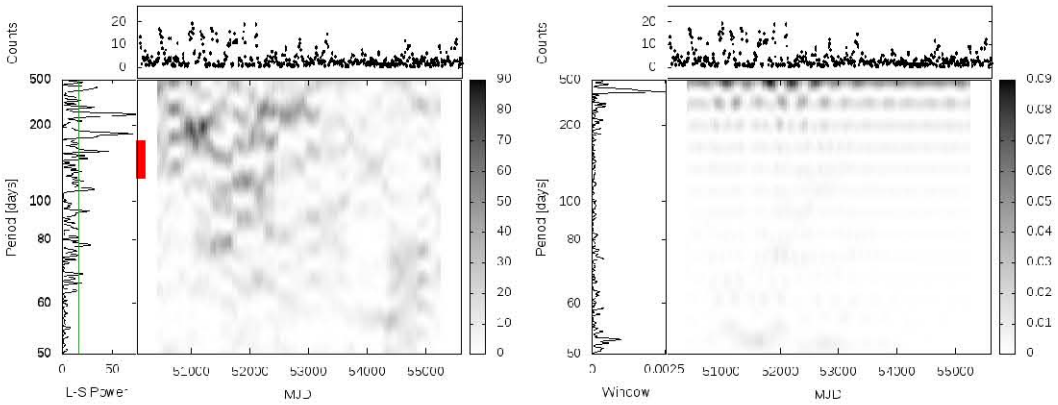

Figure 6.2: Cen X-3 with $P_{sup} \sim 120 - 165$ days (Priedhorsky & Terrell 1983b).

Schreier et al. (1972b) discovered evidence for the binary nature of Cen X-3, by interpreting the sinusoidal variations in the P_{spin} of 4.84 seconds (Giacconi et al. 1971) of the X-ray PSR in Uhuru data, as Doppler shifts resulting from its P_{orb} of 2.09 days around its companion. Krzeminski (1974) identified its V $\sim$ 13 supergiant optical counterpart V779 Cen, a.k.a. Krzeminski's star.

Hutchings (1975) initially estimated dynamical masses of $M_1 \sim 0.7 M_\odot$ and $M_2 \sim 17 M_\odot$. Ash et al. (1999) determined $M_1 \sim 1.21 \pm 0.21 M_\odot$, $M_2 \sim 20.5 \pm 0.7 M_\odot$ and $i \sim 70.2° \pm 2.7°$. However, an improved estimate of $M_1 \sim 1.34 \pm^{0.16}_{0.14} M_\odot$ was measured by van der Meer et al. (2007) using Very Large Telescope (VLT) observations.

Holt et al. (1979) discovered a candidate $P_{sup} \sim 43$ days in Ariel V data and suggested it may be the result of a precessing accretion disc. Khruzina & Cherepashchuk (1983) reported a $P_{sup} \sim 26$ days in optical data, attributing it to the precession of the rotation axis of the supergiant. However, Priedhorsky & Terrell (1983b) were unable to detect either of those P_{sup}, but instead found aperiodic modulations over a range of $P_{sup} \sim 120 - 165$ days. Raichur & Paul (2008) found an X-ray flux dependence in the orbital modulations of Cen X-3, similar to those found in LMC X-4, SMC X-1 and Her X-1, arguing that its long-term aperiodic P_{sup} may therefore also be the result of varying obscuration by a radiation-driven precessing warped accretion disc, as proposed for the latter mentioned sources.

The $P_{sup} \sim 120 - 165$ days appear to be part of rather erratically evolving features in the DPS, with strongest detection of $\sim$ 200 days at MJD $\sim$ 51000. A variety of shorter term signals are also strongly detected up to MJD $\sim$ 53500, after which the maximum flux and periodic signal strength drop dramatically. Cen X-3 is located in the disc instability zone in Figure 6.1, which the van der Meer et al. (2007) estimates do not affect significantly. It is therefore expected to develop a warped precessing accretion disc in which the warp itself might be variable, as suggested by Iping & Petterson (1990). The erratic variations in the P_{sup} may be interpreted to be the direct result of variability in the warp itself.

Cyg X-1

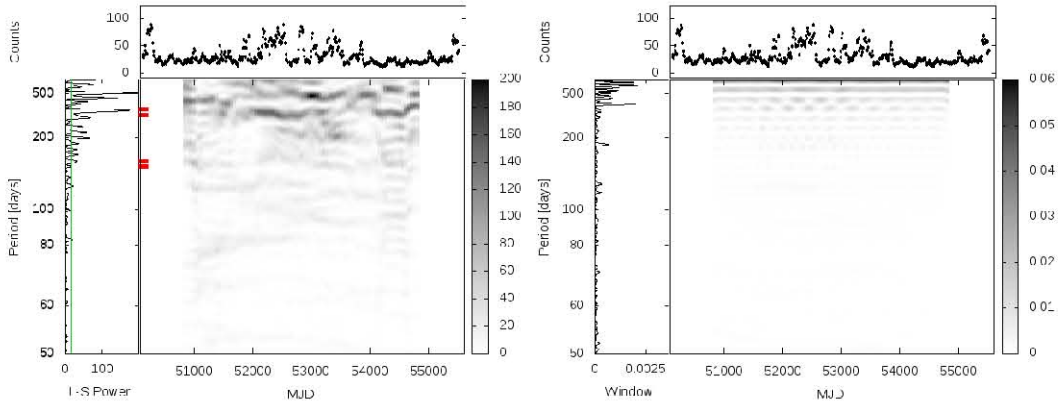

Figure 6.3: Cyg X-1 with $P_{sup} \sim 150$ days (Özdemir & Demircan 2001), ~ 150 & 290 days (Lachowicz et al. 2006) and ~ 326 days (Rico 2008).

Cyg X-1 has a generalized X-ray source designation X1956+350, but is rarely referred to as such. Oda et al. (1971) detected rapid X-ray variability of ~ 73 milliseconds in the Uhuru data, which Holt et al. (1971) suggested may be linked to harmonic components at lower frequencies. Subsequently, Schreier et al. (1971) found QPOs ~ 50 milliseconds to ~ 10 seconds in the Uhuru data, but found no single consistent period (no P_{orb} or P_{spin}).

Bolton (1972b) and Webster & Murdin (1972) independently suggested its optical counterpart to be the very bright (V $\sim$ 9) BOIb star V1357 Cyg or HD(E) 226868, based on radial velocity measurements from optical spectra and X-ray lightcurve data, which varied on the P_{orb} of 5.6 days. Bolton (1972a) determined the binary parameters: $M_1 \sim 11 M_{\odot}$ (a BHC), $M_2 \sim 20 M_{\odot}$ and $i \sim 30°$. Herrero et al. (1995) later estimated $M_1 \sim 10.1 M_{\odot}$ and $M_2 \sim 17.8 M_{\odot}$, the values used in OD01. Most recently, Shaposhnikov & Titarchuk (2007) estimated $M_1 \sim 8.7 \pm 0.8 M_{\odot}$ using low frequency QPO-photon index correlations, from which Iorio (2008) re-estimated $M_2 \sim 24 \pm 5 M_{\odot}$.

Tananbaum et al. (1972a) reported the presence of an anti-correlation between the X-ray and radio flux for the source. Coe et al. (1976) reported an anti-correlation between the spectral hardness and X-ray flux in Ariel V data, which would later become known as the LH and HS states of transients, discussed in Chapter 2. Shapiro et al. (1976) suggested a two temperature accretion flow, ADAF in the SLE model discussed in Chapter 4, to explain the LH state. Holt et al. (1976) detected the P_{orb} in X-ray data, prior to a HS state.

Kemp et al. (1978) reported $P_{sup} \sim 78$ & 39 days in optical and X-ray data. Priedhorsky et al. (1983) found a $P_{sup} \sim 294$ days in Vela 5B data. Kitamoto et al. (2000) found $P_{sup} \sim 150$ & $210 - 230$ days in Ginga ASM data. Özdemir & Demircan (2001) discovered a $P_{sup} \sim 150$ days in RXTE ASM data. Lachowicz et al. (2006) detected $P_{sup} \sim 150$ & 290 days in the Ariel V and Vela 5B datasets respectively. Rico (2008) found a $P_{sup} \sim 326$ days period in the Swift BAT and RXTE ASM data. Zdziarski et al. (2011) investigated the constant shape of the intrinsic spectrum, concluding that the P_{sup} modulations are likely

produced by a precessing accretion disc with a bulge on the edge.

The location of Cyg X-1 in Figure 6.1 on the curve associated with $r_{add} = r_c$, suggested that stable warps may develop (resulting in steady P_{sup}). However, recalculation with the Shaposhnikov & Titarchuk (2007) and Iorio (2008) estimates yields $\frac{r_b}{10^6} \sim 2.30$ and $q \sim 2.76$, moving Cyg X-1 slightly up and to the right in Figure 6.1, placing it in the instability zone with Her X-1, Cen X-3 and LMC X-4. That makes the development of a radiation-driven warped accretion disc even more likely. Aperiodic variations, that are linked to the HS and LH state transitions, are also present and complicate the detection of quasi-periodic modulations associated with precessing accretion discs. However, significantly detected periodic signals appear to be present in the vicinity of the previously reported P_{sup}.

LMC X-3

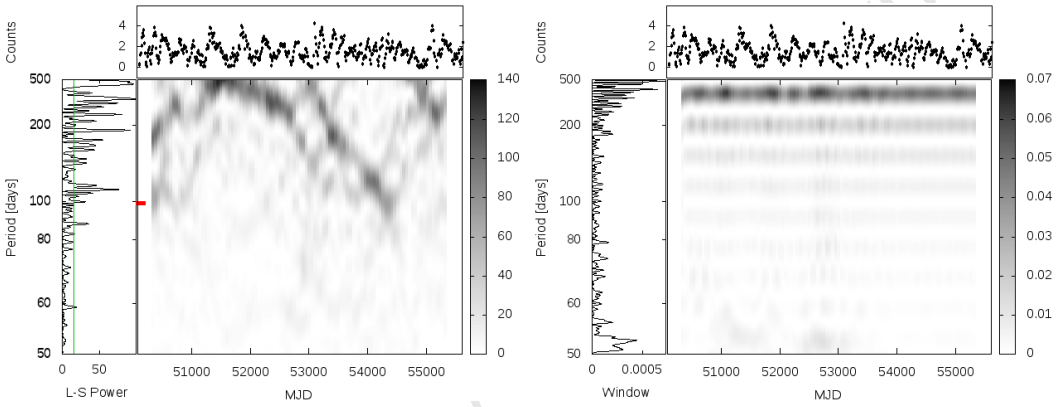

Figure 6.4: LMC X-3 with $P_{sup} \sim 99$ days (Cowley et al. 1991).

LMC X-3 has general designation X0538-64. Cowley et al. (1983) discovered the P_{orb} of 1.7 days from spectroscopic radial velocity measurements of the B3 V optical counterpart, estimating the binary system parameters as $i < 70°$ (no X-ray eclipses on P_{orb}), $M_1 > 9.0M_\odot$ (the first example of an extragalactic stellar-mass BHC) and $M_2 \sim 2.3M_\odot$. Paczynski (1983) estimated $M_1 > 10M_\odot$ and $M_2 < 6.6M_\odot$, assuming the absence of X-ray eclipses and RLO.

White & Marshall (1984) reported the extremely soft X-ray spectrum of LMC X-3 in comparison to other XRBs, and suggested that X-ray transients with ultra-soft X-ray spectra in their HS states should be considered potential BHCs. Meekins et al. (1984) detected QPOs ~ 3 and 300 milliseconds, suggesting it to be consistent with the expected variability time-scales near the inner edge of an accretion disc, surrounding a $\sim 10M_\odot$ BH.

Cowley et al. (1991) reported $P_{sup} \sim 99$ & 198 days. Paul et al. (2000) found $P_{sup} \sim 104$, 169 & 216 days (in RXTE ASM data) and $P_{sup} \sim 105$, 214 & 328 days (in Ginga ASM data). Wen et al. (2006) reported $P_{sup} \sim 100 - 500$ days in RXTE ASM data. Brocksopp et al. (2001) found correlation between the long-term optical and X-ray lightcurves, and claim their findings support those of Wilms et al. (2001), wherein the long-term P_{sup} was associated with the time-scales of recurring transitions between the LH and HS states due to $\Delta\dot{M}$.

Features in the DPS are indeed closely linked to state transitions in the lightcurve, all of which are $\sim 100 - 500$ days, and are therefore rather indicative of time-scales on which those occur. There is an initial evolution from shorter to longer term features, which reverses around MJD $\sim$ 51500 and continues past MJD $\sim$ 53000 and then collapses. However, a new long-term cycle then starts, evolves more rapidly to a shorter term feature during MJD $\sim$ 53000 $-$ 54500 and also appears to collapse, making way for another long-term cycle starting at MJD $\sim$ 54700. There are several steadily evolving long-term features covering the range $\sim 100 - 500$ days, as reported by Wen et al. (2006).

LMC X-3 was located on the OD01 curve using $r_{add} = r_o$ in Figure 6.1. However, the mass estimates used in Wijers & Pringle (1999) are those from Paczynski (1983), which differ significantly from those used in OD01. Recalculation with the Paczynski (1983) estimates yields $\frac{r_b}{10^6} \sim 0.72$ and $q \sim 0.66$, moving LMC X-3 below the curve for $r_{add} = r_o$ in Figure 6.1, where systems are not expected to develop warped precessing accretion discs. This is in better agreement with the P_{sup} behaviour and the suggestion that $\Delta\dot{M}$ is the mechanism responsible for these long-term X-ray flux modulations.

LMC X-4

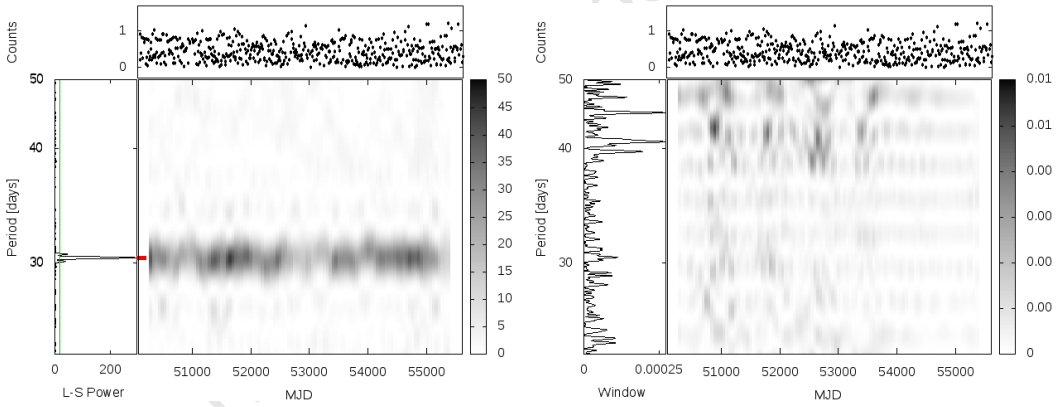

Figure 6.5: LMC X-4 with $P_{sup} \sim 30$ days (Lang et al. 1981).

LMC X-4 has general designation X0532-66. Chevalier & Ilovaisky (1977) determined its P_{orb} of 1.4 days from radial velocity measurements obtained by spectroscopic observations of the faint (V $\sim$ 14) OB optical counterpart, identified by Sanduleak & Philip (1976), Blanco & Hiltner (1977), and estimated $M_1 \sim 2M_\odot$ if assuming $M_2 \sim 20 - 25M_\odot$. Hutchings et al. (1978) suggested the optical counterpart to be an O7 star with $M_2 \sim 25M_\odot$, assuming RLO occurs. Li et al. (1978) and White & Carpenter (1978) detected X-ray eclipses on the P_{orb} time-scale, confirming the binary nature of LMC X-4. Epstein et al. (1977) and Skinner et al. (1980) found irregular recurring flaring in SAS-3 and HEAO 1 data. Kelley et al. (1983) detected the P_{spin} of 13.5 seconds during flaring events in SAS-3 data, from which they estimated $M_1 \sim 1.6 \pm^{1.0}_{0.5} M_\odot$ and $M_2 \sim 17M_\odot$ (under-massive for its luminosity). Pietsch et al. (1985) used EXOSAT data to estimate $M_1 \sim 1.34 \pm^{0.48}_{0.44} M_\odot$. van der Meer

et al. (2007) determined $M_1 \sim 1.25 \pm^{0.11}_{0.10} M_\odot$ using VLT observations.

Woo et al. (1996) used Ginga and ROSAT data, combined with archival data to investigate the P_{orb} and P_{spin}, finding only marginal evidence for orbital decay and determined the NS to be in spin equilibrium, alternating between phases of spin-up and spin-down. Levine et al. (2000) used RXTE ASM data to determine orbital decay which they attributed to tidal interactions, while suggesting the evolutionary expansion of the donor may be preventing its rotation from becoming synchronized with the orbit (tidally locked).

Lang et al. (1981) discovered the very stable P_{sup} of 30.5 days. Paul & Kitamoto (2002) reported a decay of P_{sup} to 30.3 days. Clarkson et al. (2003a) discussed the steadiness of the P_{sup} in context of radiation-driven precessing warps in accretion discs, finding it consistent with its theoretical OD01 prediction. A substantial modulation is strongly detected at $P_{sup} \sim 30$ days, for which the detection level appears to drop temporarily at MJD $\sim$ 51000, MJD $\sim$ 53000 and MJD $\sim$ 55500. LMC X-4 lies in the instability zone on Figure 6.1, closer to the solid curve where very stable warps are expected to be produced. The van der Meer et al. (2007) estimate does not affect its location on Figure 6.1 significantly. The radiation-induced warps in its accretion disc are therefore expected to be stable and consequently able to produce a steady P_{sup}.

SMC X-1

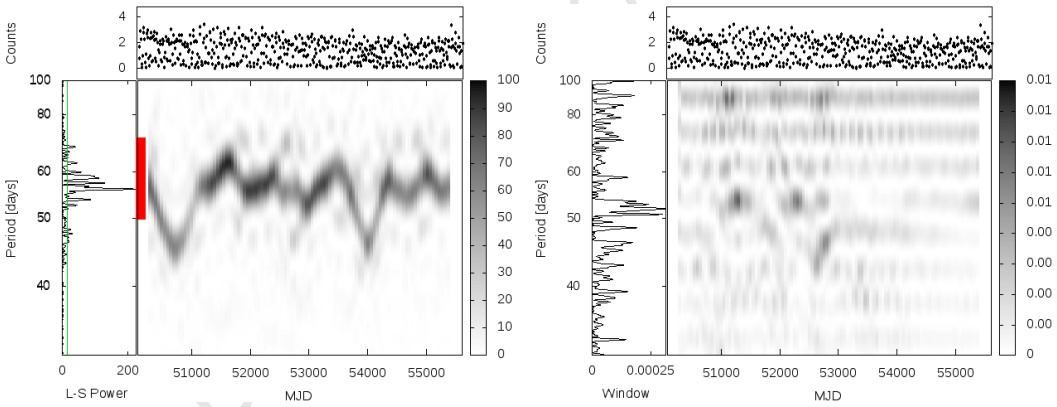

Figure 6.6: SMC X-1 with $P_{sup} \sim 50 - 70$ days (Clarkson et al. 2003b).

Schreier et al. (1972a) detected eclipses of SMC X-1 in Uhuru data with a P_{orb} of 3.89 days. Liller (1973) identified an OB supergiant as its optical counterpart (V $\sim$ 13). Lucke et al. (1976) detected a P_{spin} of 0.716 seconds in data from an Aerobee rocket flight. Hutchings et al. (1977) estimated binary parameters $M_1 \sim 1.02 M_\odot$, $M_2 \sim 16.2 M_\odot$ and $i \sim 64 - 70°$, assuming RLO takes place. van Paradijs & Zuiderwijk (1977) found observational evidence in UBVRI photometry for an accretion disc around the X-ray PSR. Khruzina & Cherepashchuk (1987) determined $M_1 \sim 1.41 \pm 0.49 M_\odot$, $M_2 \sim 16.7 \pm 1.8 M_\odot$ and $i \sim 64.5 \pm 2.5°$. Val Baker et al. (2005) determined $M_1 < 1.21 \pm 0.1 M_\odot$, $M_2 \sim 16.6 \pm 0.4 M_\odot$ and $i \sim 65.3 \pm 1.3°$. Most recently, van der Meer et al. (2007) determined $M_1 \sim 1.06 \pm^{0.11}_{0.10} M_\odot$

using VLT observations.

Khruzina & Cherepashchuk (1983) reported a $P_{sup} \sim 35$ days in archival optical data. Zhang et al. (1996) reported a quasi-periodic $P_{sup} \sim 60$ days in CGRO BATSE and RXTE ASM data, confirming previous results from HEAO 1 data (Gruber & Rothschild 1984). In Wojdowski et al. (1998) they attribute the P_{sup} to the effects of a warp in a precessing accretion disc. Simultaneous Chandra and Hubble Space Telescope (HST) observations provided further proof for the interpretation of the P_{sup} as being produced by a precessing warped disc, since the UV flux remain constant even though the X-ray flux shows significant modulation (Vrtilek et al. 2001b). Clarkson et al. (2003b) presented a DPS analysis, clearly showing the smooth variations in the $P_{sup} \sim 50 - 80$ days and interpreting this behaviour as the result of a warped precessing accretion disc in which the warp itself changes under the influence of competing bending modes of the OD01 radiation-driven warp instability analysis.

The DPS clearly shows smooth and steady evolution of its $P_{sup} \sim 42 - 70$ days. The behaviour early in the lightcurve (the feature surrounding MJD $\sim$ 50500), also included in Clarkson et al. (2003a) and Trowbridge et al. (2007), now appears to be repeated approximately 10 years later (around MJD $\sim$ 54000). There also appear to be a decrease in maximum and increase in minimum 10-day binned flux coincident with the temporal location of the minimum P_{sup} in those two features in the DPS curve. The behaviour after these two largest features does not repeat, but appears to be similar in terms of the decreased period range covered, and contains features that seem to recur on a time-scale of $\sim$ 1000 days.

SMC X-1 lies in the instability zone on Figure 6.1, closer to the dashed curve and therefore a radiation-induced warp in its accretion disc is expected to be variable, though not yet unstable. Recalculation with the Val Baker et al. (2005) and van der Meer et al. (2007) estimates yields $\frac{r_b}{10^6} \sim 12.0$ and $q \sim 15.7$, moving SMC X-1 up to a position just above the dashed curve on Figure 6.1. The steady evolution of its P_{sup} may consequently still be interpreted as the result of the precession of a warped disc in which the warp itself varies, due to the competition of warping modes, as suggested by Clarkson et al. (2003a).

SS433

SS433 is still best known by its designation in the Stephenson & Sanduleak (1977) catalogue of stars with Hα emission lines, not its generalized source designation (X1909+048) or bright (V $\sim$ 13) O star optical counterpart (V1343 Aql). Clark & Murdin (1978) suggested that it may be associated with radio SNR W50. Subsequently, Spencer (1979) detected its compact core and jet in radio wavelengths, determining that the jet had the same position angle as the extended radio SNR W50. Abell & Margon (1979) proposed a kinematic model for this source to account for the $P_{sup} \sim 162$ days seen in the Balmer and He I emission lines. Extended X-ray lobes are produced as jets interact with the ISM, which are aligned with the W50 radio structure (Watson et al. 1983). This made SS433 the prototypical microquasar whose precessing relativistic jets and their resulting $P_{sup} \sim 162$ days were determined by

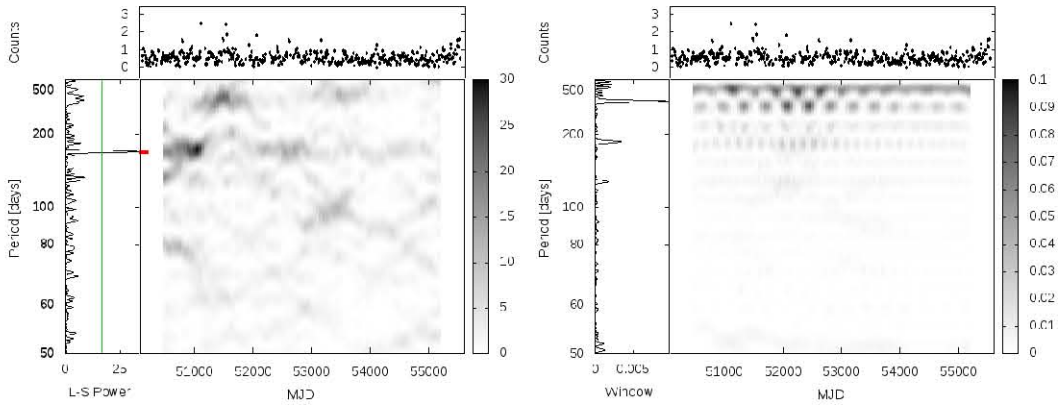

Figure 6.7: SS433 with $P_{sup} \sim 162$ days (Margon 1984).

Hjellming & Johnston (1981) and Margon (1984) from variations in the radial velocity measurements from emission lines (Chapter 4). Gies et al. (2002) presented evidence for this periodicity in the then-available (∼5 years) RXTE ASM data. The jets and their corkscrew motion have been spatially resolved at radio wavelengths (Blundell et al. 2007). The driving mechanism for this jet precession is still a matter of controversy, but Begelman et al. (2006) suggested that irradiation driven outflows are likely to play a significant role since SS433 experiences super-Eddington accretion ($L > L_{Edd}$) onto its BH. Blundell et al. (2008) decomposed the contributions to the stationary optical spectra into three emitting regions: a super-Eddington accretion disc wind, a circumbinary disc of material and the accretion disc surrounding a BH. SS433 is thought to be in a stage during its evolution where it is effectively situated inside the donor, allowing extreme accretion (Chapter 2).

Crampton et al. (1980) determined a P_{orb} of 13.1 days from their spectroscopic observations and later Crampton & Hutchings (1981) confirmed that eclipses occur on the P_{orb} time-scale. On shorter time-scales, Katz et al. (1982) predicted a nodding effect in addition to precession due to the tidal influence of the donor on the disc rim, for which they subsequently detected a nutation period of ~ 6.3 days. Hillwig & Gies (2008) used spectroscopic Gemini observations to estimate $M_1 \sim 4.3 \pm 0.8 M_\odot$ and $M_2 \sim 12.3 \pm 3.3 M_\odot$. Kubota et al. (2010) provided the most recent estimates from Subaru and Gemini spectroscopic observations of the donor (including heating of the donor) as $M_1 \sim 2.5 \pm^{0.7}_{0.6} M_\odot$ and $M_2 \sim 10.4 \pm^{2.3}_{1.9} M_\odot$. Barnes et al. (2006) warned that the weak absorption features, previously associated with the donor, may also be produced by an accretion wind.

The strongest detection is the $P_{sup} \sim 162$ days which disappears after MJD ~ 51000, reappears at MJD ~ 52000 at a weaker detection strength and remains until MJD ~ 55000. The weaker detections at the same frequency over the entire baseline and the singular strong detection in the overall L-S, suggest that $P_{sup} \sim 162$ days is stable. The detection thereof may be hampered from time to time by intrinsic fluctuations. A strong detection of a period ~ 400 days at MJD $\sim 51000 - 52000$, when the detection of the ~ 162 days period effectively disappears, makes a weaker reappearance at MJD $\sim 53000 - 54000$. During that time it is mirrored (on the opposite side of the ~ 162 days period) by an equally weakly detected

~ 100 days period, which appears to be unstable but persists to MJD ~ 55000. Furthermore, upon its reappearance at MJD $\sim 51000 - 52000$, the ~ 400 days period appears to have evolved to an even longer period. Since the ~ 400 days period is detected more strongly when the ~ 162 days period is weakly detected, this might suggest that the presence of the longer period may have something to do with the weaker detections of the $P_{sup} \sim 162$ days.

SS433 was located in the instability zone on Figure 6.1 next to Her X-1, using rough estimates for the system parameters $\frac{r_b}{10^6} \sim 3$ and $q \sim 1$. Recalculation with Hillwig & Gies (2008) estimates yields $\frac{r_b}{10^6} \sim 6.5$ and $q \sim 2.9$, moving SS433 just below the dashed line above which systems are expected to experience unstable warping (OD01 mode 1+). But, recalculation with the Kubota et al. (2010) estimates yield $\frac{r_b}{10^6} \sim 10.3$ and $q \sim 4.2$, moving SS433 just above the aforementioned dashed line. However, here the relativistic jets are well established as being responsible for the stable $P_{sup} \sim 162$ days.

X0114+650

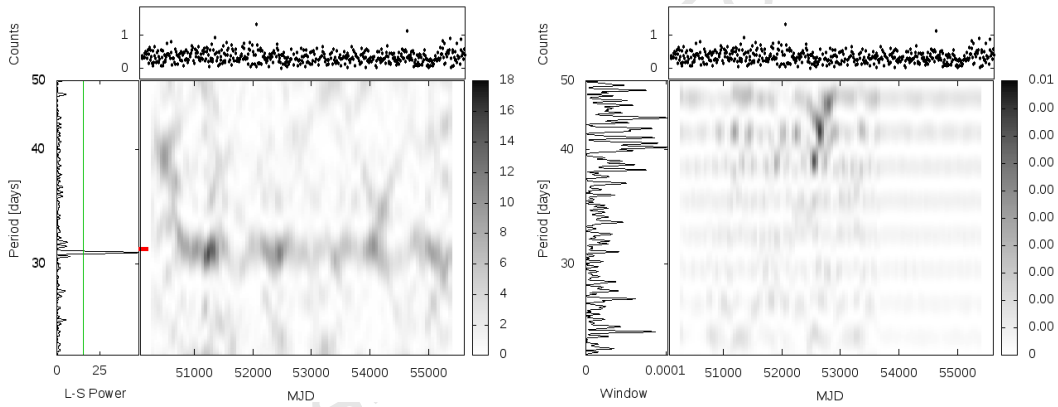

Figure 6.8: X0114+650 with $P_{sup} \sim 31$ days (Farrell et al. 2004).

X0114+650 is an X-ray source with bright (V ~ 11) optical counterpart V662 Cas, a.k.a. LSI +65 010 (Dower et al. 1977). While Koenigsberger et al. (1983) suggested X0114+650 is a BeX, Crampton et al. (1985) later argued that its optical counterpart rather resembled a B-type supergiant, finding a P_{orb} of 11.6 days and estimating $M_2 \sim 18 M_\odot$ if $M_1 \sim 1.4 M_\odot$. The latter mentioned authors suggested that the system shares characteristics of both Be and supergiant XRBs, and accretes from the stellar wind without RLO. Finley et al. (1992) reported X-ray pulsations on $P_{pulse} \sim 2.78$ hours, suggesting it may be due to β Cepheid-like pulsations in the donor star. However, Finley et al. (1994) found no coincident variability in the optical data (as would be expected for a β Cepheid pulsating star), rather suggesting that the pulsations may be due to slow NS spin. Taylor et al. (1995) presented the first evidence for optical variability on the X-ray pulsation time-scale. Reig et al. (1996) determined $M_2 \sim 16 \pm 5 M_\odot$ and $i \sim 61°$ assuming $M_1 \sim 1.4 M_\odot$ and no RLO. Farrell et al. (2004) detected a $P_{sup} \sim 31$ days in RXTE ASM data. Grundstrom et al. (2007) used spectroscopic observations of the donor and determined an eccentric orbit ($e \sim 0.18 \pm 0.05$), wherein the

X-ray flux reached maximum at periastron passage.

The $P_{sup} \sim 31$ days is weakly detected from MJD ~ 50500 in the DPS, but strongly detected in the overall L-S periodogram and DPS from MJD $\sim 50700 - 51400$, after which this signal remains relatively stable with alternating stronger and weaker detections. It appears to be relatively steady and persistent, though not like LMC X-4 or Her X-1.

Calculating the OD01 values using the Reig et al. (1996) binary parameters, yields $\frac{r_b}{10^6} \sim 18.8$ and $q \sim 11.4$, placing X0114+650 above the dashed curve on Figure 6.1, where chaotic warping prevails and stable precessing warped accretion discs are therefore not expected (OD01 mode 1+). However, it may lack P_{sup} variations as a result of its eccentric orbit, as proposed by Bildsten et al. (1997) to be the case for Cir X-1. Farrell et al. (2008) used RXTE PCA data to determine that a warped precessing accretion disc is not likely to be responsible for the P_{sup}, but rather $\Delta\dot{M}$ driven by an unknown mechanism. If X0114+650 was a BeX, $\dot{M}$ might be modulated by the expansion and contraction of the equatorial disc of the Be star (Chapter 4). However, Ashok et al. (2006) found emission lines absent in their near-infrared spectroscopy, making it unlikely for X0114+650 to be a BeX.

X1907+097

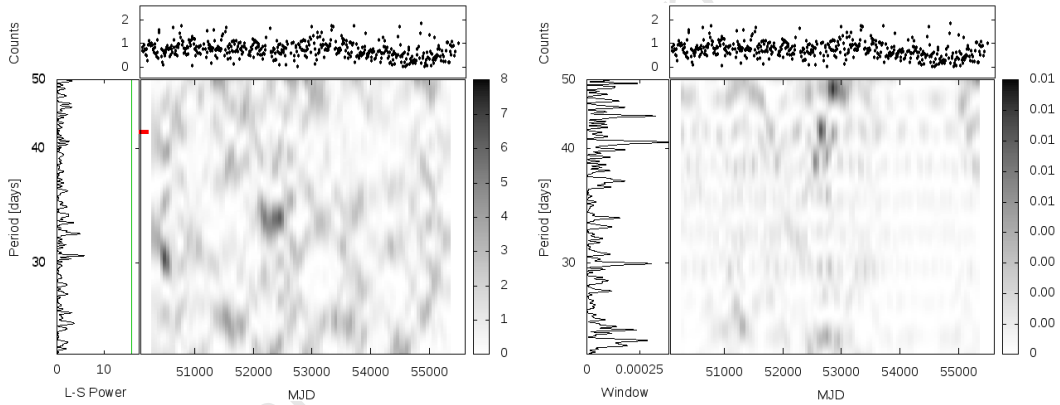

Figure 6.9: X1907+097 with $P_{sup} \sim 42$ days (Priedhorsky & Terrell 1984b) undetected.

X1907+097 is primarily known by its general X-ray source description and its variants in the catalogues of the high-energy satellite missions. Marshall & Ricketts (1980) determined its P_{orb} of 8.38 days from Ariel V data. Its optical counterpart is faint (V $\sim$ 16), but is likely an O-type supergiant (Schwartz et al. 1980). Makishima et al. (1984) published their discovery of a P_{spin} of 437.5 seconds in Tenma data, which was initially reported in Tanaka & Tenma Team (1983). Priedhorsky & Terrell (1984b) identified a quasi-periodic $P_{sup} \sim 42$ days in Vela 5B data. Cook & Page (1987) suggested that it may be a BeX with $M_2 > 13M_{\odot}$, by considering pulse heights over orbital phases in EXOSAT data. However, from optical spectroscopic studies van Kerkwijk et al. (1989) determined that the donor is more likely to be an OB supergiant than a Be star. Gradual spin-down of the X-ray PSR to a P_{spin} of 440.3 seconds from RXTE PCA data was reported by in't Zand et al. (1998), who also determined

the eccentricity as $e \sim 0.28$ and discovered transient ~ 18 seconds oscillations during an ~ 1 hour flare. The latter they attributed to the clumpy nature of the stellar wind. Makishima et al. (1999) identified electron cyclotron resonance effects in its Ginga spectra, associated with XRB PSRs. Cox et al. (2005) effectively ended the debate concerning the nature of the donor (OB supergiant or Be star), using spectra obtained at the VLT for the highly reddened O8/O9 supergiant optical counterpart, estimating $M_1 \sim 1.4 M_\odot$ and $M_2 \sim 27 M_\odot$.

No evidence is found in the DPS for the $P_{sup} \sim 42$ days (or any other) X-ray super-orbital period, confirming the result by Wen et al. (2006). X1907+097 is located above the dashed curve on Figure 6.1 where we expect chaotic warping to occur (OD01 mode 1+) and the Cox et al. (2005) estimate does not affect this location significantly. However, OD01 suggested that it may lack P_{sup} variations as a result of its eccentric orbit, which Bildsten et al. (1997) proposed to be the case for Cir X-1.

XTE J1716-389

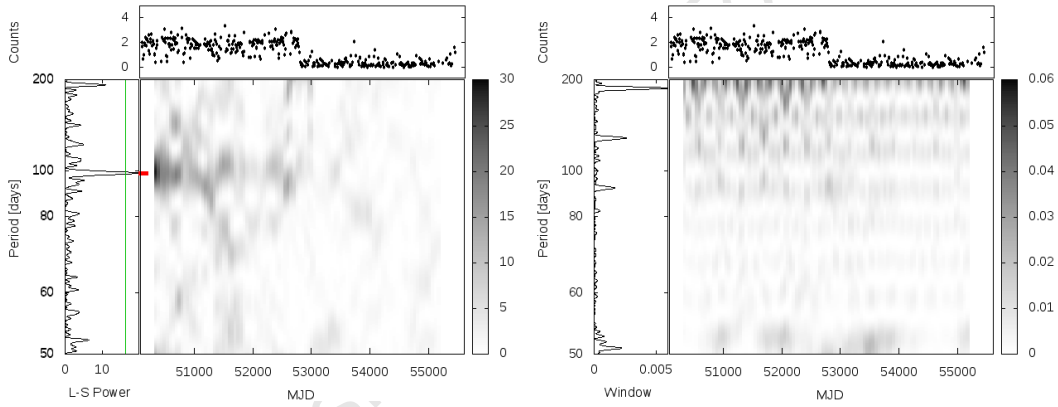

Figure 6.10: XTE J1716-389 with $P_{sup} \sim 99$ days (Cornelisse et al. 2006).

There is little information in the literature for XTE J1716-389, a.k.a. Mir Kvant source KS J1716-389 (or KS 1716-389). Cornelisse et al. (2006) identified a $P_{sup} \sim 99$ days in this quasi-persistent X-ray transient, proposing that it may be the result of obscuration by a precessing circumbinary disc which moves in and out of the field of view, and suggesting that XTE J1716-389 is likely an HMXB with a supergiant donor and similar characteristics to SS433 (a highly obscured XRB with strong emission features and a power-law spectrum). Wen et al. (2006) also identified the $P_{sup} \sim 99$ days in RXTE ASM data.

An initial detection of this P_{sup} becomes progressively weaker and is only visible in the DPS during the high flux state which lasts until MJD ~ 53000, after which there is a dramatic drop in the lightcurve to the low state. The relatively regular, weaker detections of the $P_{sup} \sim 99$ days period while the source is persistent, do seem to suggest a relatively steady P_{sup}. Its location on Figure 6.1 is unknown, but as an HMXB it is expected to be at least above the OD01 curve for $r_{add} = r_o$. As such, a stable P_{sup} associated with a steadily precessing warp while it is persistent, is not unexpected.

6.4.2 LMXBs

Cyg X-2

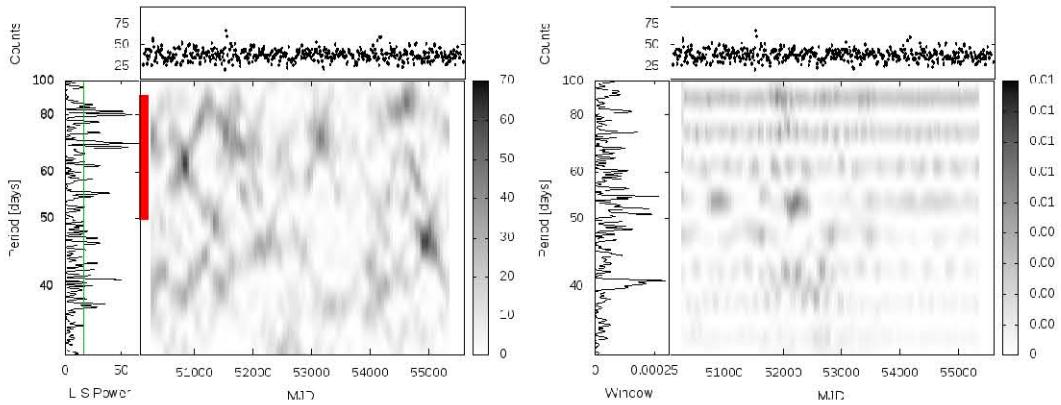

Figure 6.11: Cyg X-2 with $P_{sup} \sim 60 - 90$ days (Clarkson et al. 2003a).

Cyg X-2 has optical counterpart V1341 Cyg (Giacconi et al. 1967). Cowley et al. (1979) determined its P_{orb} of 9.84 days from spectroscopic radial velocity measurements of the donor, estimating $M_1 \sim 1.3 - 1.8 M_{\odot}$ and $M_2 \sim 0.5 - 1.1 M_{\odot}$. Casares et al. (1998) spectroscopically determined V1341 Cyg to be an A-type giant (V $\sim$ 15) with $M_2 \sim 0.6 M_{\odot}$ and estimated $M_1 \sim 1.78 \pm 0.23 M_{\odot}$. Most recently, Casares et al. (2010) used high resolution spectra to refine their previous estimate to $M_1 \sim 1.71 \pm 0.21 M_{\odot}$.

Kahn & Grindlay (1984) identified the presence of occasional type I X-ray bursts, rising in $\sim$ 2 seconds and decaying in $5 - 10$ seconds. Hasinger et al. (1986) discovered that the QPOs in the X-ray data increased in frequency with rising source flux. Hasinger & van der Klis (1989) classified it as a Z source. Wijnands et al. (1998) reported the discovery of kHz QPOs, indicating a P_{spin} of 2.9 milliseconds if the QPOs are modulated by the NS spin.

Smale & Lochner (1992) discovered a $P_{sup} \sim 77$ days in Vela 5B data, which Wijnands et al. (1996) confirmed using ASM data from RXTE, Vela 5B, and Ariel V. Paul et al. (2000) found $P_{sup} \sim 40$ & 69 days (in RXTE ASM data) and $P_{sup} \sim 54$ & 61 days (in Ginga ASM data). However, Wen et al. (2006) reported a range of periods $P_{sup} \sim 60 - 90$ days in the RXTE ASM data. Clarkson et al. (2003a) discussed the chaotic variability of the P_{sup} in context of radiation-driven precessing warps in accretion discs, finding it consistent with its theoretical OD01 prediction. Farrell et al. (2009) showed that the periodic signals in Cyg X-2 were below the modelled red noise, which agrees with the result in Figure C.27.

The P_{sup} in Cyg X-2 still exhibits chaotic/unstable behaviour, with a range of peaks from $\sim 40 - 90$ days which are strongly detected from time to time throughout the observational baseline. There is an initially weaker (but significant) detection in the range $\sim 40 - 50$ days, which becomes a much stronger detection toward the end of the lightcurve.

Cyg X-2 remains located well above the dashed curve on Figure 6.1 when using the Casares et al. (2010) estimate. It is expected to experience chaotic warping and to exhibit intermittent, highly variable periodic signals produced by precessing unstable warps.

EXO 0748-676

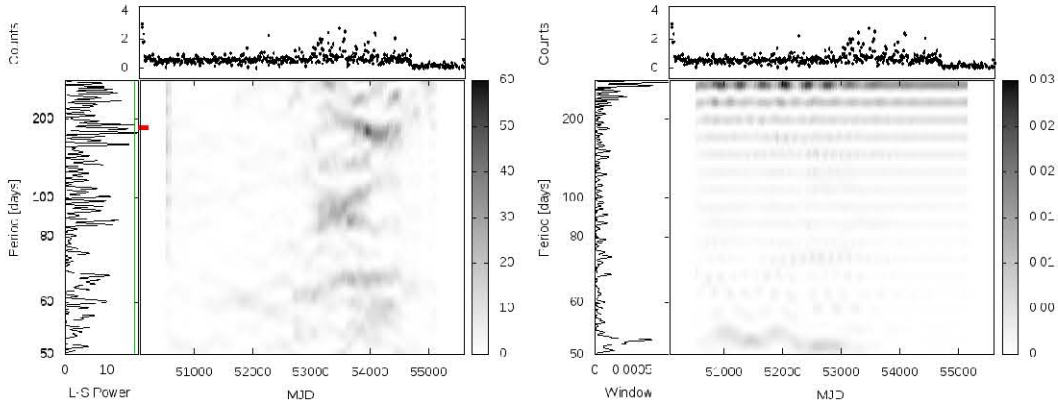

Figure 6.12: EXO 0748-676 with $P_{sup} \sim 181$ days during the higher state (Kotze et al. 2009).

The EXOSAT source EXO 0748-676 has a faint (V $\sim$ 17) optical counterpart UY Vol (Wade et al. 1985). Parmar et al. (1986) discovered a P_{orb} of 3.82 hours from X-ray eclipses observed in EXOSAT data of this dipping source, estimating $M_2 \sim 0.08 - 0.45 M_{\odot}$ and $i \sim 75 - 82°$. Bassa et al. (2009) used spectroscopic radial velocity studies of the optical counterpart to estimate $M_1 > 1.27 M_{\odot}$ and subsequently determined $0.075 < q < 0.105$, assuming $M_1 \sim 1.4 M_{\odot}$. Most recently, Muñoz-Darias et al. (2009) used high resolution VLT spectroscopy to estimate $q \sim 0.11 - 0.28$ and $M_1 \sim 1 - 2.4 M_{\odot}$, but finding $M_1 > 1.5 M_{\odot}$ if the donor is a MS star.

Gottwald et al. (1986) reported the observation of type I bursts, which increased in frequency as flux decreased. Homan et al. (1999) found QPOs $\sim 0.58 - 2.44$ Hz during both dips and bursts. Homan & van der Klis (2000) reported the discovery of a QPO ~ 695 Hz during outburst in RXTE PCA data, wherein the previously reported QPO was no longer present. Villarreal & Strohmayer (2004) detected a QPO ~ 45 Hz during burst decay in RXTE PCA data, inferring that it is the NS spin frequency.

Kotze et al. (2009) discovered a quasi-periodic $P_{sup} \sim 181$ days in this quasi-persistent transient, during its higher flux state. The DPS shows that the $P_{sup} \sim 181$ days was clearly not stable, but that it exhibits steady evolution. Several significantly detected signals at shorter time-scales are present in the DPS during the portions of the higher state with the $P_{sup} \sim 181$ days, but are not harmonics. There is no evidence for any periodic signals during the low state.

The location for EXO 0748-676 on Figure 6.1 is unknown, but it has a P_{orb} of 3.8 hours (Parmar et al. 1986) and $q \sim 0.11 - 0.28$ (Muñoz-Darias et al. 2009). Consequently, it is an LMXB with $P_{orb} < 1$ day and it is therefore not expected (according to OD01 criteria) to produce a steadily precessing warped accretion disc. However, tidal disc precession is very likely to occur since $q < 0.33$.

GRS 1747-312

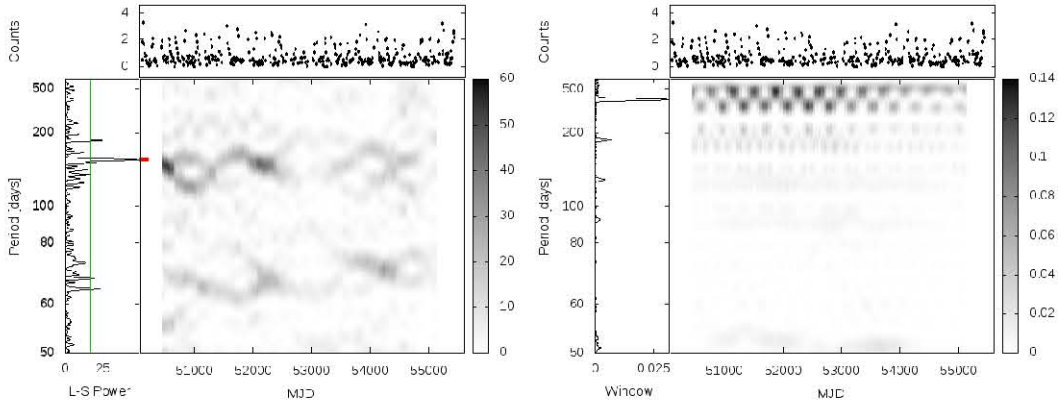

Figure 6.13: GRS 1747-312 with $P_{sup} \sim 147$ days (Wen et al. 2006).

GRS 1747-312, a.k.a. the transient in globular cluster Terzan 6, was discovered in the Galactic centre field of the Granat satellite mission (Pavlinsky et al. 1992; 1994). in't Zand et al. (2000) used BeppoSAX and RXTE PCA data to determine its P_{orb} of 12.36 hours from X-ray eclipses of duration ~ 0.72 hours, implying $i > 74.5°$. in't Zand et al. (2003) reported the observation of type I X-ray bursts and dips for this recurring transient with quasi-periodic recurrence time of several months. Galloway et al. (2008) divided type I X-ray bursts from accreting NS sources into two categories: those with long and short bursts which indicate mixed H/He accretion and those with only short bursts which indicate primarily H accretion. They placed GRS 1747-312 under low $\dot{M}$ systems exhibiting occasional giant bursts, which they associate with strong radius expansion.

Wen et al. (2006) determined a $P_{sup} \sim 147$ days in RXTE ASM data. Šimon (2009) reported the $\sim$ sinusoidal cyclic evolution of outburst recurrence times in RXTE ASM data around a mean of ~ 136 days, with the brightest outbursts occurring after the longest pauses. The cycle is ~ 5.4 years, but rather than linking it to the late-type donor's magnetic-activity cycle (Chapter 7), they proposed that the behaviour is the result of variable accretion efficiency, caused by interactions between the $\overrightarrow{B}$ of starspots and that of the accretion disc.

The $P_{sup} \sim 147$ days is strongly detected in the L-S and DPS at MJD ~ 50500 and MJD ~ 52000. However, it shows clear evolution which appears to continue through an interval with lower amplitude variations and significantly weaker detections around MJD $\sim 52500 - 53500$, to re-emerge thereafter. This agrees with the $\sim$ sinusoidal variation with mean ~ 136 days reported by Šimon (2009). There is also an evolving periodic signal at $P_{sup} \sim 70$ days, which is not a harmonic. Both aforementioned $\sim$ sinusoidal periodic signals appear to evolve overall toward slightly longer periods over the course of the entire baseline.

The location of GRS 1747-312 on Figure 6.1 is unknown, but as an LMXB with P_{orb} of 12.36 hours (in't Zand et al. 2000) it is likely situated below the OD01 curve for $r_{add} = r_o$ and is therefore not expected to develop a warped precessing disc. However, Šimon (2009) showed that P_{sup} reflects the recurrence time of the transient outbursts, linked to $\Delta\dot{M}$.

GX 339-4

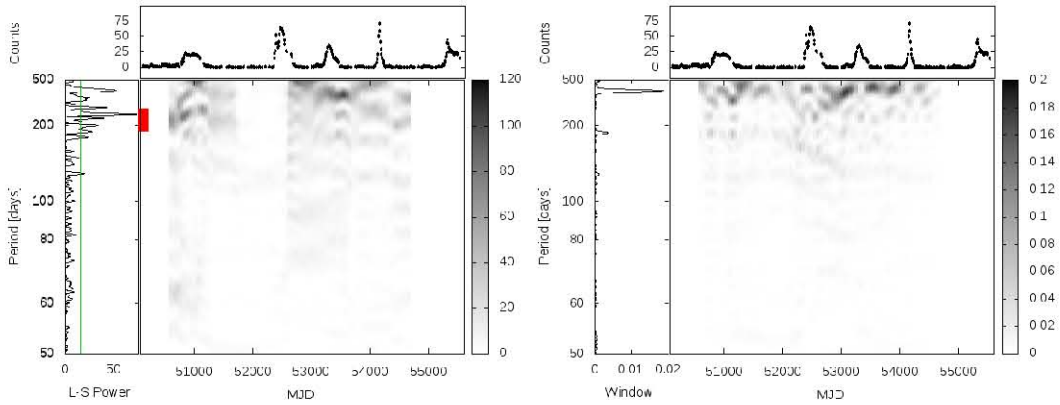

Figure 6.14: GX 339-4 with $P_{sup} \sim 190 - 240$ days (Kong et al. 2002).

GX 339-4 (a.k.a. X1658-48) was discovered by the OSO-7 mission (Markert et al. 1973) and exhibited no periodic behaviour, but rather HS, LH and off states, with aperiodic variability on time-scales from minutes to days. Samimi et al. (1979) discovered QPOs of tens of milliseconds to a few seconds, suggesting it is a BHC. Grindlay (1979) proposed that the optical counterpart V821 Ara is likely a B-type MS star. Motch et al. (1983) found QPOs ~ 20 seconds in the optical as well as Ariel V X-ray data during a particularly bright HS state (V ~ 15.5), which were anti-correlated, with optical signals leading those in the X-ray by ~ 3 seconds. Miyamoto & Kitamoto (1991) suggested a jet model to explain their Ginga observation and Fender et al. (1997) detected a jet-like structure in their high resolution Australia Telescope Compact Array (ATCA) observation at radio wavelengths. Corbel et al. (2003) found strong correlation between X-rays (using RXTE and BeppoSAX data) and radio emission (using ATCA data), presenting strong evidence for coupling between these sources of emission. Kong et al. (2002) detected variability time-scales $\sim 190 - 240$ days using archival X-ray data from Vela 5B, Ariel V, Ginga, CGCR, RXTE and BeppoSAX, which they suggested resemble the dwarf novae outburst cycles of Z Cam-type CVs.

Hynes et al. (2003) used spectroscopic radial velocity studies of the irradiated donor to determine its P_{orb} of 1.755 days and estimated $q < 0.08$ and $M_1 \sim 5.8 \pm 0.5 M_{\odot}$. Muñoz-Darias et al. (2008) estimated $M_1 > 7 M_{\odot}$, $M_2 > 0.3 M_{\odot}$ and $q < 0.125$ when taking the large $\dot{M}$ into account for the "stripped-giant" model.

$P_{sup} \sim 190 - 250$ days are detected in the lightcurve of this transient before and after removing the outbursts (the plots are included for the latter). GX 339-4 was located below the curve for $r_{add} = r_o$ on Figure 6.1. However, the $q \sim 0.7$ and P_{orb} of 0.62 days used in OD01 were rough estimates. Recalculation of the OD01 parameters with the Hynes et al. (2003) estimates, gives $\frac{r_b}{10^6} \sim 0.92$ for $q \sim 0.08$, moving GX 339-4 into the intermediate instability zone where discs may alternate between being warped and being flat. The Muñoz-Darias et al. (2008) estimates result in $\frac{r_b}{10^6} \sim 0.82$ and $q \sim 0.14$, also moving it into the intermediate instability zone. Since $q < 0.33$, tidal disc precession is very likely to occur.

GX 354-0

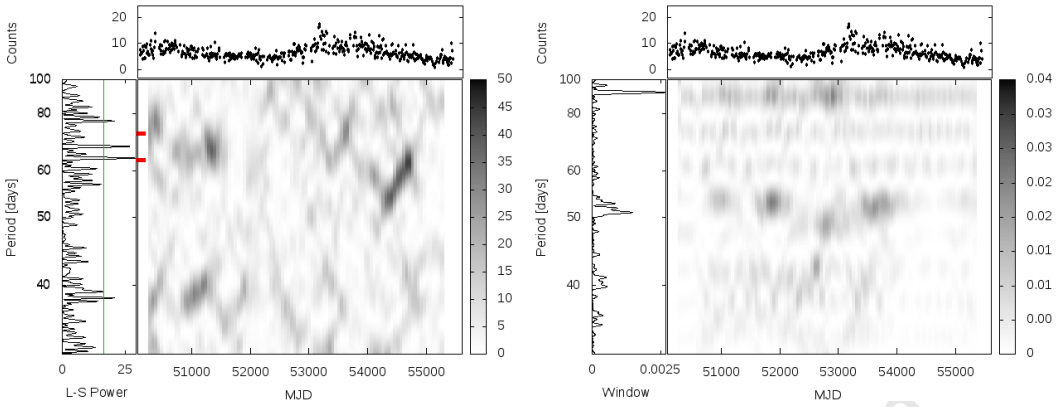

Figure 6.15: GX 354-0 with $P_{sup} \sim 63$ or 72 days (Kong et al. 1998).

Hoffman et al. (1976) reported on the discovery of type I X-ray bursts in GX 354-0 (a.k.a. Slow Burster, 3U 1727-33 or X1728-34). Strohmayer et al. (1996) used RXTE PCA data to measure pulses during bursts and inferred a P_{spin} of 2.75 milliseconds (363 Hz), also reflected in the constant separation between two QPOs in the range $\sim 650 - 1100$ Hz. As such it represented the first millisecond NS spin detected in an LMXB. Hasinger & van der Klis (1989) classified it as an Atoll source. Migliari et al. (2003) discussed the evidence for disc-jet coupling in GX 354-0, using simultaneous Very Large Array (VLA) radio data and RXTE X-ray data. They found the most variable and strongest radio emission during the transition between LH and HS X-ray states, but weaker and persistent radio emission during the HS state. The positive correlations between the 8.46 GHz radio flux and $2-10$ keV X-ray flux, as well as positive correlation between radio flux density and X-ray timing features, represented the first evidence for disc-jet coupling in an Atoll source. Kotze & Charles (2010) and Özdemir (2010) considered the very long-term variability on a $\sim$ decade long time-scale, which Kotze & Charles (2010) suggested to be associated with the magnetic-activity cycle of the donor (further discussed in Chapter 7).

Kong et al. (1998) found quasi-periodic $P_{sup} \sim 63$ or 72 days in RXTE ASM data. The DPS shows that both are initially detected, but are rapidly replaced by a single period between those values. The strongest detections are towards the end of the dataset, where a $P_{sup} \sim 50$ days evolves toward $P_{sup} \sim 70$ days. There is no evidence for a stable P_{sup}, nor for prolonged steady evolution and the behaviour rather resembles the chaotic warping observed in Cyg X-2. Its location on Figure 6.1 is unknown. Galloway et al. (2010) suggested that GX 354-0 may be a UCB, based on the detection of a possible P_{orb} of 10.77 minutes and the burst profiles that are characteristic of the accretion of H-deficient material. As such, it should have a location similar to X1820-303 on Figure 6.1, well below the curve for $r_{add} = r_o$ where systems are not expected to develop warped precessing discs. However, it would also likely have $q < 0.33$ and tidal disc precession is therefore likely to occur.

Her X-1

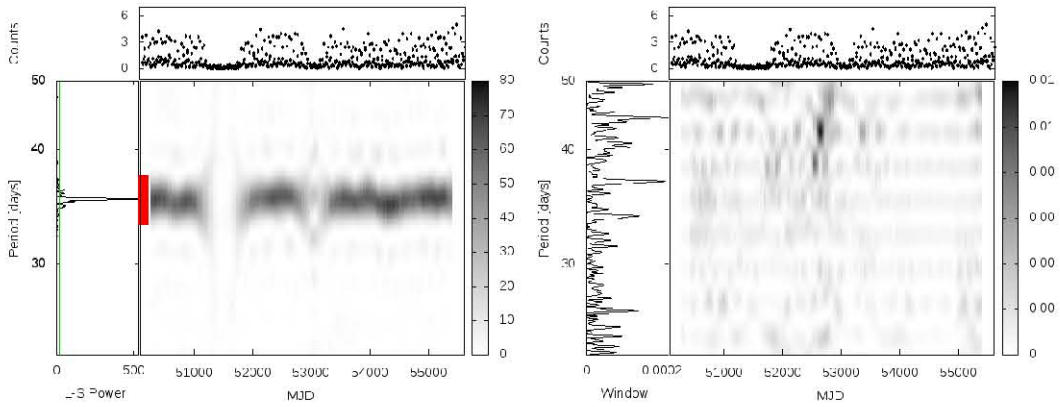

Figure 6.16: Her X-1 with $P_{sup} \sim 33-37$ days, averaged at ~ 35 days (Leahy & Igna 2010).

Tananbaum et al. (1972b) discovered the P_{spin} of 1.24 seconds of Her X-1 in Uhuru data and derived its P_{orb} of 1.7 days from cyclic variations in P_{spin}. They also discovered the $P_{sup} \sim 35$ days on-off cycle, during which it is detected for ~ 9 days. Her X-1 and its optical counterpart HZ Her both exhibit the P_{spin} (Doxsey et al. 1973), eclipses on the P_{orb} and the P_{sup} on-off cycle (Bahcall & Bahcall 1972).

Petterson (1977) interpreted the $P_{sup} \sim 35$ days as a twisted, tilted, optically thick accretion disc which obscures the central X-ray source as it precesses. Wijers & Pringle (1999) and Ogilvie & Dubus (2001) investigated irradiation by the central X-ray source as the mechanism responsible for warping/tilting the disc in Her X-1 and also considered its applicability to other XRBs with observed P_{sup}. Clarkson et al. (2003a) presented DPS results, finding the stable P_{sup} (at $\sim 20 \times P_{orb}$) consistent with its theoretical OD01 prediction.

Middleditch & Nelson (1976) estimated $M_1 \sim 1.3 \pm 0.14 M_{\odot}$, $M_2 \sim 2.18 \pm 0.11 M_{\odot}$ and $i \sim 87 \pm 3°$, from spectroscopic radial velocity measurements of the donor. Deeter et al. (1981) analysed changes in the timing of X-ray pulses in data from Uhuru, HEAO 1, OSO-8 and Einstein to redetermine the P_{orb} and estimated $M_1 \sim 1.34 M_{\odot}$, $M_2 \sim 2.22 M_{\odot}$ and $i \sim 85°$. Reynolds et al. (1997) used radial velocity measurements from optical spectroscopy of the donor to estimate $M_1 \sim 1.5 \pm 0.3 M_{\odot}$ and $M_2 \sim 2.3 \pm 0.3 M_{\odot}$. Her X-1 is the only LMXB for which $M_2 > 1 M_{\odot}$.

The DPS shows a very strong detection of the relatively stable $P_{sup} \sim 35$ days throughout the baseline, with interruptions occurring around MJD $\sim 51250-51750$ and MJD ~ 53000, which coincide with the anomalous low states (ALSs), of which the first was discussed as such in Still et al. (2001). During these states, the maximum flux drops dramatically to become comparable to the minimum flux, which also appears to be decreasing slightly. Vrtilek et al. (2001a) suggested that the ALS is not due to a cut-off in $\dot{M}$, but is rather caused by the shadowing effect of a more extreme tilt than usual. Leahy & Dupuis (2010) suggested the latter would account for the larger reduction in extreme UV flux in comparison to that in X-rays during the ALS, in simultaneous EUVE and RXTE data.

Her X-1 lies in the instability zone on Figure 6.1, approximately halfway between the solid and dashed curves. The super-orbital period is therefore expected to be relatively stable, as a result of the precession of a radiatively warped accretion disc. However, it may also show some evolution due to small-scale variation in the structure of the warp itself as competing warping modes start to exert their influence. The Leahy & Igna (2010) results of variable $P_{sup} \sim 33 - 37$ days with an average of ~ 35 days, support this interpretation.

IGR J17098-3628

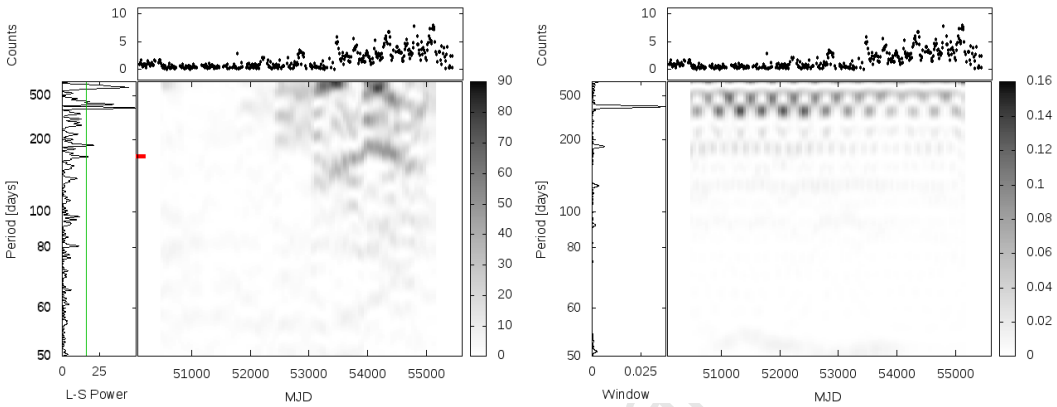

Figure 6.17: IGR J17098-3628 with $P_{sup} \sim 163$ days in the high state (Kotze et al. 2009).

IGR J17098-3628* was discovered by INTEGRAL as part of its regular monitoring of the Galactic plane and Galactic centre, within ~ 10 arcminutes of another transient X-ray source IGR J17091-3624 (Grebenev et al. 2005b), which is too close for RXTE ASM to resolve them (Chen et al. 2008). Grebenev et al. (2005a) considered the spectral evolution of this transient using INTEGRAL and RXTE data, finding a steady softening of the X-ray spectrum, normally associated with BHCs. The RXTE ASM lightcurve for IGR J17098-3628 therefore represents the combined flux of 2 transient sources, which are in close proximity ($\sim 1°$) to the bright but steady Sco X-2 (Grebenev et al. 2007). Capitanio et al. (2009) determined from XMM, Swift and INTEGRAL monitoring, that only IGR J17098-3628 was active for MJD $\sim 53450 - 54200$ and that IGR J17091-3624 appears to have been quiescent between its outbursts occurring at MJD $\sim 52750 - 53000$ and after MJD ~ 54200. Kotze et al. (2009) discovered a quasi-periodic $P_{sup} \sim 163$ days during MJD $\sim 53450 - 54200$.

The $P_{sup} \sim 163$ days was detected during the portions of the higher state to which the Kotze et al. (2009) P_{sup} applies. However, it is clearly not stable and shows steady evolution. There are also several significantly detected longer term signals in the DPS, particularly from MJD ~ 54000, which relate to the lightcurve features after MJD ~ 54200 and are therefore associated with both IGR J17091-3624 and IGR J17098-3628. There is no evidence for periodic signals in the low state.

*IGR J17098-3628 is designated IGR J17098-3626 on the RXTE ASM website, but is referenced to as such only once in the literature (Kennea et al. 2005) when in fact referring to IGR J17098-3628.

IGR J17098-3628 has an unknown location on Figure 6.1, but Kotze et al. (2009) argued that it likely also has $P_{orb} < 1$ days and $q < 0.33$, based on similarities to EXO 0748-676. As an LMXB with $P_{orb} < 1$ day, IGR J17098-3628 would not be expected to produce a steadily precessing warped accretion disc (by OD01 criteria), but tidal disc precession is likely.

KS 1731-260

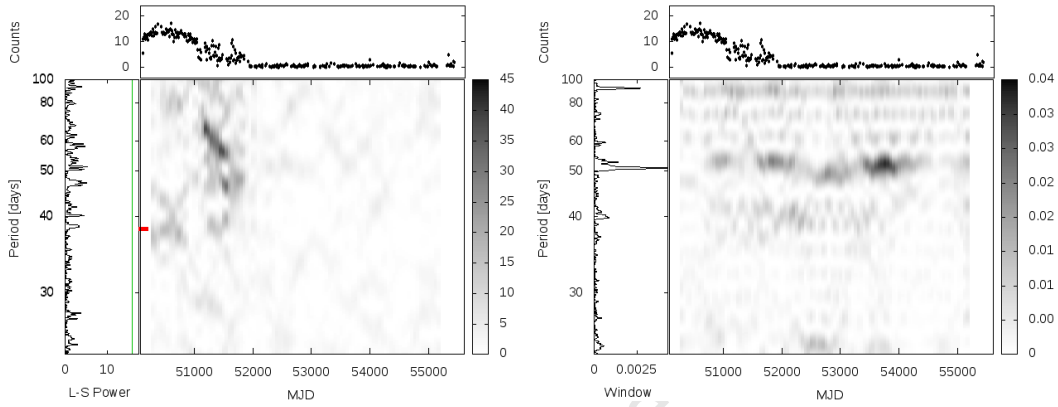

Figure 6.18: KS 1731-260 with $P_{sup} \sim 38$ days (Revnivtsev & Sunyaev 2003).

Sunyaev & the Kvant Team (1989) discovered the SXT KS 1731-260. It exhibits type I X-ray bursts, but is also a source of hard X-rays (Barret et al. 1992). Wijnands & van der Klis (1997) discovered kHz QPOs in their RXTE PCA data and inferred a P_{spin} of 3.8 milliseconds, using the beat frequency model. However, Smith et al. (1997) discovered a coherent periodic signal ~ 1.9 milliseconds using RXTE PCA data, associating it with the P_{spin} of the NS. Muno et al. (2000) confirmed the P_{spin} of 1.9 milliseconds based on a total of 9 type I X-ray bursts contained in the RXTE data. KS 1731-260 is a quasi-persistent or long-duration transient which displays extended intervals in both the high and low intensity states (Wijnands et al. 2001). Revnivtsev & Sunyaev (2003) reported the possible detection of a $P_{sup} \sim 38$ days. Cackett et al. (2006) considered the cooling curve of the NS after it had been heated by the prolonged outburst, finding that the crust cools rapidly to re-establish thermal equilibrium with the core, as suggested in Wijnands et al. (2001). Šimon (2010) suggested that echo outbursts occurred during the transition to the low state due to thermal-viscous instability in the disc at the end of the prolonged outburst, wherein the disc became divided into a thermally stable ionized inner disc and thermally unstable outer disc.

The $P_{sup} \sim 38$ days is detected during the high state (MJD < 51000) and during the transition from the high to the low state (MJD $\sim 51000 - 52000$). There appear to be two sections to the high state, namely MJD < 51000 and MJD $\sim 51000 - 52000$. Since the $P_{sup} \sim 38$ days appears in both of those, it suggests some measure of stability. The strongest detection is a quasi-periodic P_{sup} that evolves rapidly from ~ 70 days to ~ 45 days during the transition to the low state, which may be related to the echo outbursts referred to by Šimon (2010). The DWF feature at ~ 50 days is not coincident with the DPS features.

Although KS 1731-260 does not appear to be stable (like Her X-1 or LMC X-4) when it is persistent, its behaviour is not quite comparable to the chaotic warping behaviour observed in Cyg X-2. KS 1731-260's location on Figure 6.1 is unknown, but as an LMXB it is likely located below the OD01 curve for $r_{add} = r_o$ and consequently unlikely to produce a warped accretion disc. However, it will be susceptible to tidal disc precession if its $q < 0.33$.

LMC X-2

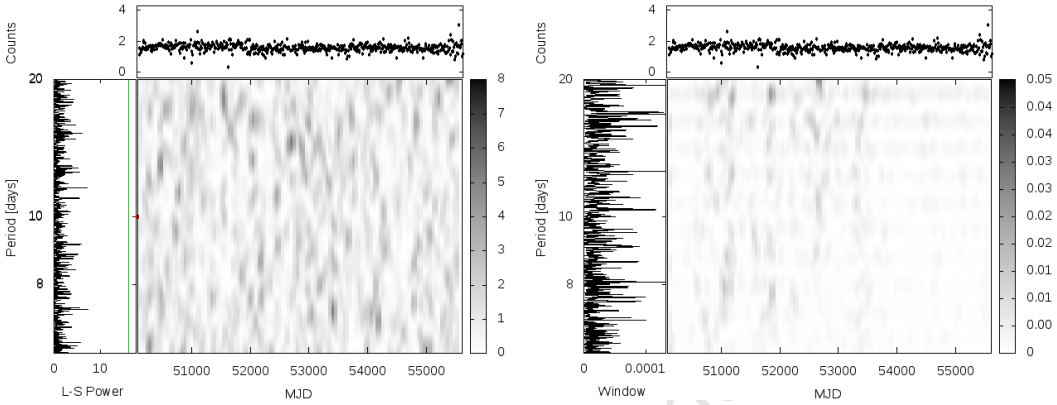

Figure 6.19: LMC X-2 with $P_{sup} \sim 10$ days Cornelisse et al. (2007b) undetected.

LMC X-2 (a.k.a. X0521-72) was discovered by Uhuru (Leong et al. 1971). Monitoring by Ariel V (Griffiths & Seward 1977) and OSO-7 (Markert et al. 1979) did not reveal any stable long-term periodic behaviour in its X-ray emission. HEAO 1 also did not reveal any X-ray periods in the range $0.6 - 16$ days (Johnston et al. 1979), but the refined position obtained led to the identification of a faint (B $\sim$ 18.5) blue variable optical counterpart (Pakull 1978). Motch et al. (1985) detected a P_{orb} of 6.4 hours in optical CCD photometry. Bonnet-Bidaud et al. (1989) detected the suggested P_{orb} with low significance in their optical photometry, but not the EXOSAT data. Callanan et al. (1990) determined the P_{orb} of 8.15 hours, based on ESO and SAAO optical monitoring of the donor, finding no evidence for the ~ 6.4 hours reported previously. Smale & Kuulkers (2000) used RXTE PCA data to determine the P_{orb} of 8.16 hours, while finding no evidence in the RXTE ASM or EXOSAT data for it. They also suggest that LMC X-2 may be the first extragalactic Z source discovered. McGowan et al. (2003) found that rapid variations in the X-ray emission (with RXTE) lead the optical by < 20 seconds, consistent with reprocessing in the accretion disc.

Crampton et al. (1990) reported the discovery of a $P_{sup} \sim 12.5$ days from spectroscopic and photometric observations of the optical counterpart. Cornelisse et al. (2007b) confirmed the P_{orb} of 8.16 hours and reported a $P_{sup} \sim 10$ days from spectroscopic radial velocity studies of the donor, for which the $P_{sup} \sim 12.5$ days in Crampton et al. (1990) may be a beat period. They also suggest that LMC X-2 may have a canonical NS with $M_1 \sim 1.4 M_\odot$ (limiting $M_2 < 0.14 M_\odot$) or possibly an even more massive NS. Detections of P_{sup} have therefore all been from optical observations only.

The DPS results show no evidence for any significant long-term X-ray periodicities and all points in the L-S periodogram are below the white noise level. Periods in the same range were very clearly detected for several other sources in Chapter 5. The location of LMC X-2 on Figure 6.1 is unknown. LMC X-2 has a P_{orb} of 8.16 hours (Callanan et al. 1990, Smale & Kuulkers 2000, Cornelisse et al. 2007b) and as an LMXB with $P_{orb} < 1$ day, it is not expected to produce a warped accretion disc (according to OD01 criteria). However, with $q \sim 0.14$ (Cornelisse et al. 2007b) tidal disc precession is likely to occur ($q < 0.33$).

MS 1603.6+2600

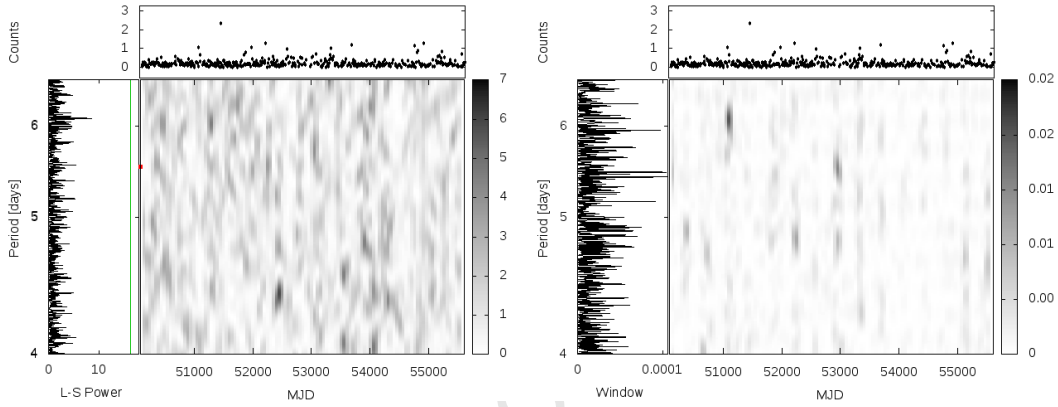

Figure 6.20: MS 1603.6+2600 with $P_{sup} \sim 5.5$ days Hakala et al. (2009) undetected.

MS 1603.6+2600, often referred to by the name of its faint red (R $\sim$ 19.4) optical counterpart UW CrB, with a P_{orb} of 112.5 minutes, was a serendipitous discovery by the Einstein Extended Medium Sensitivity Survey (Morris et al. 1990). Hakala et al. (1998) suggested that it may be a short period SXT, that has never been seen in outburst, with a BH rather than a NS as compact object, by analysing ROSAT X-ray data and optical data from the Nordic Optical Telescope (NOT) in La Palma. Mukai et al. (2001) contradicted this interpretation by detecting a type I X-ray burst in ACSA data, consistent with a NS LMXB. Jonker et al. (2003) obtained an X-ray spectrum with Chandra and argued that MS 1603.6+2600 must be an ADC source if the flare observed with ACSA was indeed a type I X-ray burst, but a SXT if it was not. Hynes et al. (2004) detected optical burst behaviour comparable to that of reprocessed type I X-ray bursts in NS LMXBs, concluding that it is therefore likely an ADC source.

Hakala et al. (2005; 2009) and Mason et al. (2008) found a $P_{sup} \sim 5.5$ days in optical lightcurves, which they associated with the precession of a warped or elliptical or otherwise geometrically variant accretion disc. Narita et al. (2009) found no evidence for the $P_{sup} \sim 5.5$ days in the archival RXTE X-ray data, but found the spectrum during the low intensity part of that variation consistent with increased absorption, as would be applicable for partial obscuration of the central source by the accretion disc. Detections of P_{sup} have therefore all been from optical observations only.

Predictably, the DPS results show no evidence for any significant long-term X-ray periodicities and all points in the L-S periodogram are below the white noise level. The location for MS 1603.6+2600 on Figure 6.1 is unknown. As an LMXB with $P_{orb} < 1$ day, it is not expected to produce a warped accretion disc (according to OD01 criteria). It likely shares properties with the other short period systems, such as having a $q < 0.33$, which would make tidal disc precession likely.

Sco X-1

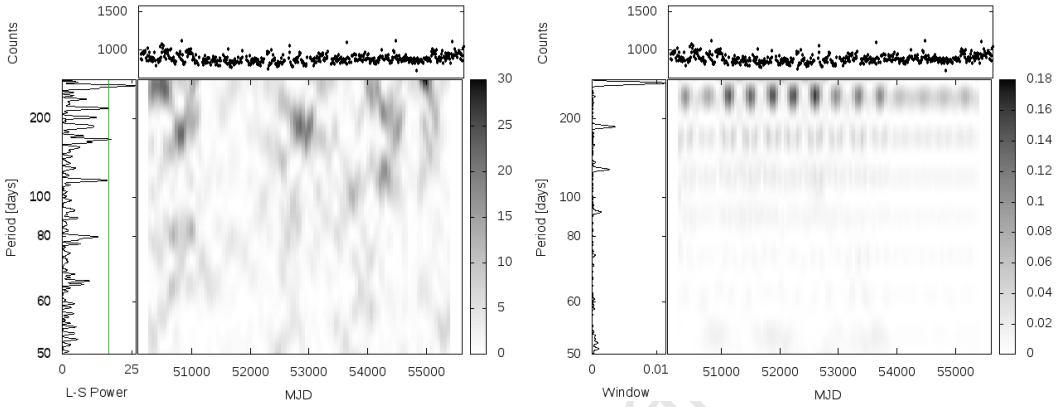

Figure 6.21: Sco X-1.

Sco X-1 is the brightest X-ray source in the sky, with a bright (V $\sim$ 12) optical counterpart V818 Sco (Sandage et al. 1966). Cowley & Crampton (1975) and Gottlieb et al. (1975) discovered the P_{orb} of 18.9 hours, from radial velocity studies of optical spectra of the donor and Uhuru X-ray data respectively. Crampton et al. (1976) estimated $M_1 \sim 1.3M_{\odot}$, $M_2 \sim 1M_{\odot}$ and $i \sim 30°$ from spectroscopic measurements. Miyamoto & Matsuoka (1977) reviewed radio, optical and X-ray observations of Sco X-1 to present a theoretical model, wherein the source contains a spherical, optically thick, hot plasma. Priedhorsky et al. (1986) identified a QPO $\sim$ 6 Hz that is anti-correlated to intensity during quiescence, but QPOs $\sim 10-20$ Hz that are correlated to intensity during the active state in EXOSAT data. van der Klis et al. (1987) suggested an oscillating thick disc obscuration model to account for the bimodal distribution of QPOs. Kudryavtsev et al. (1989) identified a $P_{sup} \sim 62$ hours in data from the Prognoz-9 satellite. Hjellming et al. (1990) determined that Sco X-1 was radio-quiet when in the X-ray flaring branch of Z source behaviour, and radio-loud during the X-ray normal branch. van der Klis et al. (1996) discovered the first kHz QPOs in a celestial X-ray source in the RXTE data of Sco X-1. Fomalont et al. (2001) used Very Long Baseline Interferometry (VLBI) radio observations to determine that the motion of the radio components were consistent with radio lobes formed by relativistic jets ($v \sim 0.45c$) as they interact with the ISM. Steeghs & Casares (2002) presented the first detection of the irradiated donor, by using phase-resolved spectroscopy which allowed the likely binary parameters to be estimated as $M_1 \sim 1.4M_{\odot}$, $M_2 \sim 0.42M_{\odot}$ and $i \sim 38°$.

The previously reported $P_{sup} \sim 62$ days in OD01 was an incorrect quote of $P_{sup} \sim 62$ hours (Kudryavtsev et al. 1989). Neither of these are significantly detected in the RXTE ASM data for Sco X-1. However, unstable $P_{sup} \sim 200$ days are detected and appear to recur after essentially disappearing temporarily from MJD $\sim 51000 - 52000$. Sco X-1 was located in the OD01 intermediate instability zone on Figure 6.1, where discs are expected to alternate between being warped and flat. However, the $q \sim 0.7$ used in OD01 was only a rough estimate, and it has since been determined to be $q \sim 0.3$ (Steeghs & Casares 2002), making tidal disc precession likely ($q < 0.33$). Recalculation gives $\frac{r_b}{10^6} \sim 1.47$, so that Sco X-1 remains in the intermediate instability zone.

X1636-536

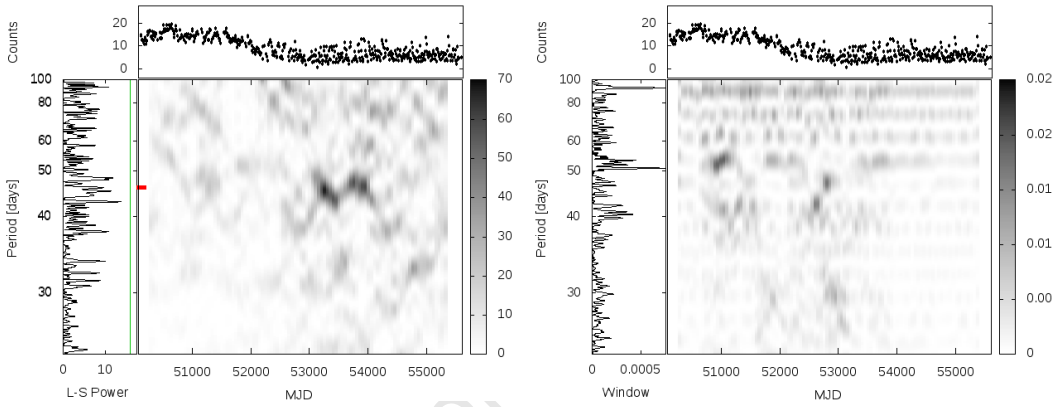

Figure 6.22: X1636-536 with $P_{sup} \sim 46$ days (Shih et al. 2005).

X1636-536, a.k.a. MXB 1636-53(6)*, has a faint (V $\sim$ 17.5) optical counterpart V801 Ara (Jernigan et al. 1977). Hoffman et al. (1977) investigated the spectra of its type I X-ray bursts and determined the emitting region to be of NS size. Pedersen et al. (1981) suggested the P_{orb} of 3.8 hours, confirmed by Smale & Mukai (1988). Hasinger & van der Klis (1989) classified it as an Atoll source. Wijnands & van der Klis (1997) reported the discovery of kHz QPOs at 1150 and 1193 Hz, with a constant frequency separation of 276$\pm$10 Hz. Strohmayer & Markwardt (2002) discovered a coherent QPO $\sim$ 582 Hz during a super-burst, from which they inferred a P_{spin} of 1.72 milliseconds. Shih et al. (2005) discovered a $P_{sup} \sim 46$ days in RXTE data, during its decline from the high state, and an anti-correlation between soft and hard X-rays. However in Shih et al. (2011), optical and soft X-rays have been found to be correlated, as the latter are reprocessed in the accretion disc. Casares et al. (2006) estimated $q \sim 0.21 - 0.34$ from phase-resolved VLT spectroscopy of the donor.

The $P_{sup} \sim 46$ days shows similar behaviour to that of another quasi-persistent transient, KS 1731-260. It is strongly detected at MJD $\sim 53000 - 54000$, after the transition to a lower state. However, it does not appear to be stable during either state, but rather appears to be persistent and steadily evolving during the first half of the low state.

*The prefix MXB indicates a MIT X-ray Burster.

The location of X1636-536 on Figure 6.1 makes the formation of a warped precessing disc unlikely, since it is below the $r_{add} = r_o$ curve. Recalculation of the OD01 parameters using the Casares et al. (2006) estimates, did not influence its location significantly. Since $q \lesssim 0.33$, tidal disc precession may likely occur. However, during the decline from the high to the low state, X1636-536 displayed variations consistent with modulations of $\dot{M}$, comparable with the viscous time-scale in the outer disc (Shih et al. 2005; 2011).

X1730-333

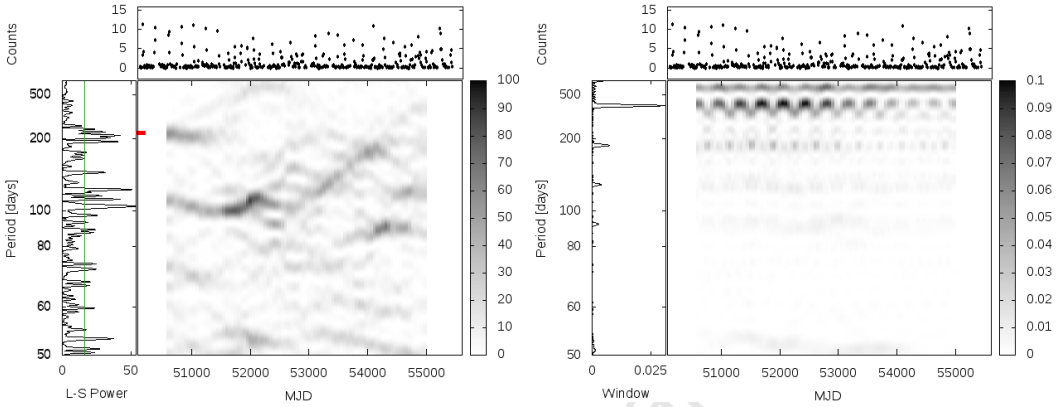

Figure 6.23: X1730-333 with $P_{sup} \sim 218$ days (Guerriero et al. 1999).

X1730-333 (a.k.a. MXB 1730-335) is the prototypical Rapid Burster, introduced in Chapter 2. Liller (1977) identified the highly reddened globular cluster in which it resides, subsequently named Liller 1. Marshall et al. (1979) analysed type I and type II X-ray bursts in SAS-3 data and found two modes of recurrence in the type II bursts and suggested a model for the Rapid Burster wherein instability in the accretion flow leads to type II bursts, while ignition of accumulated material on the NS surface results in type I bursts. They also reported the presence of pre- and post-burst dips. Apparao & Chitre (1979) expanded the model to include a gate mechanism, discussed in Chapter 2. Loznikov & Iamburenko (1982) interpreted the 2 modes of type II bursts as arising from accretion onto the magnetic poles of a NS with a P_{spin} of 250 seconds. Stella et al. (1988) discovered QPOs $\sim 2-5$ Hz during type II X-ray bursts in EXOSAT data and Fox et al. (2001) found a coherent QPO $\sim$ 306.5 Hz during the rise of type I bursts in RXTE data. Moore et al. (2000) reported the identification of a likely radio counterpart in VLA observations and Falanga et al. (2004) discovered hard X-ray emission in INTEGRAL data during transient outburst, but its optical counterpart has not been identified yet.

Grindlay & Gursky (1977) determined the recurrence time of transient outbursts in Uhuru, ANS, Ariel V and SAS-3 to be $P_{sup} \sim 180-360$ days. Guerriero et al. (1999) found $P_{sup} \sim 218$ days in RXTE data for $1996-1998$ and $P_{sup} \sim 180$ days in archival data from various satellites for $1976-1983$. Masetti (2002) reported the change from ~ 200 days to ~ 100 days in outburst recurrence time after 2000.

An initial strong detection of the $P_{sup} \sim 218$ days appears to remain steady up to MJD ~ 51500 (end of 1999). However, during that time there are also a number of shorter term periods, that do not appear to be simply harmonics. A period of ~ 100 days is strongly detected and steadily drifting until MJD ~ 52500, after which its evolution from shorter to longer periods begins. There appears to be a variety of steadily evolving periods, indicative of the time-scale on which transient outbursts recur. The location of X1730-333 on Figure 6.1 is unknown and so is its P_{orb}.

X1820-303

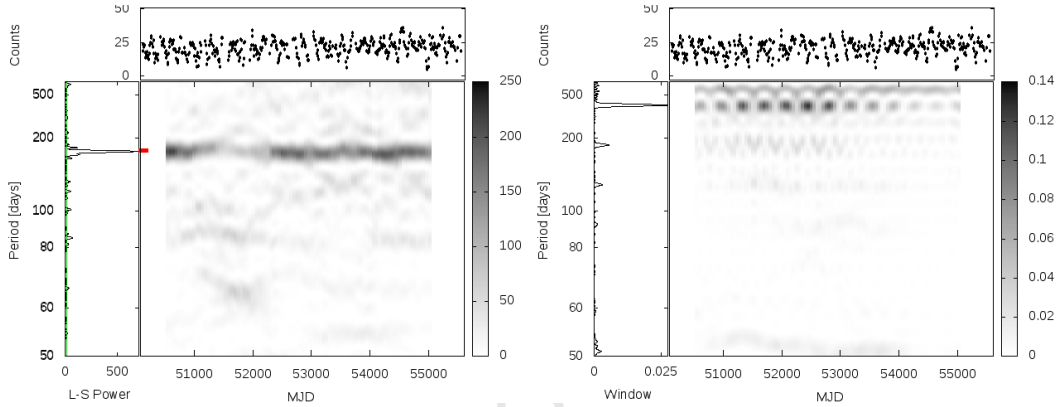

Figure 6.24: X1820-303 with $P_{sup} \sim 171$ days (Chou & Grindlay 2001).

X1820-303 (a.k.a. Sgr X-4 or MXB 1820-30) is located at the core of globular cluster NGC 6624. Grindlay et al. (1976) reported X-ray bursts observed in ANS data. Stella et al. (1987) discovered its P_{orb} of 685 seconds in EXOSAT data, making it the shortest period UCB identified. Rappaport et al. (1987) suggested that the donor is likely a He WD. Hasinger & van der Klis (1989) classified it as an Atoll source. Smale et al. (1997) discovered a kHz QPO in RXTE data during the low state. Wijnands et al. (1999) discovered a QPO ~ 7 Hz in RXTE data. Tarana et al. (2007) discovered hard X-ray emission in INTEGRAL data. Migliari et al. (2004) reported the identification of a likely radio counterpart in VLA observations, during its HS state, coincident with radio PSR 1820-30A.

Priedhorsky & Terrell (1983a; 1984a) reported their discovery of a $P_{sup} \sim 176$ days in Vela 5B data. Chou & Grindlay (2001) suggested the extremely stable $P_{sup} \sim 171$ in RXTE, Vela 5B and Ginga data is likely the consequence of the effect of a third body on the $\dot{M}$ in the system, as discussed in Chapter 4. Šimon (2003) determined $P_{sup} \sim 172$ days in RXTE ASM data. Zdziarski et al. (2007) performed a comprehensive analysis of the triple system scenario and how binary eccentricity oscillations could then modulate $\dot{M}$ through L_1, finding agreement between theoretical and observed lightcurves. However, Wang & Chakrabarty (2010) suggest that a beat period of ~ 694 seconds discovered in the far UV data, may be the result of the superhump effect and estimated $q \sim 0.06$ for that scenario. Güver et al. (2010) estimated $M_1 \sim 1.58 \pm 0.06 M_\odot$ from spectroscopic measurements.

The $P_{sup} \sim 171$ days in this LMXB is strongly detected and appears stable. Its detection is weaker during MJD $\sim 51200 - 52200$ (but still significant) and simultaneously there are detections of shorter term periods during that time. The ~ 86 days period is the first harmonic thereof, but the ~ 65 days period is not a harmonic. The minor variations visible in the DPS for the $P_{sup} \sim 171$ days are within conservative error estimates for the periods determined in each window, and are therefore not significant.

The location of X1820-303 on Figure 6.1, makes it highly unlikely that any P_{sup} in the system would be related to a precessing warped accretion disc, but its very low q makes it a prime candidate for tidal disc precession. However, since it has been interpreted as a triple system the P_{sup} is rather associated with the $\Delta\dot{M}$ resulting from the effects of the third body and is therefore expected to be extremely stable. Fabian et al. (1975) suggested that tidal capture in dense globular cluster cores likely form such close binaries, which involve triple star interactions during their evolution, as discussed in Chapter 2.

X1916-053

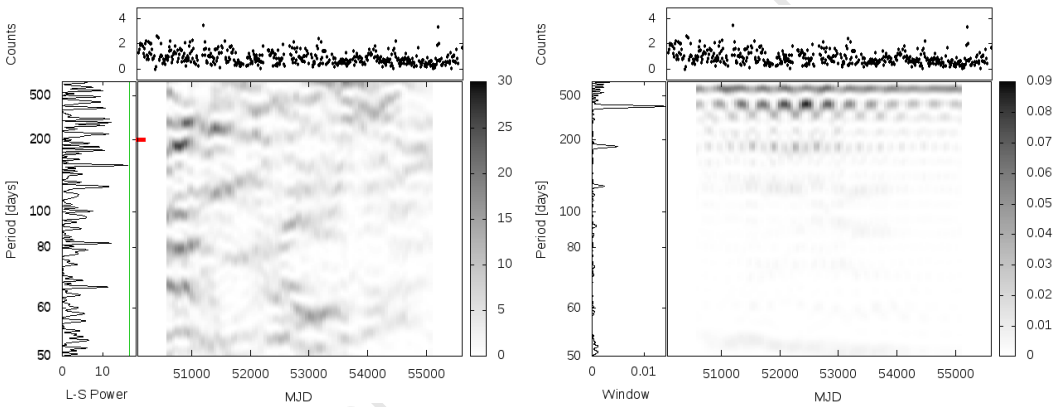

Figure 6.25: X1916-053 with $P_{sup} \sim 199$ days (Priedhorsky & Terrell 1984b).

X1916-053 (a.k.a. MXB 1916-05 or 4U 1915-05) has a very faint (V $\sim$ 21) optical counterpart V1405 Aql. Lewin & Joss (1977), Becker et al. (1977) identified it as a type I burst source candidate using SAS-3 and OSO-8 data. Walter et al. (1982) and White & Swank (1982) independently discovered the P_{orb} of 50 minutes from the recurrence of X-ray absorption dips, providing the first direct evidence for the binary nature of X-ray burst sources. Rappaport & Joss (1984) suggested that the donors in UCBs are evolved semi-degenerate H-deficient stars or degenerate WDs with $M_2 > 0.035 M_\odot$ and in this particular case estimated $M_2 \sim 0.008 - 0.1 M_\odot$.

Hasinger & van der Klis (1989) classified it as an Atoll source. Boirin et al. (2000) identified high-frequency QPOs $\sim 200 - 1300$ Hz and low-frequency QPOs $\sim 5 - 80$ Hz in RXTE PCA data. Galloway et al. (2001) discovered a coherent oscillation ~ 269.4 Hz during a type I X-ray burst in RXTE data, which has been associated with a P_{spin} of 3.7 milliseconds in Liu et al. (2007).

Priedhorsky & Terrell (1984b) discovered a $P_{sup} \sim 199$ days in Vela 5B data and Grindlay et al. (1988) suggested that it might be a triple system. Schmidtke (1988) detected the P_{orb} of 50.458 ± 0.037 minutes, as well as a beat period $\sim 48.746 \pm 0.035$ minutes associated with the precession of an elliptical disc on a time-scale of ~ 4 days, in the optical lightcurves of the donor. Chou et al. (2001) used RXTE and optical data to determine $P_{sup} \sim 3.9$ days, which is also observed as variations in the dip shape. Homer et al. (2001) used variations of the dip in RXTE X-ray data and NOT optical data to determine a quasi-periodic negative superhump $P_{sup} \sim 4.74$ days. Retter et al. (2002) interpreted the latter mentioned result as firm evidence for the appropriateness of the superhump model above the triple model. Hu et al. (2008) estimated $q \sim 0.045$, assuming the negative superhump model using the $P_{sup} \sim 4.87$ days determined from the variation in dip width in RXTE data.

There is an initial strong detection of the $P_{sup} \sim 199$ days before MJD ~ 51000, but we found no evidence for any modulation near 5 days during the entire baseline. In fact, several unrelated periodic signals are detected initially, but none that remain stable or show steady evolution and their behaviour is rather reminiscent of that in Cen X-3. Šimon (2005) reported similar findings from RXTE ASM data, arguing that the disc may alternate between thermally stable and unstable to modulate $\dot{M}$ on long-term time-scales.

The location of X1916-053 on Figure 6.1 makes it highly unlikely that any P_{sup} in the system would be related to a precessing warped accretion disc. However, with $q < 0.33$ it is highly susceptible to disc precession due to tidal interactions with the donor, as suggested in Homer et al. (2001). The $P_{sup} \sim 5$ days associated with this behaviour was not determined from X-ray flux variations, but rather changes in the structure of the X-ray dips or from optical data, which the DPS analysis is unequipped to detect.

X1957+115

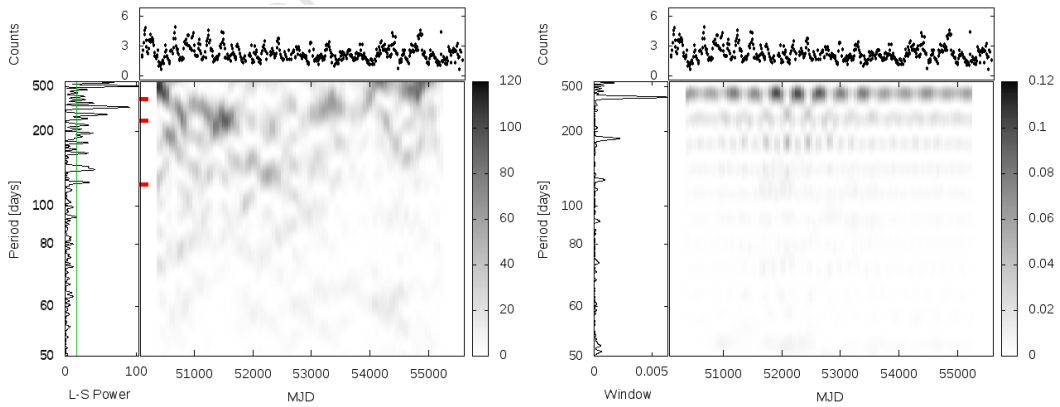

Figure 6.26: X1957+115 with $P_{sup} \sim 117$, 235 & 352 days (Nowak & Wilms 1999).

X1957+115 (a.k.a. 3U 1956+11) has a faint (V ~ 18.7) optical counterpart V1408 Aql identified by Margon et al. (1978). Thorstensen (1987) discovered the P_{orb} of 9.33 hours from CCD photometry of the counterpart.

Yaqoob et al. (1993) argued that the compact object is a NS, even though it has an ultra-soft X-ray spectrum which is normally associated with BHCs, as suggested by White & Marshall (1984). Wijnands et al. (2002) report that the spectrum hardens as the intensity increases and suggest that it may harbour a BH in a persistent high state. Nowak et al. (2008) determined from RXTE PCA observations that X1957+115 may host the most rapidly spinning galactic BH, but with unknown mass and distance they had to estimate normalized spin (a^*) over a range while using rapid-spin models: $a^* \sim 0.83$ for $M_1 \sim 3M_\odot$ at 10 kpc, up to $a^* \sim 1$ for $M_1 \sim 16M_\odot$ at 22 kpc.

Nowak & Wilms (1999) suggested that a precessing warped accretion disc may be responsible for the $P_{sup} \sim 117$, 235 & 352 days in RXTE ASM data. Hakala et al. (1999) suggested that changes in the optical lightcurve shape indicate an evolving accretion disc structure, such as a warp. However, OD01 pointed out that there was little observational evidence to support the claims for a warped accretion disc and that the radiation-driven stability criteria rule out the presence of a warped disc in X1957+115. Bayless et al. (2011) suggested that the optical lightcurve can be reproduced by a model wherein a thin, symmetric accretion disc does not get eclipsed, but the changes in orientation of the irradiated secondary are responsible for the orbital modulation.

$P_{sup} \sim 100 - 500$ days are detected and there appear to be several unsteadily evolving features in the DPS, with the longer term features more significantly detected. According to the location of X1957+115 on Figure 6.1, based on rough estimates, it is not expected to develop a warped precessing disc. Furthermore, OD01 suggested periodic signals may rather be the result of the time-scale of features in the lightcurve, occuring due to $\Delta\dot{M}$.

6.5 Summary

The complexity of super-orbital behaviour is best conveyed by the DPS plots themselves. The long-term behaviour of the P_{sup} for all 25 sources is summarized in Tables 6.3 & 6.4, for HMXBs and LMXBs respectively. Therein, concise descriptions of the behaviour of their P_{sup} are given, together with the mechanisms likely or believed to be responsible. Relevant references regarding mechanisms are contained in the discussion of each source in the previous section. The recalculated values for q and $r_b/10^6$ (in units of $\left[\frac{GM_1}{c^2}\right]$), based on the latest system parameters are included, with references to the estimates on which they were based included in the footnotes. These values were used to revise Figure 6.1 and the updated figure is presented as Figure 6.27.

Chaotic behaviour refers to unstable or highly variable periodic signals, such as those displayed by Cyg X-2. A source that *varies*, may evolve *steadily* (like SMC X-1) or *erratically* (like Cen X-3). *Steady* refers to persistent or intermittent periodic signals that display no significant variation (like Her X-1 & LMC X-4), i.e. the variations are within conservative error estimates for the periods. Conclusions drawn from these results are presented in Chapter 8.

Table 6.3: Characterization of P_{sup} behaviour in HMXBs

Source	**Behaviour**	q $\left(\frac{M_2}{M_1}\right)$	$r_b/10^6$ $\left[\frac{GM_1}{c^2}\right]$	**Mechanism**
Cen X-3	varies erratically	17.9[1]	7.1[1]	mode 0-1*
Cyg X-1	steady	2.8[2],[3]	2.3[2],[3]	mode 0-1*
LMC X-3	varies steadily	0.7[4]	0.7[4]	$\Delta\dot{M}$
LMC X-4	steady	13.6[1]	5.2[1]	mode 0-1*
SMC X-1	varies steadily	15.7[1],[5]	12.0[1],[5]	mode 1+*
SS433	steady	4.2[6]	10.3[6]	jet
X0114+650	steady	11.4[7]	18.8[7]	$\Delta\dot{M}$/BeX?
X1907+097	–	19.3[8]	17.8[8]	–
XTE J1716-389	steady			circumbinary disc (like SS433)?

* OD01, [1] van der Meer et al. (2007), [2] Shaposhnikov & Titarchuk (2007), [3] Iorio (2008), [4] Paczynski (1983), [5] Val Baker et al. (2005), [6] Kubota et al. (2010), [7] Reig et al. (1996), [8] Cox et al. (2005)

Table 6.4: Characterization of P_{sup} behaviour in LMXBs

Source	**Behaviour**	q	$r_b/10^6$	**Mechanism**
Cyg X-2	chaotic	0.35[1]	7.0[1]	mode 1+*
EXO 0748-676	varies steadily	0.11-0.28[2]		low $q/\Delta\dot{M}$
GRS 1747-312	varies steadily			$\Delta\dot{M}$
GX 339-4	varies steadily	0.14[3]	0.82[3]	low q/intermediate*
GX 354-0	chaotic			likely low q
Her X-1	steady	1.56*	3.1*	mode 0-1*
IGR J17098-3628	varies steadily			likely low $q/\Delta\dot{M}$
KS 1731-260	varies steadily			low q?/$\Delta\dot{M}$
LMC X-2	optical only	0.14[4]		low q
MS 1603.6+2600	optical only			likely low q
Sco X-1	chaotic	0.3[5]	1.47[5]	low q/intermediate*
X1636-536	varies steadily	0.3[6]	0.5[6]	low $q/\Delta\dot{M}$
X1730-333	varies steadily			$\Delta\dot{M}$
X1820-303	steady	0.06[7]	0.06[7],[8]	low q/triple
X1916-053	varies steadily	0.05[9]	0.17[9]	low $q/\Delta\dot{M}$
X1957+115	varies erratically	[0.7]*	[0.4]*	$\Delta\dot{M}$

* OD01, [1] Casares et al. (2010), [2] Muñoz-Darias et al. (2009), [3] Muñoz-Darias et al. (2008), [4] Cornelisse et al. (2007b), [5] Steeghs & Casares (2002), [6] Casares et al. (2006), [7] Wang & Chakrabarty (2010), [8] Güver et al. (2010), [9] Hu et al. (2008)

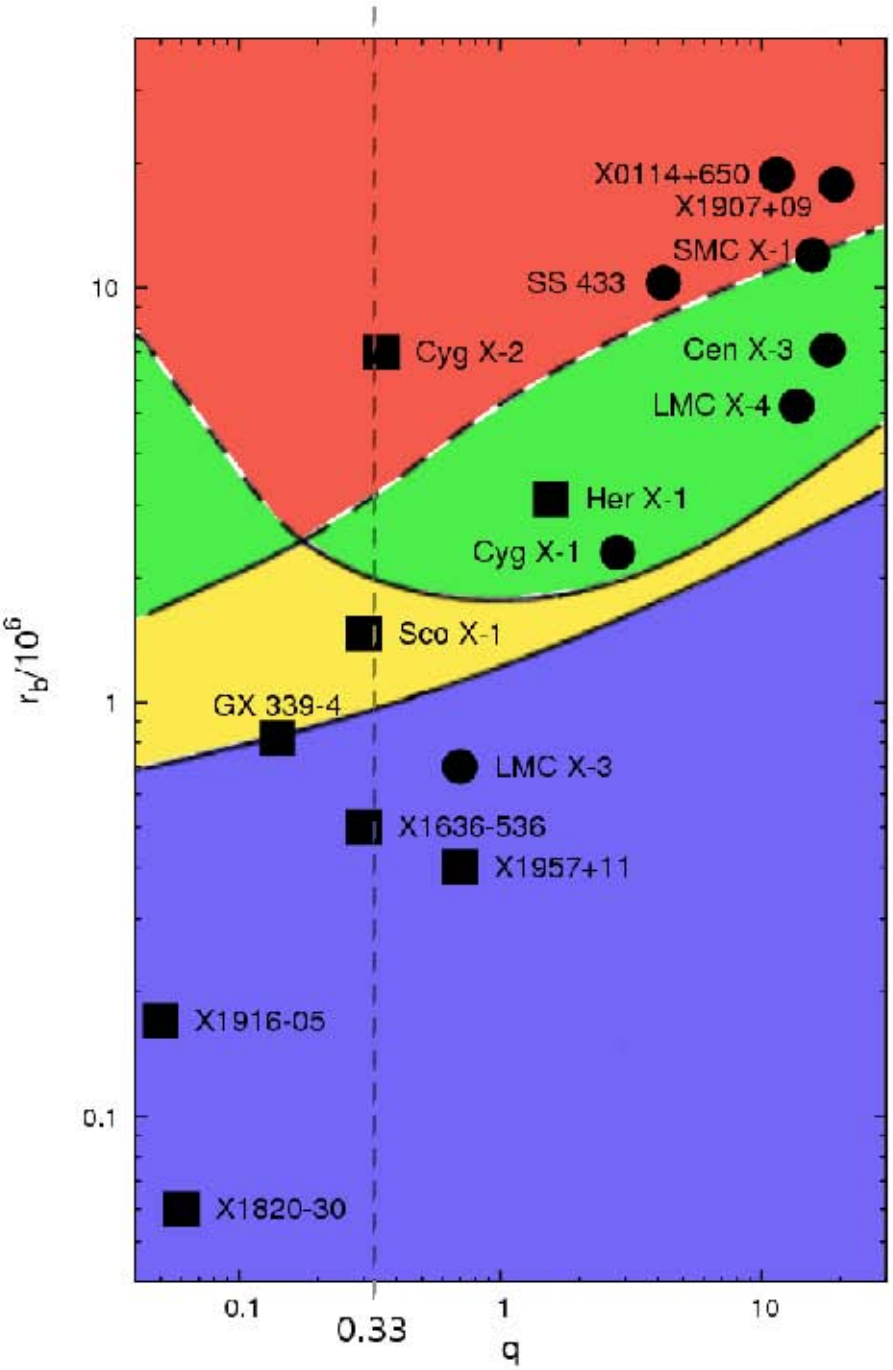

Figure 6.27: The updated diagram of accretion disc stability to radiation-driven warping in XRBs, as functions of q and r_b (in units of $\left[\frac{GM_1}{c^2}\right]$), adapted from OD01 to include only XRBs with known P_{sup}. Squares indicate LMXBs and circles HMXBs. XRBs in the red zone are expected to experience chaotic/unstable warping, but in the green zone stable warps are expected. In the yellow zone discs are expected to alternate between being warped and not being warped. XRBs in the blue zone are not expected to develop warps, but those to the left of the vertical dashed line ($q \sim 0.33$ boundary) are susceptible to tidal disc precession (Whitehurst & King 1991, Murray et al. 2000).

Chapter 7

Very Long-term Behaviour

The lightcurves of several significantly detected sources (included in Appendix B) display large-amplitude, very long-term ($\sim$ several years to decades) quasi-periodic modulations. They are: GX 3+1, GX 9+1, GX 9+9, GX 354-0, 4U 1636-536, 4U 1708-40, 4U 1735-444, 4U 1746-37 and Ser X-1. These are all LMXBs that were classified as Atoll sources in Liu et al. (2007), with the exception of 4U 1708-40. In contrast, classified Z sources show very little variation on these time-scales. Subsequently, a mechanism which might explain the origin of these very long time-scales and the contrast between the long-term behaviour of Atoll and Z sources, was proposed in Kotze & Charles (2010). It covered a $\sim$ 13-year baseline, while the results presented here were updated to include the $\sim$ 15-year RXTE ASM observational baseline. Durant et al. (2010) independently, but virtually coincidentally, reported similar time-scales in the RXTE ASM data of the 16 brightest persistent LMXBs.

7.1 Source Selection

The full RXTE ASM sum-band one-day-average lightcurves of all 45 significantly detected LMXBs were considered. Transients were excluded, as it was only their outburst(s) that resulted in their detection above the 3σ level. Since the very long-term variations in quasi-persistent transients are the result of prolonged high and low states, they were also excluded. 4U 1705-44 is completely dominated by high-amplitude quasi-periodic variations < 2 years (Figure C.14), complicating the detection of a longer term modulation. 4U 1820-30 is likely a triple system (Chou & Grindlay 2001), in which the effects of the third body would lead to $\dot{M}$ variations. Cir X-1 was excluded, since its highly eccentric orbit (Murdin et al. 1980) will introduce large phase-dependent changes in the donor's Roche lobe. The Liu et al. (2007) classifications of the remaining sources were extracted and added in square brackets on their plots. Explanation of their abbreviations have been included as a footnote in Table 7.1. The subsequent analysis focused on the Z and Atoll sources, since they appear to represent the two extremes in the very long-term behaviour of LMXBs. All excluded sources are listed in Table 7.1, together with the reason for their exclusion from further analysis.

Table 7.1: Sources excluded from very long-term analysis

Reason for exclusion	**Source names**
Transients	Aql X-1, GROJ 1655-40, GX 339-4, H 1743-322, 4U 1543-47, 4U 1608-52, 4U 1630-47, SWIFTJ 1753-0127, XTEJ 1550-564, XTEJ 1701-462, XTEJ 1859+226
Quasi-persistent transients	4U 1636-536, KS 1731-260
Long-term dominated	4U 1705-44
Triple system	4U 1820-30
Highly eccentric	Cir X-1
Not Atoll or Z sources	4U 1254-69 [B,D,(SB)], 4U 1556-60, 4U 1624-49 [D], Her X-1 [P,D,E], 4U 1708-40 [B], 4U 1822-000, 2A 1822-371 [P,E], GS 1826-238 [T,B], GRS 1915+105 [T,D,M,R], 4U 1957+11 [U]

[A] Atoll, [B] X-ray burst, [D] dipping source, [E] eclipsing or partially eclipsing source, [G] globular-cluster, [M] microquasar, [P] X-ray pulsar, [R] radio loud X-ray binary, [T] transient, [U] ultra-soft X-ray spectrum, [Z] Z-type, [(SB)] Super-burster

7.2 Variability Analysis

ASM dwell-by-dwell data were binned into 10-day bins using the prescribed filters, as discussed in Chapter 5. Since the long-term modulations displayed in these lightcurves have time-scales that exceed or are comparable to the observational baseline, the usual period analysis tools (such as power spectra) are not as useful as they would normally be. In order to obtain estimates for the time-scale and size of these long-term variations, single sine-waves that minimize the reduced χ^2_ν were fitted to all the sources. For GX 9+9 a linear term was added, consistent with Harris et al. (2009) who noted the presence of a steadily climbing, approximately sinusoidal modulation of ~ 1500 days. The F-statistic was calculated for two models: a constant fit and a single sine-wave fit to the data. For GX 9+9, the simpler model considered was a linear variation with time.

7.3 Results

The results of the fits for the Atoll sources displaying the most significant long-term modulations are contained in Table 7.2 and their 10-day binned lightcurves in Figure 7.1. The results for the remaining Atoll sources are included in Table 7.3 and Figure 7.2. Although the lightcurves of the Z sources appear remarkably steady over the long term, they can also be fitted with single sine-waves, but with much lower amplitudes. The results of their fits are contained in Table 7.4 and Figure 7.3. No significant deviations from the previous analysis by Kotze & Charles (2010) occurred, except for GX 9+9. The latter shows a deviation from its previous trend, which now implies the presence of a very long-term variation with a larger amplitude, in addition to the ~ 1500 days modulation.

The F-statistic values are included in the three aforementioned tables. F-values > 1 were obtained throughout, indicating that the more complex functions are highly significant

(> 99% confidence level). The F-values are highest in the Atoll sources with the largest amplitude modulations. However, even the lowest F-values determined are still highly significant, indicating that all the sources considered here (except GX 9+9) were better fitted with a single sine-wave (plus linear term) than with a constant value (straight line).

Uncertainties in the values obtained are included in the tables in parentheses and represent 1σ errors on the fits. The errors for binned data are extremely small in comparison to the larger flux variations and must be inflated to yield more sensible errors on the sine-wave parameters. Consequently, the flux errors for binned data were adjusted by inflation factors, to obtain fits for which $\chi^2_\nu \sim 1$. The largest factors applied were: 43 for Cyg X-2 and 33 for Sco X-1. The factors applied to the rest of the sources ranged from $1 - 15$, which are comparable to the factor of 3 required for a constant fit to the Crab.

Table 7.2: Fitted properties of the significantly modulating Atoll sources

Source	**Average Flux** [counts/s]	**Amplitude** [% of Flux]	**Period** [years]	**F-statistic**	P_{orb} * [hours]
GX 9+9	19.2(1)	9(2)	4.06(3)	139	4.2
GX 354-0	6.7(2)	34(9)	8.1(2)	50	
4U 1735-444	14.42(8)	30(2)	10.0(1)	429	4.65
GX 3+1	21.3(3)	39(2)	5.70(6)	129	
4U 1746-37	2.47(8)	31(5)	12(1)	25	5.16
GX 9+1	39.0(1)	10.4(4)	10.3(1)	202	
Ser X-1	15.85(8)	11.0(7)	7.2(1)	91	

Table 7.3: Fitted properties of the remaining Atoll sources

Source	**Average Flux** [counts/s]	**Amplitude** [% of Flux]	**Period** [years]	**F-statistic**	P_{orb} * [hours]
4U 0614+091	3.00(6)	18(2)	12(1)	29	
4U 1702-429	3.44(7)	20(3)	5.8(2)	17	
4U 1724-307	2.2(2)	29(9)	6.8(7)	3	
GX 13+1	22.9(8)	1.0(5)	7(1)	2	577.6

Table 7.4: Fitted properties of the Z sources

Source	**Average Flux** [counts/s]	**Amplitude** [% of Flux]	**Period** [years]	**F-statistic**	P_{orb} * [hours]
LMC X-2	1.49(1)	9(2)	8.8(4)	16	8.16
Sco X-1	903(3)	3.6(6)	10.8(6)	27	18.9
GX 340+0	30.7(2)	6.2(8)	15(1)	23	
GX 349+2	51.4(2)	2.9(6)	13(1)	8	22.5
GX 5-1	72.6(3)	2.5(6)	13(1)	8	
GX 17+2	45.9(1)	1.2(4)	6.3(5)	4	
Cyg X-2	37.0(3)	3(1)	4.7(4)	2	236.2

* Liu et al. (2007)

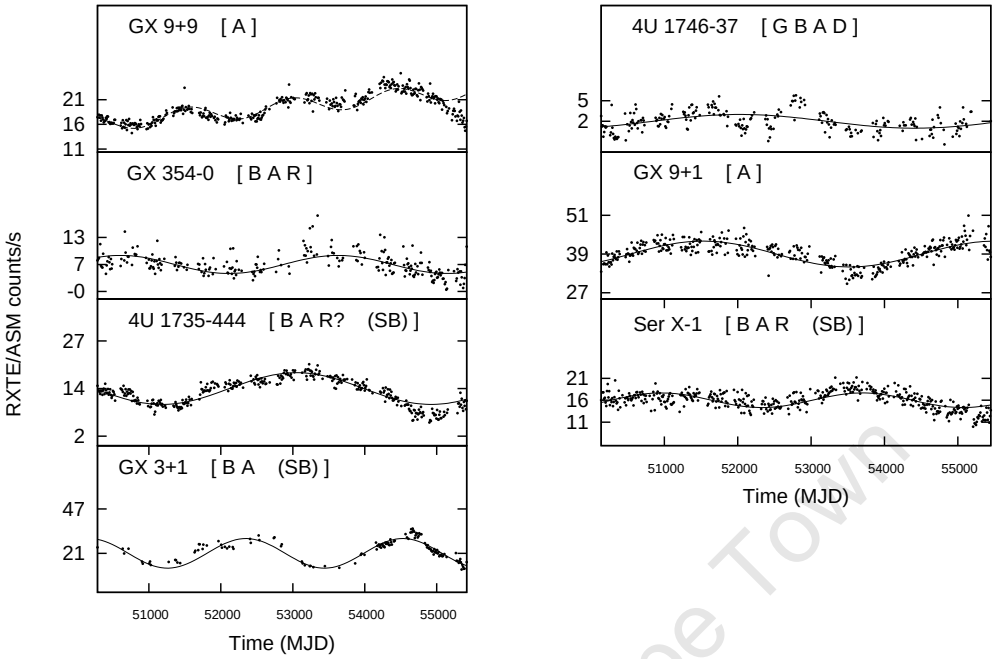

Figure 7.1: Significantly modulating Atoll sources: 10-day-binned RXTE ASM lightcurves.

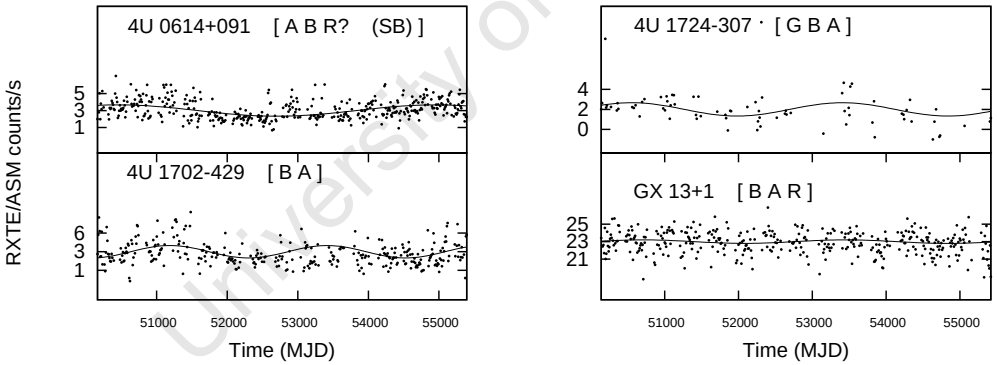

Figure 7.2: Remaining Atoll sources: 10-day-binned RXTE ASM lightcurves

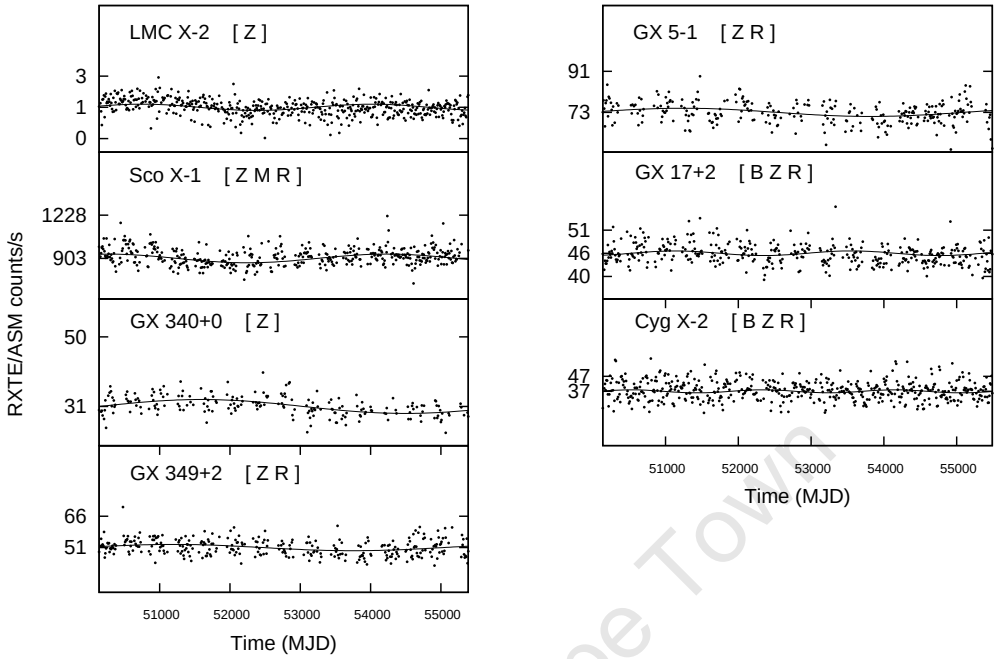

Figure 7.3: Z sources: 10-day-binned RXTE ASM lightcurves.

7.4 Discussion

The time-scales for the modulations based on fitted sine-waves are $\sim 5-15$ years, for both Atoll and Z sources. However, the size of the modulations are of greater interest. Flux modulations of $\sim 10-30\%$ of the average flux values are present in the Atoll sources, with the exception of the super-burster GX 3+1 ($> 30\%$) and the burster GX 13+1 ($< 5\%$). In contrast, flux modulations are $< 10\%$ for the Z sources, with the brighter Z sources having amplitudes $< 5\%$.

The results therefore show that Atoll sources have larger amplitudes in the very long-term time-scale modulations than Z sources. This trend is apparent in a plot of the amplitude and average flux of all the sources (Figure 7.4). The only exception is GX 13+1, which is classified as an Atoll source, but shares certain properties with Z sources (Liu et al. 2007). Indeed, the amplitude for its very long-term modulation agrees with those found in the Z sources, rather than with those obtained for the Atoll sources.

Both Atoll and Z sources contain NSs, but Z sources have fluxes that are $\sim 0.5-1 L_{Edd}$, whereas Atoll sources and bursters have fluxes $\sim 0.01-0.5 L_{Edd}$ (Lewin & van der Klis 2006). Once at the Eddington limit, Z sources are therefore unlikely to show any X-ray flux modulation due to additional changes in the mass-transfer rate ($\dot{M}$). However, Atoll sources could be expected to modulate their flux in response to overall changes in $\dot{M}$. The trend in Figure 7.4 may therefore result directly from the response of Atoll and Z sources to large long-term variations in $\dot{M}$.

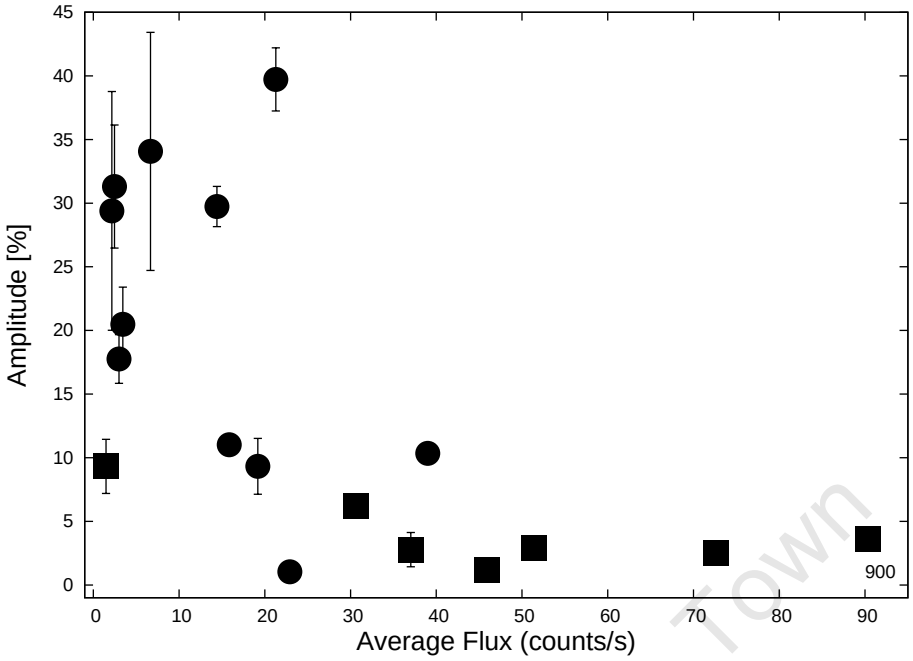

Figure 7.4: Amplitude of long-term modulations as a percentage of Average Flux for Atoll (circles) and Z (squares) sources.

All the Atoll sources have shorter orbital periods and larger amplitude modulations than Z sources (with the exception of the Atoll source with Z source properties). Other than that, there is no clear evidence for a relationship between the amplitudes and orbital periods.

7.4.1 Solar-cycle Type Time-scales

These very long-term, high-amplitude modulations appear to be approximately sinusoidal on the order of decades, while previously reported super-orbital periods were non-sinusoidal and <1 year. Alternative mechanisms were therefore considered than those that are likely to be responsible for shorter time-scale super-orbital periods.

Baliunas & Vaughan (1985) detected long-term variability changes in the surface activity of stars (such as starspot activity) on time-scales similar to the $\sim$ 11 year magnetic-activity cycle of our Sun. Applegate & Patterson (1987) and Warner (1988) explained the presence of quasi-periodic variations on those time-scales in CVs, as a consequence of the modulation in the $\dot{M}$ due to such magnetic-activity cycles in their donors. Applegate (1992) later suggested that magnetically active donors become more oblate as their outer layers are spun up, due to changes in angular momentum distribution brought about by their magnetic activity. As a result, the volume of the Roche lobe changes during the magnetic cycle, while the volume of the donor remains unchanged. The donor's magnetic-activity cycle therefore governs the Roche-lobe volume and the structure of the donor, which varies in oblateness as the cycle progresses. The latter will modulate the amount by which the donor overfills the Roche lobe and therefore the $\dot{M}$ will also vary on the magnetic-activity time-scale. Richman et al.

(1994) presented observational evidence for these very long-term variations in CVs.

Aspects relating to accretion in astrophysics, particularly in accretion-powered binaries, were reviewed in Frank et al. (2002). CVs are very similar to LMXBs, but contain WDs, while LMXBs have either NSs or BHs as their compact objects. Flux from LMXBs is predominantly in X-rays which originate from the inner accretion disc and the NS surface (if applicable). In contrast, the flux from CVs is predominantly in the optical and originates from the entire accretion disc, the hot spot(s) on the WD surface and the bright spot where the mass-transfer stream impacts the accretion disc. The donor stars in short-period LMXBs and CVs are tidally locked and therefore rotate at the orbital period (P_{orb}) of the binary system. Schrijver & Zwaan (1992) suggested that this rapid rotation is expected to generate a much stronger $\overrightarrow{B}$. Considering the similarities between LMXBs and CVs, it is not unreasonable to expect similar very long-term modulations in LMXBs, for the same reason as proposed for CVs.

The current X-ray observational baseline for LMXBs is too short to cover multiple cycles and establish the stability of these variations. Since most of the sources were only marginally detected in previous missions, the RXTE ASM baseline could not be extended with additional archival data. Richman et al. (1994) proposed that magnetic-activity cycles in the donors was the mechanism responsible for very long-term variations in CVs. Their approach is used here to determine if the latter may also be applicable to LMXBs. They calculated the $\dot{M}$ variation ($\frac{\Delta \dot{M}}{\dot{M}}$), associated with the observed P_{orb} variation ($\frac{\Delta P}{P}$), thought to be produced by this mechanism in CVs. They proposed that changes in the rotation of a thin outer shell (mass M_s) of the donor (mass M_2), rotating with angular velocity (Ω), will affect the orbital period according to Equation 7.1. M_1 is the mass of the compact object and the mass ratio $q = \frac{M_2}{M_1}$.

$$\frac{\Delta P}{P} = -0.04 \left(\frac{q}{1+q} \right)^{2/3} \frac{M_s}{M_2} \frac{\Delta \Omega}{\Omega} \tag{7.1}$$

They noted that the Applegate (1992) variable differential rotation rates follow the Hall (1991) differential rotation-orbital period relation, and consequently applied it to the orbital periods for CVs to obtain $\frac{\Delta \Omega}{\Omega} \sim 0.0015$. Furthermore they assumed that $\frac{M_s}{M_2} \sim 0.1$ and calculated a $\frac{\Delta \dot{M}}{\dot{M}}$ consistent with the observed long-term quasi-periodic flux variations in CVs. However, they considered the observed $\frac{\Delta P}{P}$ to be the best evidence for long-term modulations, with a preferred time-scale of decades ($5 - 30$ years), reminiscent of solar-like magnetic cycles determined by Warner (1988).

Equation 7.1 is applied to GX 9+9, an Atoll source with $P_{orb} = 4.1958 \pm 0.0005$ hours (Kong et al. 2006) and $q = 0.25$ (Cornelisse et al. 2007a). This gives $\frac{\Delta P}{P} = -2 \times 10^{-6}$. However, Cornelisse et al. (2007a) found no significant change in P_{orb} in RXTE ASM data over a ~ 11 year baseline. Considering the result for $\frac{\Delta P}{P}$, it is not expected that a change in P_{orb} would be detected in the RXTE ASM dwell-by-dwell data, since the ΔP implied is smaller than the error in P_{orb}.

Richman et al. (1994) determined that such a ΔP will result in a corresponding change in the size of the donor's Roche lobe (R_2) and therefore $\dot{M}$ will be modulated according to Equation 7.2, where H is the photospheric scale height of a main sequence donor.

$$\frac{\Delta \dot{M}}{\dot{M}} = -\frac{1}{3}\left(\frac{a}{R_2}\right)^2 \frac{R_2}{H}\frac{M_2}{M_s}\frac{\Delta P}{P} \tag{7.2}$$

Assuming the standard Paczyński (1971) relation for the size of the donor's Roche lobe, yields $\frac{R_2}{a} = 0.27$. If the donor in GX 9+9 follows the CV secondary relation $\frac{R}{R_\odot} = \left(\frac{M}{M_\odot}\right)^{0.88}$, then $\frac{R_2}{H} = 3200$ (Richman et al. 1994). By replacing Equation 7.1 in Equation 7.2 and substituting the quantities for $\frac{\Delta\Omega}{\Omega}$, $\frac{R_2}{H}$ and $\frac{R_2}{a}$, the equation is simplified to:

$$\frac{\Delta \dot{M}}{\dot{M}} = \frac{1}{3}\left(\frac{1}{0.27}\right)^2 (3200)(0.04)\left(\frac{q}{1+q}\right)^{2/3}(0.0015) = 0.8779\left(\frac{q}{1+q}\right)^{2/3} \tag{7.3}$$

Therefore the resultant $\dot{M}$ variation $\frac{\Delta \dot{M}}{\dot{M}} = 0.3$ for GX 9+9, implying a maximum flux modulation or amplitude of $\sim$ 30%. The amplitude determined from the fit of a sine-wave with linear term was $\sim$ 9 % for a time-scale of $\sim$ 4 years, with F-statistic of 139. However, the previous trend in GX 9+9 appears to have been broken in the last 2 years of the observational baseline and a much longer term variation ($\sim$ 19 years) with considerably larger amplitude ($\sim$ 15%) can be fitted with F-statistic of $\sim$ 4. Though the latter has a far lower F-statistic, it is still significant and its amplitude is also $< 30\%$.

The maximum amplitude is therefore determined by q, the mass-ratio. The amplitudes for the sources considered are all $\lesssim 30\%$, except for super-burster GX 3+1 where it is 39%. That implies $q < 0.25$ for all the sources considered here and $q \sim 0.42$ for GX 3+1, which are very reasonable q values for LMXBs. Of course, for $q < 0.33$ tidally induced disc precession is likely (Whitehurst & King 1991), although the time-scales associated with the resulting quasi-periodic modulations are normally much shorter than those considered here.

It is therefore plausible that these very long-term modulations observed in the RXTE ASM lightcurves of LMXBs might originate from magnetic-activity cycles in the donor. These results are in agreement with the investigation and observational evidence presented by Richman et al. (1994) for CVs, which supported the predictions of such modulations by Applegate & Patterson (1987) and Warner (1988).

Chapter 8

Conclusion

Quasi-periodic variations on super-orbital time-scales have been the main theme of this work, using RXTE ASM data spanning $\sim$ 15 years to study the long-term behaviour of XRBs. Major results from this work were presented in Chapters 6 and 7. The conclusions drawn from those results are included in Sections 8.1 and 8.2 hereafter. Conclusions from the results in Chapter 5, which have not already been discussed under either of the aforementioned sections, are discussed in Section 8.3.

8.1 Long-term Behaviour of Known P_{sup}

Long-term behaviour in this context refers to modulations on time-scales of hundreds of days. The conclusions from the results presented in Chapter 6, published in Kotze & Charles (2012), are included herein.

8.1.1 Warped/Tilted Accretion Discs

OD01 (Ogilvie & Dubus 2001) predicted that only a small fraction of X-ray binaries should display steady P_{sup} associated with stable, steadily precessing, radiation-driven warped accretion discs. Furthermore, they suggested that it would be even less common in LMXBs, since only those with $P_{orb} > 1$ day are expected to produce warps. However, 16 of the 25 sources contained herein are LMXBs. With 114 HMXBs and 187 LMXBs contained in the catalogues of Liu et al. (2006) and Liu et al. (2007), it implies that P_{sup} have been detected in roughly equal fractions of LMXBs and HMXBs.

Recent Smooth Particle Hydrodynamics (SPH) simulations by Foulkes et al. (2010) on SMC X-1, Cyg X-1, Cyg X-2, X1916-053, LMC X-3, Her X-1, SS433 and a generalized LMXB, produced warps over all orbital periods considered. Contrary to OD01, they predict that P_{sup} should be very common in LMXBs, suggesting that the analytical OD01 approach is necessarily approximate and that the SPH simulations should incorporate the complexities involved in an irradiated accretion disc more accurately.

It is important to remember that the OD01 predictions for stability of accretion discs against radiation-driven warping are for specific α and ϵ values and that the instability criteria depend largely on α and to a slightly lesser extent on ϵ, making the predictions approximate. Different α and ϵ values would yield very different predictions and these values are expected to differ from system to system. Other mechanisms, such as wind-driven tilting and magnetic warping, may also produce warped/tilted accretions discs.

Furthermore, warps need to be sustained for prolonged intervals to produce steady P_{sup} (as in Her X-1 & LMC X-4). Lodato & Price (2010) used SPH simulations to consider the diffuse propagation of warps in viscous thin discs, where they determined the diffusion coefficient to be $\sim 1/\alpha$ (for small amplitude warps and $\alpha < 0.1$), in general finding that higher viscosity leads to slower diffusion and lower viscosity to more rapid diffusion.

Of the 25 X-ray binaries considered here, 15 could be directly compared to their OD01 predictions. The results were generally consistent with their predictions, which have been updated with the most recent estimates for their binary system parameters (Figure 6.27).

Firstly, our results support the OD01 prediction that LMXBs are unlikely to produce stable precessing warped discs, since they are mostly located below the $r_{add} = r_o$ line and their accretion discs are therefore too small to become unstable against warping in the expected radiation field. Her X-1 remains the only LMXB to have a steady P_{sup} that can be associated with its accretion disc, since X1820-303 is likely a triple system. Her X-1 is not a typical LMXB, since it has higher donor mass than most other LMXBs and therefore it might share some HMXB properties or be an intermediate-mass X-ray binary (IMXB), described in Podsiadlowski et al. (2003). One of these properties appears to be its ability to produce a warped precessing disc, with its associated steady P_{sup}.

Secondly, OD01 predictions implied that HMXBs are more likely to produce stable warped precessing discs, although eccentric orbits would suppress stable radiation-driven warping. Our DPS analysis has shown that not only LMC X-4 displays a stable super-orbital period, but also Cyg X-1, SS433, X0114+650 & XTE J1716-389. Only the locations of the latter two sources on Figure 6.27 are unknown. Cyg X-1, LMC X-4 & SS433 are located in the OD01 instability zone and therefore expected to have warped precessing accretion discs that produce steady P_{sup} while they are persistent. However, the steady P_{sup} in SS433 and X0114+650 may have other origins, since the former experiences relativistic jet precession and the latter may be a BeX.

Thirdly, we included 5 quasi-persistent sources for which P_{sup} have been published. Four of these are LMXBs (X1636-536, KS 1731-260, EXO 0748-676 & IGR J17098-3628) and XTE J1716-389 is the only HMXB. As OD01 predicted, these quasi-persistent sources produce P_{sup} during their persistent (high) states, with the exception of X1636-536, where stronger detections occurred during the lower state. Its low state is certainly not an *off* state where the flux goes to zero, as seen in the other four sources. It also displayed an anti-correlation between hard and soft X-ray components (Shih et al. 2005). Furthermore, only the HMXBs produced a relatively steady P_{sup} while the LMXBs all produced multiple periodic signals that were either evolving or unstable/chaotic.

Finally, OD01 predicted that Sco X-1 would be marginally unstable or stable and show variability, since it is located in the intermediate instability zone. Our results show long-term behaviour that may be interpreted in this manner.

Clarkson et al. (2003a) suggested that competing radiation-driven warping modes may cause variations in the warp itself, resulting in the steady evolution/variation of the P_{sup} in SMC X-1, consistent with its OD01 prediction. Her X-1, with $P_{sup} \sim 33 - 37$ days (Leahy & Igna 2010) might be subject to the same effect, to a lesser extent.

8.1.2 Tidal Disc Precession

Tidally induced disc precession (Whitehurst & King 1991) may produce quasi-periodic P_{sup} in many LMXBs, which are more likely to have $q < 0.33$. Tidal disc precession may account for the observed P_{sup} in several LMXBs, for which warped discs were deemed unlikely to be produced. In the tidal disc precession scenario, the shape of the outer edge of the accretion disc is affected and its precession causes a modulation of the flux.

8.1.3 Obscuration of the X-ray Source

Warps and tilts affect the inner regions of the accretion disc, which are closer to the intense radiation source responsible for irradiating the disc. Clarkson et al. (2003a) suggested that varying absorption of X-rays from the central source by a warped inner disc or the variation in the uncovered X-ray emitting area, occurs as a result of variations in the accretion disc structure. Multi-wavelength observations may help to determine if the X-ray flux is modulated by varying obscuration of the central source, since longer wavelengths (such as UV and optical) are absorbed more readily than shorter wavelengths (X-rays).

8.1.4 Complex $\dot{M}$ Variations

Many of the P_{sup} already detected may be the result of the modulation of the $\dot{M}$, rather than only being associated with warped precessing accretion discs. Many may therefore also indicate the time-scale on which transitions occur between high and low flux states. The HMXBs Cen X-3, Cyg X-1 & LMC X-3 and the LMXB X1957+115 have very similar lightcurves that clearly show these transitions on varying time-scales. For Cyg X-1 there is also evidence for a precessing warped accretion disc (Zdziarski et al. 2011). Cen X-3 shows evidence for the presence of a variable warp (Iping & Petterson 1990, Raichur & Paul 2008).

The recurrence time-scale of transient outbursts also manifest as P_{sup}, as observed in transients GRS 1747-312 and X1730-333. Although their lightcurves show some similarity to Her X-1, their P_{sup} are not steady and appear to be evolving or varying.

Clarkson et al. (2003a) suggested that warps may also manifest themselves as $\dot{M}$ modulations. Intense irradiation of the accretion disc, by the central X-ray source, affects its temperature and viscosity (van Paradijs 1996, King & Ritter 1998). Dubus et al. (1999) showed that irradiation extends asymmetrically beyond the inner disc in warped discs, while the effect is reduced by self-screening in flat discs. Irradiation in warped discs can therefore

heat the disc significantly (Hynes et al. 2002). Consequently, $\dot{M}$ may be modulated due to the variation of the accretion rate onto the compact object or modulation of the mass flow rate through the disc (Dubus 2003).

The majority of the P_{sup} are clearly not steady, with many of those showing unsteady evolution of multiple periodic signals while they are persistent. Such behaviour may also be associated with a variety of time-scales produced by $\dot{M}$ variations.

8.1.5 Time-dependent Period Analysis

The DPS results emphasize the importance of using a time-dependent periodic analysis when investigating the long-term quasi-periodic behaviour, that have been associated with accretion disc properties such as precession/warping/tilting and $\dot{M}$ variations. Traditional period analysis could miss sources with intermittent periodic signals, since their overall periodograms may show no significant peaks above the noise. Moreover, all the variations and complex behaviour of quasi-periodic signals may completely go unnoticed.

The complex behaviour observed in the majority of the sources, may rather be attributed to a combination of the proposed mechanisms. Future (very difficult) simulations should ideally include radiation-driven warping, tidal precession and their effects on $\dot{M}$, in order to reproduce the complex observed long-term behaviour which has been presented here.

8.2 Very Long-term Behaviour in LMXBs

Very long-term behaviour in this context refers to modulations on time-scales of thousands of days, most notably observed in the Atoll sources: GX 3+1, GX 9+1, GX 9+9, GX 354-0, 4U 1636-536, 4U 1735-444, 4U 1746-37 and Ser X-1. The conclusions of the results presented in Chapter 7, published in Kotze & Charles (2010), are included here.

$\dot{M}$ variations should translate into quasi-periodic modulations of the X-ray flux for sources in which the additional material can be accreted onto the NS without violating the Eddington limit, such as Atoll sources. However, in Z sources very little (if any) of the additional material will be accreted and much lower amplitude (if any) long-term X-ray flux modulations are expected as a result of the magnetic-activity cycle of the donor. Figure 7.4 very clearly shows that this trend holds for Atoll and Z sources, while bearing in mind that GX 13+1 is an Atoll source which is known to display Z source properties.

Variation of the $\dot{M}$ due to the magnetic-activity cycle of the donor was proposed by Applegate & Patterson (1987) and Warner (1988) for accretion-powered binaries, particularly CVs. The amplitudes of the very long-term modulations observed in LMXBs are in agreement with their predicted maxima for such a scenario, using the approach that Richman et al. (1994) applied to CVs to present observational evidence of these $\dot{M}$ variations. Therefore, the RXTE ASM archival data may provide the first evidence for very long-term quasi-periodic modulations of the X-ray flux as a result of the modulation in the $\dot{M}$ due to a solar-type magnetic-activity cycle in the low-mass donor.

8.3 The RXTE ASM

RXTE ASM data archives clearly contain a wealth of information for XRBs. Its energy range is particularly suited to their study, since the vast majority of significantly detected ASM sources (contained in Appendix B) are XRBs. Long observational baselines are clearly required to probe the very interesting long-term behaviour of XRBs (Sections 8.1 & 8.2). While archival data are available for a large number of previous X-ray missions, many sources that were significantly detected by RXTE ASM, were only marginally detected by other missions and their datasets can therefore not be extended in a systematic way. Future missions plan to extend the ~ 15 year RXTE ASM datasets, but it is particularly unfortunate that RXTE shut down at the end of 2011, before a replacement mission was launched.

Nevertheless, the RXTE ASM archival data represent the most comprehensive long-term X-ray lightcurves of the 585 sources included in its catalogue. As such, it contains a wealth of information on all manner of X-ray sources and for this particular reason, the SIMBAD types and ASM properties of all its sources were included in Appendix A, to serve as a reference source for future work. Their lightcurves, plotted in the same format used for Appendix B, have been made available online*.

During the course of this work, the DPS analysis was actually undertaken for all 585 sources in the RXTE ASM data archive. Those results have been made available online† in the same format used for Appendix C, over period ranges $2-20$ days and $20-1000$ days respectively. It includes results in addition to those presented in this work, which may be included in future publications.

8.4 The Future of X-ray Monitoring

In order to build on the success of the RXTE ASM, future X-ray all-sky monitors should ideally cover the same areas (Galactic bulge and disc, SMC and LMC) with similar sensitivity instruments ($1.5-12$ keV) at comparable sampling rates ($5-10\times$ per day). The mission lifetimes should preferably also be $\sim$ decade or more.

The broad spectral band Indian astronomy satellite ASTROSAT is intended to include a Scanning Sky Monitor (SSM), described in Seetha et al. (2006). It is similar in design to the RXTE ASM (using position-sensitive proportional counters) and aims to detect and locate X-ray transients in the $2-10$ keV range. The multi-wavelength on-board instruments may then be used for follow-up observations. The intention is to monitor the same areas as RXTE ASM, since they represent the largest populations of observable X-ray binaries.

The lobster-eye design proposed for the X-ray all-sky monitor on board the International Space Station (Lobster-ISS), represents an order-of-magnitude improvement in sensitivity in the $0.1-3$ keV range (Black et al. 2003). It includes micro-patterned imaging proportional counters, able to map the entire sky every ~ 90 minutes through its lobster-eye optics.

*http://www.saao.ac.za/~marissa/LC
†http://www.saao.ac.za/~marissa/DPS

Charles et al. (2010) reviewed the 7 types of super-orbital modulations (Chapter 4) observed in interacting binaries, of which 6 were included in Charles et al. (2008) and to which the 7th was added by Kotze & Charles (2010). These modulations were summarized in a table, which is included here as Table 8.1. The longer time-scales can only be probed by analysing monitoring data that achieved sufficient coverage over long observational baselines. The OGLE & MACHO optical databases and the RXTE ASM X-ray database have proven to be invaluable resources in the study of such time-scales (τ) in XRBs.

Table 8.1: Long-term modulations in X-ray binaries (Charles et al. 2010)

	Type	Examples	P_{sup} (days)	Physical origin
1	Tilted precessing disc	Her X-1, LMC X-4, SS433	30-200	Mode 0 (OD01)
2	Warped precessing disc	SMC X-1	1500	Mode 0-1 (OD01)
3	Multi-periods	Cyg X-2	50-100	Mode 1+ (OD01)
4	X-ray state changes	LMC X-3, GX 339-4 X1636-536, KS 1731-26	40-400	Changes in $\dot{M}$ (viscous τ in outer disc)
5	Superhumps	SU UMas, SXTs, UCBs	5-50	Donor-induced tides cause disc precession
6	Donor activity cycle (early-type)	BeX (A0538-66)	300-3000	Variations in equatorial disc
7	Donor activity cycle (late-type)	LMXBs (Atoll) Polars	1500-6500	"Solar-cycle" variations in donor modulate P_{orb}

Weak periodic signals in marginally detected sources are amplified by long observational baselines (Chapter 5), allowing for the discovery of new periods (Levine et al. 2011). This work presents a time-dependent period analysis of XRBs with known super-orbital behaviour (Chapter 6), which required sufficient coverage over long observational baselines. It showed that P_{sup} tend to be quasi-periodic or aperiodic and that very few sources appear to have stable super-orbital behaviour, emphasizing the importance of a time-dependent approach in studying them. Very long-term modulations in LMXBs were also identified (Chapter 7). These very long-term P_{sup} themselves and trends in the behaviour of P_{sup} in some sources certainly warrant further investigation. Whatever the future holds for X-ray monitoring, there are ample reasons to extend the coverage that has already been attained.

8.5 Distinguishing between Mechanisms

The DPS analysis has shown some rather characteristic features associated with specific mechanisms that have been independently verified by other methods. It appears that the stable (mode 0) warp presents a steady P_{sup} (e.g. LMC X-4) and the variable (mode 1) warp presents a steadily evolving P_{sup} (e.g. SMC X-1), while chaotic warping (mode 1+) introduces multiple rapidly evolving and/or intermittent features in the DPS (e.g. Cyg X-2) or no features at all (e.g. X1907+097).

Clarkson et al. (2003b) already showed that the features in the DPS extended to dates prior to RXTE's ASM data by including CGRO's BATSE data in the DPS they presented for SMC X-1. This thesis sought to investigate known super-orbital behaviour in a completely systematic way using the most comprehensive coverage available from a single mission. Complementary data from other missions/band-passes may be added in future to allow a more detailed analysis of particularly interesting sources (like SMC X-1). However, the DPS alone cannot be used to distinguish the likely mechanism responsible for super-orbital behaviour. A multi-wavelength approach may allow further distinction.

The anti-correlation of hard and soft X-rays on the super-orbital time-scale has been linked to state/accretion-rate changes (Shih et al. 2005). Alternatively, if the X-ray flux is modulated by varying obscuration of the central source by the disc, hard and soft X-rays should be correlated on the super-orbital time-scale and hard X-rays should exhibit smaller flux modulations than soft X-rays. Such correlation/ anti-correlation can be investigated by comparing the lightcurves of the different RXTE ASM energy bands and Swift BAT data over intervals of super-orbital activity, which are clearly distinguishable in the DPS results presented in this thesis. Distinguishing observationally between obscuration by warped inner disc regions and flared/bulged edges of an eccentric disc is more problematic.

If sources are optically bright enough (V<20) compared to the other stars in the field of view, data from OGLE and MACHO archives may be used to search for super-orbital behaviour in the optical lightcurves (but extraction is often hampered by source crowding) of stars situated in the bulge and the Magellanic clouds. Accretion rate modulations result in variations in optical lightcurves that are correlated with those observed at soft X-ray wavelengths (Shih et al. 2011).

X-ray spectra may be investigated for episodes of super-orbital behaviour to determine if there were changes in the source spectra. Apart from identifying X-ray state changes, variations in absorption may also be identified. The absorbing material in a warped inner disc should be significantly hotter than that of a bulge on the edge of an elliptical disc.

Appendix A

Summary of All ASM Sources

Tables A.1-A.13 contain a summary of the average flux analysis of the Rossi X-ray Timing Explorer (RXTE) All Sky Monitor (ASM) sum-band one-day-averages over the entire observational baseline, from 20 February 1996 (MJD 50133) to 12 February 2011 (MJD 55608), listed in ascending RA. The lightcurve data were made available online* by the ASM/RXTE teams at MIT and at the RXTE Science Operations Facility (SOF) and Guest Observer Facility (GOF) at NASA's Goddard Space Flight Center (GSFC).

The averages of the flux and the error therein were determined for each source, using data points for which |flux| > |estimated flux error|. The detection significance was defined for each source as its average flux divided by its average estimated flux error. It was quoted in terms of σ. If the detection significance $> 3\sigma$ and average flux > 0.5 counts s^{-1}, a source was considered significantly detected. Sources which were not significantly detected or contain few data points, were considered marginally detected. Subsequently, sources were assigned to a category according to the following criteria:

- "marginal" if not significantly detected
- "transient" if transient outbursts (> 500% average flux) occurred
- "recurring" if multiple outbursts occurred
- "persistent" if no outbursts occurred

SIMBAD types for all sources were extracted from the SIMBAD website† via url queries where possible, alternatively the Liu et al. (2007) classifications or classifications contained in the Astronomer's Telegrams‡ (Atel) were listed, in which case the number of the Atel is included as a footnote to the table. ASM source names prefixed with 'bl' are all BL Lac-type objects and those containing '.cg.' are clusters of galaxies.Some of the SIMBAD types were abbreviated as follows: high-mass X-ray binary (HMXB), low-mass X-ray binary (LMXB), active galactic nuclei (AGN), supernova remnant (SNR) and cataclysmic variable (CV).

*http://xte.mit.edu/ASMlc.html
†http://simbad.u-strasbg.fr/simbad/
‡http://www.astronomerstelegram.org/

Table A.1: Summary of all RXTE ASM sources (RA: 00-02)

ASM name	**SIMBAD type**	**Average flux(error)** [counts s^{-1}]	**Category**	**Detection significance**
mkn335	Seyfert 1 galaxy	0.2(5)	marginal	0.4σ
ss0019+21	X-ray binary	0.2(5)	marginal	0.4σ
igrj00234+6141	CV	0.2(4)	marginal	0.6σ
psr0021-72j	Pulsar	0.2(5)	marginal	0.3σ
tychosnr	SNR	1.3(3)	persistent	4.2σ
v709cas	DQ Her-type CV	0.1(5)	marginal	0.3σ
igrj00291+5934	LMXB	0.3(4)	marginal	0.7σ
rxj0033.9+6126	X-ray source	0.2(3)	marginal	0.6σ
1es0033+595	BL Lac-type object	0.4(3)	marginal	1.3σ
rxj0037.2+6121	HMXB	0.2(4)	marginal	0.6σ
x0042+327	LMXB	0.1(5)	marginal	0.2σ
mkn348	Seyfert 2 galaxy	0.3(5)	marginal	0.5σ
saxj0051.7-7218	HMXB	0.2(5)	marginal	0.4σ
smcx3	HMXB	0.2(5)	marginal	0.4σ
rxj0052.1-7319	HMXB	0.2(5)	marginal	0.5σ
smcx2	HMXB	0.1(5)	marginal	0.3σ
rxj0054.9-7226	HMXB	0.2(5)	marginal	0.5σ
gammacas	Be star	0.6(3)	marginal	2.2σ
rxj0059.2-7138	HMXB	0.2(5)	marginal	0.4σ
snr0101-72.4	HMXB	0.2(5)	marginal	0.4σ
rxj0103.6-7201	HMXB	0.2(5)	marginal	0.4σ
ncas1995	Nova	0.2(4)	marginal	0.6σ
snr0104-72.3	SNR	0.2(5)	marginal	0.4σ
h0107-750	HMXB	0.1(5)	marginal	0.3σ
xtej0111-733	HMXB	0.2(5)	marginal	0.4σ
smcx1	HMXB	1.7(4)	persistent	4.2σ
x0114+650	HMXB	0.5(3)	marginal	1.7σ
x0115+634	HMXB	1.0(4)	marginal	2.9σ
pks0118-272	BL Lac-type object	0.1(4)	marginal	0.3σ
rxj0121.4-7258	X-ray source	0.1(5)	marginal	0.2σ
hd8357	X-ray binary	0.2(5)	marginal	0.4σ
bl0120+340	BL Lac-type object	0.3(5)	marginal	0.7σ
fairall9	Seyfert 1 galaxy	0.2(4)	marginal	0.5σ
ngc526a	Seyfert 1 galaxy	0.3(4)	marginal	0.7σ
igrj01363+6610	HMXB	0.1(3)	marginal	0.4σ
b3_0133+388	BL Lac-type object	0.2(5)	marginal	0.5σ
x0142+614	Variable star	0.5(3)	marginal	1.6σ
rxj0146.9+6121	HMXB	0.3(4)	marginal	0.9σ
1es0145+318	BL Lac-type object	0.2(5)	marginal	0.4σ
igrj01572-7259	HMXB	0.1(5)	marginal	0.3σ
igrj01583+6713	X-ray binary	0.2(3)	marginal	0.6σ
3egj0204+15	Blazar	0.2(5)	marginal	0.4σ
b0206+5212	Seyfert 1 galaxy	0.3(4)	marginal	0.8σ
rgb0214+517	BL Lac-type object	0.3(4)	marginal	0.7σ
mkn590	Seyfert 1 galaxy	0.3(5)	marginal	0.7σ
pks0219-164	Quasar	0.1(5)	marginal	0.3σ

Table A.2: Summary of all RXTE ASM sources (RA: 02-05)

ASM name	**SIMBAD type**	**Average flux(error)** [counts s^{-1}]	**Category**	**Detection significance**
3c66a	BL Lac-type object	0.3(5)	marginal	0.6σ
bl0224+014	BL Lac-type object	0.2(5)	marginal	0.4σ
1es0229+200	BL Lac-type object	0.2(5)	marginal	0.5σ
ngc985	Seyfert 1 galaxy	0.3(5)	marginal	0.7σ
1es0235+164	BL Lac-type object	0.2(5)	marginal	0.4σ
lsi+61303	HMXB	0.3(3)	marginal	0.9σ
algol	Algol - eclipsing binary	0.7(4)	marginal	1.7σ
he0309-2057	Seyfert 1 galaxy	0.2(5)	marginal	0.4σ
eferi	Nova-like star	0.2(5)	marginal	0.4σ
ngc1275.cg	Seyfert 2 galaxy	2.6(4)	persistent	5.9σ
rgbj0324.7+3410	Seyfert 1 galaxy	0.2(5)	marginal	0.5σ
bl0323+022	BL Lac-type object	0.1(5)	marginal	0.3σ
uxari	Double or multiple star	0.4(5)	marginal	0.8σ
ngc1333	Reflection nebula	0.1(5)	marginal	0.1σ
gkper	CV	0.4(4)	marginal	1.2σ
ngc1365	Seyfert 1 galaxy	0.1(5)	marginal	0.2σ
v0332+53	HMXB	1.5(4)	transient	4.0σ
ngc1386	Seyfert 1 galaxy	0.1(5)	marginal	0.2σ
hr1099	RS CVn-type variable	0.4(5)	marginal	0.9σ
ic348	Open (galactic) cluster	0.2(5)	marginal	0.4σ
1es0347-121	BL Lac-type object	0.2(5)	marginal	0.5σ
xper	HMXB	1.6(4)	persistent	4.2σ
vwhyi	Dwarf Nova	0.2(3)	marginal	0.6σ
hd283447	Double or multiple star	0.2(5)	marginal	0.4σ
bl0414+009	BL Lac-type object	0.2(5)	marginal	0.4σ
sgr0418+5729	Gamma-ray source	0.1(3)	marginal	0.4σ
xtej0421+560	HMXB	0.2(4)	marginal	0.5σ
groj0422+32	LMXB	0.2(5)	marginal	0.4σ
hd283572	Orion-type variable	0.1(5)	marginal	0.3σ
3c120	Seyfert 1 galaxy	0.4(4)	marginal	1.0σ
psrj0437-4715	Pulsar	0.2(4)	marginal	0.6σ
lsv+4417	Emission-line star	0.3(5)	marginal	0.7σ
3egj0442-00	Quasar	0.2(5)	marginal	0.4σ
3c129.cg	Radio galaxy	0.7(4)	marginal	1.8σ
3egj0450+11	Possible quasar	0.2(5)	marginal	0.4σ
swiftj0451.1-6948	Star	0.2(4)	marginal	0.5σ
h0449-55	Star	0.1(4)	marginal	0.3σ
iras04575-7537	Seyfert 2 galaxy	0.2(4)	marginal	0.6σ
igrj05007-7047	HMXB	0.2(4)	marginal	0.5σ
sgr0501+4516	X-ray source	0.2(4)	marginal	0.4σ
3egj0500-02	Quasar	0.2(5)	marginal	0.5σ
v1062tau	Nova	0.3(5)	marginal	0.6σ
rxj0502.9-6626	HMXB	0.2(4)	marginal	0.4σ
ngc1808	Seyfert 2 galaxy	0.2(4)	marginal	0.4σ
bl0502+675	BL Lac-type object	0.3(3)	marginal	1.0σ
s5_0454+844	BL Lac-type object	0.1(3)	marginal	0.5σ

Table A.3: Summary of all RXTE ASM sources (RA: 05-07)

ASM name	**SIMBAD type**	**Average flux(error)** [counts s^{-1}]	**Category**	**Detection significance**
swiftj0513.4-6547	Carbon star	0.1(5)	marginal	0.3σ
rxj0513.9-6951	X-ray binary	0.2(4)	marginal	0.6σ
x0512-401	LMXB	0.7(3)	marginal	2.0σ
akn120	Seyfert 1 galaxy	0.4(4)	marginal	0.9σ
pica	Seyfert 1 galaxy	0.3(4)	marginal	0.6σ
lmcx2	LMXB	1.6(4)	persistent	4.4σ
iras05189-2524	Seyfert 2 galaxy	0.2(4)	marginal	0.4σ
v420aur	Be star	0.2(4)	marginal	0.4σ
sgr-n49	Pulsar	0.1(5)	marginal	0.3σ
abdor	Rotationally variable	0.3(4)	marginal	0.6σ
rxj0529.8-6556	HMXB	0.2(5)	marginal	0.4σ
3egj0530+13	Quasar	0.1(5)	marginal	0.3σ
exo0531-661	HMXB	0.1(5)	marginal	0.2σ
lmcx4	HMXB	0.6(4)	marginal	1.7σ
crab	SNR	75.1(9)	persistent	82.5σ
trap.cg	Cluster of galaxies	0.5(4)	marginal	1.4σ
sn1987a	Supernova	0.3(5)	marginal	0.6σ
x0535-668	HMXB	0.1(5)	marginal	0.3σ
pks0537-441	BL Lac-type object	0.2(4)	marginal	0.6σ
x0535+262	Be star	1.8(5)	recurring	3.8σ
lmcx3	HMXB	1.7(4)	persistent	4.6σ
lmcx1	HMXB	1.6(4)	persistent	4.3σ
igrj05414-6858	X-ray source	0.3(5)	marginal	0.6σ
xmmj05416-6826	HMXB	0.2(4)	marginal	0.5σ
ngc2024	Cluster of stars	0.3(4)	marginal	0.6σ
bycam	AM Her-type CV	0.3(3)	marginal	0.9σ
cal83	X-ray binary	0.2(4)	marginal	0.4σ
rxj0544.1-7100	Be star	0.2(4)	marginal	0.5σ
cal87	Eclipsing binary	0.2(4)	marginal	0.6σ
pks0548-322	BL Lac-type object	0.3(4)	marginal	0.8σ
ngc2110	Seyfert 2 galaxy	0.5(4)	marginal	1.1σ
maxij0556-332	X-ray source	0.1(4)	marginal	0.3σ
exo0556-386	X-ray source	0.2(4)	marginal	0.4σ
pks0558-504	Seyfert 1 galaxy	0.3(4)	marginal	0.7σ
igrj06074+2205	HMXB	0.1(5)	marginal	0.3σ
ic443snr	SNR	0.6(5)	marginal	1.3σ
x0614+091	LMXB	3.3(4)	persistent	7.8σ
2e0618.0+1326	X-ray source	0.2(5)	marginal	0.4σ
x0620-003	LMXB	0.1(5)	marginal	0.2σ
mwc148	Be star	0.2(5)	marginal	0.3σ
saxj0635+0533	Pulsar	0.2(5)	marginal	0.3σ
bl0647+250	BL Lac-type object	0.3(4)	marginal	0.6σ
x0656-072	Emission-line star	0.8(4)	marginal	1.8σ
psrj0700+6418	Pulsar	0.2(3)	marginal	0.6σ
exo0706+592	BL Lac-type object	0.3(3)	marginal	0.9σ
mkn376	Seyfert 1 galaxy	0.2(4)	marginal	0.6σ

Table A.4: Summary of all RXTE ASM sources (RA: 07-10)

ASM name	**SIMBAD type**	**Average flux(error)** [counts s^{-1}]	**Category**	**Detection significance**
rxj0720.4-3125	Star	0.2(4)	marginal	0.4σ
s5_0716+714	BL Lac-type object	0.2(3)	marginal	0.6σ
x0726-260	HMXB	0.2(4)	marginal	0.6σ
swiftj0732.5-1331	CV	0.2(4)	marginal	0.5σ
pks0735+178	BL Lac-type object	0.2(5)	marginal	0.3σ
mkn79	Seyfert 1 galaxy	0.2(4)	marginal	0.7σ
3egj0743+55	Quasar	0.2(4)	marginal	0.6σ
sigmagem	RS CVn-type variable	0.3(4)	marginal	0.8σ
exo0748-676	LMXB	0.8(3)	marginal	2.3σ
rxj0749.1-0549	AM Her-type CV	0.2(5)	marginal	0.3σ
psrj0751+1807	Pulsar	0.1(5)	marginal	0.3σ
ugem	Dwarf Nova	0.2(5)	marginal	0.4σ
rxj0759.7-3844	X-ray source	0.2(4)	marginal	0.5σ
1es0806+524	BL Lac-type object	0.2(4)	marginal	0.4σ
rxj0812.4-3115	X-ray source	0.2(4)	marginal	0.5σ
puppisa	SNR	0.7(7)	marginal	1.1σ
1es0821-426	X-ray source	0.8(6)	marginal	1.3σ
bl0829+046	BL Lac-type object	0.2(5)	marginal	0.5σ
velapulsar	Pulsar	0.8(4)	marginal	2.0σ
gs0834-430	X-ray binary	0.4(4)	marginal	0.8σ
saxj0835.9+5118	LMXB	0.2(4)	marginal	0.5σ
x0836-429	LMXB	0.5(5)	marginal	1.1σ
saxj0840.7+2248	X-ray source	0.2(5)	marginal	0.4σ
igrj08408-4503	HMXB	0.5(4)	marginal	1.3σ
3egj0852-12	Quasar	0.2(5)	marginal	0.4σ
oj287	BL Lac-type object	0.1(5)	marginal	0.2σ
velax1	HMXB	4.1(4)	persistent	9.9σ
x0918-548	LMXB	0.8(4)	marginal	2.2σ
x0921-630	LMXB	0.4(4)	marginal	1.1σ
x0922-314	X-ray source	0.6(4)	marginal	1.7σ
rxj0925.7-4758	X-ray binary	0.1(4)	marginal	0.2σ
mkn705	Seyfert 1 galaxy	0.2(5)	marginal	0.4σ
xtej0929-314	X-ray binary	0.1(5)	marginal	0.2σ
1es0927+500	BL Lac-type object	0.2(4)	marginal	0.7σ
ffuma	Variable star	0.2(3)	marginal	0.5σ
ngc2992	Seyfert 2 galaxy	0.3(5)	marginal	0.8σ
mcg-5-23-16	Seyfert 2 galaxy	0.5(4)	marginal	1.3σ
bl0954+65	BL Lac-type object	0.2(3)	marginal	0.5σ
ngc3081	Seyfert 2 galaxy	0.2(5)	marginal	0.4σ
groj1008-57	HMXB	0.3(5)	marginal	0.7σ
igrj10109-5746	Symbiotic star	0.2(5)	marginal	0.4σ
psrj1012+5307	Pulsar	0.2(4)	marginal	0.4σ
grs1009-45	LMXB	0.1(5)	marginal	0.3σ
bl1011+496	BL Lac-type object	0.2(4)	marginal	0.6σ
psrj1022+1001	Pulsar	0.2(5)	marginal	0.3σ
ngc3227	Seyfert 1 galaxy	0.4(5)	marginal	0.9σ

Table A.5: Summary of all RXTE ASM sources (RA: 10-12)

ASM name	**SIMBAD type**	**Average flux(error)** [counts s^{-1}]	**Category**	**Detection significance**
1e1024.1-5733	Wolf-Rayet star	0.2(5)	marginal	0.4σ
bl1028+511	BL Lac-type object	0.2(4)	marginal	0.6σ
rxj1037.5-5648	HMXB	0.3(5)	marginal	0.6σ
etacar	Double or multiple star	0.6(4)	marginal	1.5σ
1e1048.1-5937	HMXB	0.3(5)	marginal	0.7σ
dmuma	RS CVn-type variable	0.2(3)	marginal	0.6σ
bl1101-232	BL Lac-type object	0.4(5)	marginal	0.8σ
mkn421	BL Lac-type object	1.4(4)	persistent	3.5σ
ngc3516	Seyfert 1 galaxy	0.3(3)	marginal	1.0σ
cha.1n	Region in the sky	0.1(5)	marginal	0.1σ
cha.1s	Region in the sky	0.1(5)	marginal	0.2σ
1es1113+432	AM Her-type CV	0.1(5)	marginal	0.3σ
gb1114+203	BL Lac-type object	0.2(5)	marginal	0.4σ
xtej1118+480	LMXB	0.3(4)	marginal	0.8σ
1es1118+424	BL Lac-type object	0.2(5)	marginal	0.4σ
x1118-616	HMXB	0.3(5)	marginal	0.5σ
cenx3	HMXB	4.5(5)	persistent	9.8σ
igrj11215-5952	HMXB	0.4(5)	marginal	0.7σ
gs1124-684	LMXB	0.2(5)	marginal	0.4σ
igrj11305-6256	HMXB	0.2(5)	marginal	0.5σ
igrj11321-5311	Gamma-ray source	0.2(5)	marginal	0.3σ
mkn180	BL Lac-type object	0.2(3)	marginal	0.7σ
rxj1136.5+6737	BL Lac-type object	0.2(3)	marginal	0.5σ
ngc3783	Seyfert 1 galaxy	0.5(4)	marginal	1.1σ
hd101379	Star in double system	0.6(5)	marginal	1.2σ
igrj11435-6109	HMXB	0.3(5)	marginal	0.7σ
pks1144-379	BL Lac-type object	0.1(5)	marginal	0.2σ
x1145-616	HMXB	0.8(5)	marginal	1.6σ
x1145-619	Be star	0.6(5)	marginal	1.2σ
bl1147+245	BL Lac-type object	0.2(5)	marginal	0.5σ
3egj1200+29	Quasar	0.2(5)	marginal	0.4σ
ngc4051	Seyfert 1 galaxy	0.3(4)	marginal	0.6σ
ngc4151	Seyfert 1 galaxy	0.6(4)	marginal	1.7σ
x1210-646	X-ray source	0.6(5)	marginal	1.3σ
1es1212+078	BL Lac-type object	0.3(5)	marginal	0.6σ
on325	BL Lac-type object	0.1(5)	marginal	0.2σ
ngc4258	LINER-type AGN	0.2(4)	marginal	0.5σ
bl1219+305	BL Lac-type object	0.2(5)	marginal	0.4σ
on231	BL Lac-type object	0.1(5)	marginal	0.1σ
ngc4388	Seyfert 2 galaxy	0.4(4)	marginal	1.0σ
gx301-2	HMXB	2.0(4)	persistent	4.6σ
3c273	Quasar	0.6(4)	marginal	1.5σ
m87	LINER-type AGN	1.5(5)	persistent	3.1σ
igrj12349-6434	Symbiotic star	0.4(5)	marginal	0.9σ
ngc4507	Seyfert 2 galaxy	0.2(5)	marginal	0.5σ
ngc4593	Seyfert 1 galaxy	0.3(4)	marginal	0.6σ

Table A.6: Summary of all RXTE ASM sources (RA: 12-15)

ASM name	**SIMBAD type**	**Average flux(error)** [counts s^{-1}]	**Category**	**Detection significance**
x1239-599	HMXB	0.2(5)	marginal	0.4σ
hd110432	Be star	0.3(5)	marginal	0.6σ
cen.cg	Cluster of galaxies	1.0(5)	marginal	1.9σ
x1246-588	LMXB	0.8(4)	marginal	1.9σ
exhya	DQ Her-type CV	0.6(5)	marginal	1.4σ
3c279	Quasar	0.2(5)	marginal	0.3σ
1es1255+244	BL Lac-type object	0.2(5)	marginal	0.4σ
x1254-690	LMXB	2.5(4)	persistent	5.8σ
coma.cg	Cluster of galaxies	1.0(4)	marginal	2.6σ
gx304-1	HMXB	0.6(5)	marginal	1.1σ
psr1259-63	Pulsar	0.3(5)	marginal	0.6σ
ngc4941	Seyfert 2 galaxy	0.2(5)	marginal	0.3σ
ngc5033	Seyfert 1 galaxy	0.1(5)	marginal	0.3σ
iras13197-164	Seyfert 2 galaxy	0.3(6)	marginal	0.5σ
bl1320+084	BL Lac-type object	0.2(5)	marginal	0.4σ
saxj1324.5-6313	X-ray source	0.3(5)	marginal	0.5σ
cena	Seyfert 2 galaxy	1.0(4)	marginal	2.4σ
x1323-619	LMXB	0.8(4)	marginal	1.9σ
hr5110	RS CVn-type variable	0.2(5)	marginal	0.4σ
mcg-6-30-15	Seyfert 1 galaxy	0.5(5)	marginal	1.2σ
ngc5252	Seyfert 2 galaxy	0.2(5)	marginal	0.4σ
x1344-603	Seyfert galaxy	0.4(5)	marginal	1.0σ
ic4329a	Seyfert 1 galaxy	0.8(5)	marginal	1.7σ
mkn279	Seyfert 1 galaxy	0.3(3)	marginal	1.0σ
mkn464	Seyfert 1 galaxy	0.2(4)	marginal	0.4σ
mkn463	Seyfert 2 galaxy	0.2(5)	marginal	0.3σ
x1354-644	X-ray source	0.3(5)	marginal	0.6σ
maxij1409-619	X-ray source	2(1)	marginal	1.5σ
3egj1409-08	Quasar	0.3(6)	marginal	0.4σ
cir.galaxy	Seyfert 2 galaxy	0.3(5)	marginal	0.5σ
ngc5506	Seyfert 2 galaxy	0.6(5)	marginal	1.1σ
ngc5548	Seyfert 1 galaxy	0.4(5)	marginal	0.9σ
oq530	BL Lac-type object	0.2(3)	marginal	0.4σ
x1417-624	HMXB	0.4(5)	marginal	0.9σ
bl1426+427	BL Lac-type object	0.3(4)	marginal	0.8σ
saxj1428.6-5422	X-ray source	0.3(5)	marginal	0.5σ
mkn478	Seyfert 1 galaxy	0.2(4)	marginal	0.5σ
igrj14488-5942	Gamma-ray source	0.5(5)	marginal	0.9σ
vv780	Seyfert 2 galaxy	1.3(7)	marginal	1.9σ
cenx4	LMXB	0.2(6)	marginal	0.3σ
pks1510-08	Quasar	0.4(7)	marginal	0.6σ
aplib	BL Lac-type object	0.2(6)	marginal	0.3σ
bl1517+656	BL Lac-type object	0.2(3)	marginal	0.7σ
cirx1	LMXB	45.8(8)	persistent	59.5σ
x1524-617	LMXB	0.4(5)	marginal	0.7σ
mkn290	Seyfert 1 galaxy	0.2(3)	marginal	0.6σ

Table A.7: Summary of all RXTE ASM sources (RA: 15-17)

ASM name	**SIMBAD type**	**Average flux(error)** [counts s^{-1}]	**Category**	**Detection significance**
swiftj1539.2-6227	Star	0.5(7)	marginal	0.7σ
or165	BL Lac-type object	0.2(5)	marginal	0.4σ
x1538-522	HMXB	1.1(5)	marginal	2.3σ
xtej1543-568	HMXB	0.5(6)	marginal	0.8σ
x1543-475	LMXB	2.4(6)	transient	3.7σ
igrj15479-4529	X-ray binary	0.4(6)	marginal	0.7σ
x1543-624	LMXB	2.6(5)	persistent	5.1σ
1e1547.0-5408	Pulsar	0.2(6)	marginal	0.3σ
xtej1550-564	LMXB	9.7(6)	transient	15.2σ
pg1553+113	BL Lac-type object	0.3(5)	marginal	0.7σ
x1553-542	HMXB	0.2(6)	marginal	0.4σ
x1556-605	LMXB	1.5(5)	persistent	3.1σ
saxj1603.9-7753	X-ray source	0.2(5)	marginal	0.4σ
ms1603.6+2600	LMXB	0.3(4)	marginal	0.6σ
x1608-522	LMXB	4.9(6)	recurring	8.9σ
rcw103	SNR	0.5(6)	marginal	0.9σ
igrj16195-4945	HMXB candidate	0.5(6)	marginal	0.7σ
igrj16194-2810	Gamma-ray source	0.4(6)	marginal	0.6σ
scox1	LMXB	890(6)	persistent	142.6σ
psrj1622-4950	Pulsar	0.4(6)	marginal	0.6σ
3egj1626-25	Quasar	0.3(7)	marginal	0.4σ
doar21	Orion-type variable	0.4(7)	marginal	0.5σ
3egj1625-30	Quasar	0.2(7)	marginal	0.4σ
swiftj1626.6-5156	LMXB candidate	0.4(7)	marginal	0.6σ
x1624-490	LMXB	3.5(6)	persistent	6.1σ
igrj16283-4838	HMXB	0.4(6)	marginal	0.7σ
rxj1628.8-4152	RS CVn-type variable	0.2(7)	marginal	0.3σ
igrj16318-4848	HMXB	0.4(6)	marginal	0.7σ
igrj16320-4751	HMXB	0.7(6)	marginal	1.1σ
x1627-673	LMXB	0.9(4)	marginal	2.1σ
x1630-472	LMXB	7.4(6)	transient	11.5σ
sgr-ctb33	SNR	1(1)	marginal	0.5σ
igrj16393-4643	HMXB	0.5(7)	marginal	0.8σ
x1636-536	LMXB	9.1(6)	persistent	15.4σ
igrj16418-4532	HMXB	0.8(8)	marginal	1.0σ
rxj1644.6+5959	Star	0.1(3)	marginal	0.3σ
gx340+0	LMXB	28.9(8)	persistent	35.2σ
igrj16479-4514	HMXB	0.7(7)	marginal	1.0σ
igrj16493-4348	LMXB candidate	0.4(7)	marginal	0.5σ
xtej1650-500	LMXB	1.1(7)	marginal	1.5σ
xtej1652-453	X-ray source	0.6(9)	marginal	0.7σ
mkn501	BL Lac-type object	0.6(3)	marginal	1.9σ
groj1655-40	LMXB	30.8(8)	recurring	36.7σ
swiftj1656.3-3302	Possible AGN	0.3(7)	marginal	0.4σ
herx1	LMXB	1.6(3)	persistent	4.8σ
maxij1659-152	Black hole candidate	19(3)	marginal	6.5σ

Table A.8: Summary of all RXTE ASM sources (RA: 17)

ASM name	**SIMBAD type**	**Average flux(error)** [counts s^{-1}]	**Category**	**Detection significance**
axj1700.2-4220	HMXB	0.3(8)	marginal	0.3σ
x1657-415	HMXB	1.3(6)	marginal	2.0σ
xtej1701-462	LMXB	5.8(8)	transient	7.2σ
xtej1701-407	LMXB	0.6(8)	marginal	0.7σ
x1658-298	LMXB	0.9(7)	marginal	1.2σ
gx339-4	LMXB	9.7(7)	recurring	14.2σ
x1700-377	HMXB	4.5(7)	persistent	6.3σ
3c351	Seyfert 1 galaxy	0.1(3)	marginal	0.4σ
gx349+2	LMXB	50(1)	persistent	47.3σ
x1702-429	LMXB	3.2(7)	persistent	4.9σ
igrj17062-6143	Gamma-ray source	0.4(5)	marginal	0.8σ
x1704+240	LMXB	0.5(4)	marginal	1.3σ
x1705-250	LMXB	0.4(9)	marginal	0.4σ
rxj1708.9-3219	LMXB	0.6(8)	marginal	0.8σ
x1705-440	LMXB	11.8(7)	persistent	16.4σ
rxj1709.5-2639	LMXB	1.0(8)	marginal	1.2σ
igrj17098-3626	Gamma-ray source	2.3(9)	marginal	2.7σ
rxj1710.2-2808	LMXB	1(1)	marginal	0.8σ
saxj1711.6-3808	X-ray source	0.5(9)	marginal	0.6σ
x1708-407	LMXB	2.2(6)	persistent	3.4σ
oph.cg	Cluster of galaxies	2.0(8)	marginal	2.5σ
saxj1712.6-3739	LMXB	1.3(7)	marginal	1.8σ
psrj1713+0747	Pulsar	0.2(5)	marginal	0.4σ
x1711-339	Variable star	0.7(8)	marginal	0.9σ
xtej1716-389	HMXB	1.4(7)	marginal	2.1σ
xtej1716-379	X-ray source	0(1)	marginal	0.3σ
rxj1718.4-4029	LMXB	0.6(8)	marginal	0.8σ
x1715-321	LMXB	0(1)	marginal	0.5σ
igrj17191-2821	Gamma-ray source	0.5(9)	marginal	0.6σ
xtej1719-291	X-ray source	0.3(9)	marginal	0.4σ
grs1716-249	LMXB	0(1)	marginal	0.4σ
saxj1719.6-4254	X-ray source	0.2(8)	marginal	0.3σ
xtej1720-318	LMXB	0.8(8)	marginal	1.1σ
mkn506	Seyfert 1 galaxy	0.2(4)	marginal	0.6σ
xtej1723-376	LMXB	0.6(8)	marginal	0.7σ
bl1722+119	BL Lac-type object	0.3(4)	marginal	0.6σ
exo1722-363	HMXB	0.6(8)	marginal	0.7σ
igrj17254-3257	LMXB	0.7(8)	marginal	0.9σ
xtej1726-476	Gamma-ray source	0.4(7)	marginal	0.5σ
x1724-307	LMXB	2.1(7)	persistent	3.2σ
bl1zw187	BL Lac-type object	0.2(3)	marginal	0.6σ
igrj17285-2922	X-ray binary candidate	0.5(9)	marginal	0.5σ
hd159023	Pulsating variable star	0.2(3)	marginal	0.6σ
igrj17303-0601	CV	0.3(5)	marginal	0.5σ
gx9+9	LMXB	19.5(8)	persistent	23.2σ
gx354-0	LMXB	6.7(7)	persistent	9.9σ

Table A.9: Summary of all RXTE ASM sources (RA: 17)

ASM name	**SIMBAD type**	**Average flux(error)** [counts s^{-1}]	**Category**	**Detection significance**
gx1+4	LMXB	1.4(8)	marginal	1.7σ
x1730-333	LMXB	2.0(7)	marginal	3.0σ
ks1730-312	LMXB	0.7(9)	marginal	0.8σ
ks1731-260	LMXB	5(1)	persistent	5.4σ
rxj1735.4-3540	Star	0.6(8)	marginal	0.8σ
igrj17354-3255	Gamma-ray source	0.6(8)	marginal	0.8σ
hk1732-304	LMXB	0(1)	marginal	0.4σ
ks1732-273	X-ray source	0(1)	marginal	0.5σ
grs1734-292	Seyfert 1 galaxy	0(1)	marginal	0.4σ
sl1735-269	LMXB	1.5(8)	marginal	1.8σ
x1735-444	LMXB	12.8(7)	persistent	18.3σ
xtej1739-302	HMXB	0.6(9)	marginal	0.7σ
xtej1739-285	LMXB	1(1)	marginal	0.8σ
grs1737-31	X-ray source	0.6(8)	marginal	0.8σ
igrj17407-2808	Gamma-ray source	0.9(9)	marginal	1.0σ
rxj1741.9-1212	Seyfert 1 galaxy	0.4(7)	marginal	0.6σ
grs1739-278	Nova-like star	3(1)	marginal	2.7σ
xtej1743-363	Gamma-ray source	0.6(8)	marginal	0.7σ
1e1740.7-2942	LMXB	1.4(9)	marginal	1.5σ
1es1741+196	BL Lac-type object	0.3(4)	marginal	0.7σ
groj1744-28	LMXB	2(1)	marginal	1.8σ
gctr_diffuse	Gal. centre transient	5(1)	persistent	3.6σ
gcx-1	LMXB	2.2(9)	marginal	2.5σ
h1743-322	LMXB	4.5(8)	transient	5.5σ
saxj1747.0-2853	LMXB	0(1)	marginal	0.2σ
xmmj1747.3-2811	Gamma-ray source	1(1)	marginal	0.9σ
igrj17473-2721	Gamma-ray source	1.3(9)	marginal	1.4σ
sl1744-300	LMXB	1.9(9)	marginal	2.2σ
gx3+1	LMXB	22(1)	persistent	20.5σ
xtej1748-288	LMXB	1.1(9)	marginal	1.2σ
exo1745-248	LMXB	1(1)	marginal	1.3σ
x1744-361	Infrared source	0.7(8)	marginal	0.9σ
igrj17488-3253	Seyfert 1 galaxy	0.6(9)	marginal	0.8σ
x1745-203	LMXB	1.0(9)	marginal	1.1σ
axj1749.1-2733	HMXB candidate	1(1)	marginal	0.6σ
groj1750-27	HMXB	1(2)	marginal	0.6σ
swiftj1749.4-2807	X-ray binary	1(1)	marginal	0.7σ
igrj17497-2821	Gamma-ray source	1(1)	marginal	0.8σ
sl1746-331	LMXB	1.2(8)	marginal	1.5σ
x1746-370	LMXB	2.5(6)	persistent	3.9σ
rsoph	Symbiotic star	0.1(5)	marginal	0.2σ
saxj1750.8-2900	LMXB	1(1)	marginal	0.5σ
exo1747-214	LMXB	0.6(9)	marginal	0.7σ
grs1747-312	LMXB	1.1(7)	marginal	1.5σ
xtej1751-305	X-ray binary	1(1)	marginal	0.5σ
xtej1752-223	X-ray source	1.3(9)	marginal	1.4σ

Table A.10: Summary of all RXTE ASM sources (RA: 17-18)

ASM name	**SIMBAD type**	**Average flux(error)** [counts s^{-1}]	**Category**	**Detection significance**
gx1-1	LMXB	1(1)	marginal	0.6σ
saxj1752.3-3128	LMXB	0.7(9)	marginal	0.8σ
swiftj1753.5-0127	LMXB	1.5(5)	transient	3.2σ
saxj1753.5-2349	LMXB	1(1)	marginal	0.9σ
axj1754.2-2754	X-ray source	1(1)	marginal	0.5σ
igrj17544-2619	HMXB	1(1)	marginal	0.7σ
xtej1755-324	LMXB	0.7(8)	marginal	0.8σ
swiftj1756.9-2508	X-ray binary	1(1)	marginal	0.9σ
sao085590	Semi-regular pulsation	0.1(4)	marginal	0.4σ
x1755-338	LMXB	1(1)	marginal	0.5σ
xtej1759-220	LMXB	0.9(8)	marginal	1.2σ
gx5-1	LMXB	70(1)	persistent	56.4σ
grs1758-258	LMXB	2.2(9)	marginal	2.5σ
gx9+1	LMXB	38(1)	persistent	39.6σ
igrj18027-2017	HMXB	0.9(9)	marginal	1.0σ
igrj18027-1455	Seyfert 1 galaxy	0.5(7)	marginal	0.7σ
saxj1805.5-2031	X-ray source	0.8(9)	marginal	0.9σ
saxj1806.5-2215	X-ray source	0.8(9)	marginal	0.9σ
3c371	BL Lac-type object	0.2(3)	marginal	0.6σ
x1803-245	LMXB	1(1)	marginal	1.5σ
xtej1807-294	LMXB	0(1)	marginal	0.5σ
hd347929	Variable star	0.2(4)	marginal	0.4σ
saxj1808.4-3658	LMXB	0.6(7)	marginal	0.8σ
sgr1806-20	Pulsar	0.6(8)	marginal	0.7σ
xtej1810-197	Pulsar	0.4(9)	marginal	0.5σ
xtej1810-189	X-ray source	0.3(8)	marginal	0.4σ
saxj1810.8-2609	LMXB	1(1)	marginal	1.0σ
g12-0snr	SNR	0.8(8)	marginal	1.0σ
xmmj18125-1813	X-ray source	0.5(8)	marginal	0.6σ
igrj18135-1751	SNR	0.6(7)	marginal	0.8σ
xtej1814-338	X-ray binary	0.4(8)	marginal	0.6σ
gx13+1	LMXB	22.5(8)	persistent	27.4σ
x1812-121	LMXB	1.5(5)	marginal	2.8σ
gx17+2	LMXB	44.4(9)	persistent	48.3σ
amher	AM Her-type CV	0.3(3)	marginal	1.2σ
swiftj1816.7-1613	X-ray source	0.6(8)	marginal	0.8σ
xtej1817-155	Gamma-ray source	0.6(8)	marginal	0.8σ
xtej1817-330	X-ray binary	2.1(8)	marginal	2.5σ
xtej1818-245	X-ray source	1.0(9)	marginal	1.1σ
saxj1818.6-1703	HMXB	0.8(8)	marginal	1.0σ
saxj1818.7+1424	X-ray source	0.2(4)	marginal	0.4σ
v4641sgr	LMXB	0.8(9)	marginal	0.9σ
axj1820.5-1434	HMXB	0.8(8)	marginal	1.1σ
x1820-303	LMXB	21.0(9)	persistent	24.7σ
xtej1824-141	X-ray binary	0.7(9)	marginal	0.8σ

* ATel #1981

Table A.11: Summary of all RXTE ASM sources (RA: 18-19)

ASM name	**SIMBAD type**	**Average flux(error)** [counts s^{-1}]	**Category**	**Detection significance**
x1822-000	LMXB	2.3(4)	persistent	5.3σ
x1822-371	LMXB	1.7(6)	persistent	3.1σ
rxj1826.2-1450	HMXB	0.6(8)	marginal	0.8σ
igrj18284-0345	Hard X-ray transient *	0.3(5)	marginal	0.6σ
gs1826-238	LMXB	3.0(7)	persistent	4.2σ
xtej1829-098	X-ray source	0.5(5)	marginal	0.9σ
sgr1833-0832	Unknown nature	0.4(5)	marginal	0.8σ
bydra	BY Dra-type variable	0.1(3)	marginal	0.4σ
sctx1	HMXB	0.5(5)	marginal	0.9σ
x1832-330	LMXB	0.9(6)	marginal	1.5σ
m22	Globular cluster	0.4(8)	marginal	0.5σ
xtej1837+037	X-ray source	0.3(5)	marginal	0.6σ
iras18325-5926	Seyfert 2 galaxy	0.4(5)	marginal	0.7σ
eso103-G35	Seyfert 2 galaxy	0.4(5)	marginal	0.8σ
serx1	LMXB	15.8(5)	persistent	29.3σ
v4745sgr	Nova	0.2(7)	marginal	0.3σ
axj1841.0-0536	HMXB	0.5(5)	marginal	1.0σ
1e1841-045	Pulsar	0.5(5)	marginal	1.2σ
3c390.3	Seyfert 1 galaxy	0.3(2)	marginal	1.3σ
swiftj1842.5-1124	X-ray source	0.6(6)	marginal	1.1σ
xtej1842-042	X-ray source	0.3(5)	marginal	0.7σ
axj1845.0-0258	HMXB	0.2(7)	marginal	0.2σ
xtej1845-003	Be star	0.2(5)	marginal	0.5σ
igrj18450-0435	HMXB	0.4(6)	marginal	0.6σ
gs1843+009	HMXB	0.4(5)	marginal	0.9σ
igrj18462-0223	Gamma-ray source	0.2(7)	marginal	0.2σ
x1845-024	Gamma-ray source	0.3(5)	marginal	0.7σ
igrj18483-0311	HMXB	0.4(5)	marginal	0.9σ
exo1846-031	LMXB	0.3(5)	marginal	0.6σ
x1850-087	LMXB	0.9(5)	marginal	2.0σ
igrj18539+0727	X-ray binary	0.2(5)	marginal	0.3σ
v1223sgr	DQ Her-type CV	0.6(6)	marginal	1.0σ
xtej1855-026	HMXB	0.5(5)	marginal	1.0σ
xtej1856+053	LMXB	0.7(5)	marginal	1.3σ
cor.cg	Cluster of galaxies	0.2(6)	marginal	0.3σ
xtej1859+226	LMXB	1.2(4)	transient	3.2σ
xtej1858+034	HMXB	0.4(5)	marginal	0.7σ
xtej1859+083	X-ray source	0.2(5)	marginal	0.4σ
hetej1900.1-2455	LMXB	1.2(7)	marginal	1.9σ
xtej1901+014	X-ray binary	0.6(5)	marginal	1.2σ
x1901+031	HMXB	0.8(5)	marginal	1.6σ
xtej1906+090	HMXB	0.1(6)	marginal	0.2σ
sgr1900+14	Gamma-ray Burst	0.3(5)	marginal	0.6σ
x1905+000	Infrared source	0.3(6)	marginal	0.5σ
xtej1908+094	HMXB	0.4(7)	marginal	0.5σ
x1907+097	HMXB	1.0(5)	marginal	1.9σ

Table A.12: Summary of all RXTE ASM sources (RA: 19-21)

ASM name	**SIMBAD type**	**Average flux(error)** [counts s^{-1}]	**Category**	**Detection significance**
psr1908+00	Pulsar	0.2(6)	marginal	0.4σ
x1908+075	HMXB	0.7(5)	marginal	1.5σ
aqlx1	LMXB	3.4(5)	recurring	6.8σ
ss433	HMXB	0.7(4)	marginal	1.8σ
igrj1914+0951	HMXB	0.7(6)	marginal	1.1σ
grs1915+105	LMXB	54.5(8)	persistent	72.7σ
x1916-053	LMXB	1.1(4)	marginal	2.5σ
chcyg	Symbiotic star	0.2(3)	marginal	0.5σ
hd182928	Star	0.2(6)	marginal	0.3σ
igrj19294+1816	Gamma-ray source	0.2(4)	marginal	0.6σ
3egj1935-40	Quasar	0.3(6)	marginal	0.4σ
x1942+274	X-ray binary	0.6(4)	marginal	1.7σ
ks1947+300	HMXB	0.6(4)	marginal	1.8σ
swiftj1955.2+2614	X-ray source	0.1(4)	marginal	0.3σ
x1953+319	HMXB	0.9(4)	marginal	2.5σ
cygx1	HMXB	31.2(5)	persistent	61.2σ
x1957+115	LMXB	2.4(4)	persistent	5.8σ
cyga	Seyfert 2 galaxy	0.5(3)	marginal	1.6σ
psr1957+20	Eclipsing binary	0.2(4)	marginal	0.4σ
1es1959+650	BL Lac-type object	0.5(2)	marginal	1.9σ
swiftj2000.6+3210	HMXB	0.4(4)	marginal	1.0σ
gs2000+250	LMXB	0.2(4)	marginal	0.4σ
s5_2007+777	BL Lac-type object	0.1(3)	marginal	0.4σ
rxj2008.7-6023	X-ray source	0.2(5)	marginal	0.3σ
bl2005-489	BL Lac-type object	0.4(5)	marginal	0.8σ
xtej2012+381	LMXB	0.7(4)	marginal	1.7σ
axj2018.4+4614	X-ray source	0.1(4)	marginal	0.4σ
igrj20188+3647	Gamma-ray source	0.3(4)	marginal	0.8σ
hd193793	Wolf-Rayet star	0.4(4)	marginal	1.0σ
gs2023+338	LMXB	0.1(4)	marginal	0.3σ
exo2030+375	HMXB	2.2(4)	transient	5.9σ
cygx3	HMXB	12.4(4)	persistent	30.2σ
swiftj2037.2+4151	X-ray source	0.5(4)	marginal	1.3σ
atmic	Flare star	0.4(6)	marginal	0.6σ
mkn509	Seyfert 1 galaxy	0.5(5)	marginal	0.9σ
psrj2051-0827	Pulsar	0.2(6)	marginal	0.3σ
ic5063	Seyfert 2 galaxy	0.2(5)	marginal	0.4σ
groj2058+42	HMXB	0.3(4)	marginal	0.7σ
saxj2103.5+4545	HMXB	0.5(3)	marginal	1.5σ
h2106-099	Seyfert 1 galaxy	0.2(6)	marginal	0.3σ
igrj21117+3427	Gamma-ray source	0.2(4)	marginal	0.5σ
xtej2123-058	LMXB	0.3(6)	marginal	0.5σ
igrj21247+5058	Seyfert 1 galaxy	0.3(3)	marginal	1.1σ
x2127+119	X-ray binary	1.1(4)	marginal	2.7σ
x2129+470	LMXB	0.1(4)	marginal	0.4σ
cepx4	HMXB	0.2(3)	marginal	0.7σ

Table A.13: Summary of all RXTE ASM sources (RA: 21-24)

ASM name	**SIMBAD type**	**Average flux(error)** [counts s^{-1}]	**Category**	**Detection significance**
sscyg	Dwarf Nova	0.5(4)	marginal	1.5σ
cygx2	LMXB	37.6(6)	persistent	67.1σ
psrj2145-0750	Pulsar	0.2(6)	marginal	0.4σ
rxj2146.7-8543	High proper-motion	0.1(5)	marginal	0.3σ
pks2155-304	BL Lac-type object	0.4(6)	marginal	0.6σ
ngc7172	Seyfert 2 galaxy	0.3(6)	marginal	0.5σ
bllac	BL Lac-type object	0.2(4)	marginal	0.6σ
x2206+543	HMXB	0.6(3)	marginal	2.0σ
arlac	RS CVn-type variable	0.3(4)	marginal	0.7σ
ngc7213	Seyfert 1 galaxy	0.3(6)	marginal	0.5σ
3c445	Seyfert 1 galaxy	0.2(5)	marginal	0.4σ
saxj2224.9+5421	X-ray source	0.2(3)	marginal	0.7σ
4c11.69	Quasar	0.3(5)	marginal	0.5σ
ngc7314	Seyfert 1 galaxy	0.3(5)	marginal	0.7σ
saxj2239.3+6116	HMXB	0.2(3)	marginal	0.5σ
3egj2321-03	Quasar	0.2(5)	marginal	0.4σ
sao108231	RS CVn-type variable	0.2(5)	marginal	0.3σ
3c454.3	Quasar	0.2(5)	marginal	0.3σ
mr2251-178	Seyfert 1 galaxy	0.4(5)	marginal	0.9σ
cepa-east	Region in the sky	0.1(3)	marginal	0.3σ
oy091	BL Lac-type object	0.2(5)	marginal	0.3σ
pks2255-282	Seyfert 1 galaxy	0.2(5)	marginal	0.3σ
1e2259.0+5836	HMXB	1.0(4)	marginal	2.3σ
ngc7469	Seyfert 1 galaxy	0.3(5)	marginal	0.7σ
mkn926	Seyfert 1 galaxy	0.3(4)	marginal	0.6σ
ngc7582	Seyfert 2 galaxy	0.2(5)	marginal	0.5σ
casa	SNR	5.0(3)	persistent	14.6σ
1es2321+419	BL Lac-type object	0.2(4)	marginal	0.6σ
ngc7674	Seyfert 2 galaxy	0.3(5)	marginal	0.6σ
eqpeg	Flare star	0.2(5)	marginal	0.5σ
zand	Symbiotic star	0.2(4)	marginal	0.4σ
1es2344+514	BL Lac-type object	0.3(3)	marginal	0.8σ
iipeg	RS CVn-type variable	0.3(5)	marginal	0.7σ
bl2356-309	BL Lac-type object	0.3(4)	marginal	0.6σ

Appendix B

Significant ASM Detections

Of the 585 ASM sources (data publicly available at http://xte.mit.edu/ASMlc.html), there are 520 sources in the "marginal" category. The remaining 65 significantly detected sources contained in the RXTE ASM archival data, include the following object types:

- 45 Low-mass X-ray binaries (LMXBs)
- 12 High-mass X-ray binaries (HMXBs)
- 3 Supernova remnants (SNRs)
- 1 LINER-type AGN
- 1 BL Lac-type AGN
- 1 Seyfert 2 galaxy
- 1 Be star (therefore an HMXB)
- 1 Galactic centre transient

These include 13 sources (all XRBs) clearly displaying transient or recurring transient behaviour, namely: v0332+53, x0535+262, x1543-475, xtej1550-564, x1608-522, x1630-472, groj1655-40, xtej1701-462, gx339-4, h1743-322, swiftj1753.5-0127, xtej1859+226 and aqlx1. Although exo2030+375 clearly is a transient, it remains above the detection criteria after removing the outburst, while the other aforementioned sources do not. The remaining 52 sources are considered persistent.

Among them, there are several XRBs that exhibit large amplitude, very long-term modulations. They include xper, cirx1, x1636-536, x1708-407, gx9+9, gx354-0, ks1731-260, x1735-444, gx3+1, x1746-370, gx9+1 and serx1.

In contrast thereto, there are sources that appear relatively steady over the long term. They are: tychosnr (SNR), ngc1275.cg (Seyfert 2 galaxy), lmcx2, crab (SNR), lmcx1, velax1, m87 (LINER-type AGN), x1254-690, x1543-624, x1556-605, scox1, x1624-490, gx340+0, x1700-377, gx349+2, x1724-307, gctr_diffuse (Galactic centre transient), gx15-1, gx13+1, gx17+2, x1822-000, x1822-371, gs1826-238 and casa (SNR).

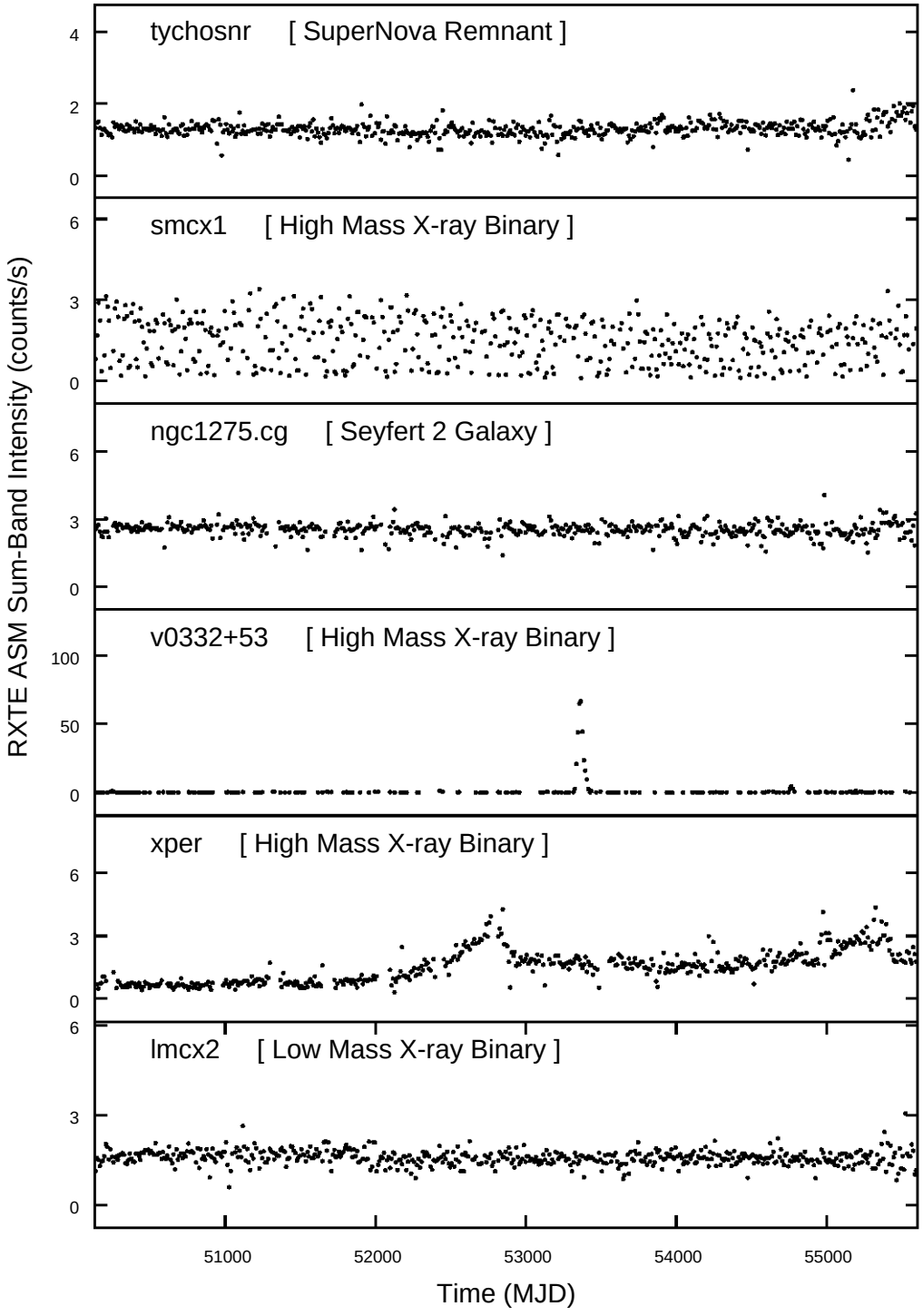

Figure B.1: RXTE ASM lightcurves of significantly detected sources (RA: 00-05)

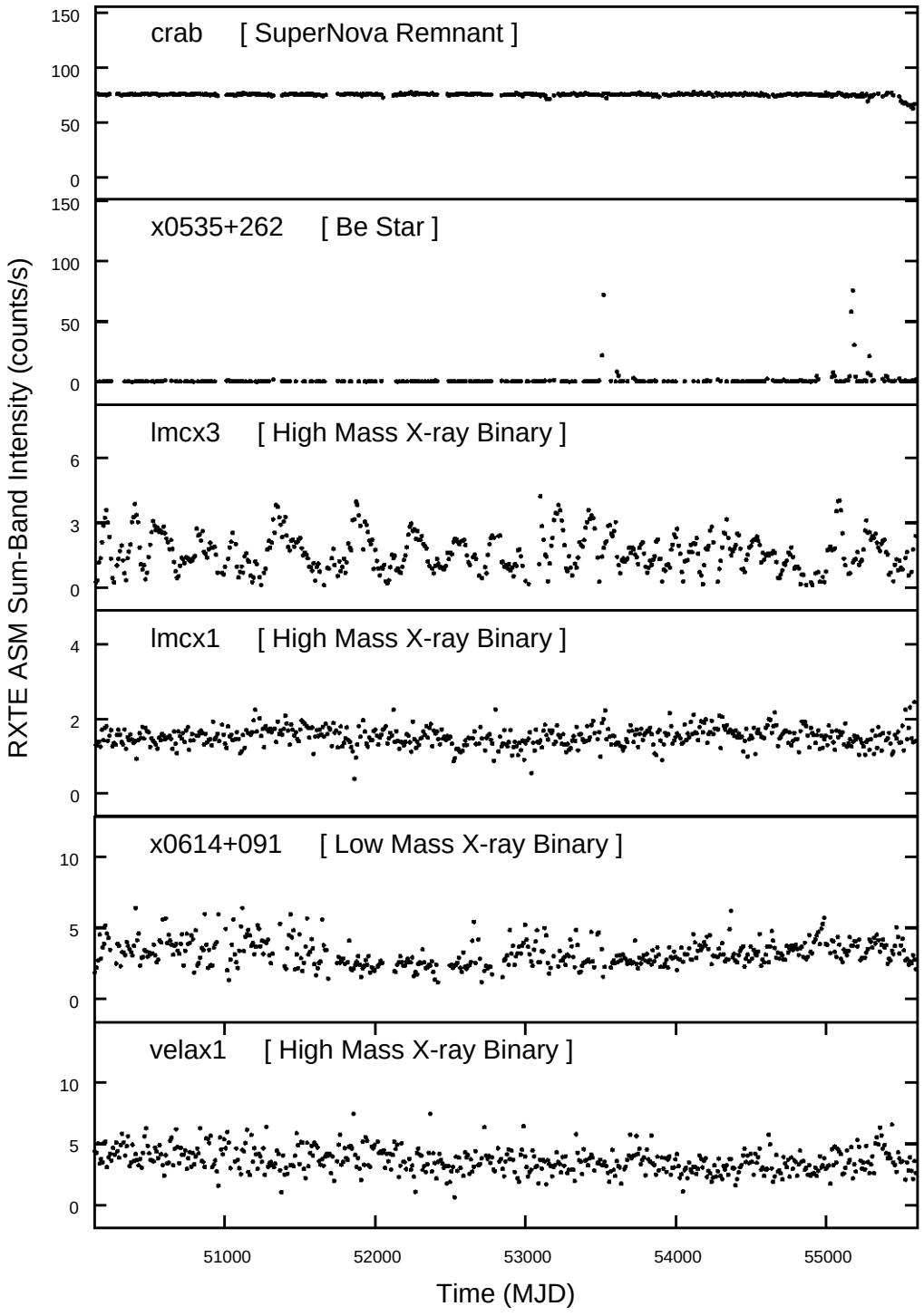

Figure B.2: RXTE ASM lightcurves of significantly detected sources (RA: 05-09)

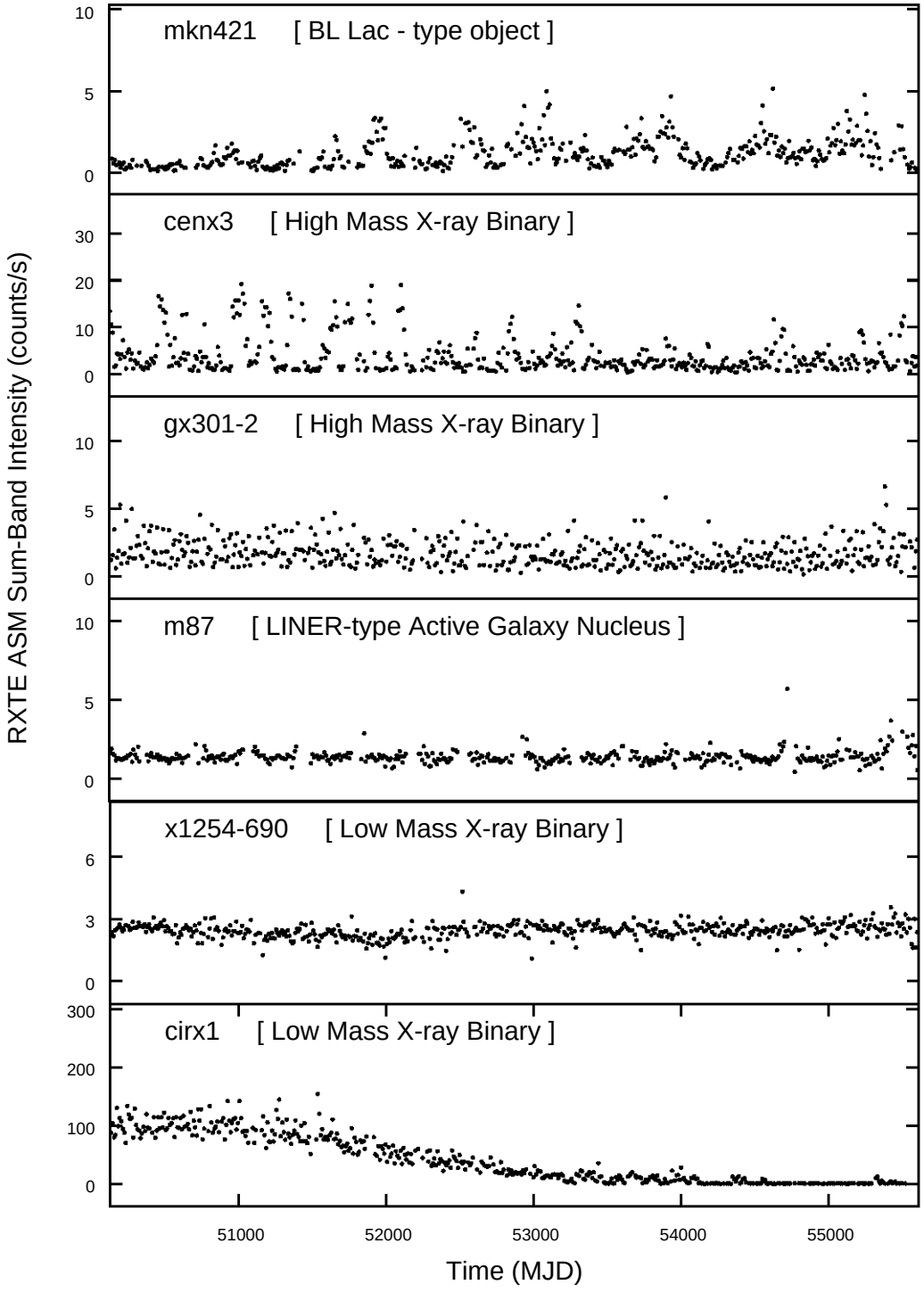

Figure B.3: RXTE ASM lightcurves of significantly detected sources (RA: 09-15)

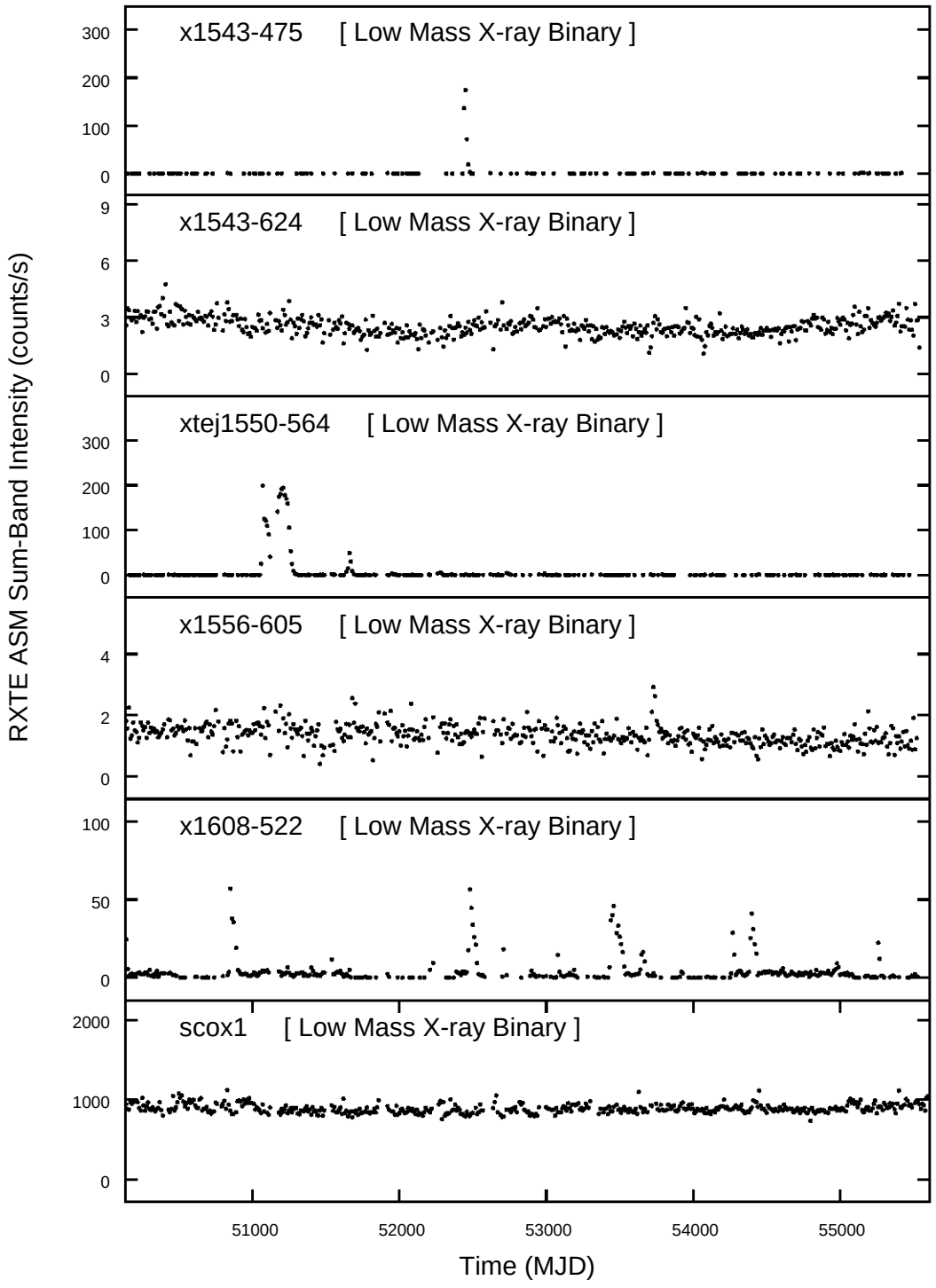

Figure B.4: RXTE ASM lightcurves of significantly detected sources (RA: 15-16)

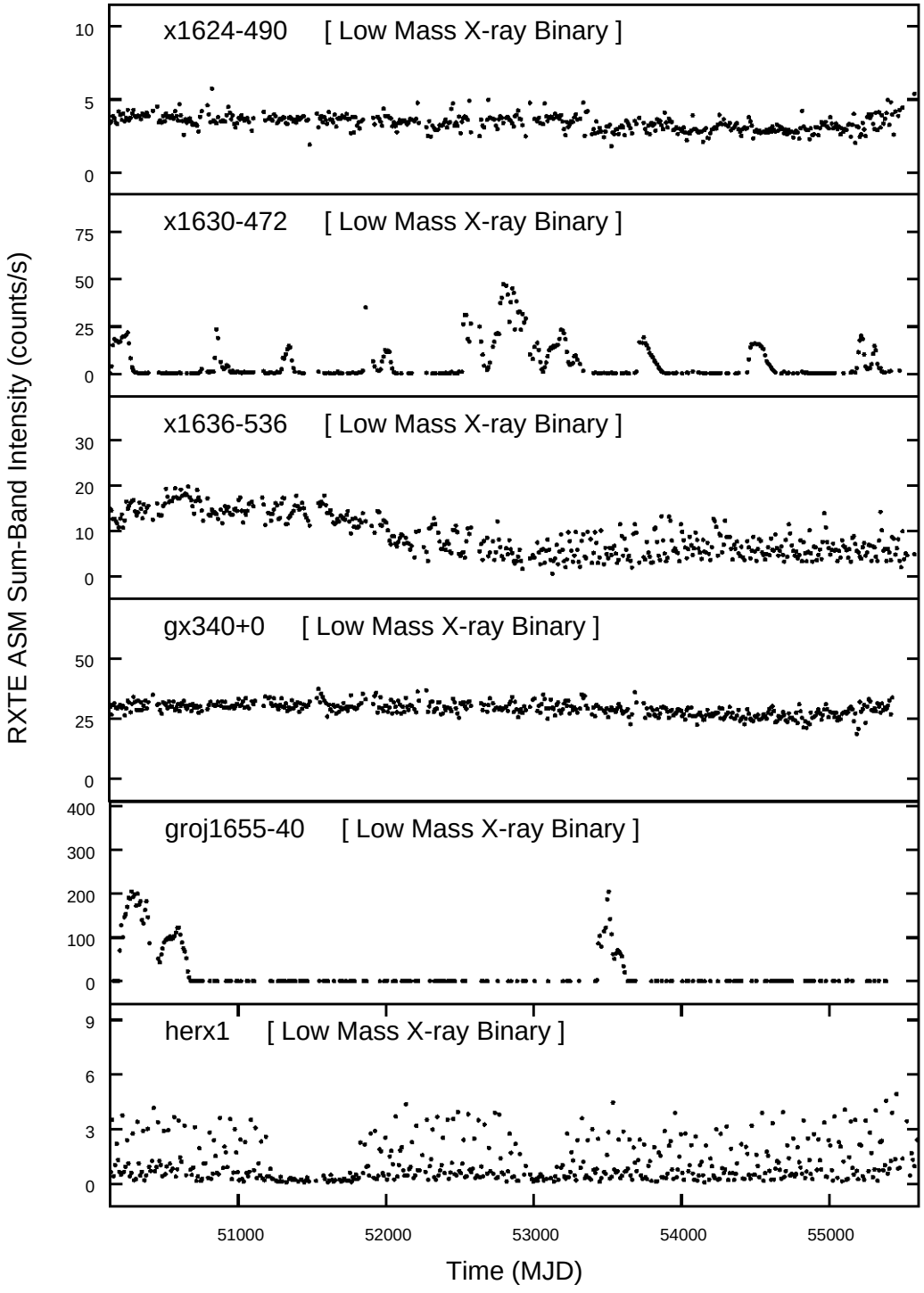

Figure B.5: RXTE ASM lightcurves of significantly detected sources (RA: 16)

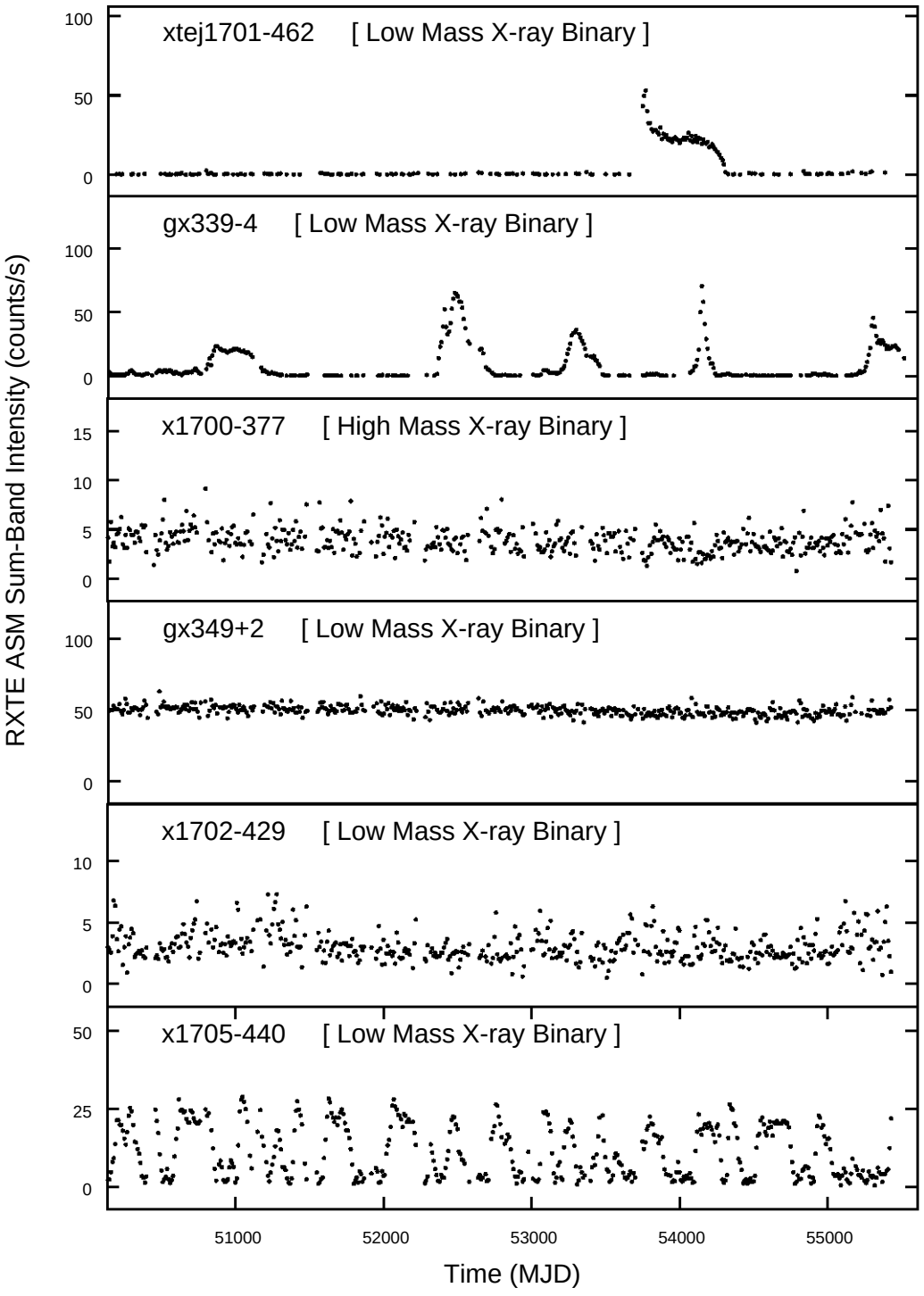

Figure B.6: RXTE ASM lightcurves of significantly detected sources (RA: 17)

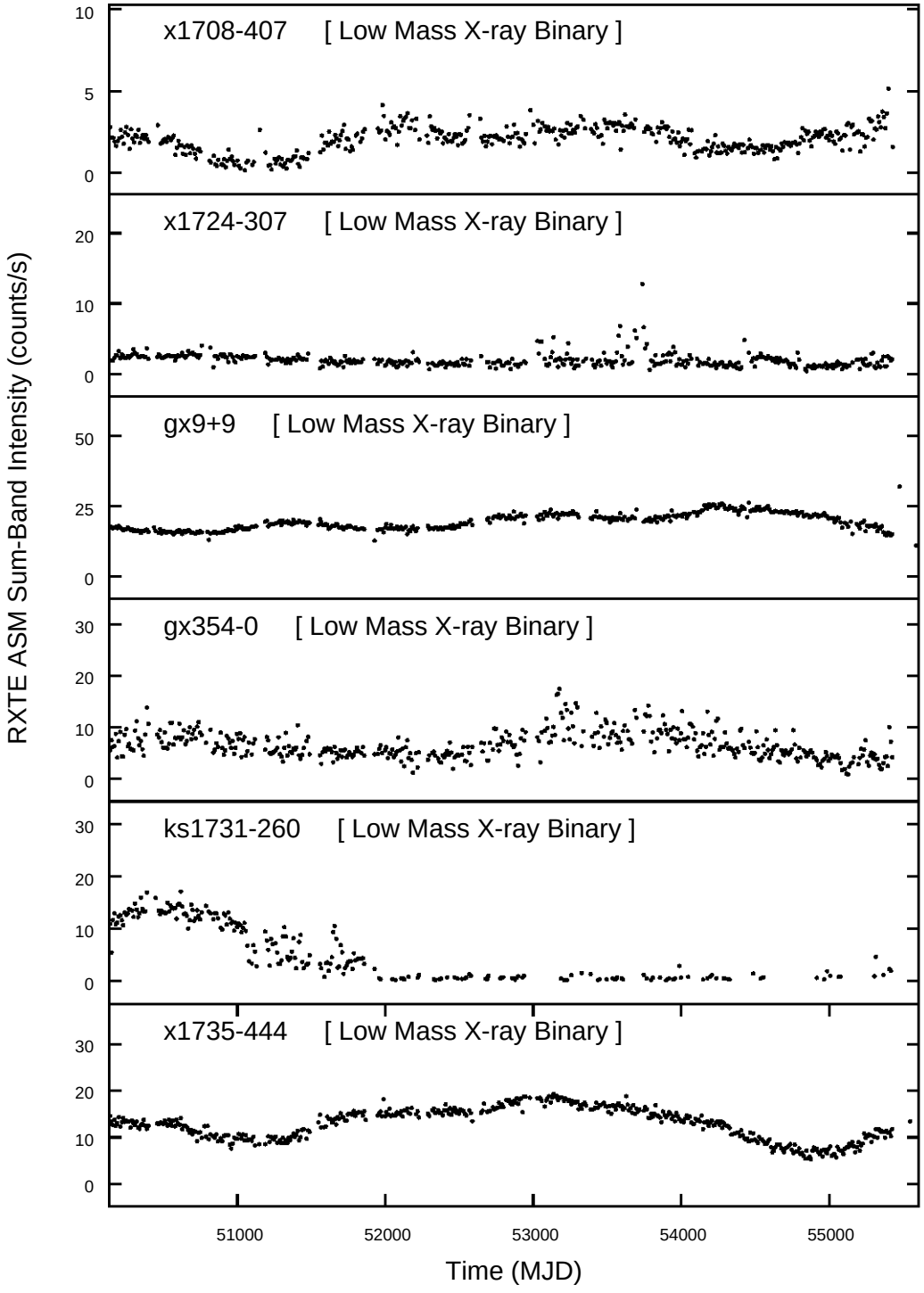

Figure B.7: RXTE ASM lightcurves of significantly detected sources (RA: 17)

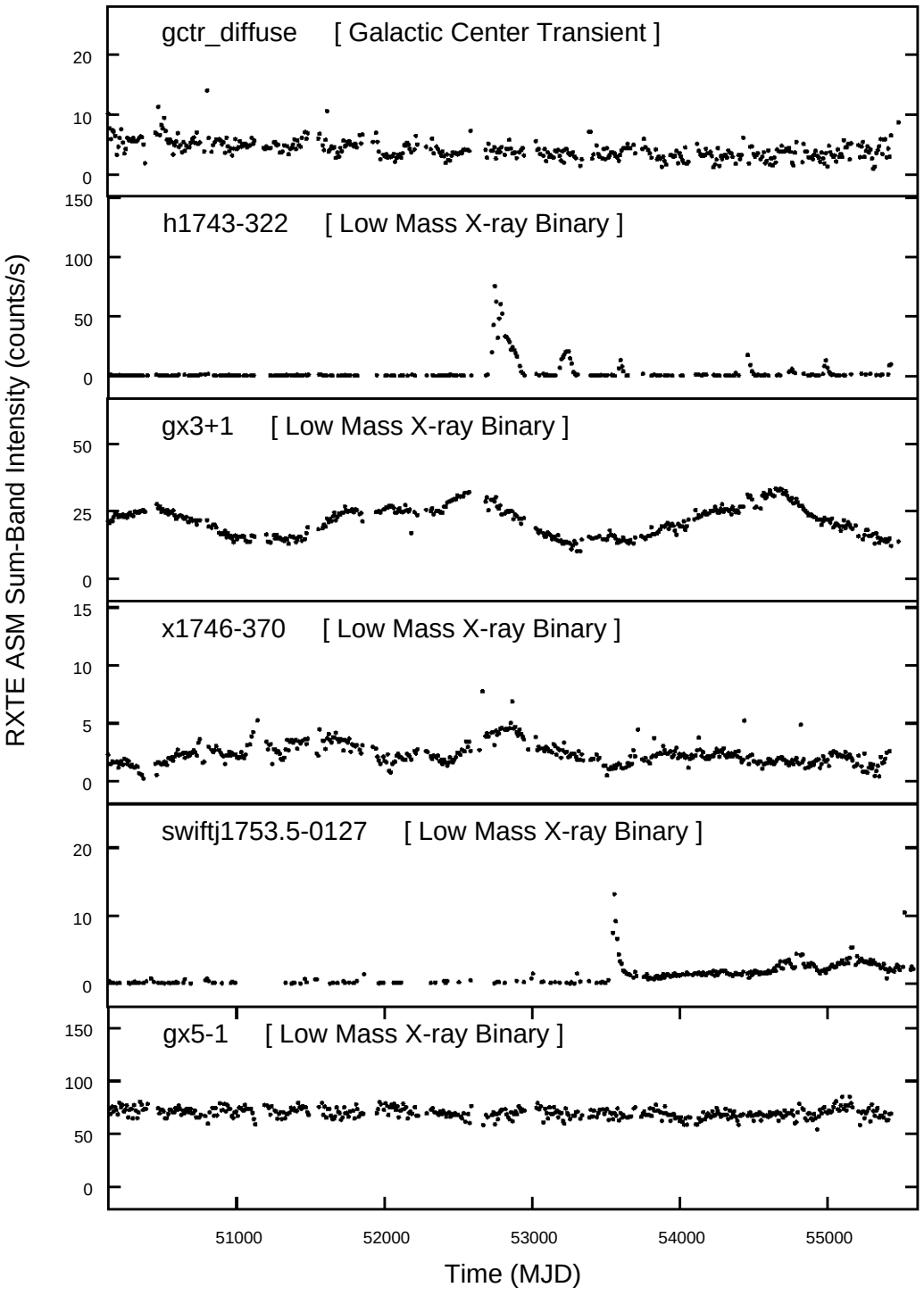

Figure B.8: RXTE ASM lightcurves of significantly detected sources (RA: 17)

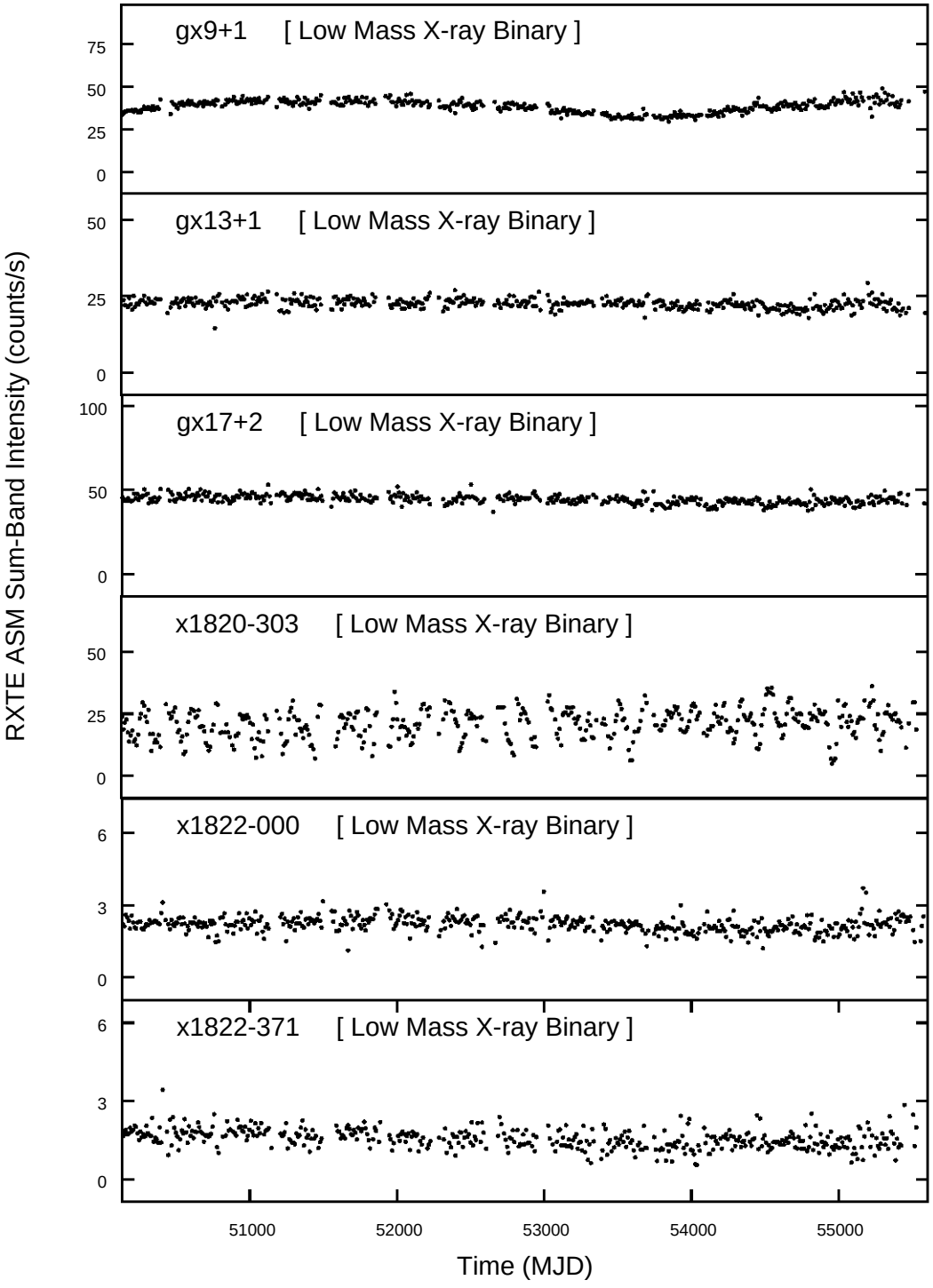

Figure B.9: RXTE ASM lightcurves of significantly detected sources (RA: 18)

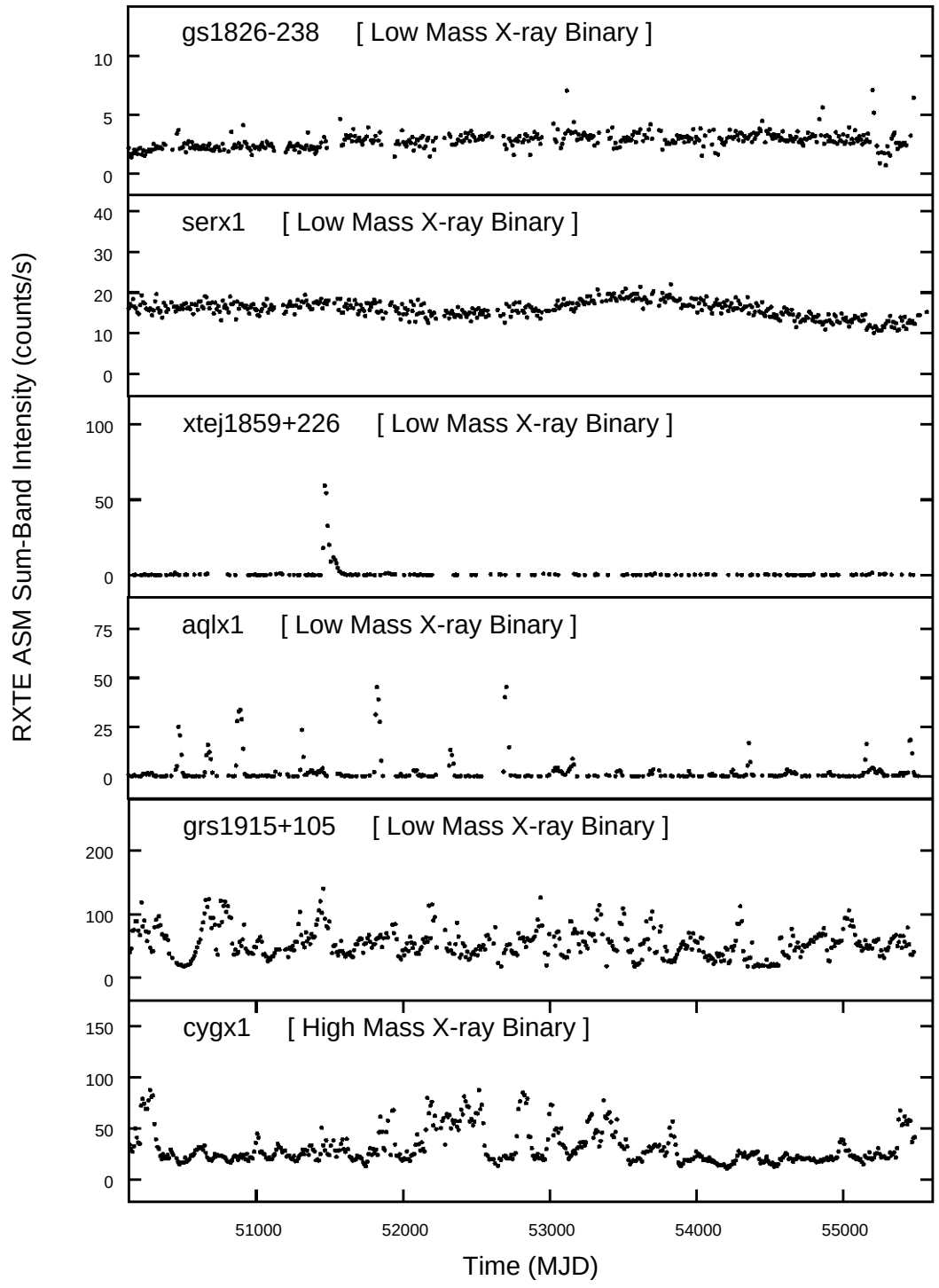

Figure B.10: RXTE ASM lightcurves of significantly detected sources (RA: 18-19)

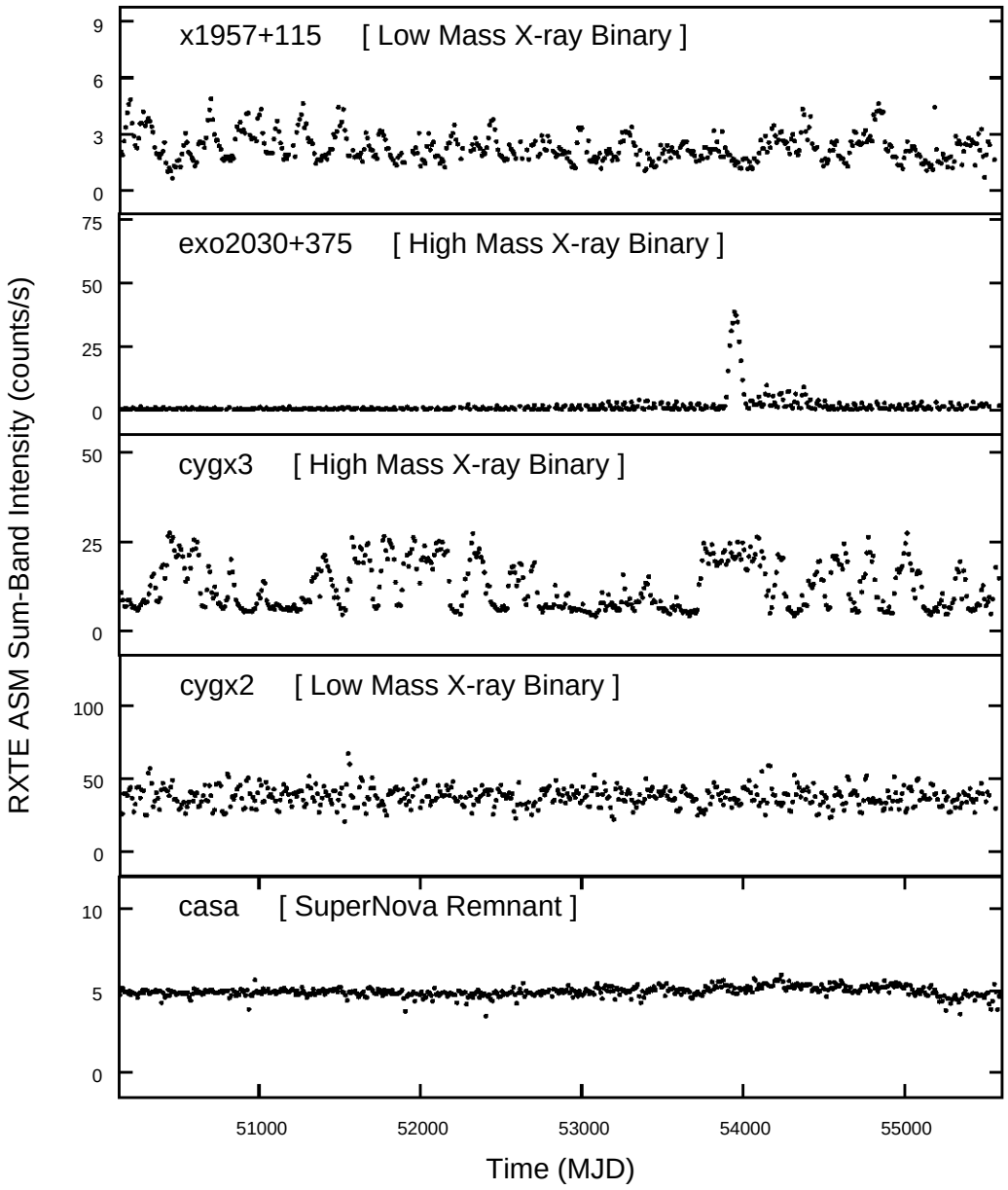

Figure B.11: RXTE ASM lightcurves of significantly detected sources (RA: 19-24)

Appendix C

Period Analysis Results

The period analysis results for all the potentially periodic RXTE ASM sources are presented here. Firstly, the 27 significantly detected ($> 3\sigma$) sources are presented, for which the period analysis should yield the most reliable results. They are followed, in a separate section, by the additional sources that were marginally detected ($< 3\sigma$).

The process for obtaining these results was discussed in Chapters 3 & 5 and the results themselves were discussed in Chapter 5. The period analysis was conducted over the period range $2 - 1000$ days, using the entire observational baseline of ~ 15 years to generate the L-S, PDM and window functions. For each source, the first set of plots include the following:

- L-S periodogram (top panel)
- PDM (centre panel)
- Window function (bottom panel)
- Noise estimate(s) plotted as horizontal lines/curves (top panel)
- Labels (in days) are included at the peaks for dominant periods (top panel)

The datasets were also split into sliding data windows of length 400 days, with each successive data window overlapping the previous one by 350 days, so that each such window slides along the temporal axis by 50 days in comparison to the previous one. The DPS for a source was constructed from the L-S results from each such data window. For each source, the second set of plots include the following over the period range $20 - 1000$ days:

- RXTE ASM one-day-average sum-band lightcurve re-binned to 10 days (top panel)
- L-S over entire ~ 15 year dataset (left panel)
- DPS time vs period in x-y plane and power in z (main panel)
- scale bar to indicate DPS power (right)

C.1 Significant Sources

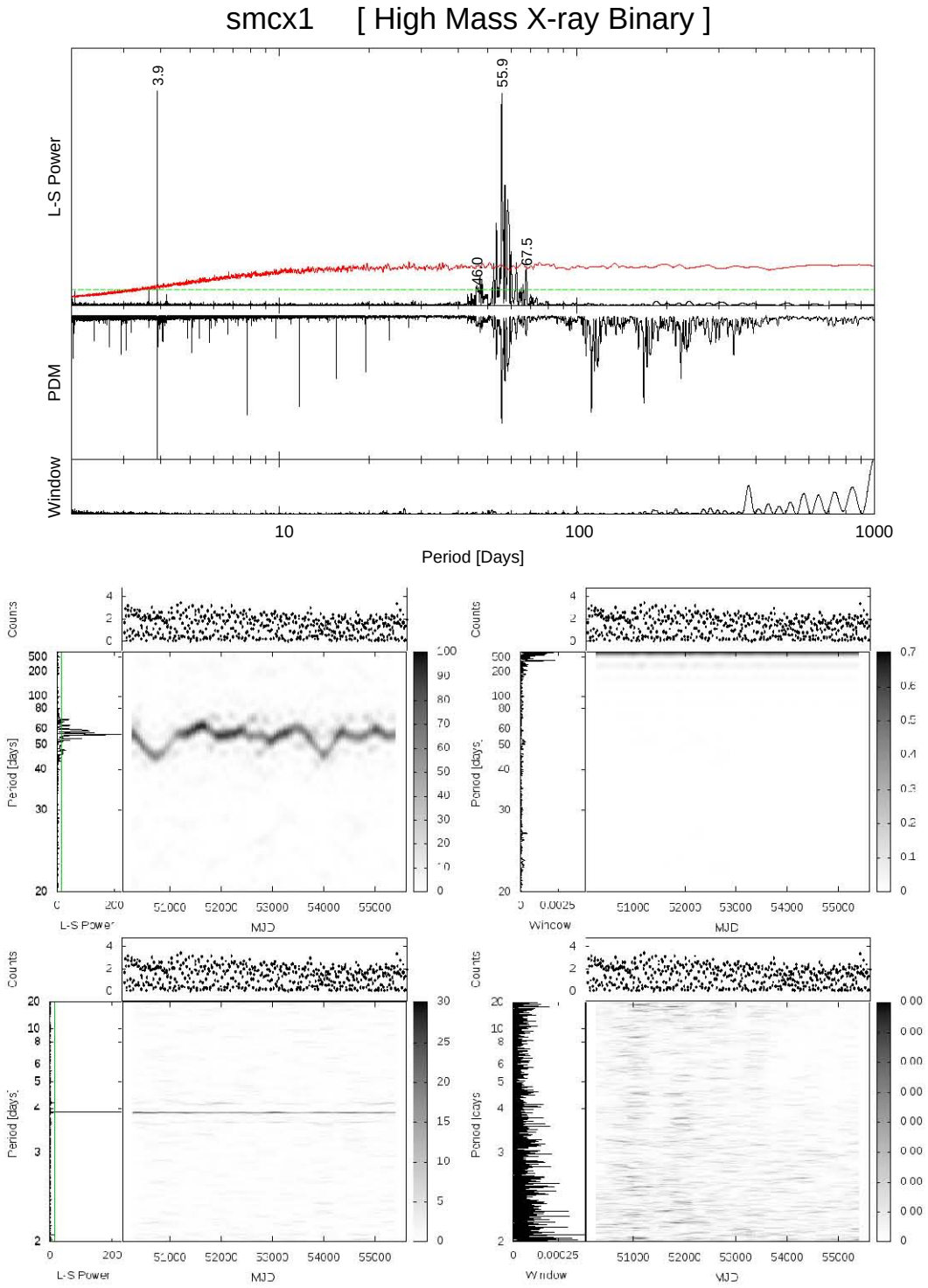

Figure C.1: Lightcurve, L-S, PDM, window, noise, DPS and DWF of smcx1

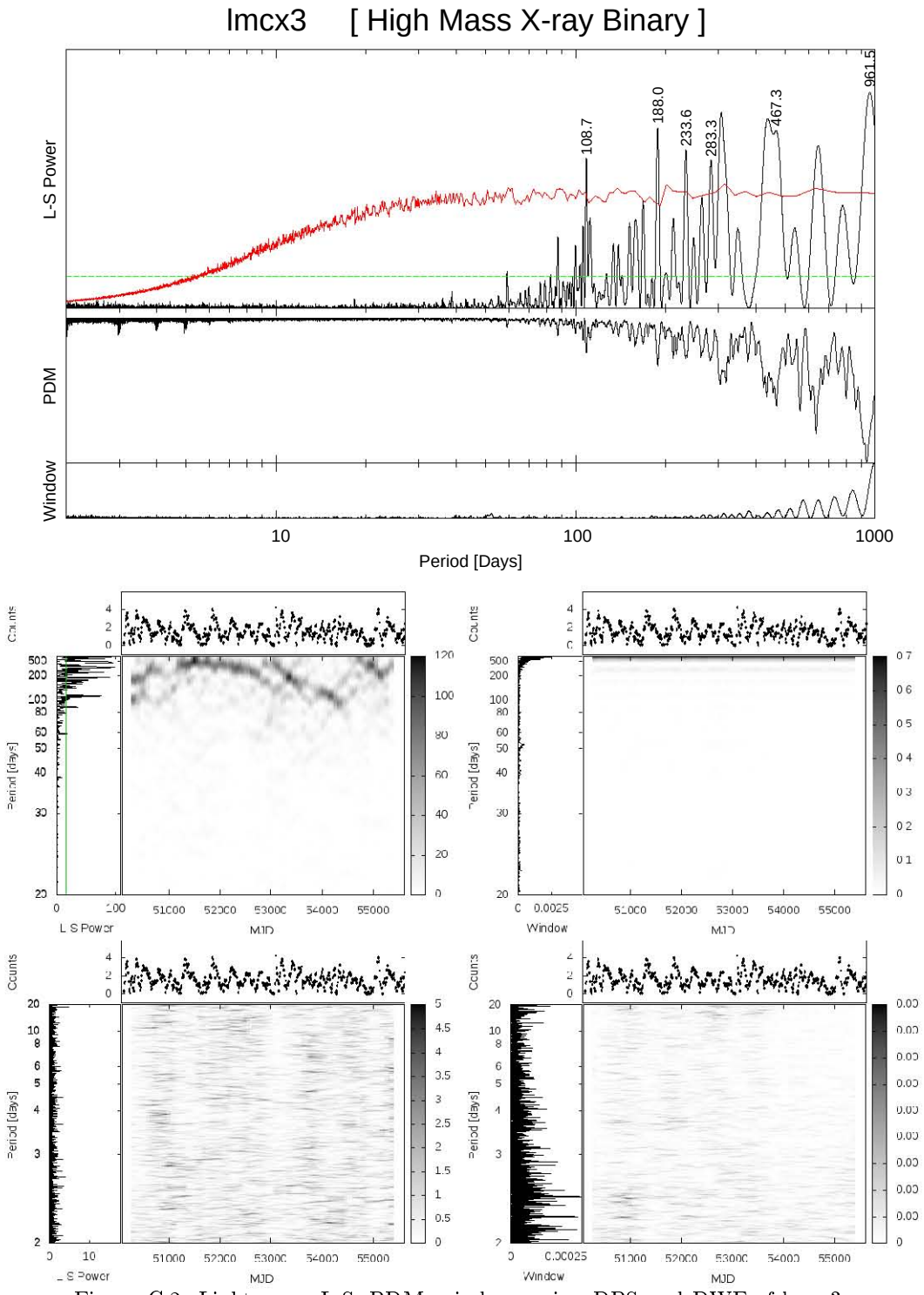

Figure C.2: Lightcurve, L-S, PDM, window, noise, DPS and DWF of lmcx3

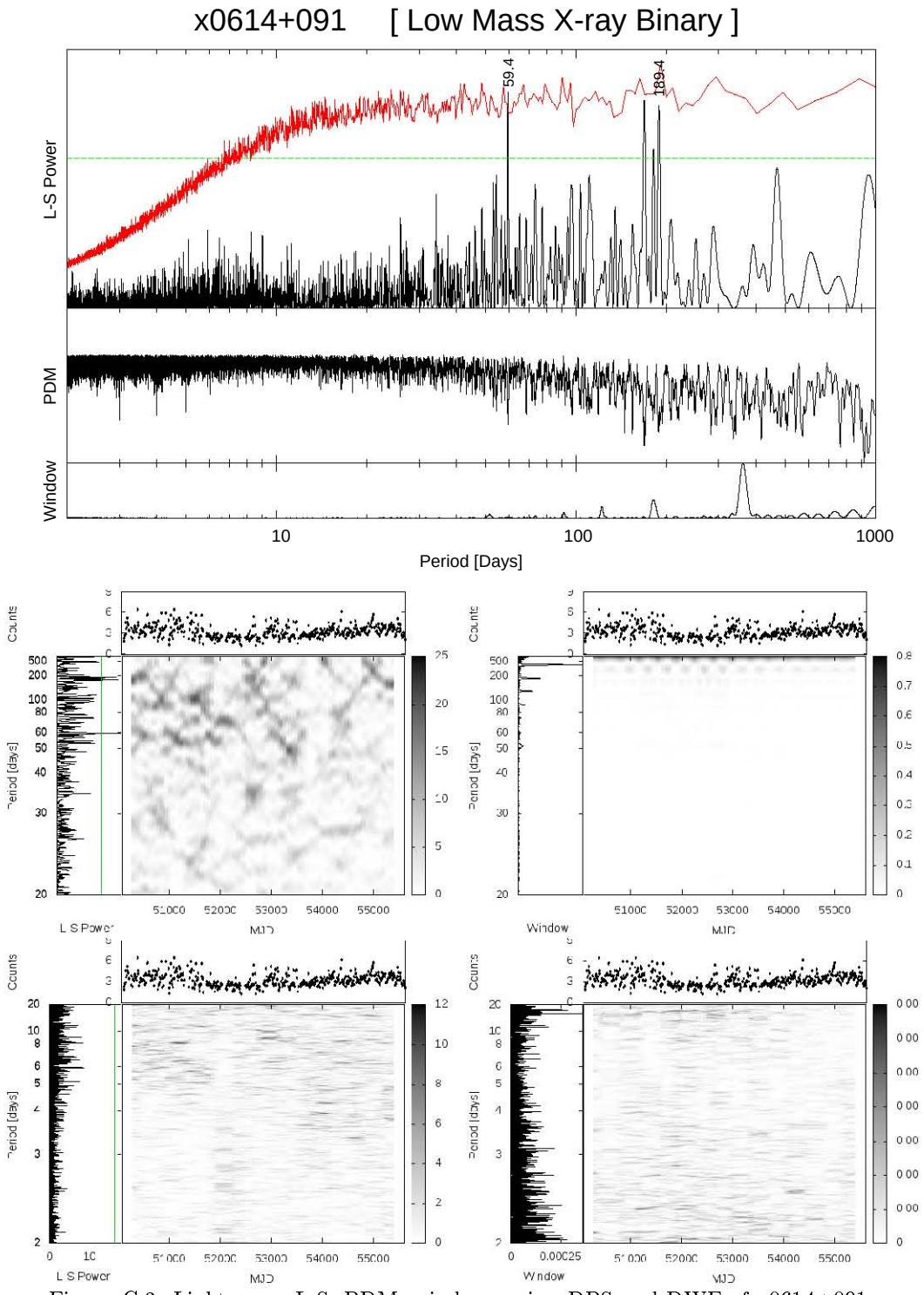

Figure C.3: Lightcurve, L-S, PDM, window, noise, DPS and DWF of x0614+091

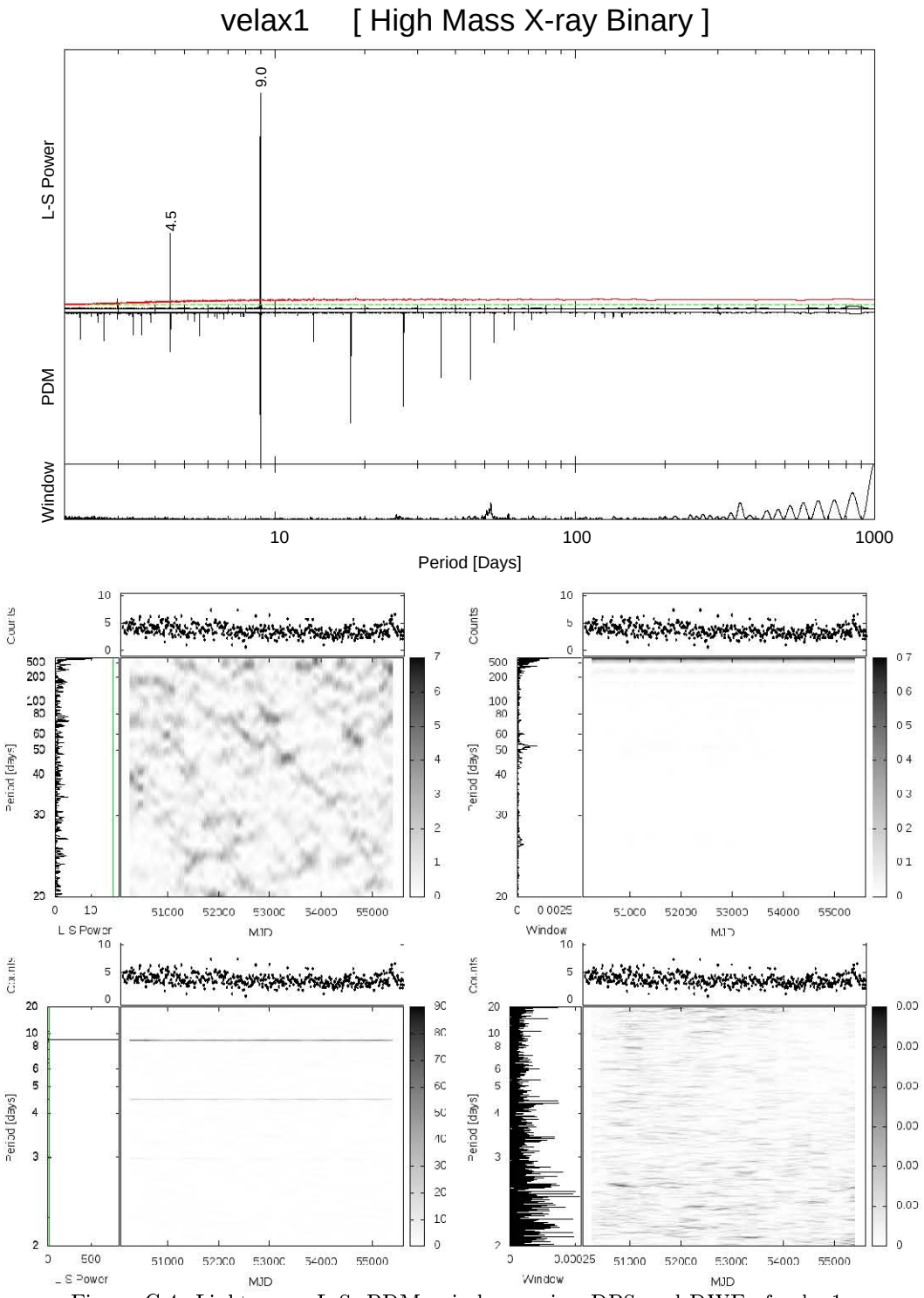

Figure C.4: Lightcurve, L-S, PDM, window, noise, DPS and DWF of velax1

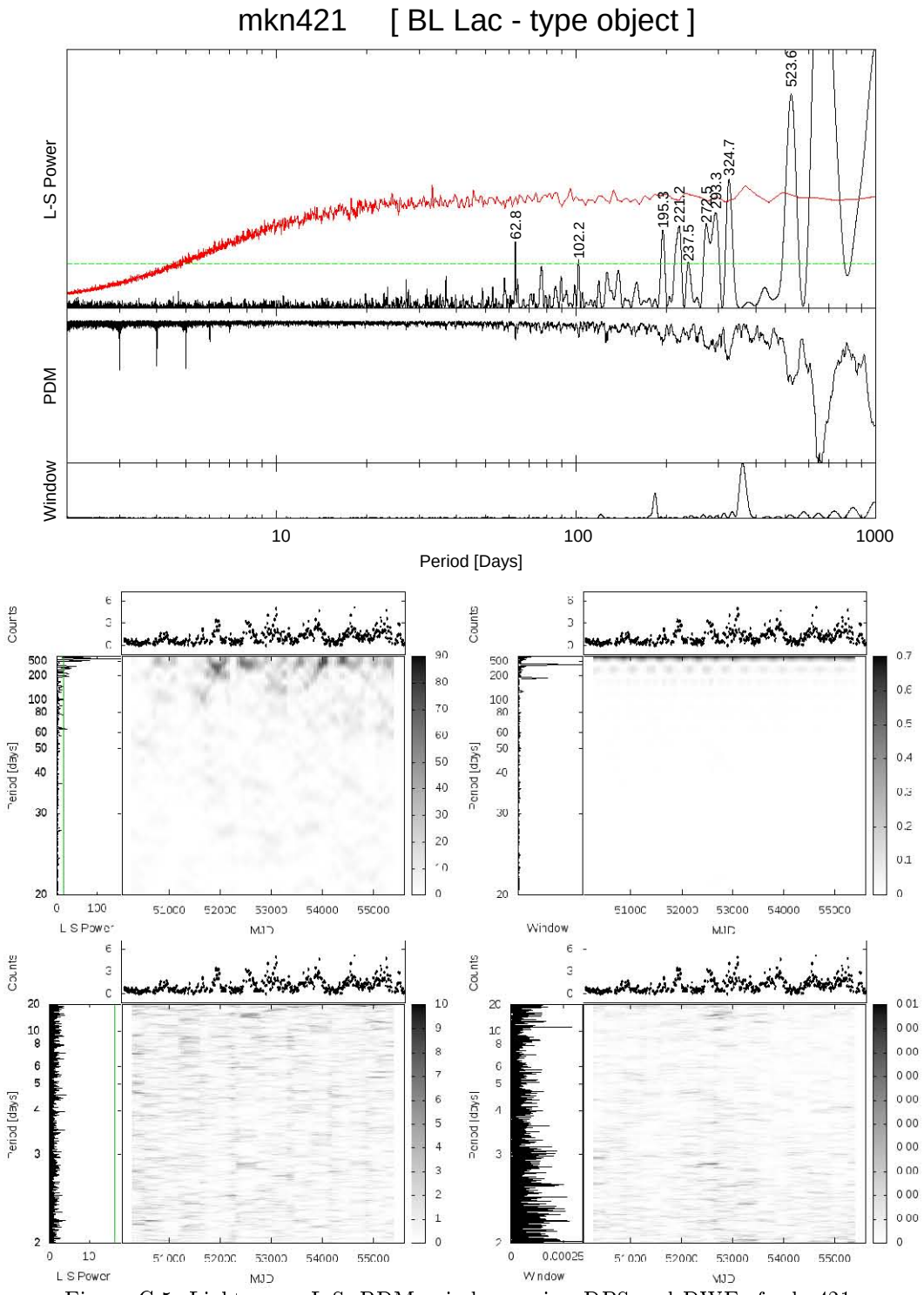

Figure C.5: Lightcurve, L-S, PDM, window, noise, DPS and DWF of mkn421

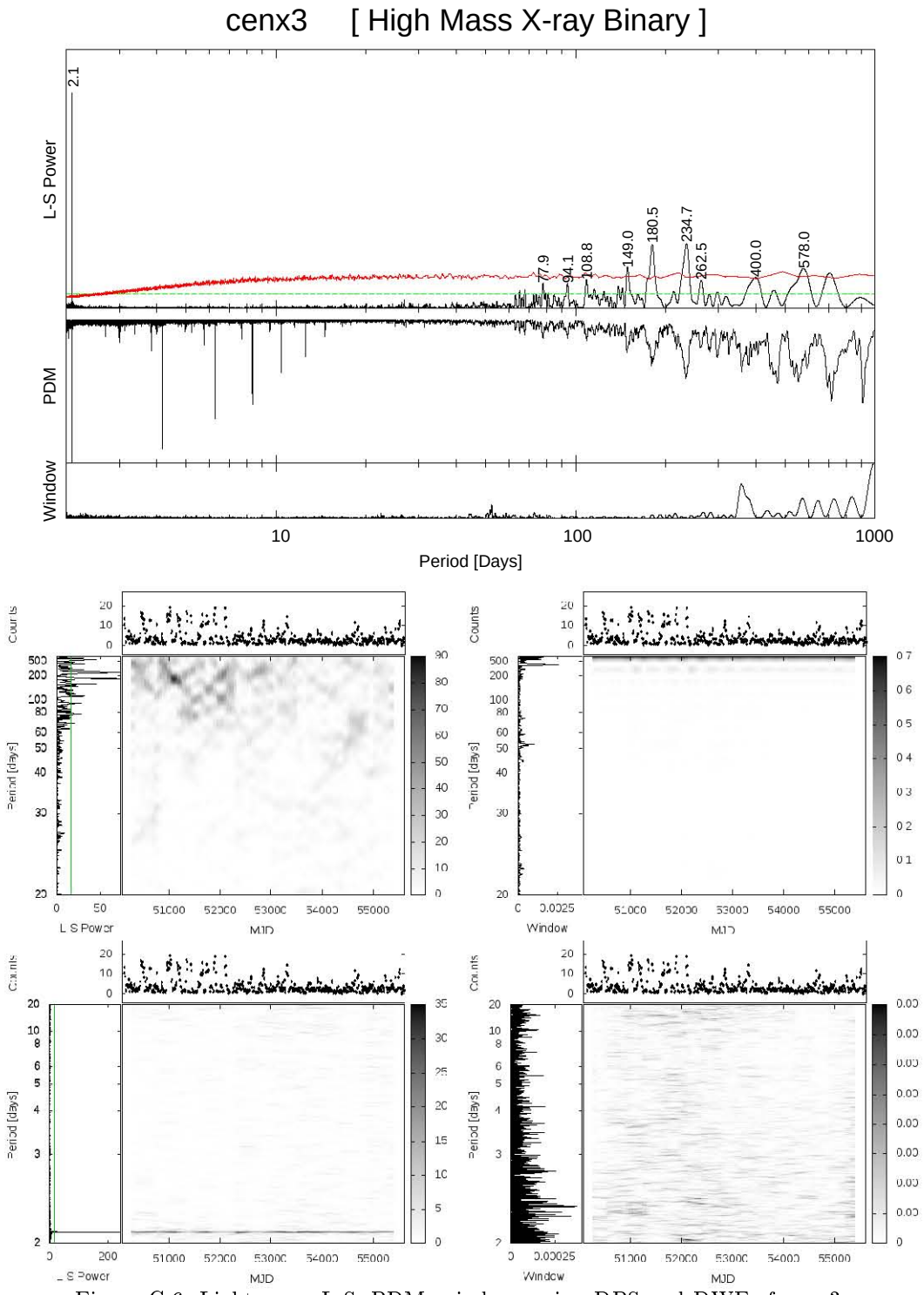

Figure C.6: Lightcurve, L-S, PDM, window, noise, DPS and DWF of cenx3

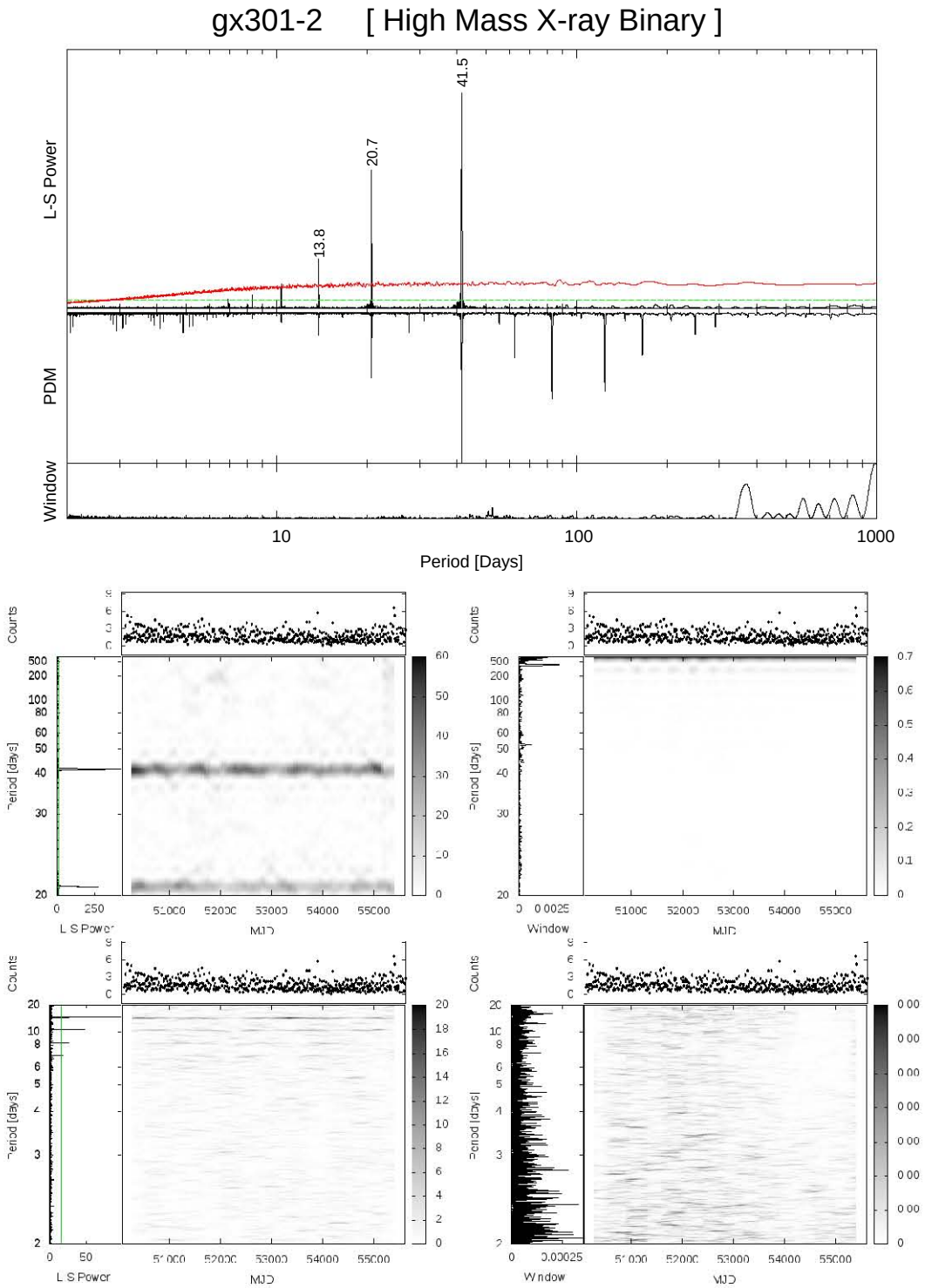

Figure C.7: Lightcurve, L-S, PDM, window, noise, DPS and DWF of gx301-2

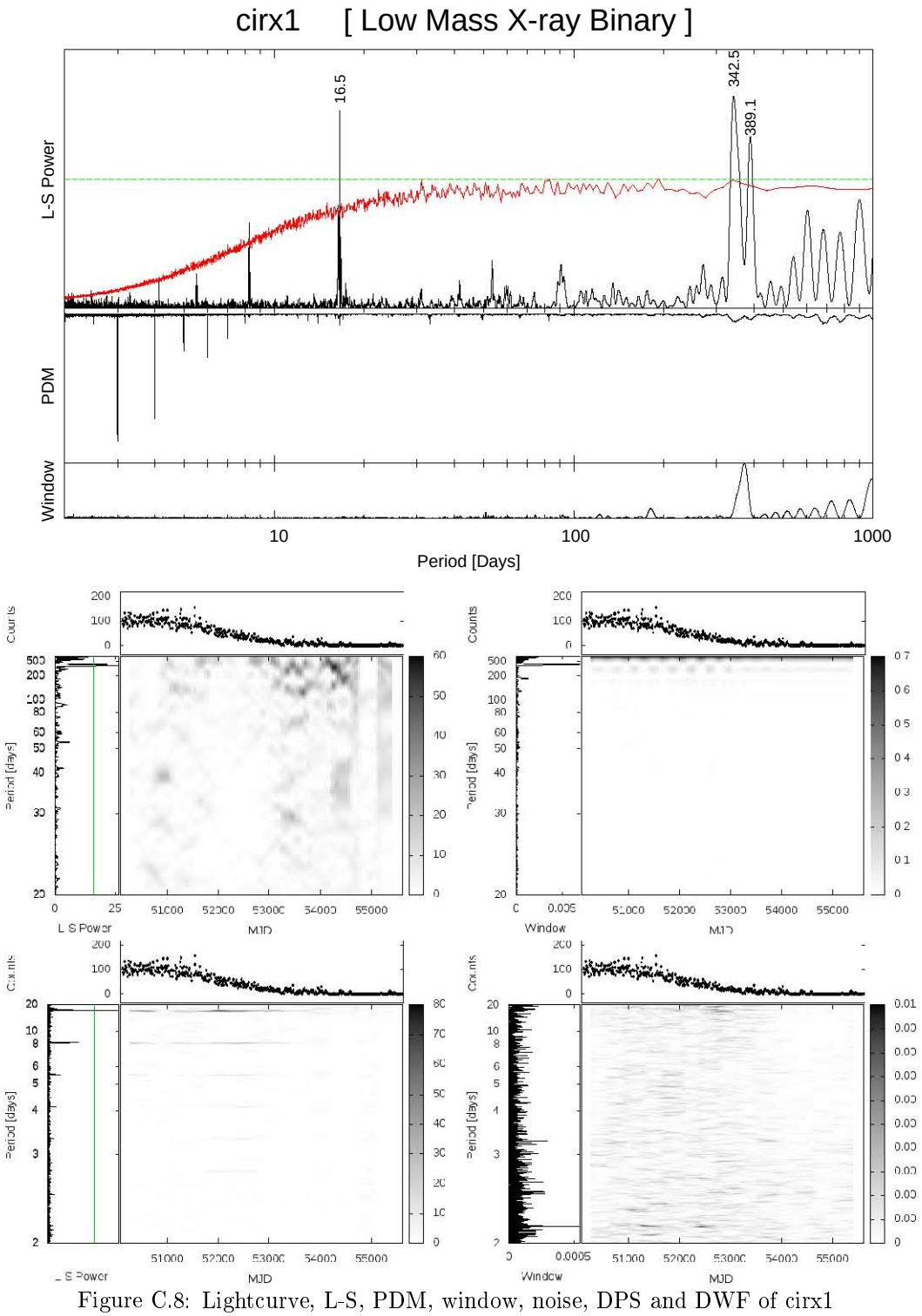

Figure C.8: Lightcurve, L-S, PDM, window, noise, DPS and DWF of cirx1

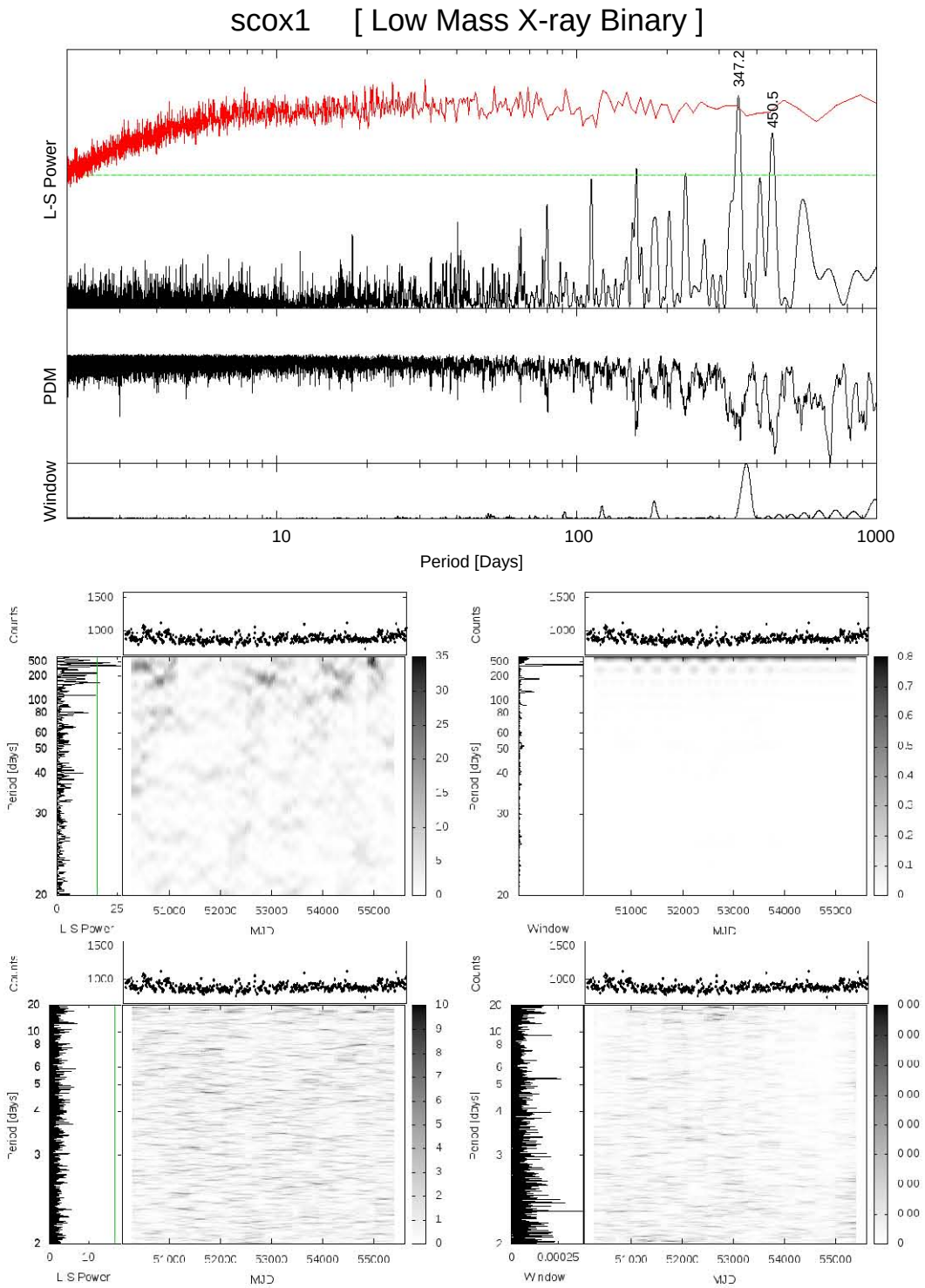

Figure C.9: Lightcurve, L-S, PDM, window, noise, DPS and DWF of scox1

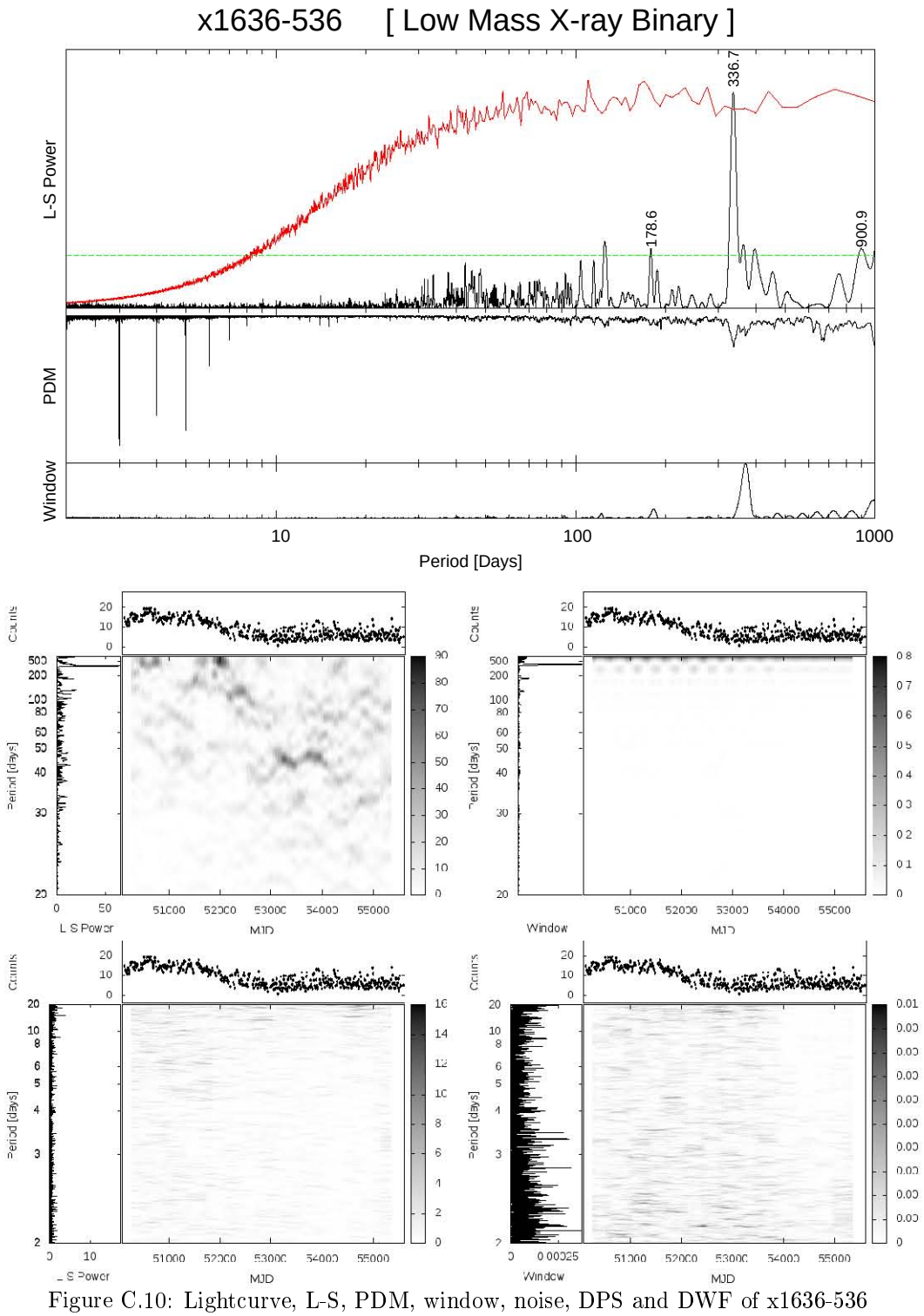

Figure C.10: Lightcurve, L-S, PDM, window, noise, DPS and DWF of x1636-536

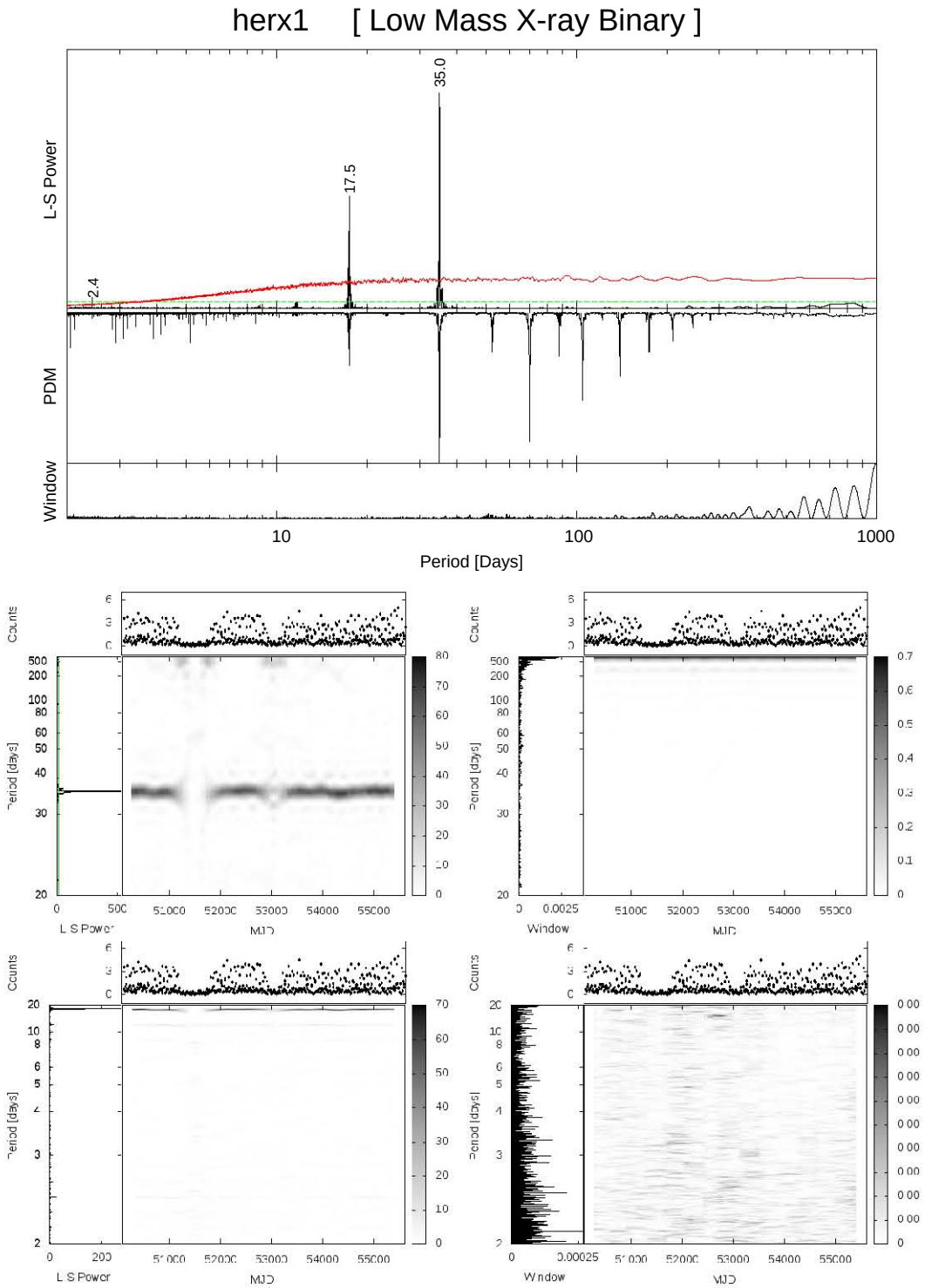

Figure C.11: Lightcurve, L-S, PDM, window, noise, DPS and DWF of herx1

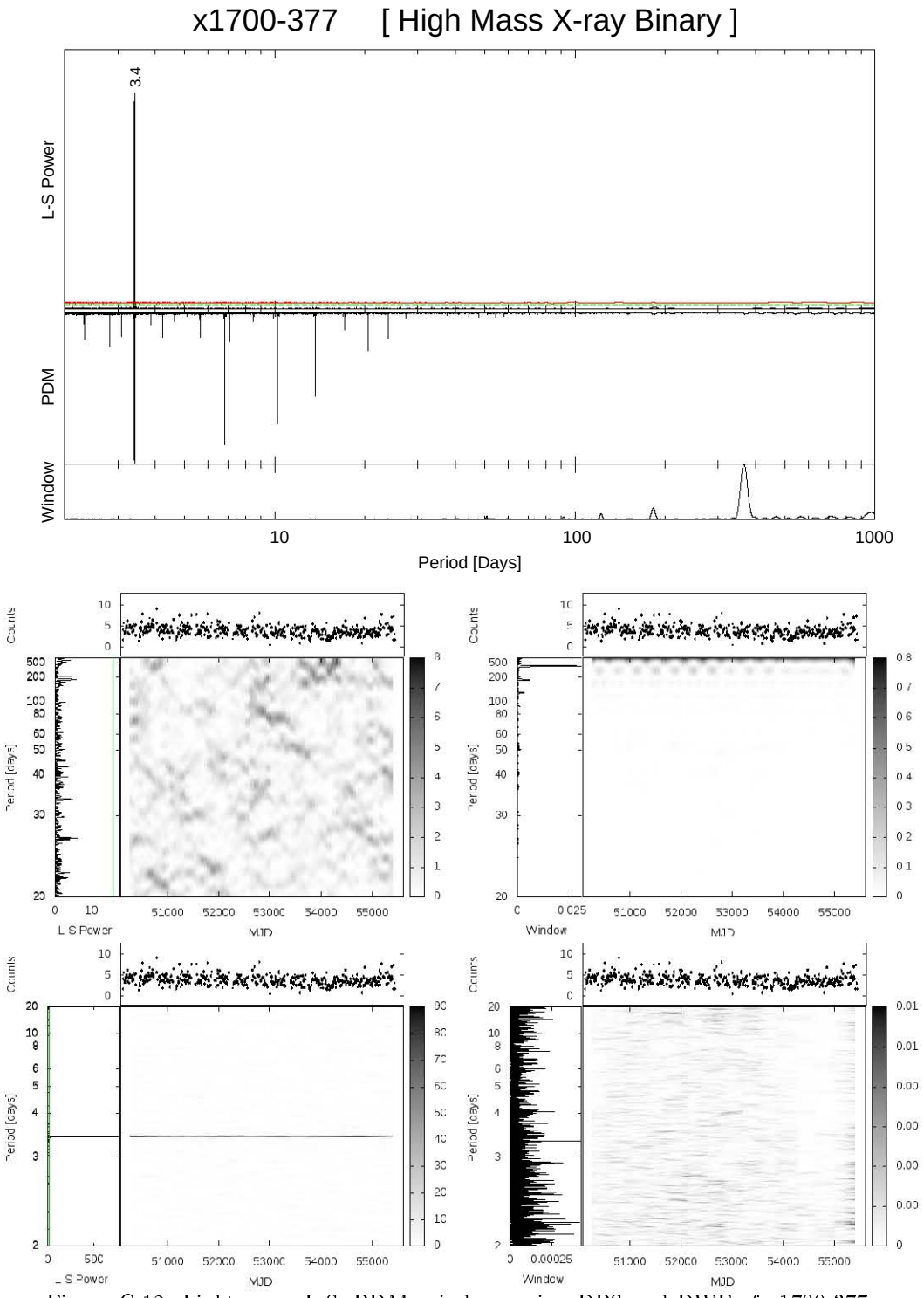

Figure C.12: Lightcurve, L-S, PDM, window, noise, DPS and DWF of x1700-377

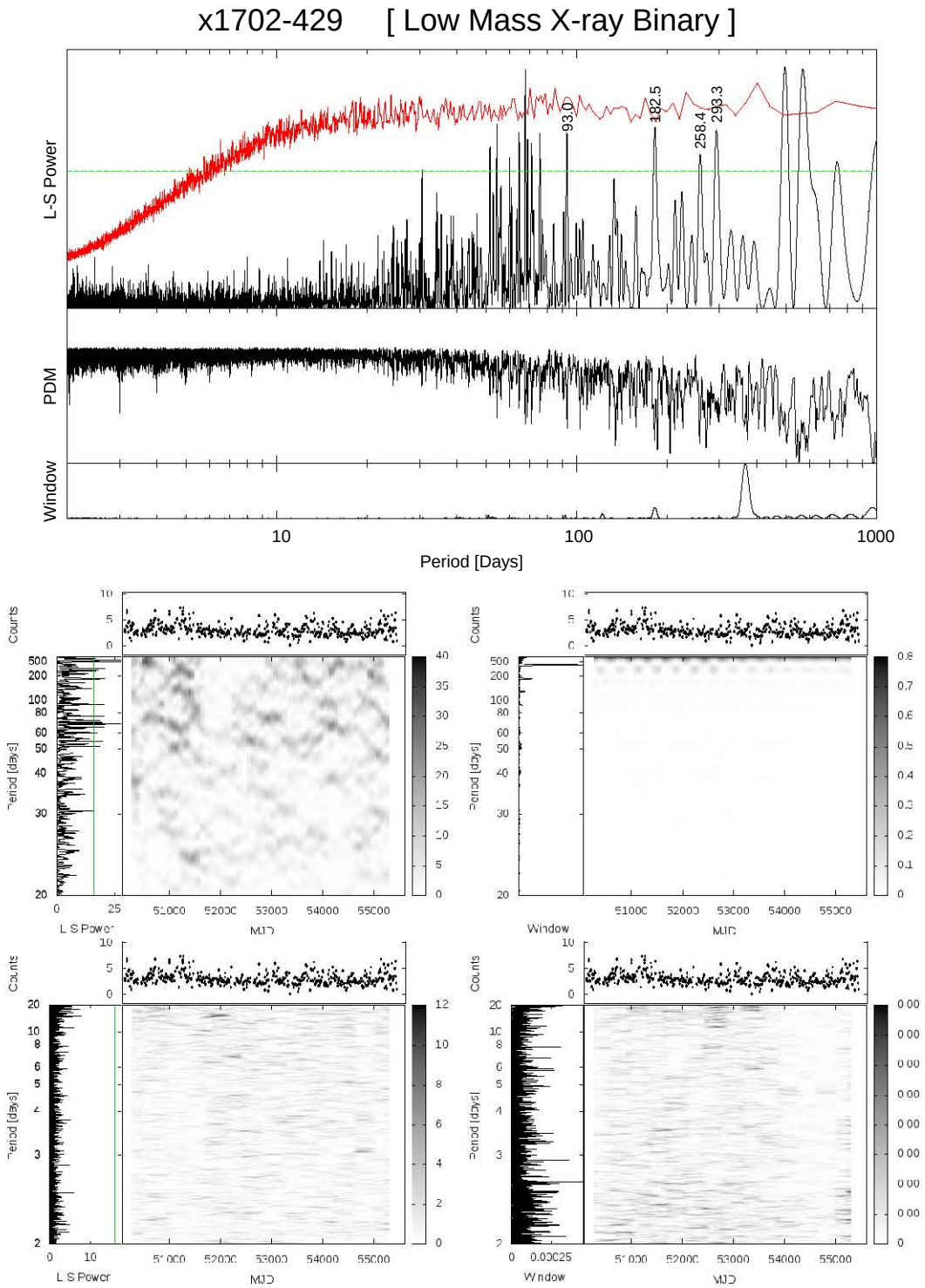

Figure C.13: Lightcurve, L-S, PDM, window, noise, DPS and DWF of x1702-429

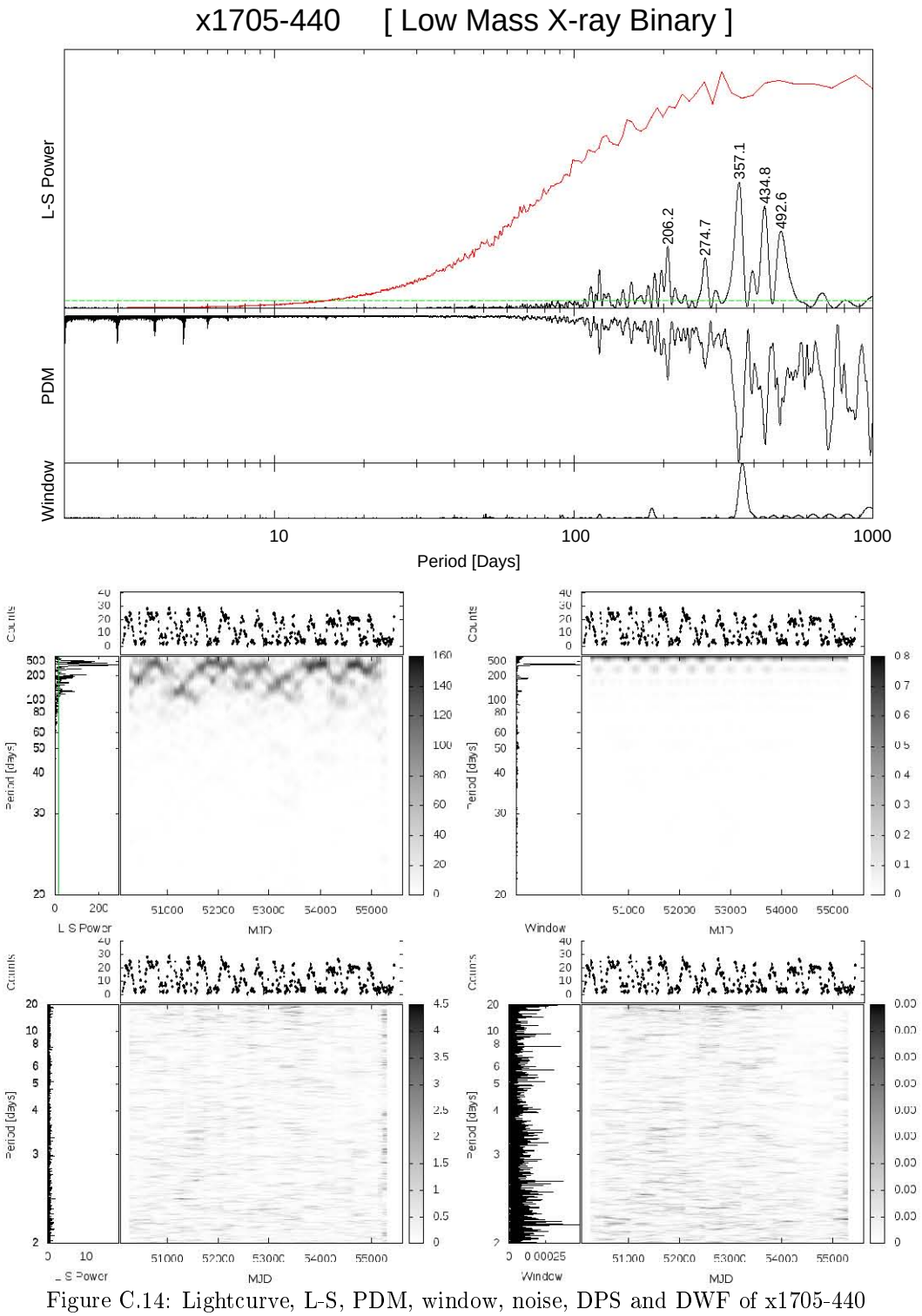

Figure C.14: Lightcurve, L-S, PDM, window, noise, DPS and DWF of x1705-440

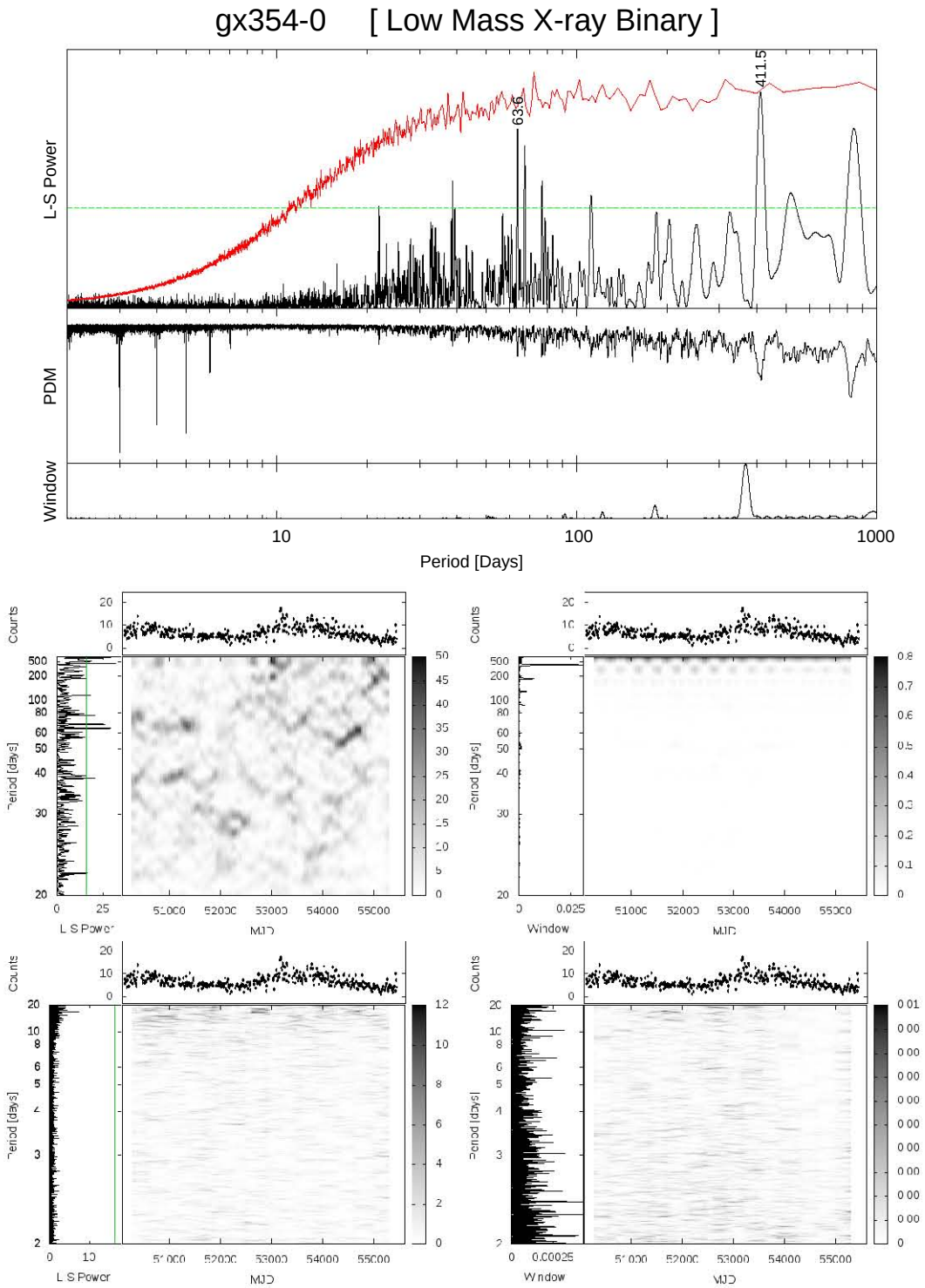

Figure C.15: Lightcurve, L-S, PDM, window, noise, DPS and DWF of gx354-0

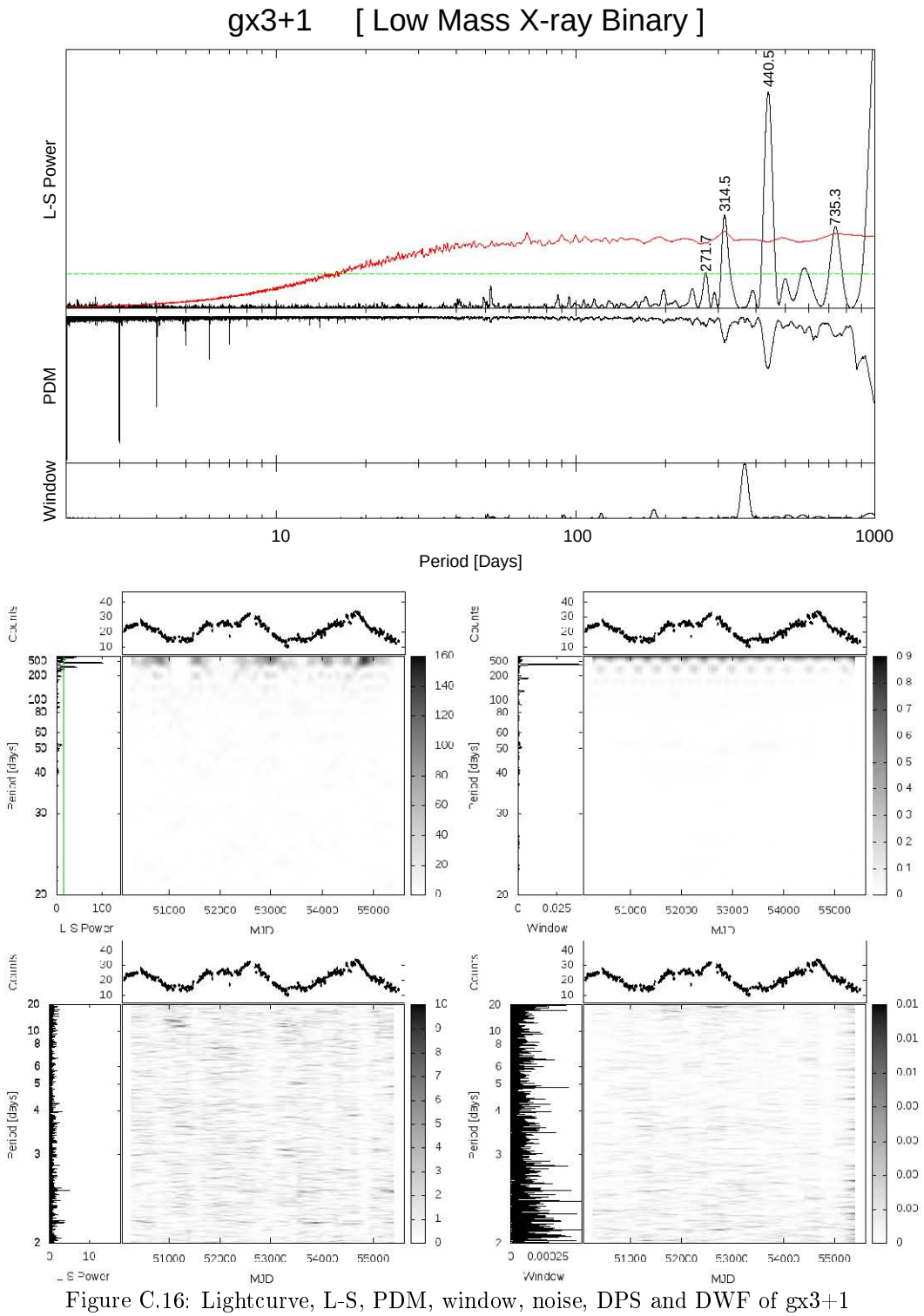

Figure C.16: Lightcurve, L-S, PDM, window, noise, DPS and DWF of gx3+1

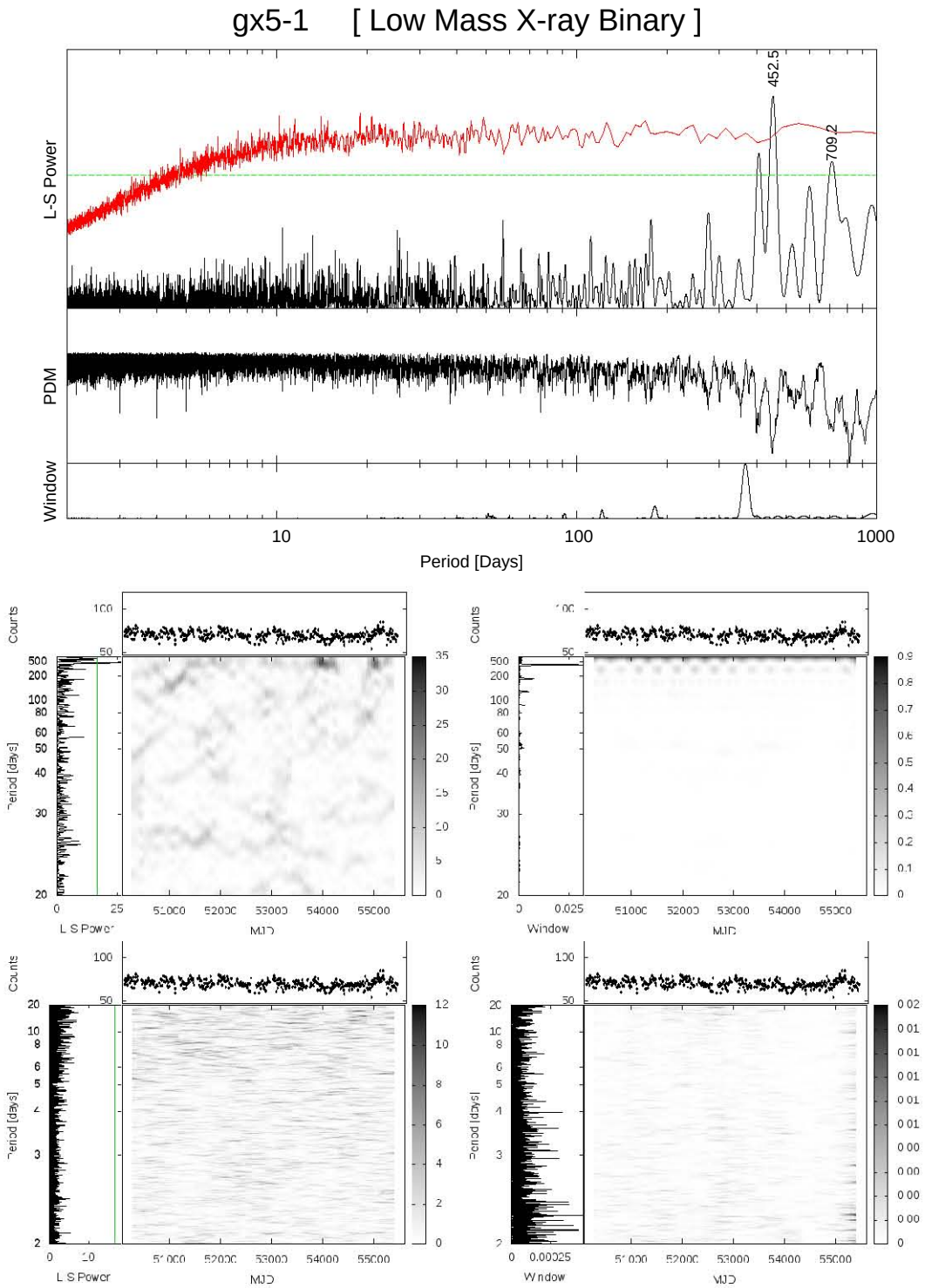

Figure C.17: Lightcurve, L-S, PDM, window, noise, DPS and DWF of gx5-1

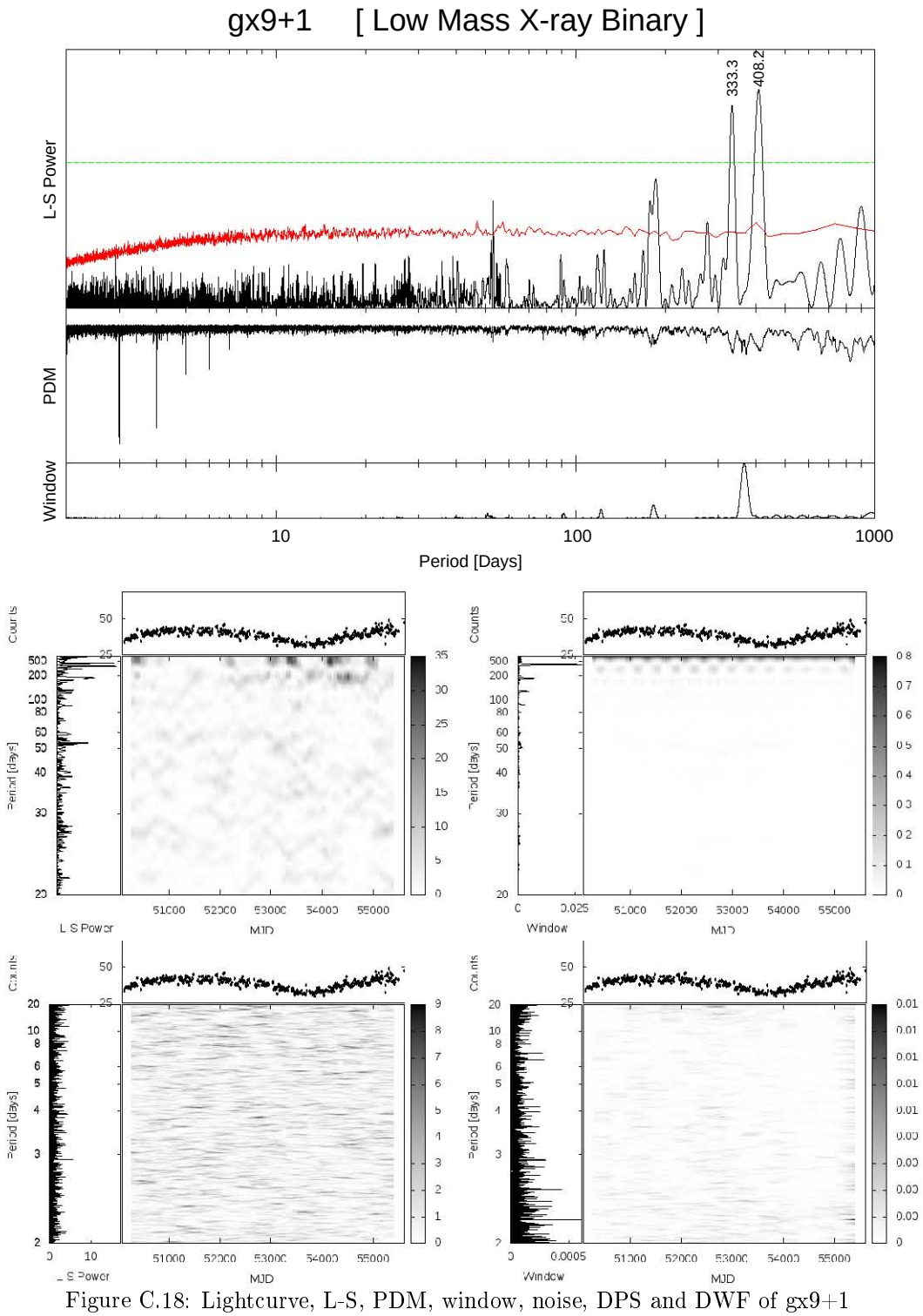

Figure C.18: Lightcurve, L-S, PDM, window, noise, DPS and DWF of gx9+1

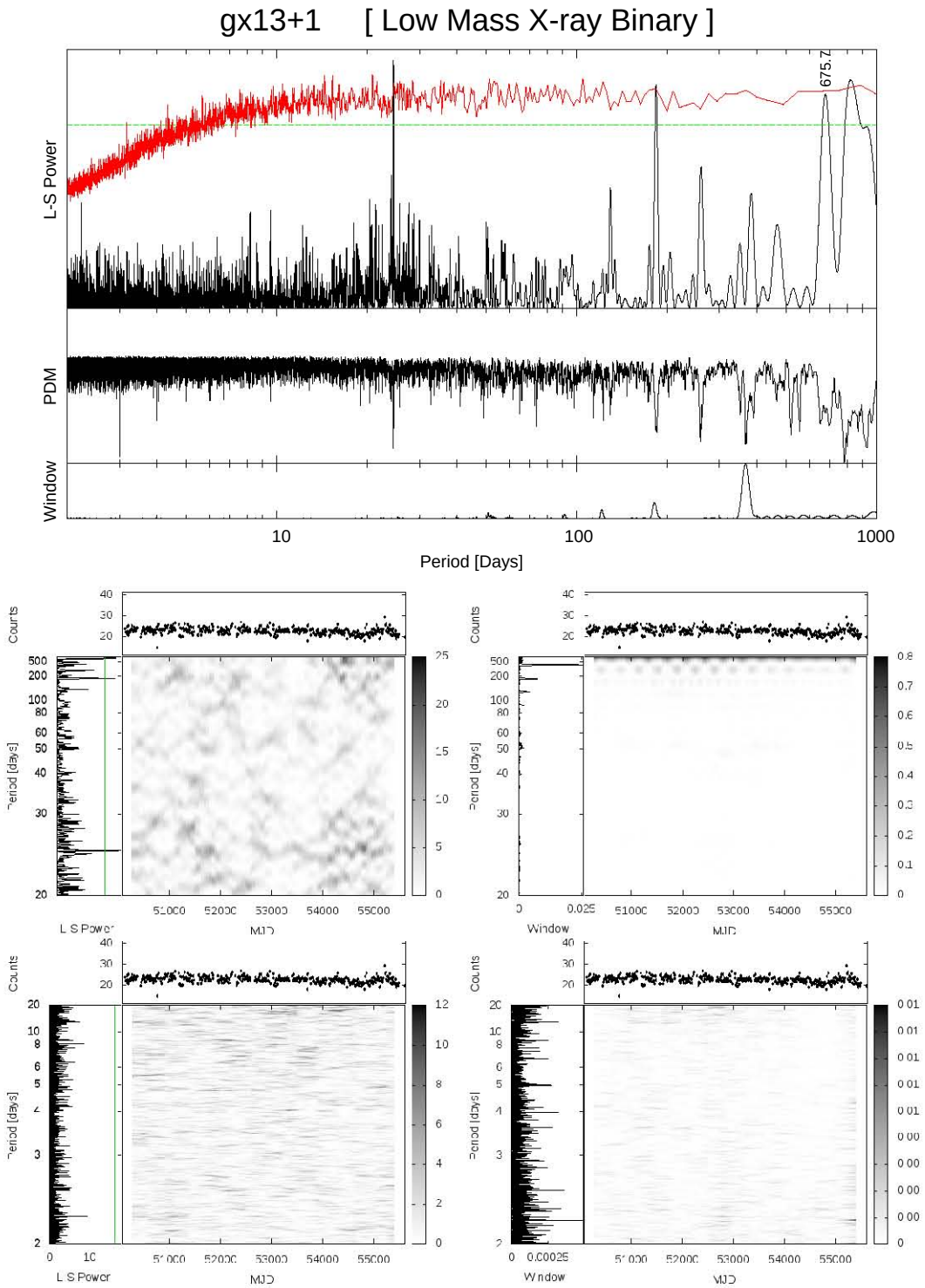

Figure C.19: Lightcurve, L-S, PDM, window, noise, DPS and DWF of gx13+1

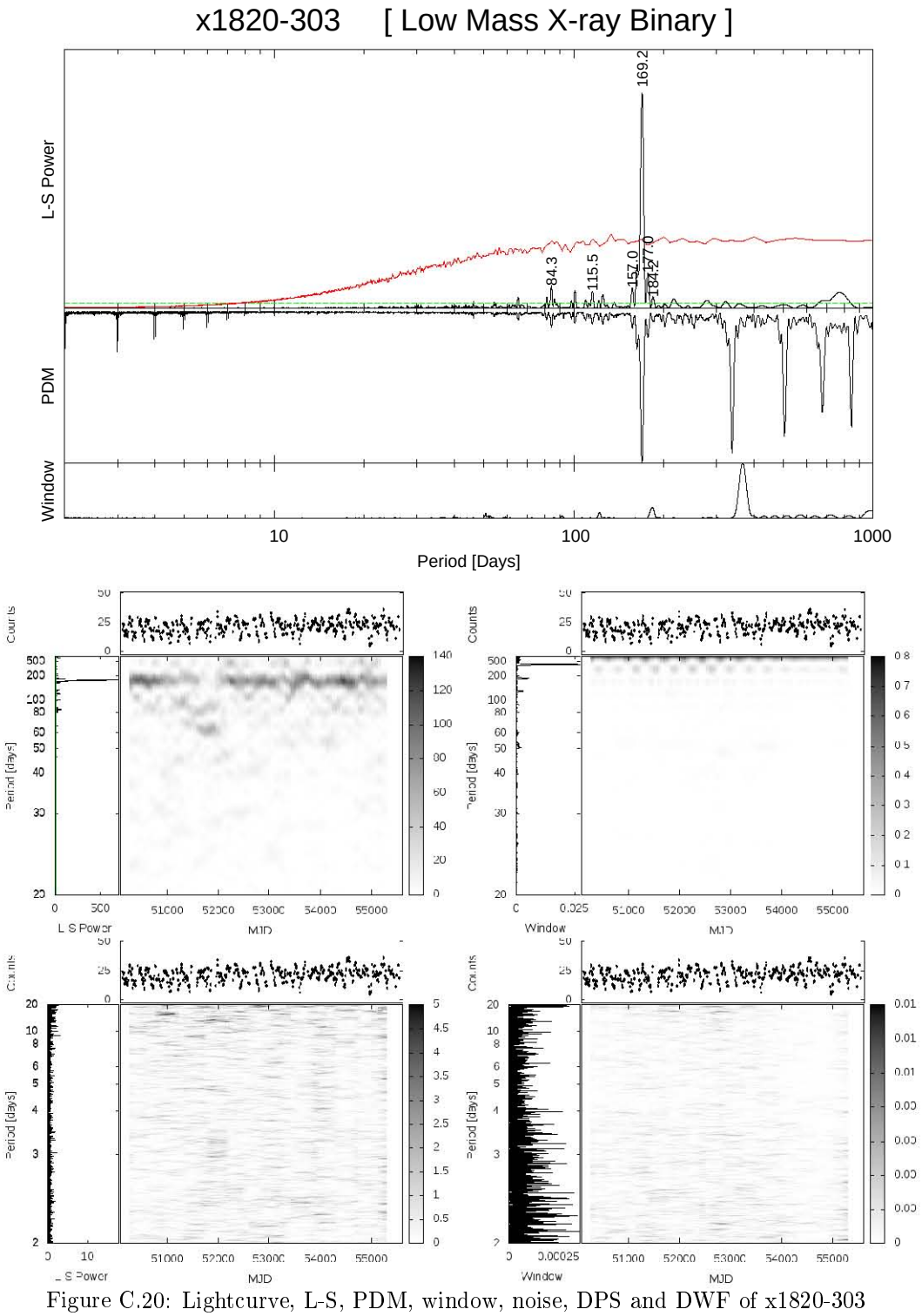

Figure C.20: Lightcurve, L-S, PDM, window, noise, DPS and DWF of x1820-303

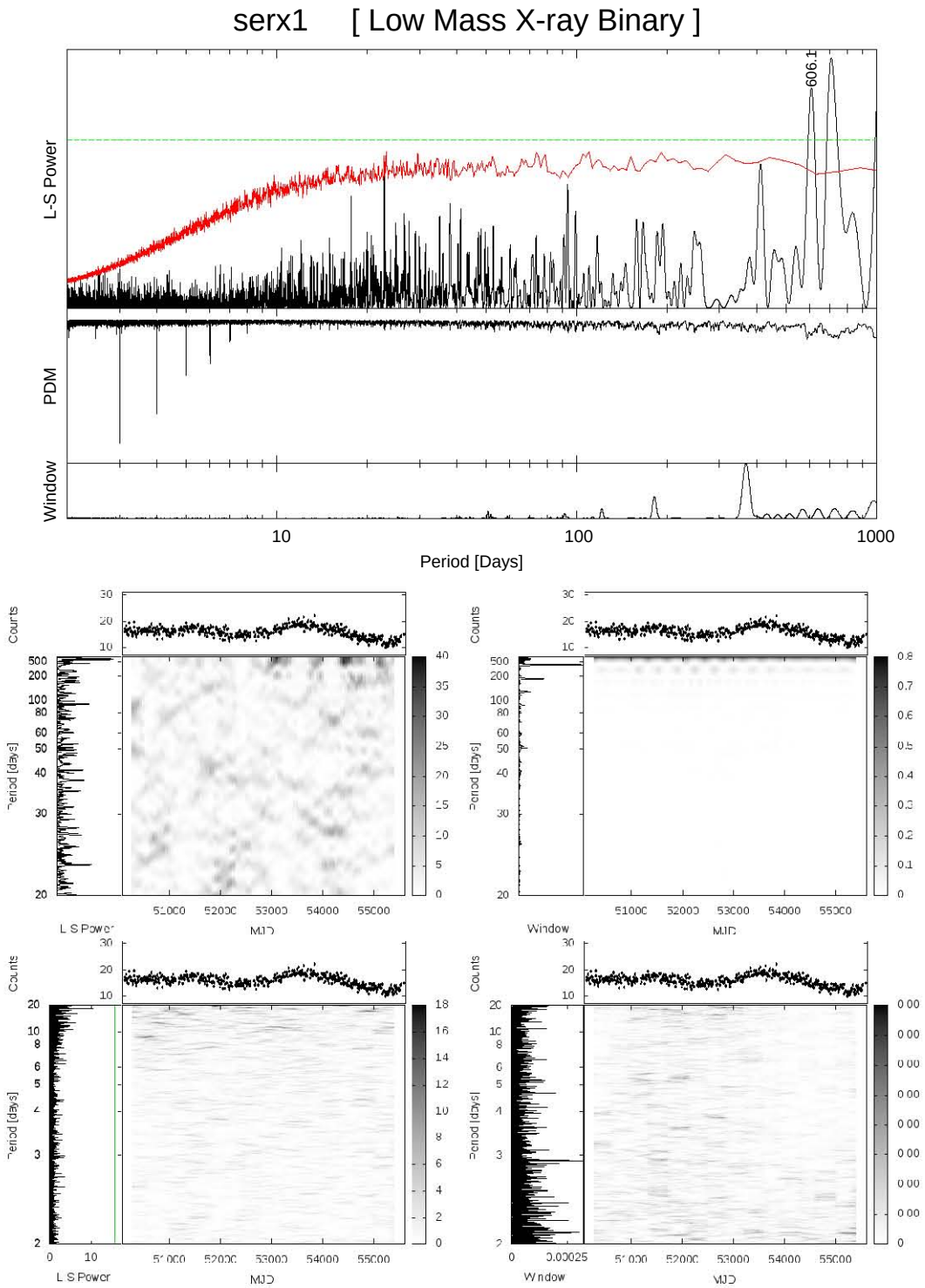

Figure C.21: Lightcurve, L-S, PDM, window, noise, DPS and DWF of serx1

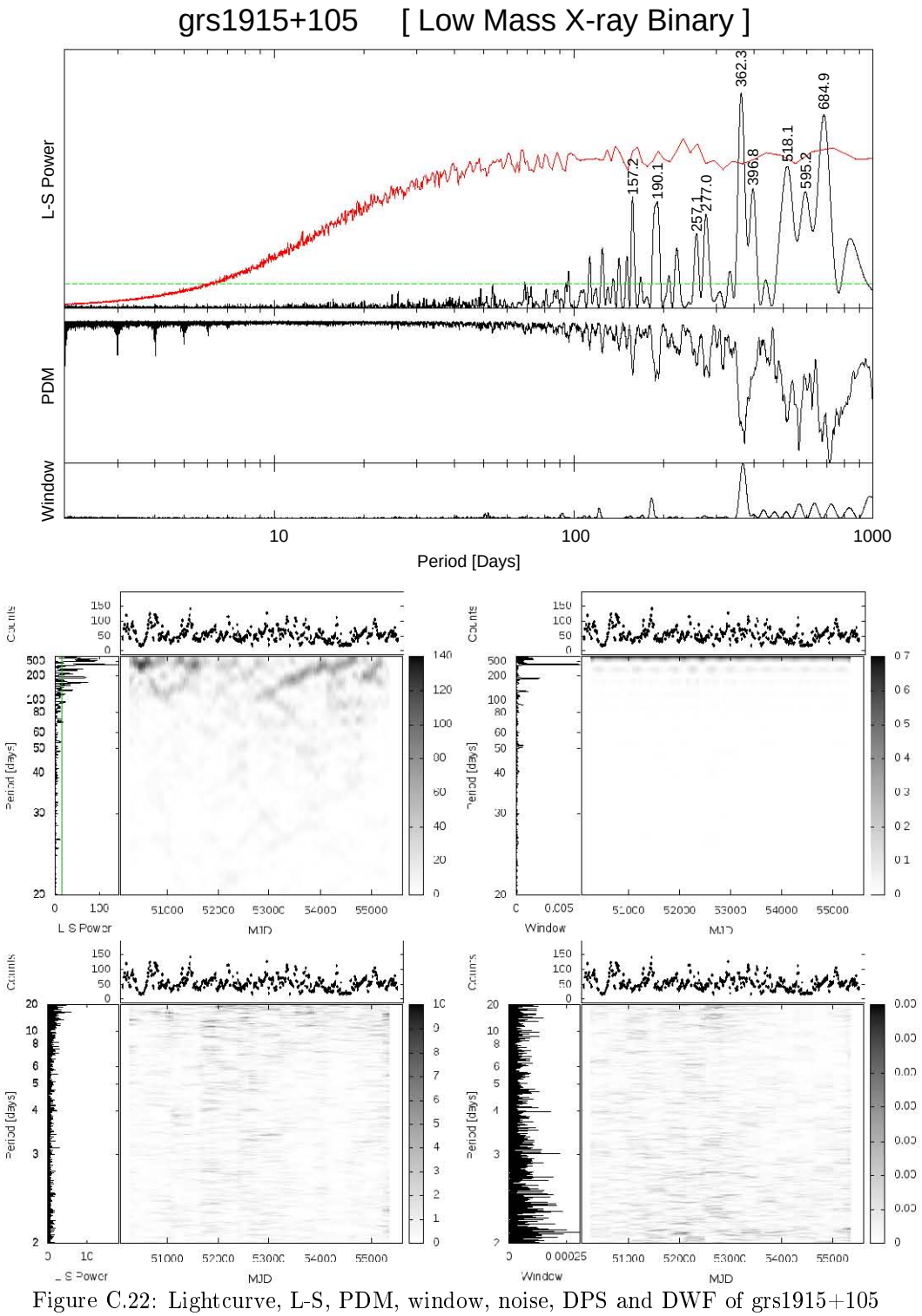

Figure C.22: Lightcurve, L-S, PDM, window, noise, DPS and DWF of grs1915+105

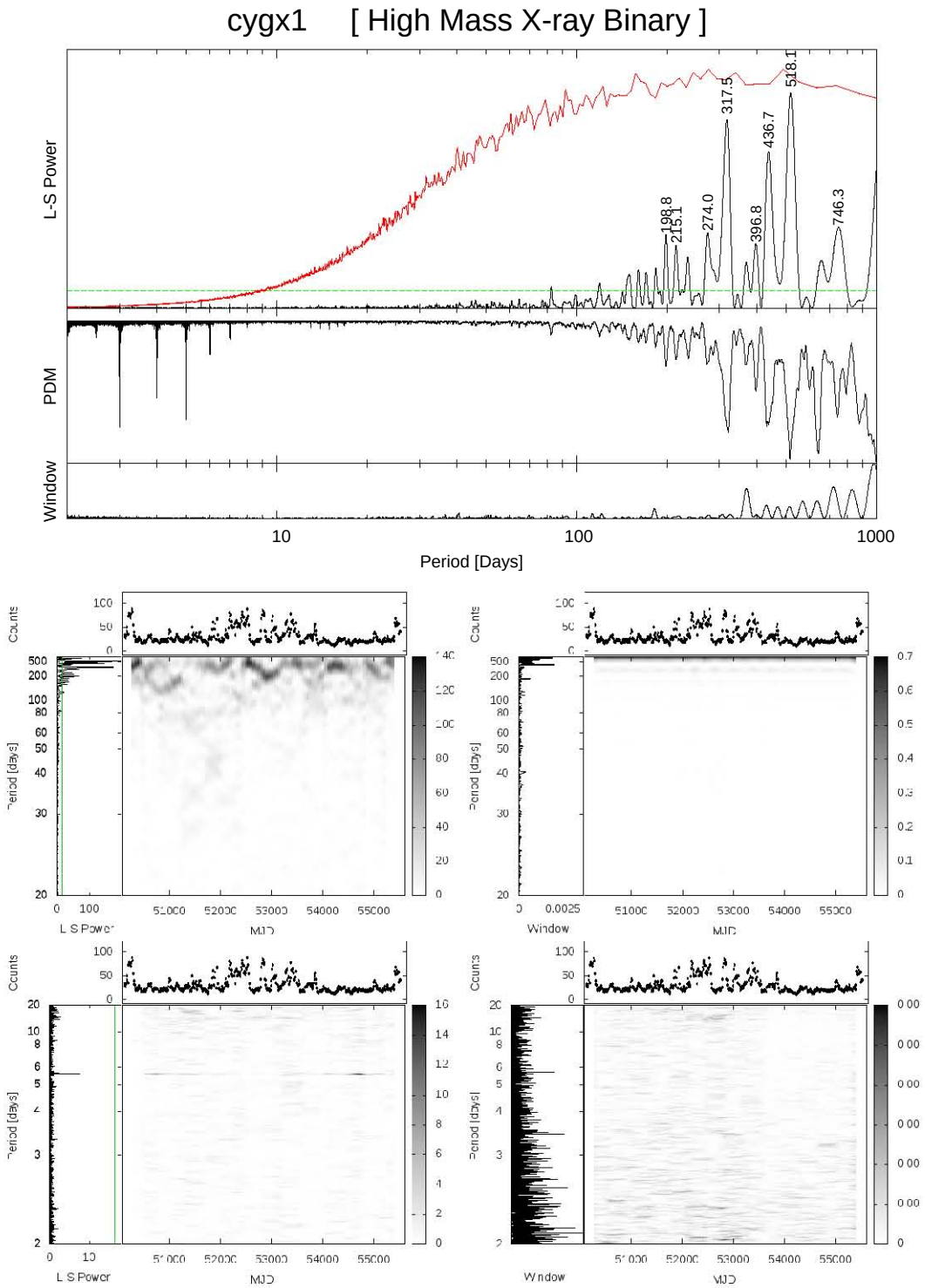

Figure C.23: Lightcurve, L-S, PDM, window, noise, DPS and DWF of cygx1

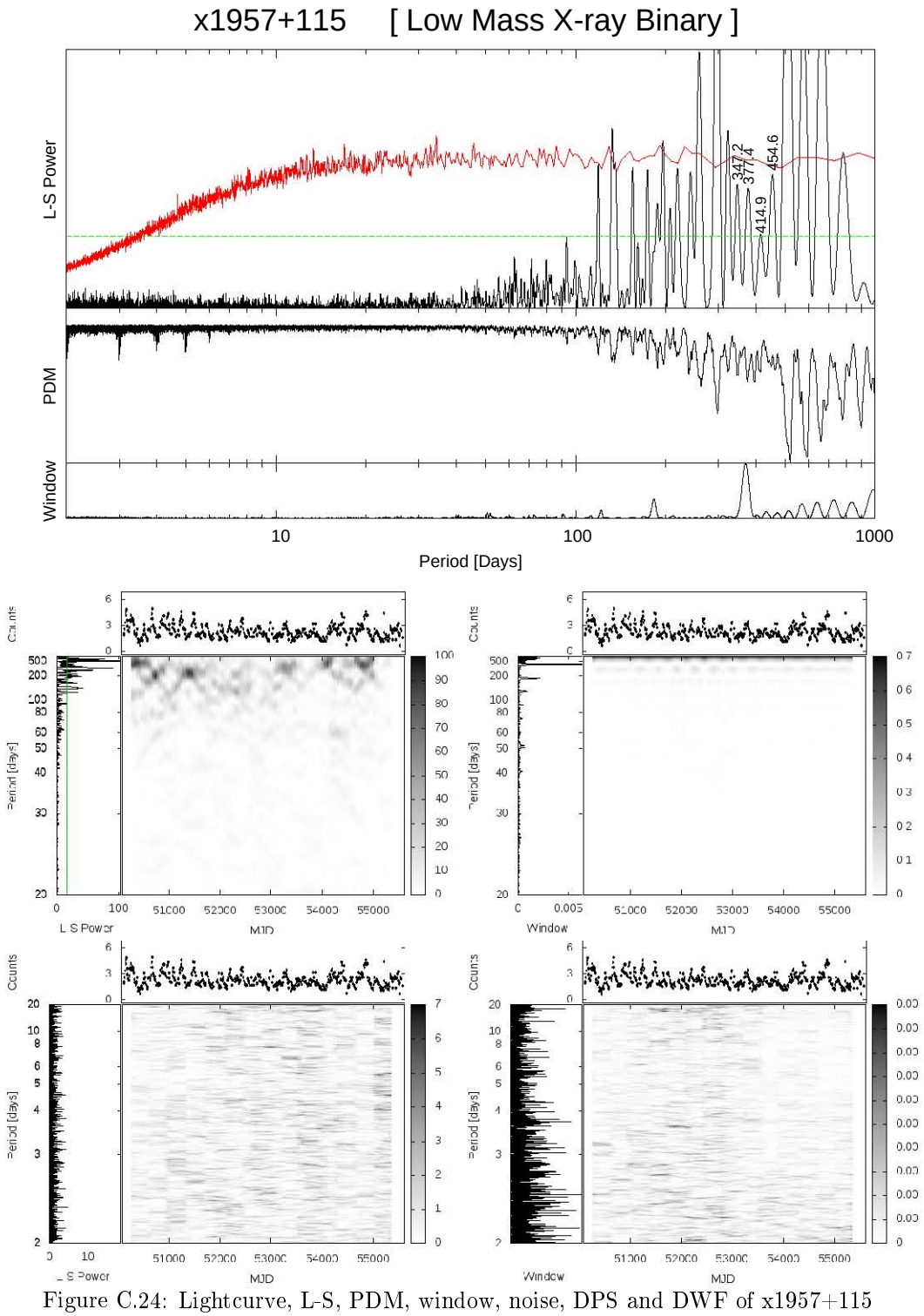

Figure C.24: Lightcurve, L-S, PDM, window, noise, DPS and DWF of x1957+115

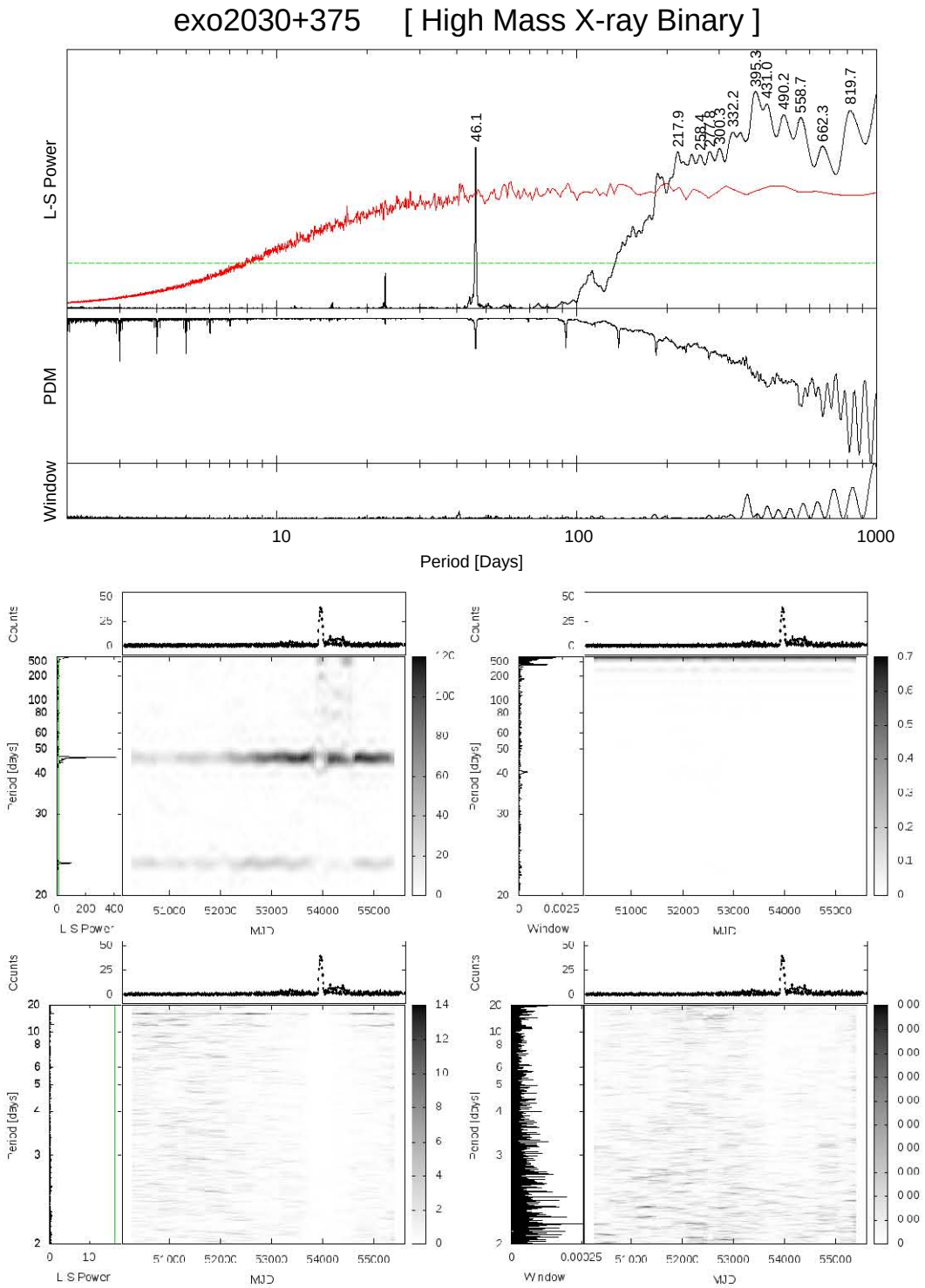

Figure C.25: Lightcurve, L-S, PDM, window, noise, DPS and DWF of exo2030+375

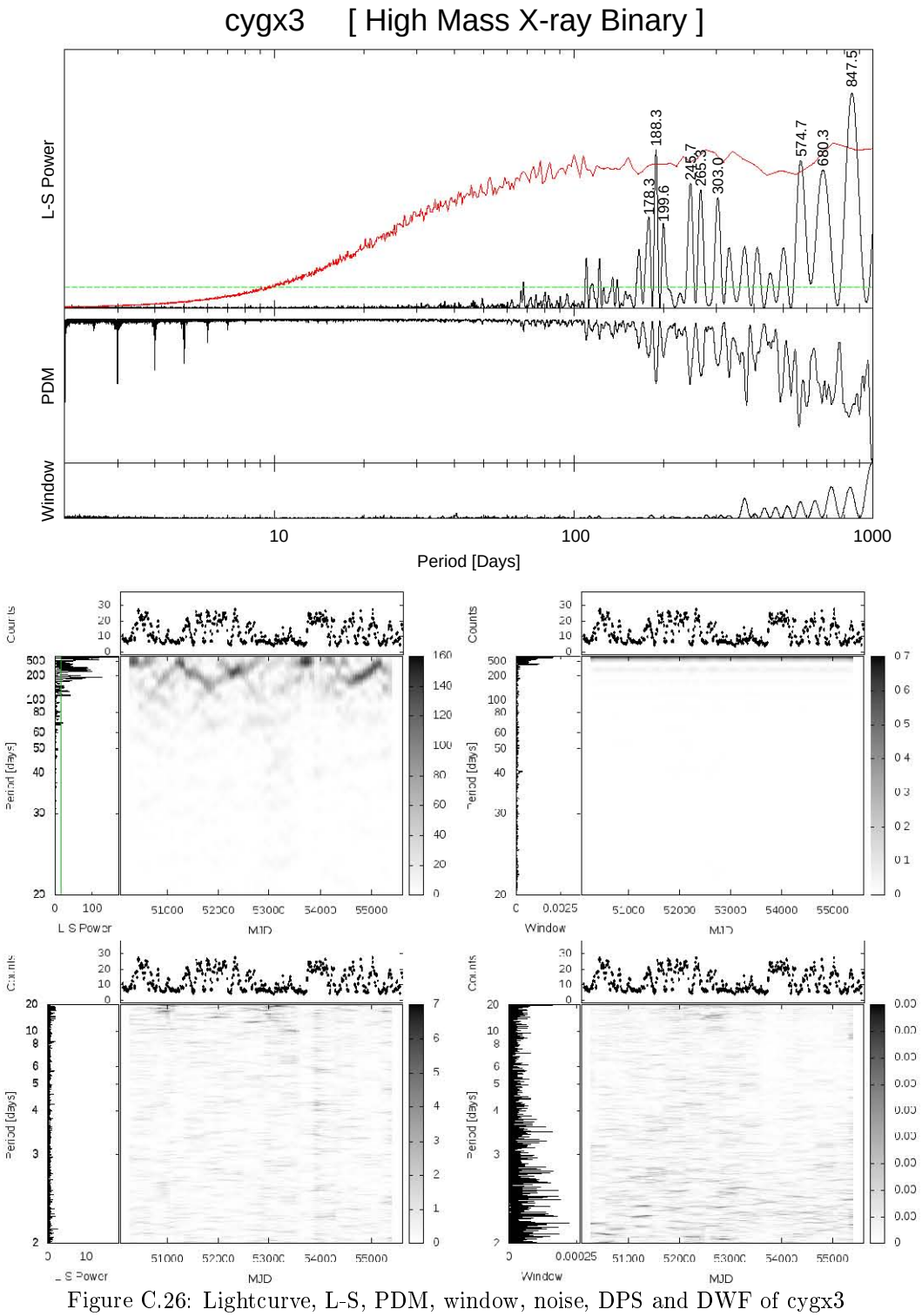

Figure C.26: Lightcurve, L-S, PDM, window, noise, DPS and DWF of cygx3

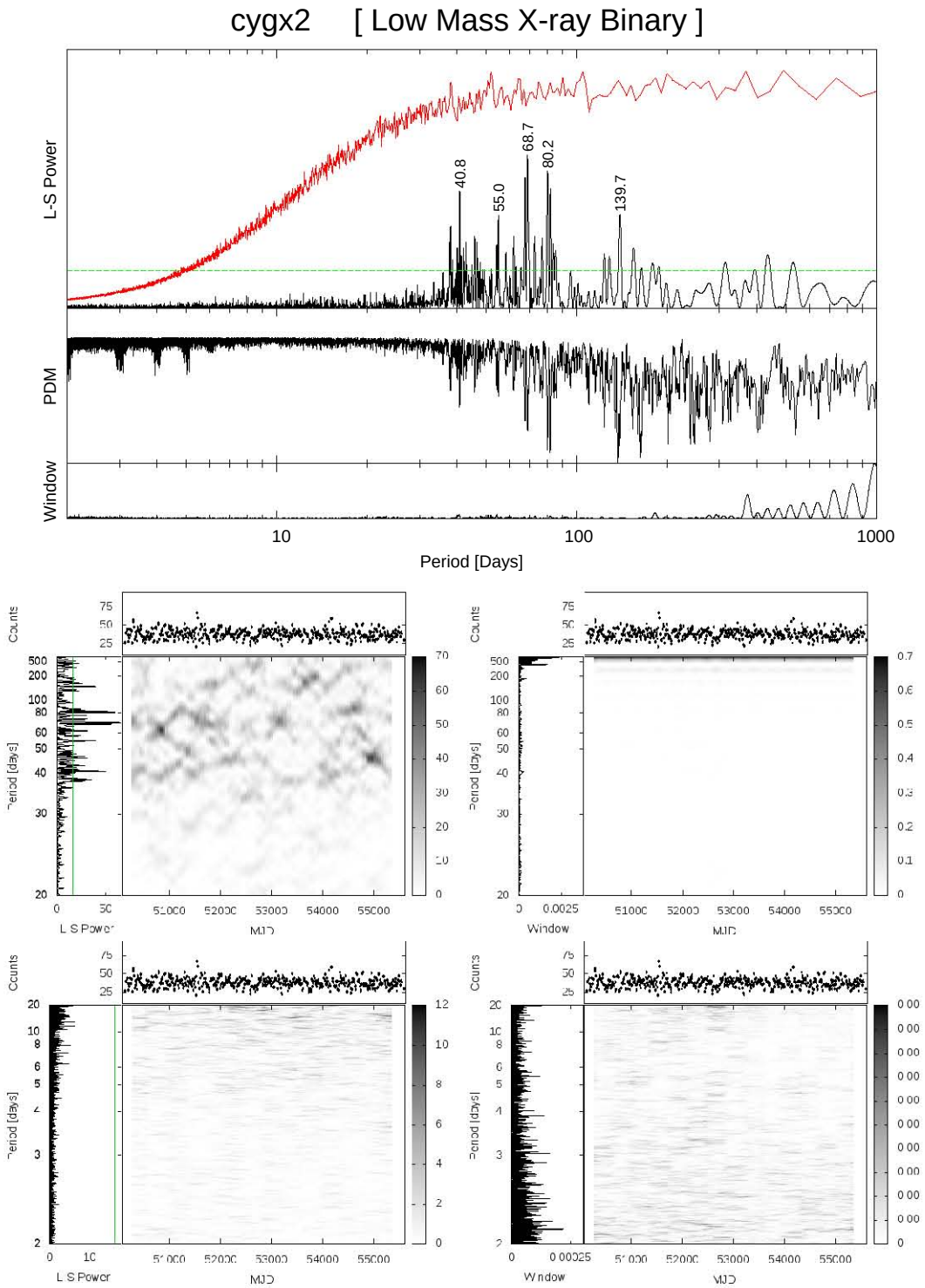

Figure C.27: Lightcurve, L-S, PDM, window, noise, DPS and DWF of cygx2

C.2 Marginal Sources

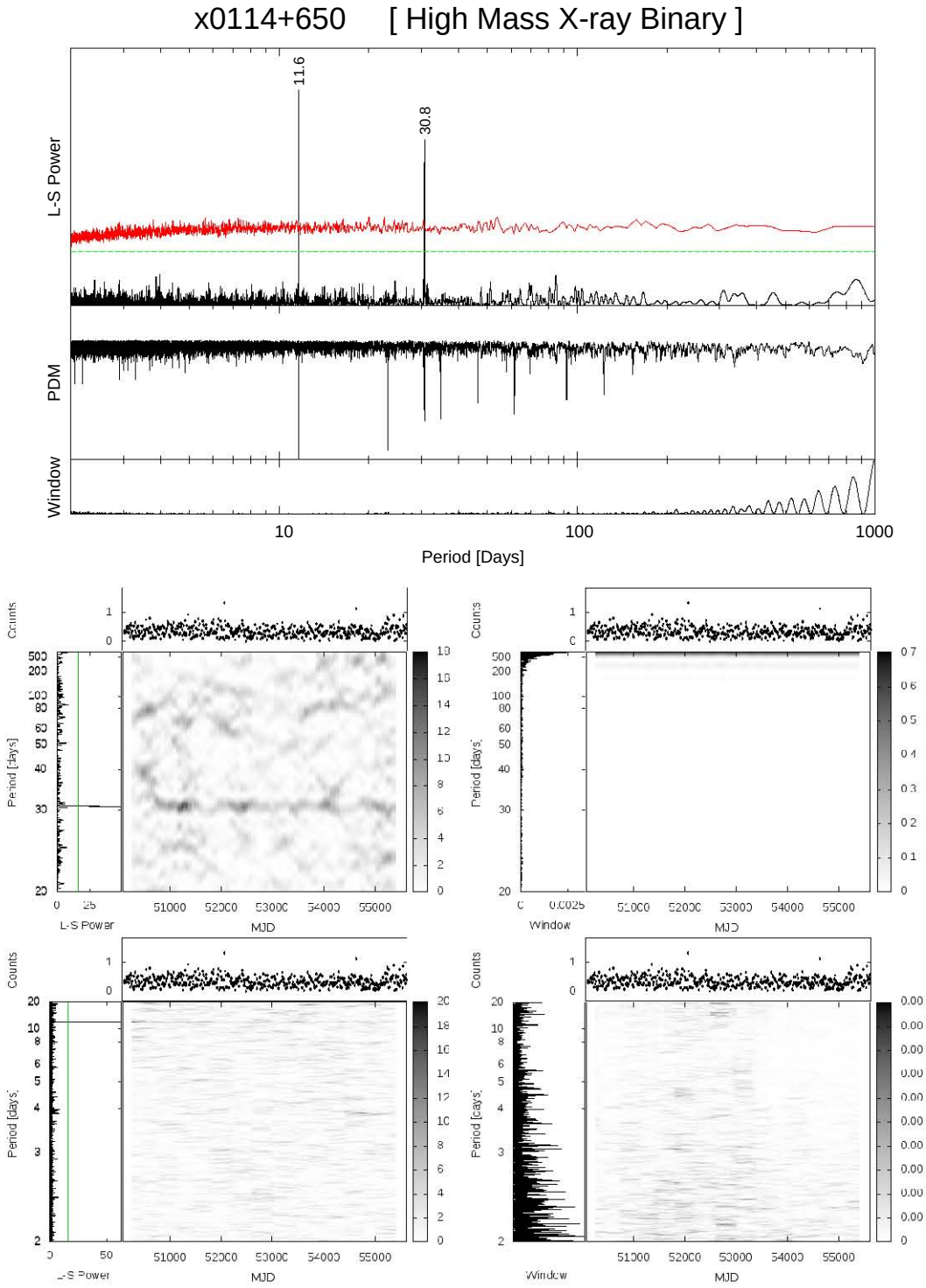

Figure C.28: Lightcurve, L-S, PDM, window, noise, DPS and DWF of x0114+650

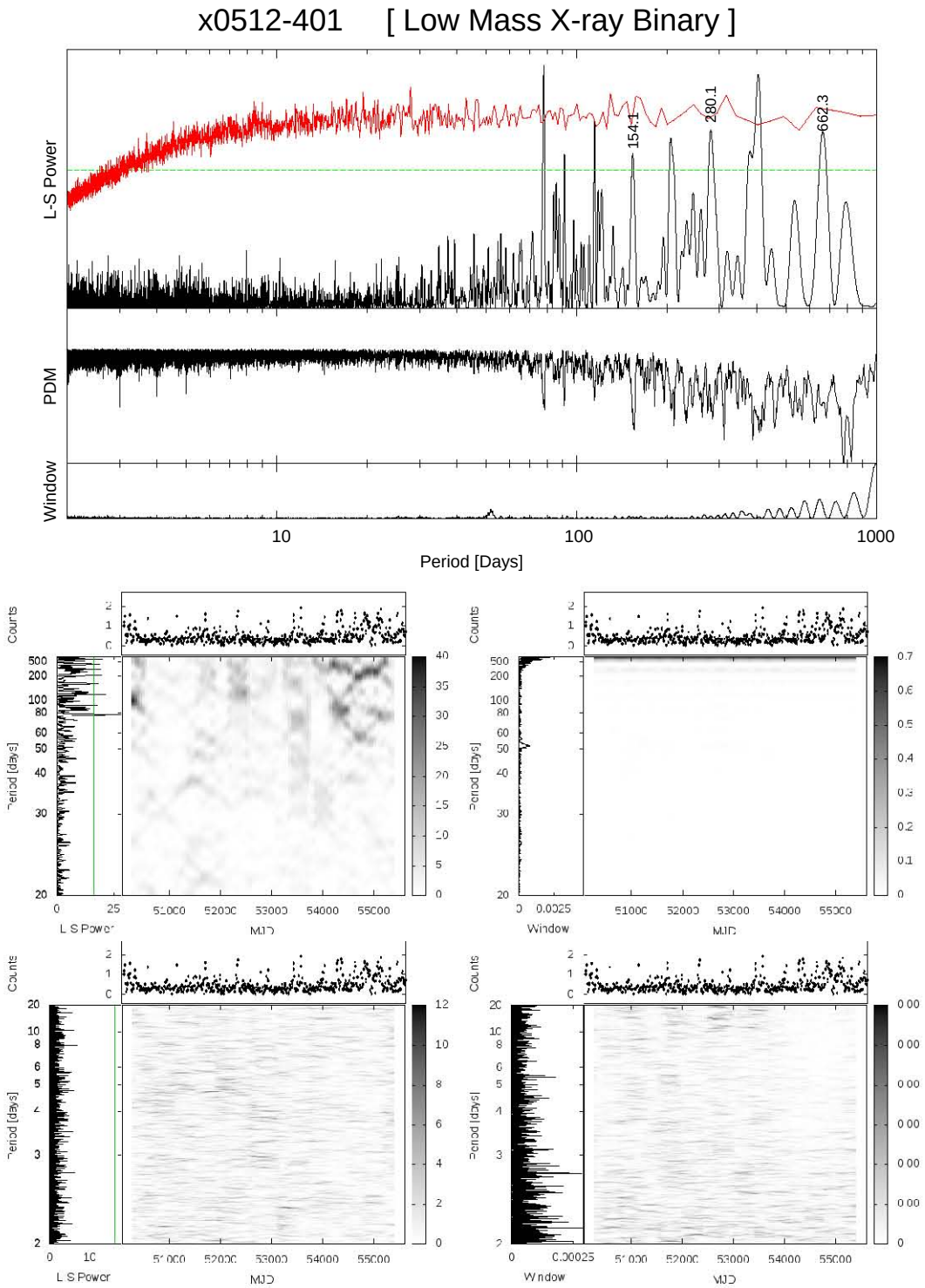

Figure C.29: Lightcurve, L-S, PDM, window, noise, DPS and DWF of x0512-401

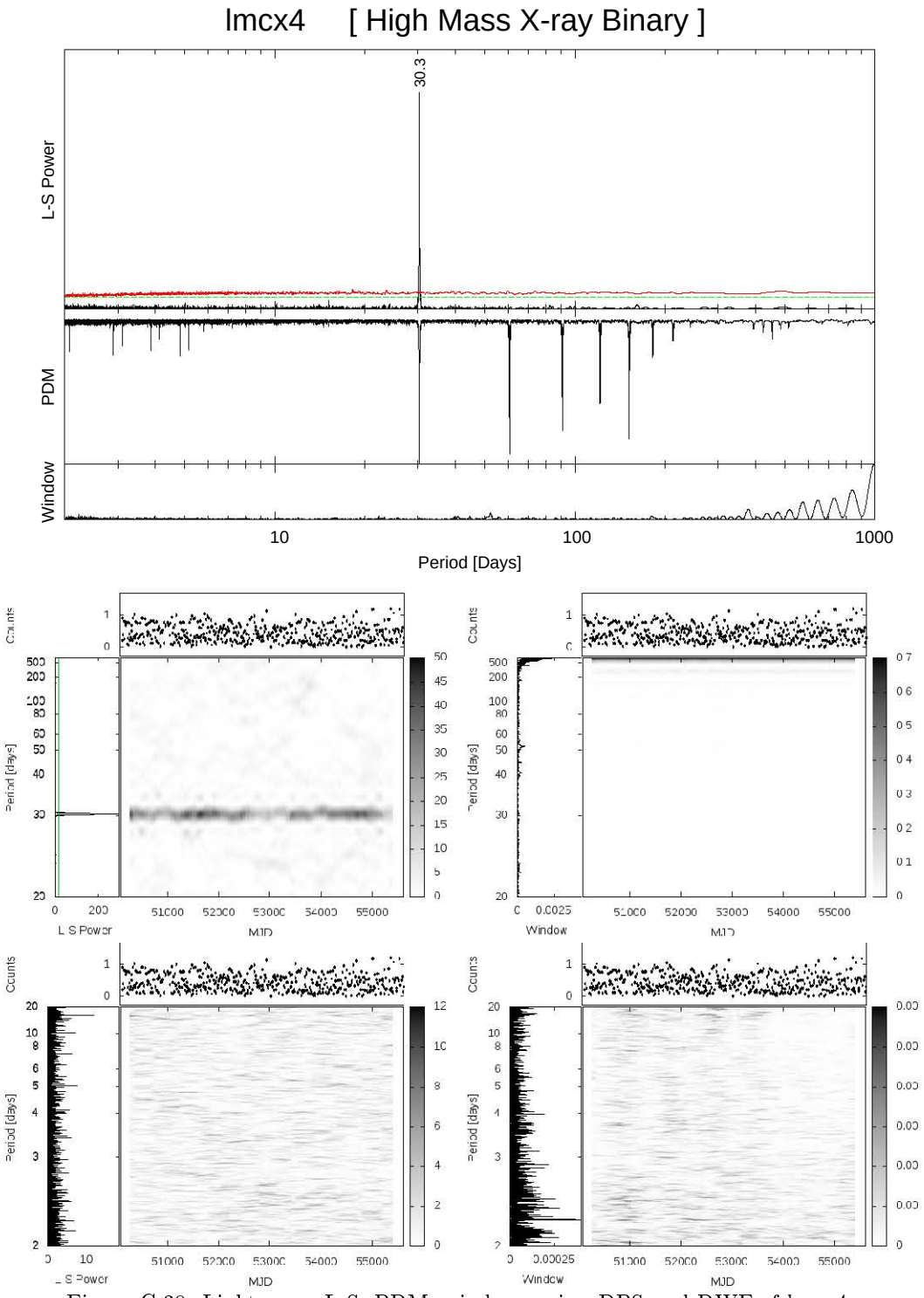

Figure C.30: Lightcurve, L-S, PDM, window, noise, DPS and DWF of lmcx4

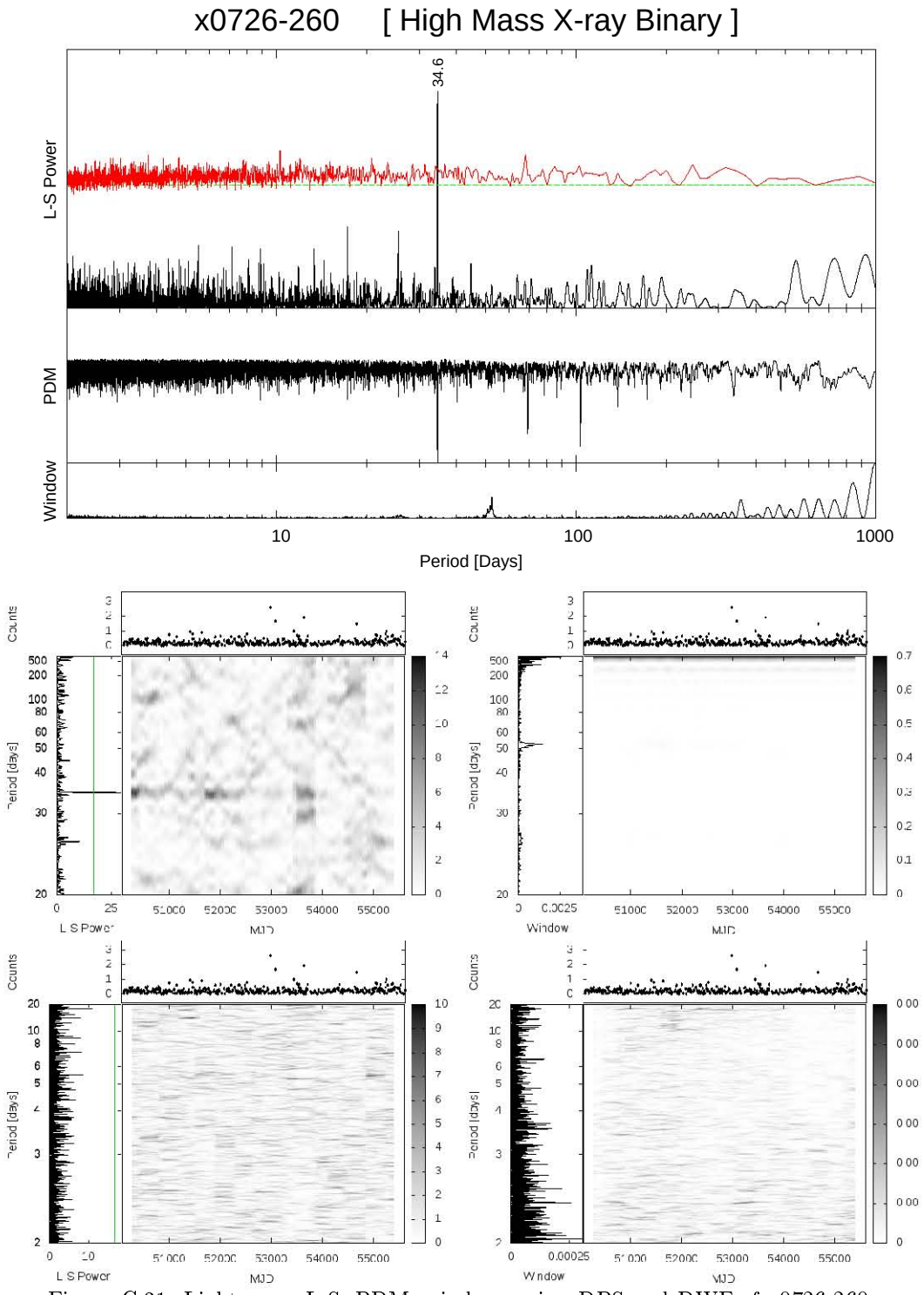

Figure C.31: Lightcurve, L-S, PDM, window, noise, DPS and DWF of x0726-260

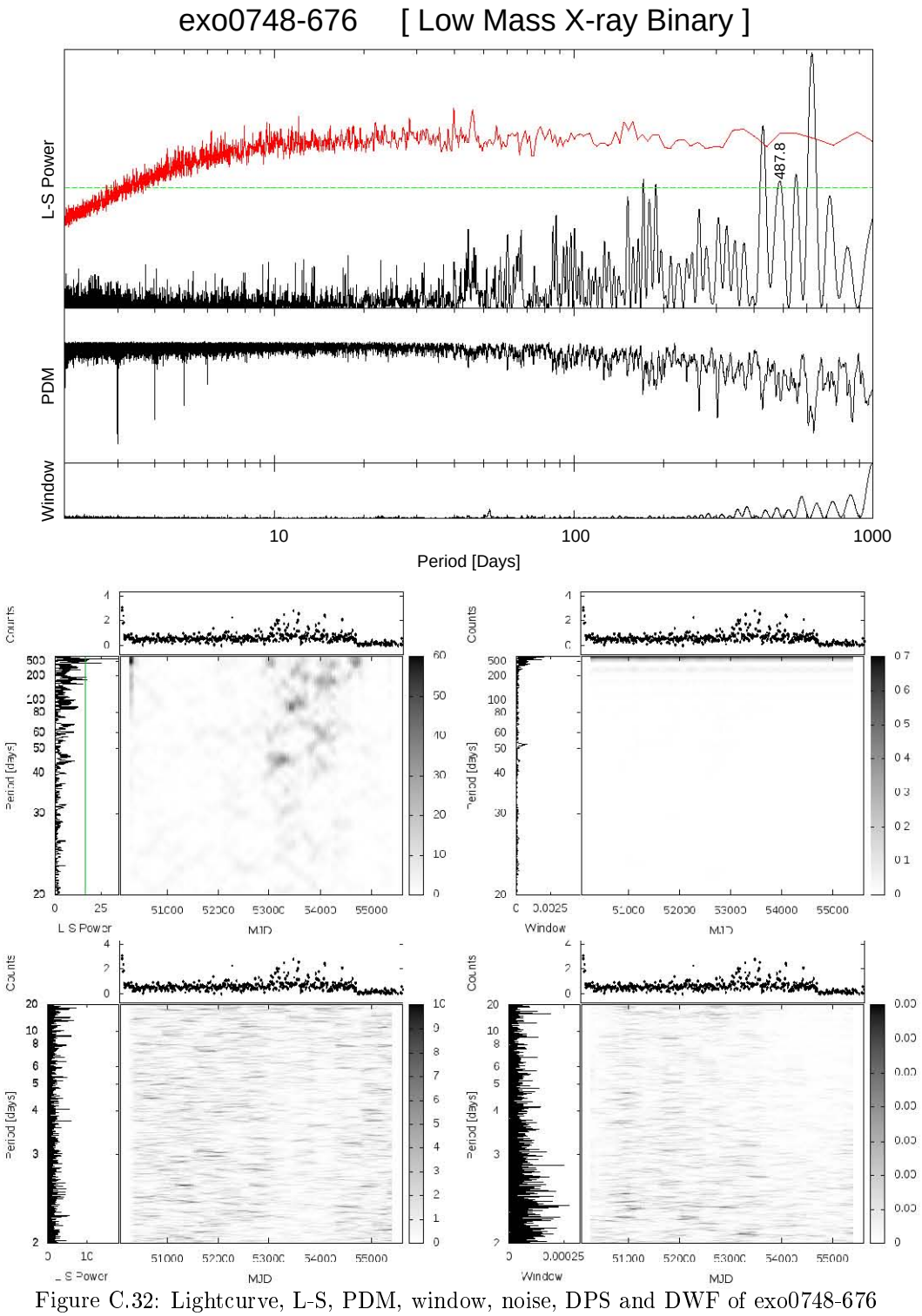

Figure C.32: Lightcurve, L-S, PDM, window, noise, DPS and DWF of exo0748-676

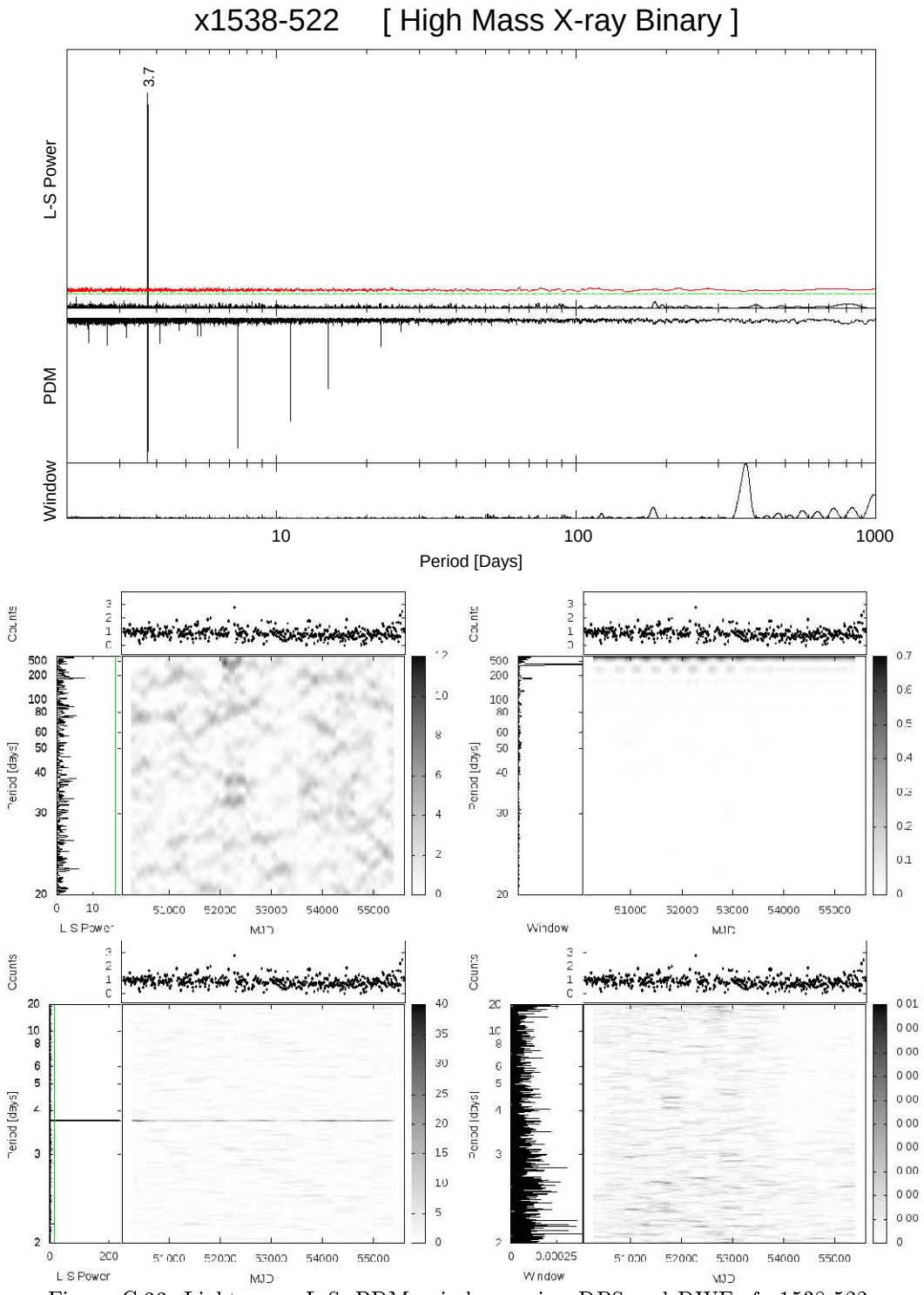

Figure C.33: Lightcurve, L-S, PDM, window, noise, DPS and DWF of x1538-522

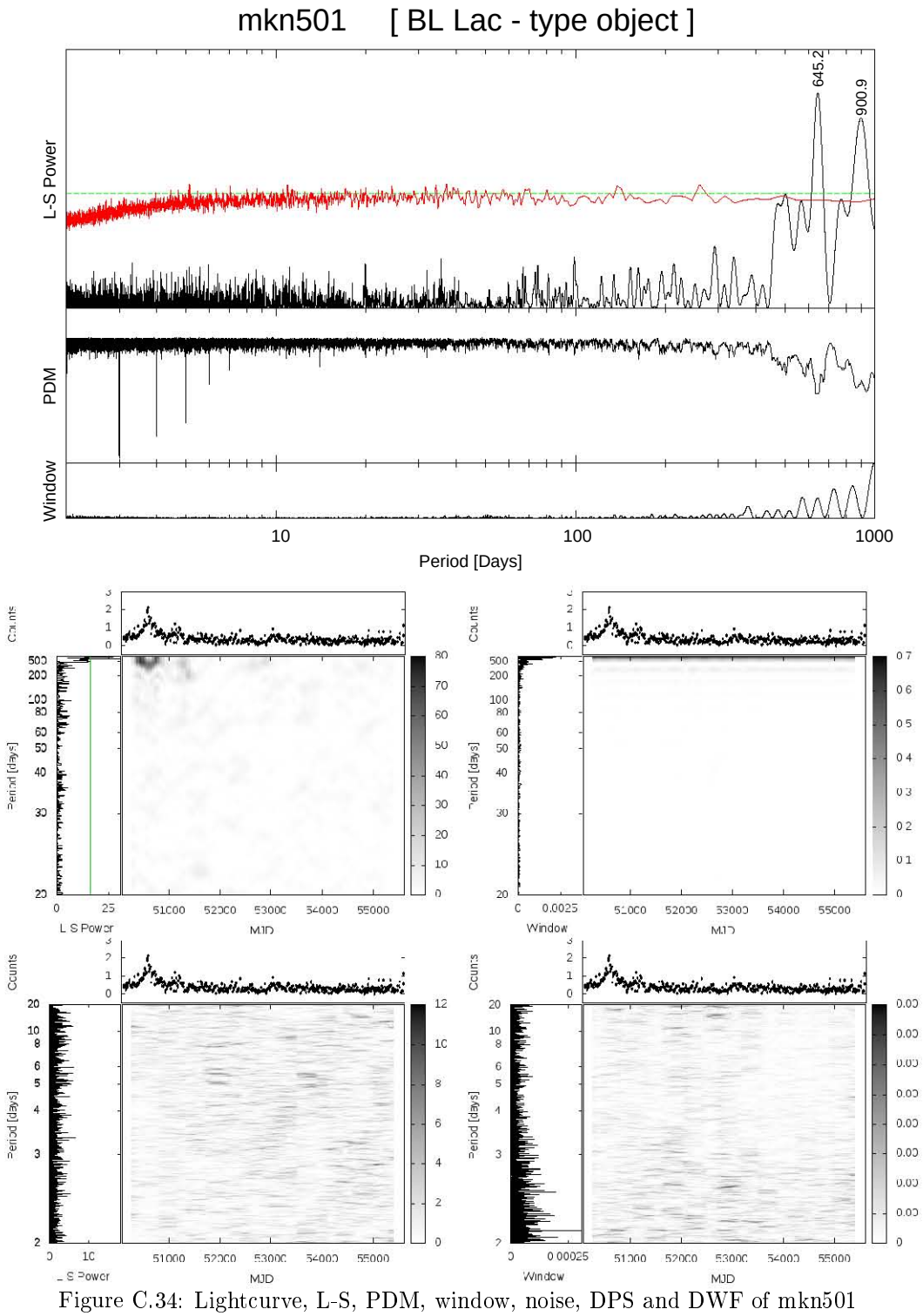

Figure C.34: Lightcurve, L-S, PDM, window, noise, DPS and DWF of mkn501

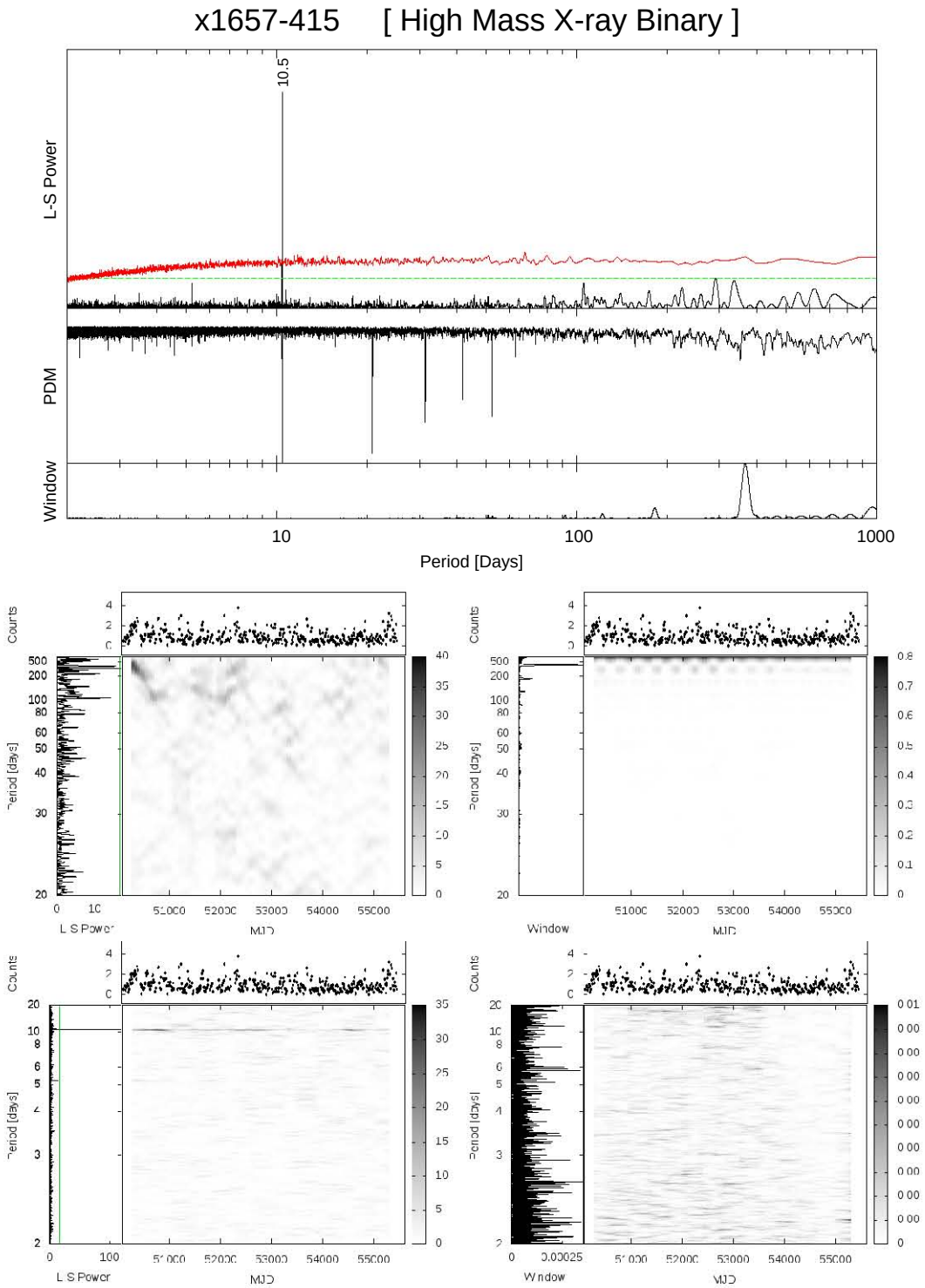

Figure C.35: Lightcurve, L-S, PDM, window, noise, DPS and DWF of x1657-415

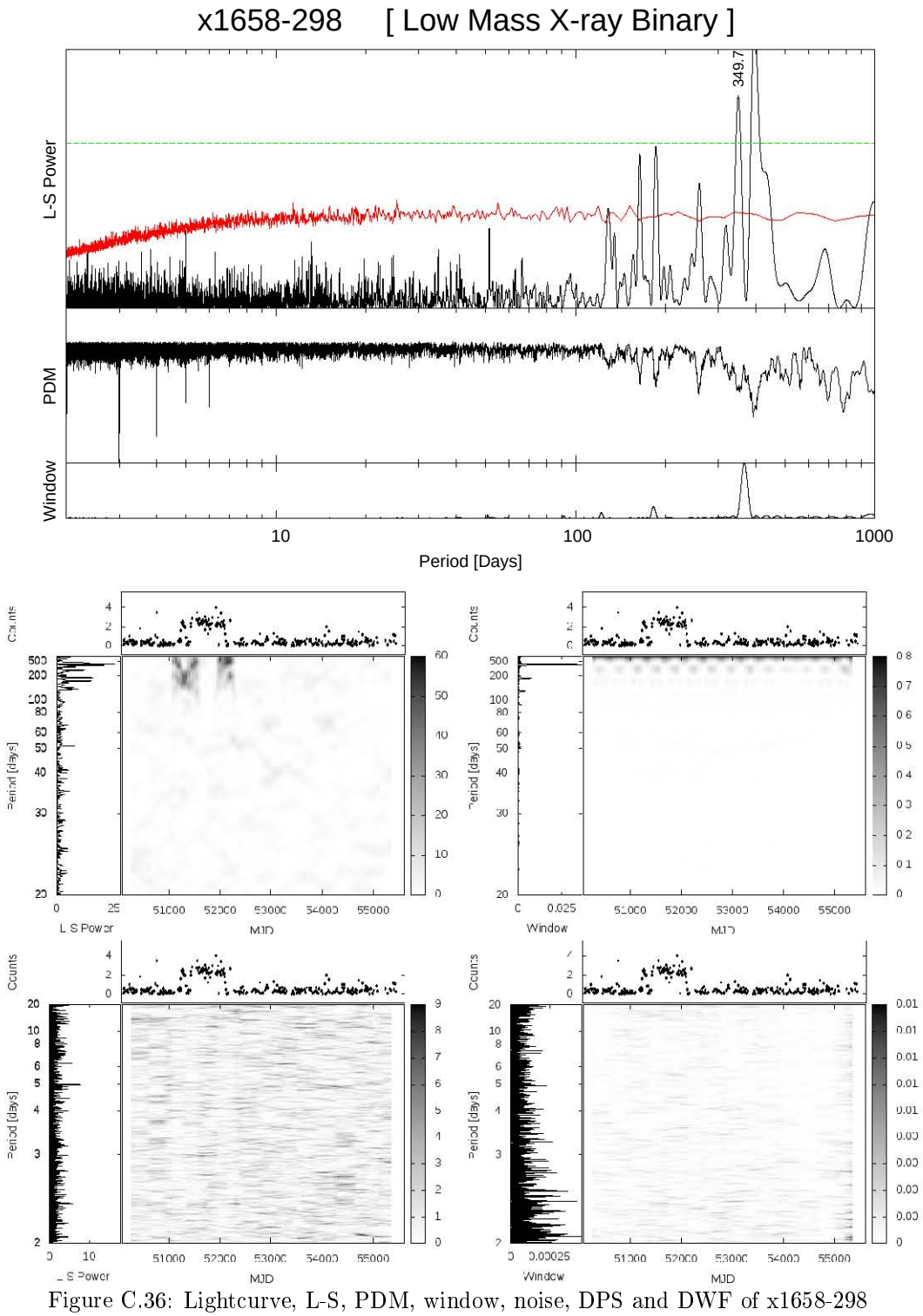

Figure C.36: Lightcurve, L-S, PDM, window, noise, DPS and DWF of x1658-298

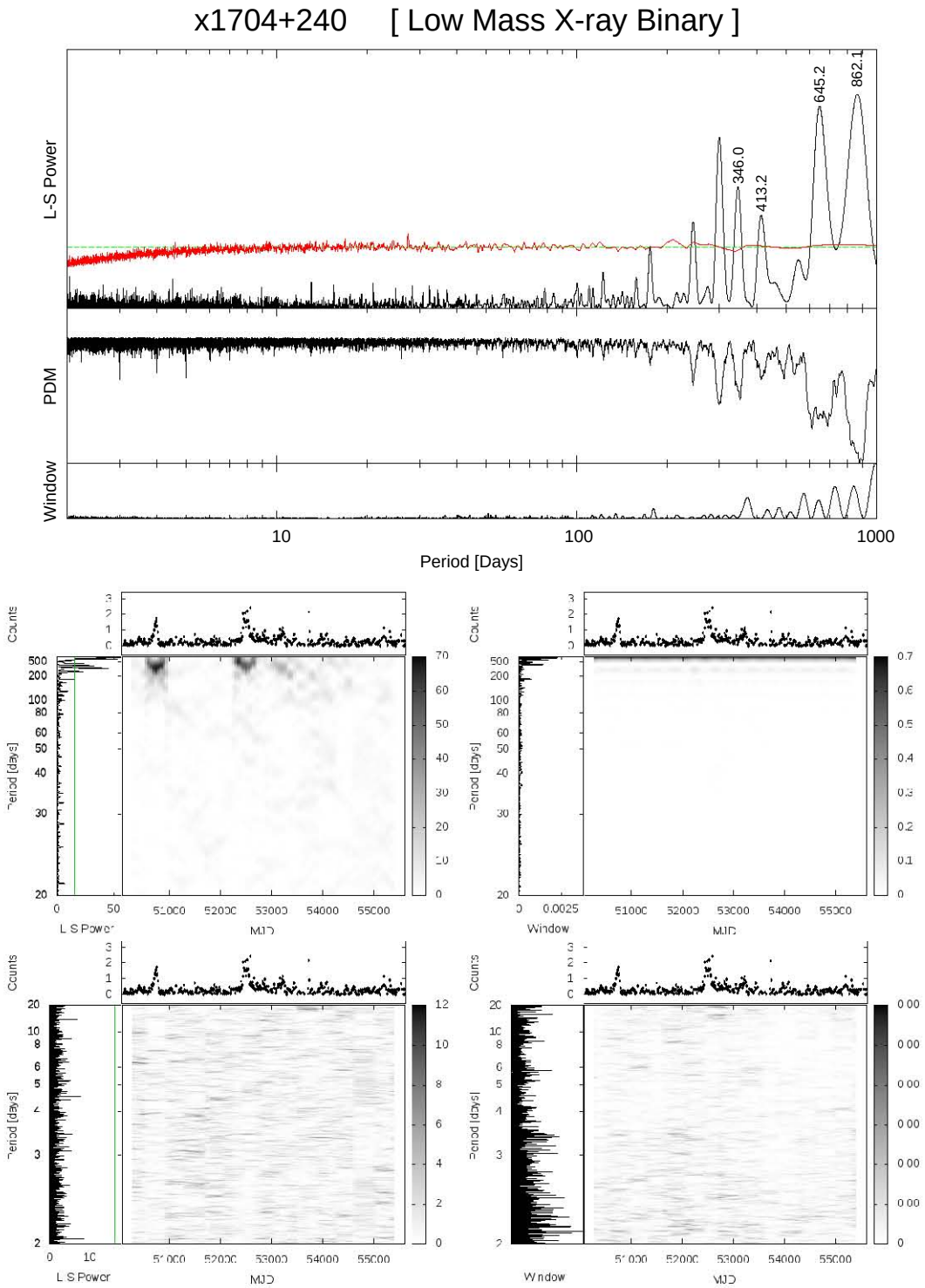

Figure C.37: Lightcurve, L-S, PDM, window, noise, DPS and DWF of x1704+240

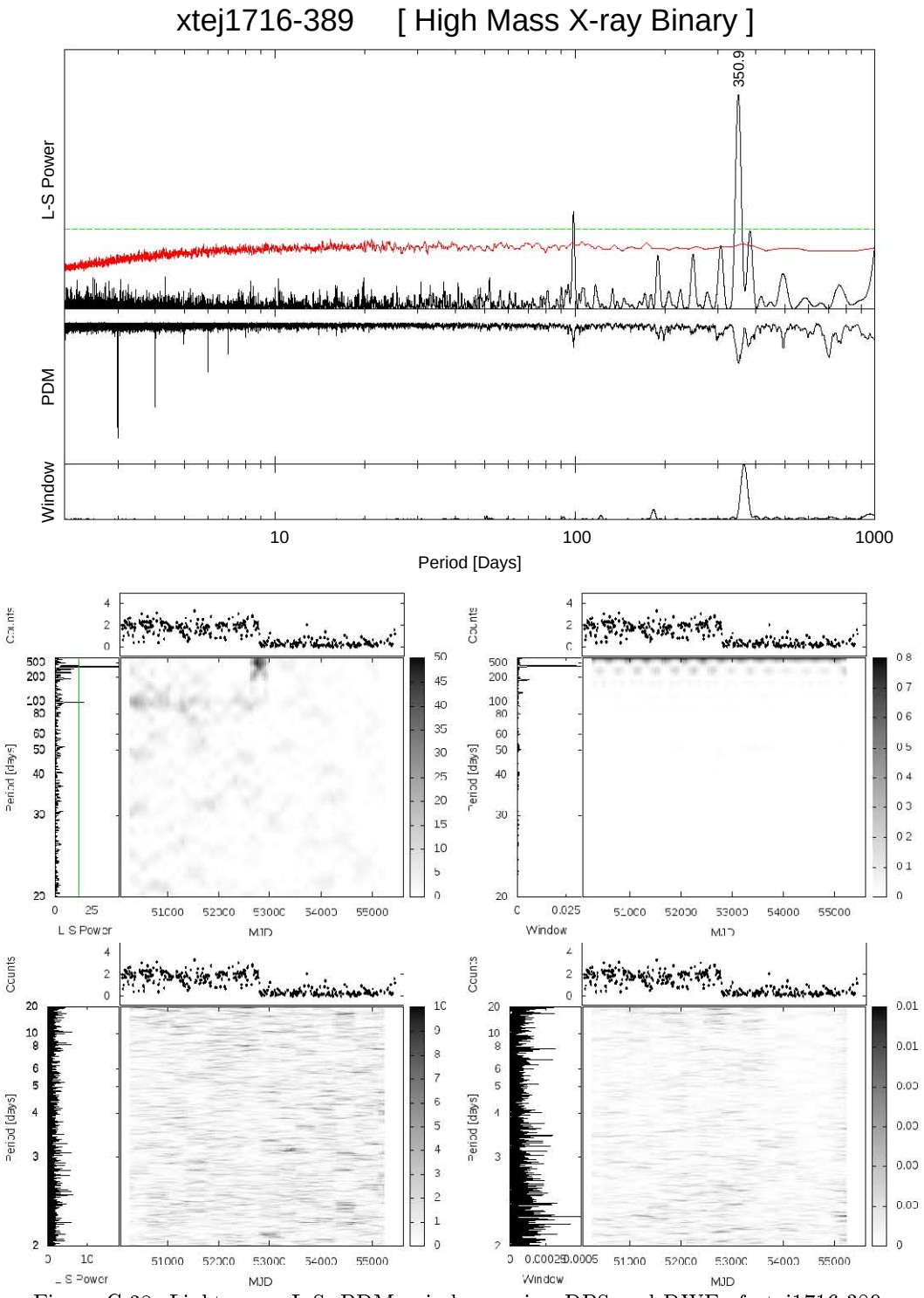

Figure C.38: Lightcurve, L-S, PDM, window, noise, DPS and DWF of xtej1716-389

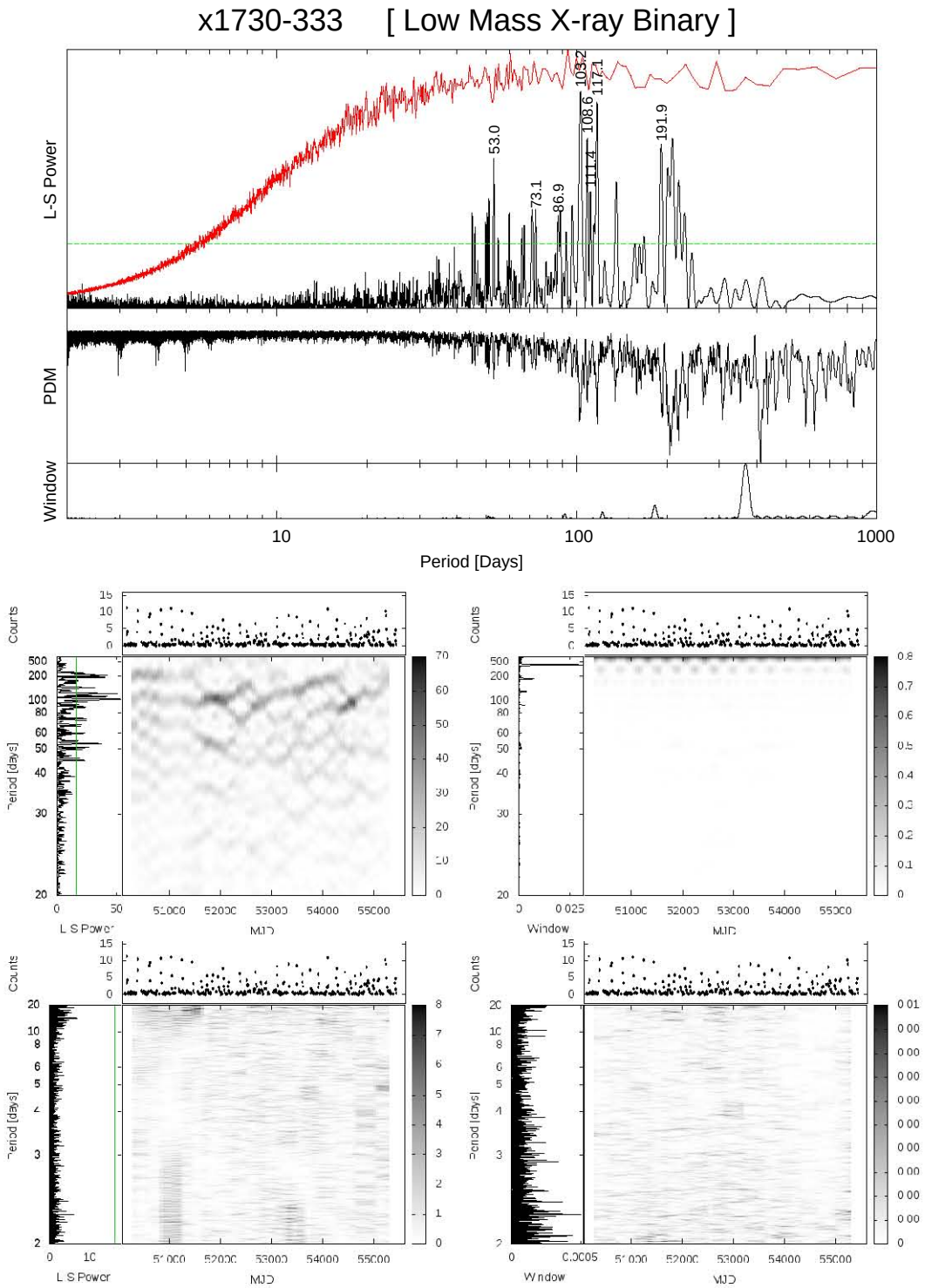

Figure C.39: Lightcurve, L-S, PDM, window, noise, DPS and DWF of x1730-333

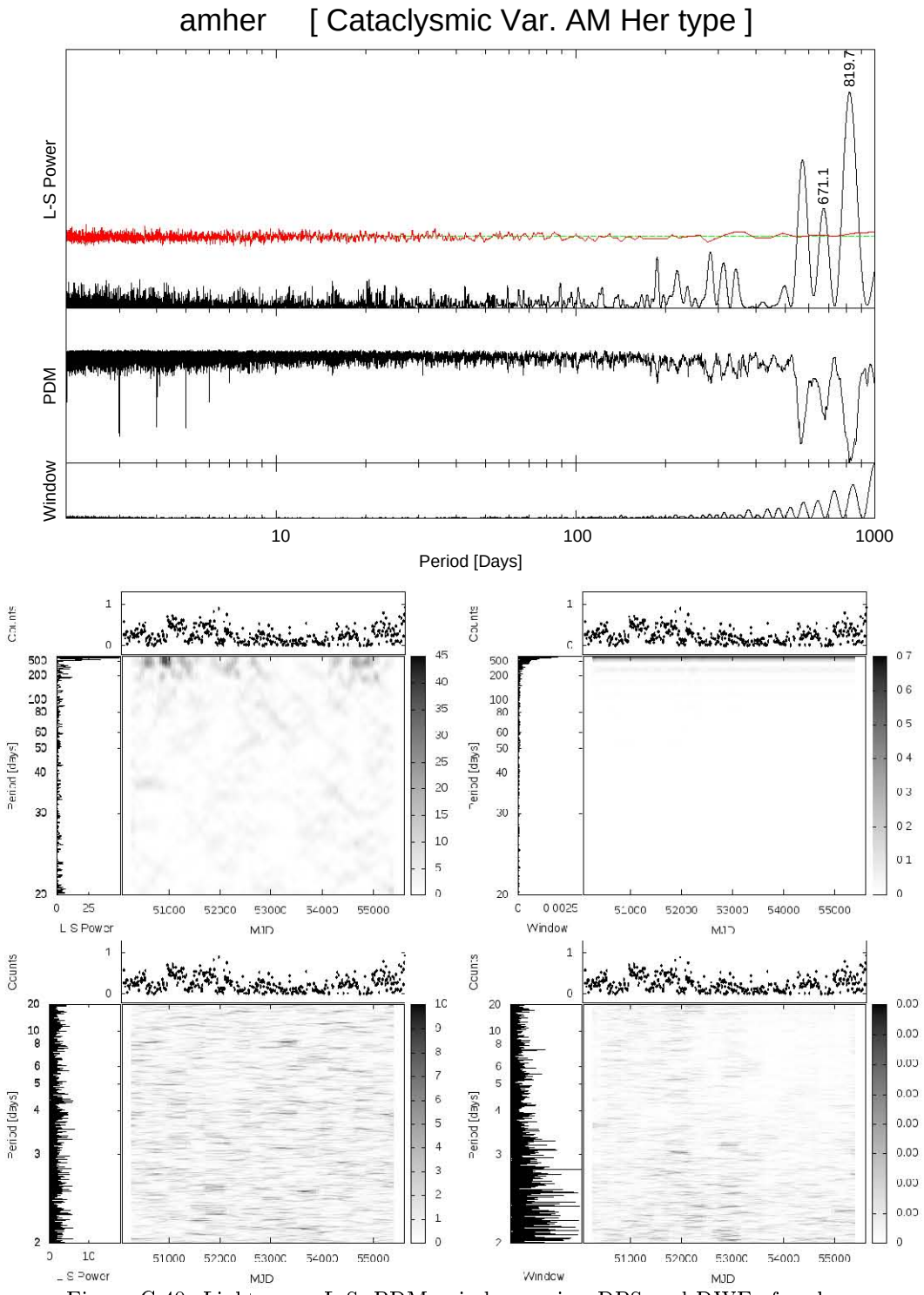

Figure C.40: Lightcurve, L-S, PDM, window, noise, DPS and DWF of amher

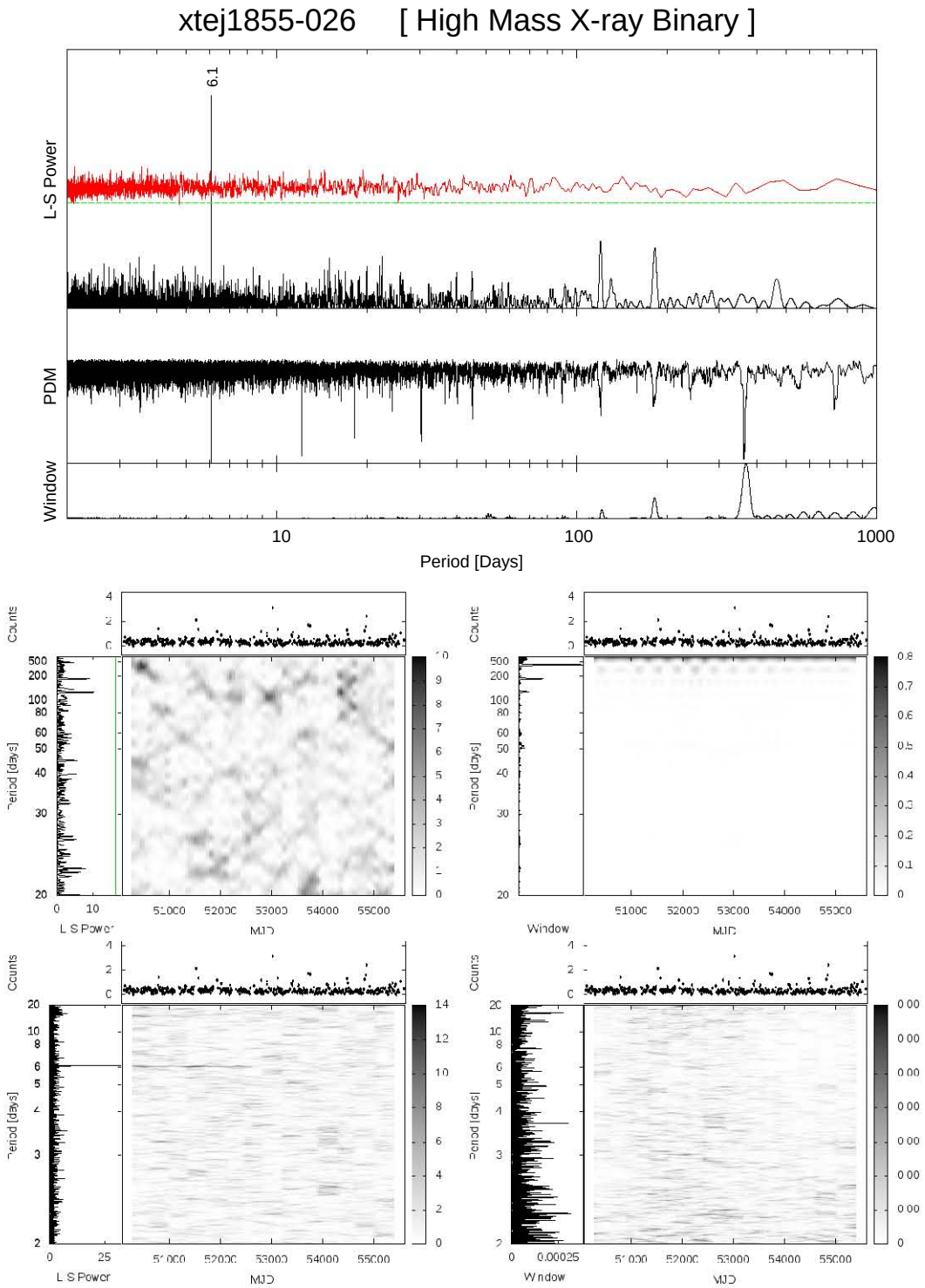

Figure C.41: Lightcurve, L-S, PDM, window, noise, DPS and DWF of xtej1855-026

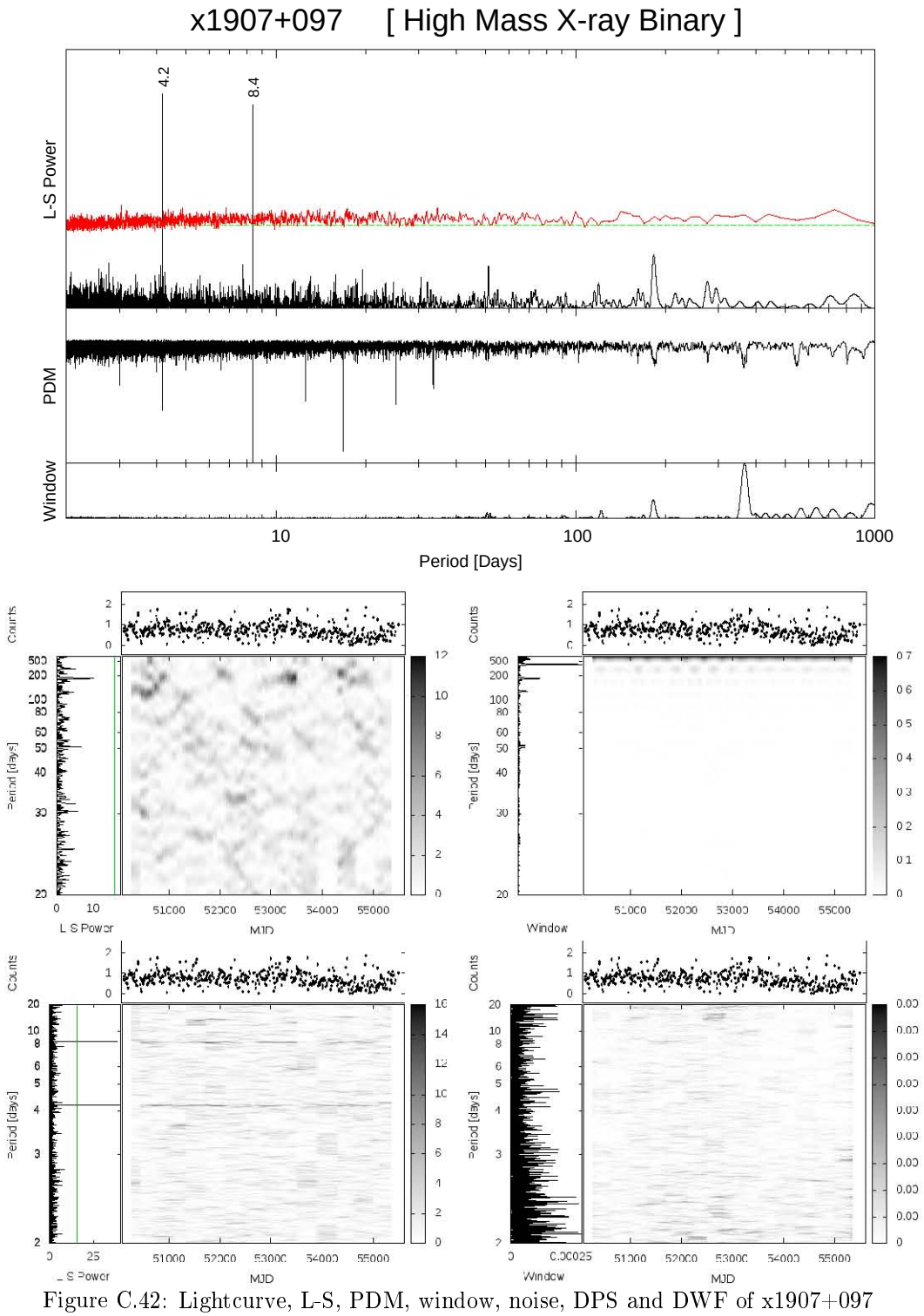

Figure C.42: Lightcurve, L-S, PDM, window, noise, DPS and DWF of x1907+097

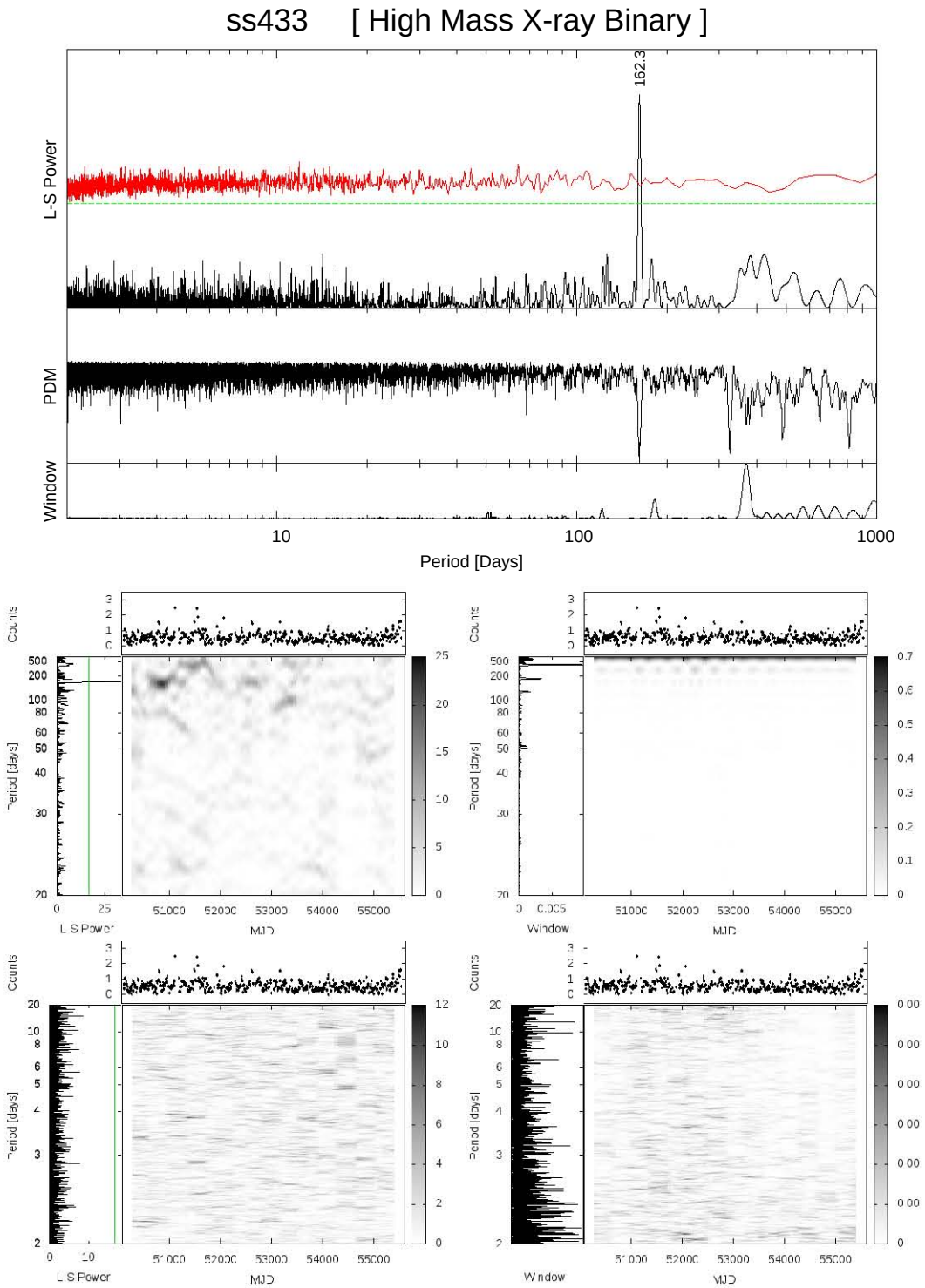

Figure C.43: Lightcurve, L-S, PDM, window, noise, DPS and DWF of ss433

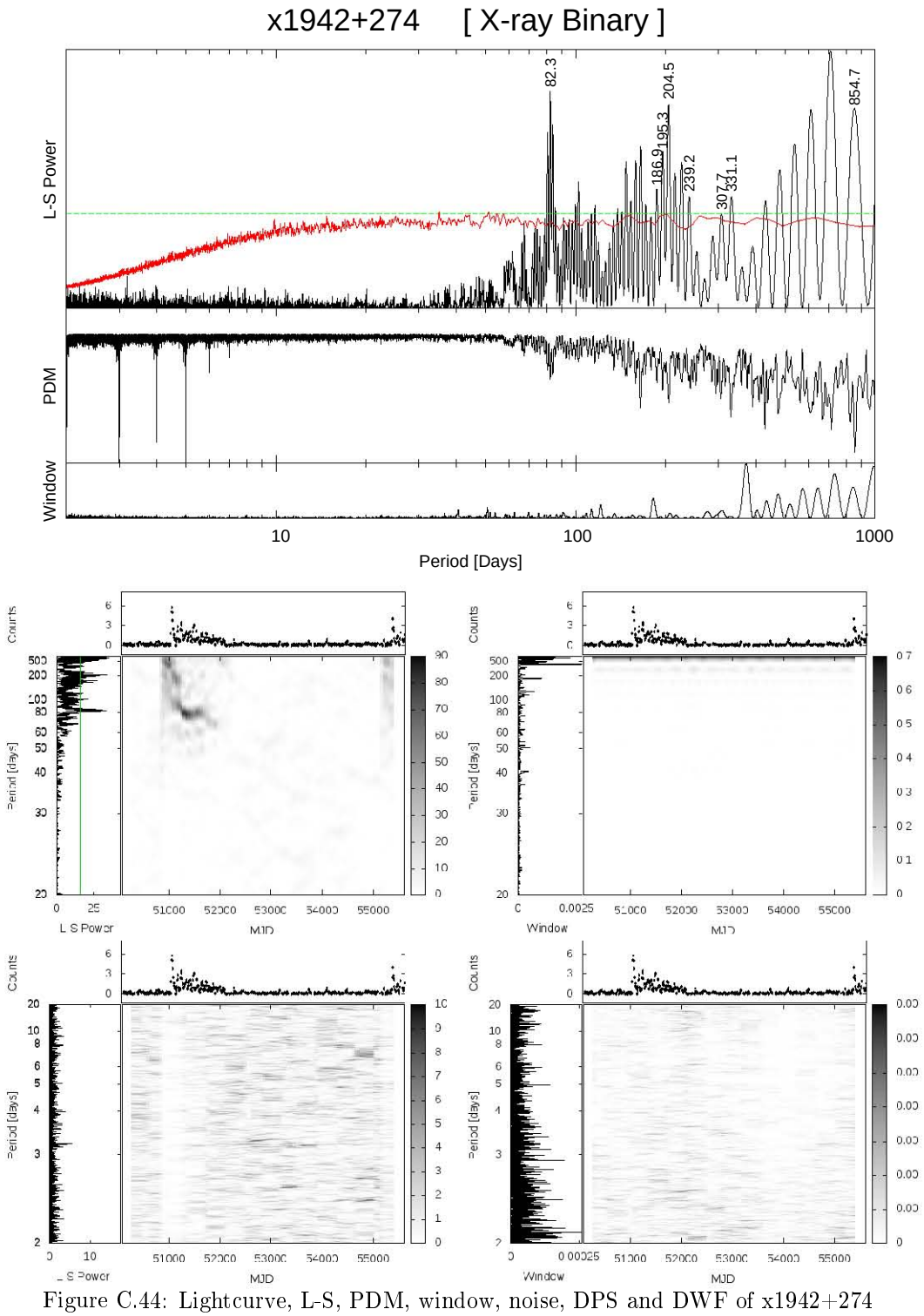

Figure C.44: Lightcurve, L-S, PDM, window, noise, DPS and DWF of x1942+274

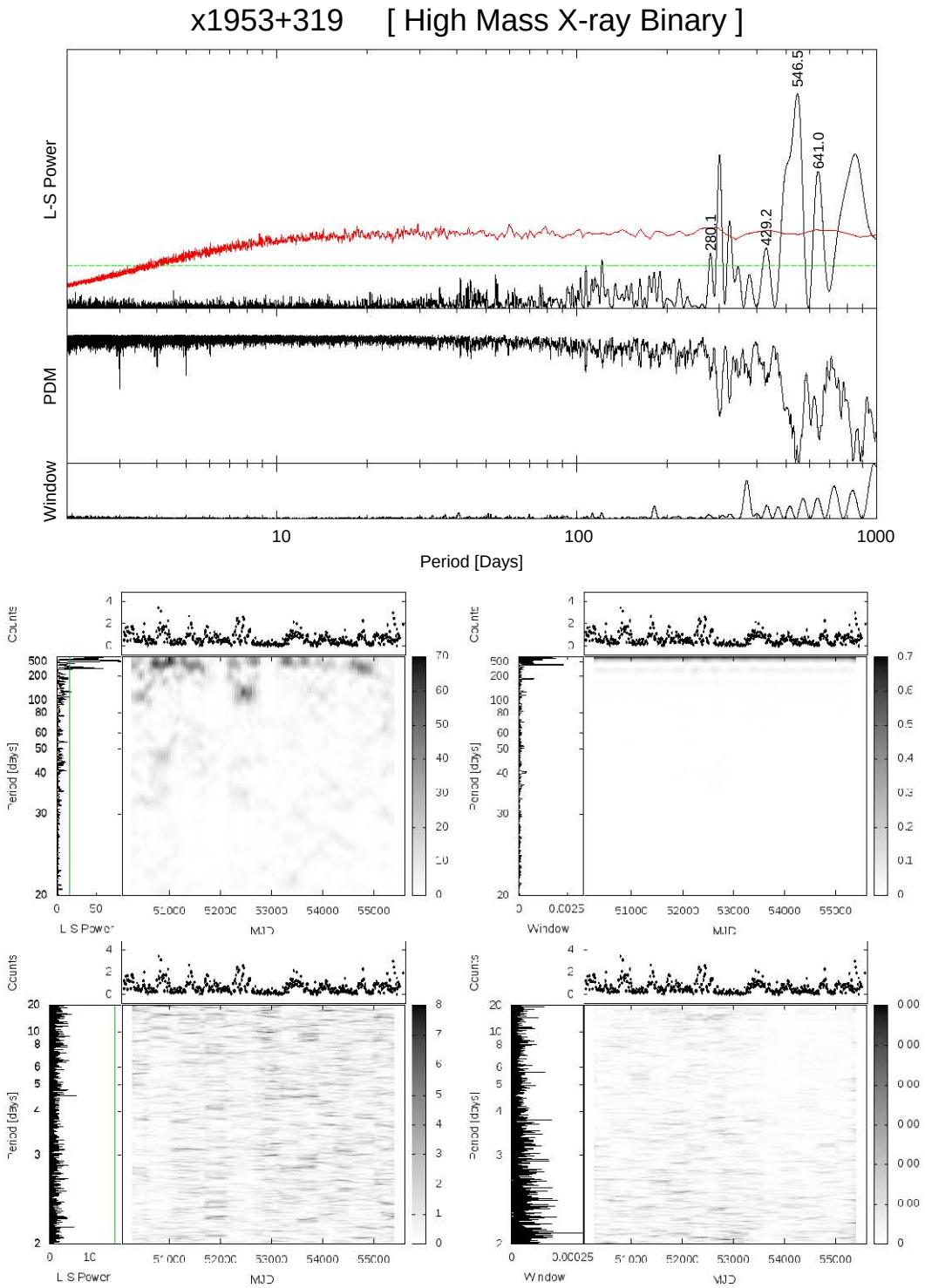

Figure C.45: Lightcurve, L-S, PDM, window, noise, DPS and DWF of x1953+319

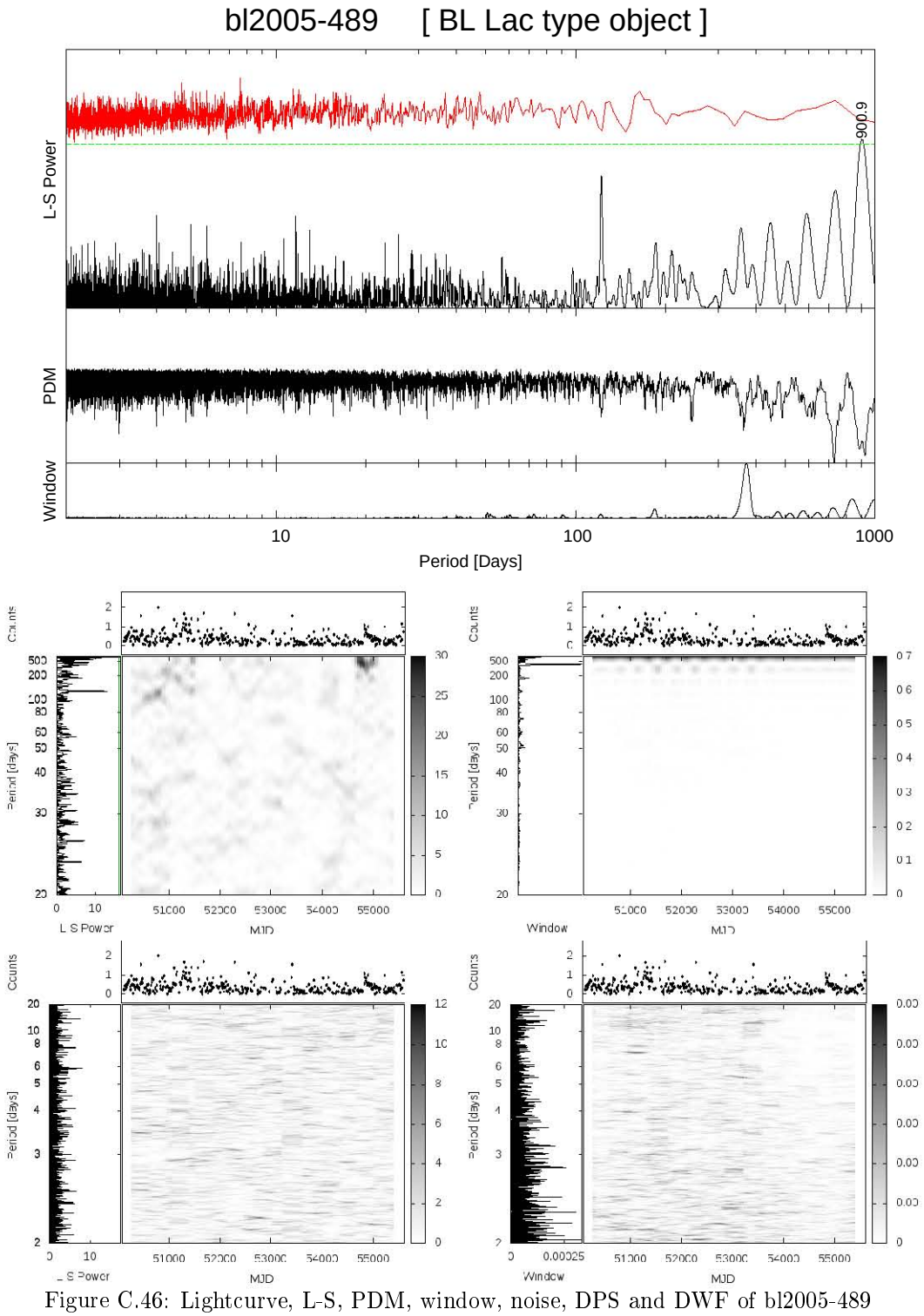

Figure C.46: Lightcurve, L-S, PDM, window, noise, DPS and DWF of bl2005-489

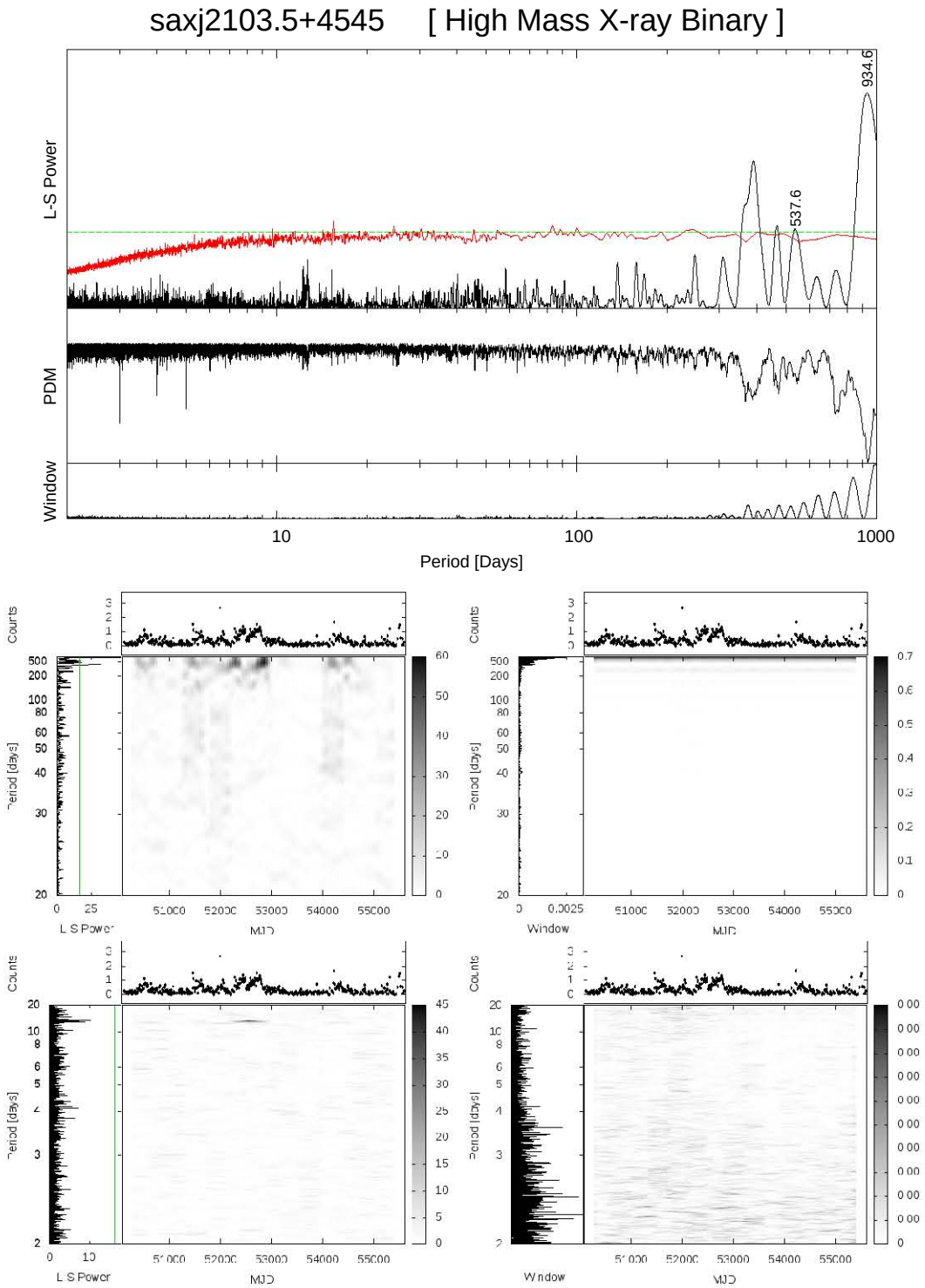

Figure C.47: Lightcurve, L-S, PDM, window, noise, DPS and DWF of saxj2103.5+4545

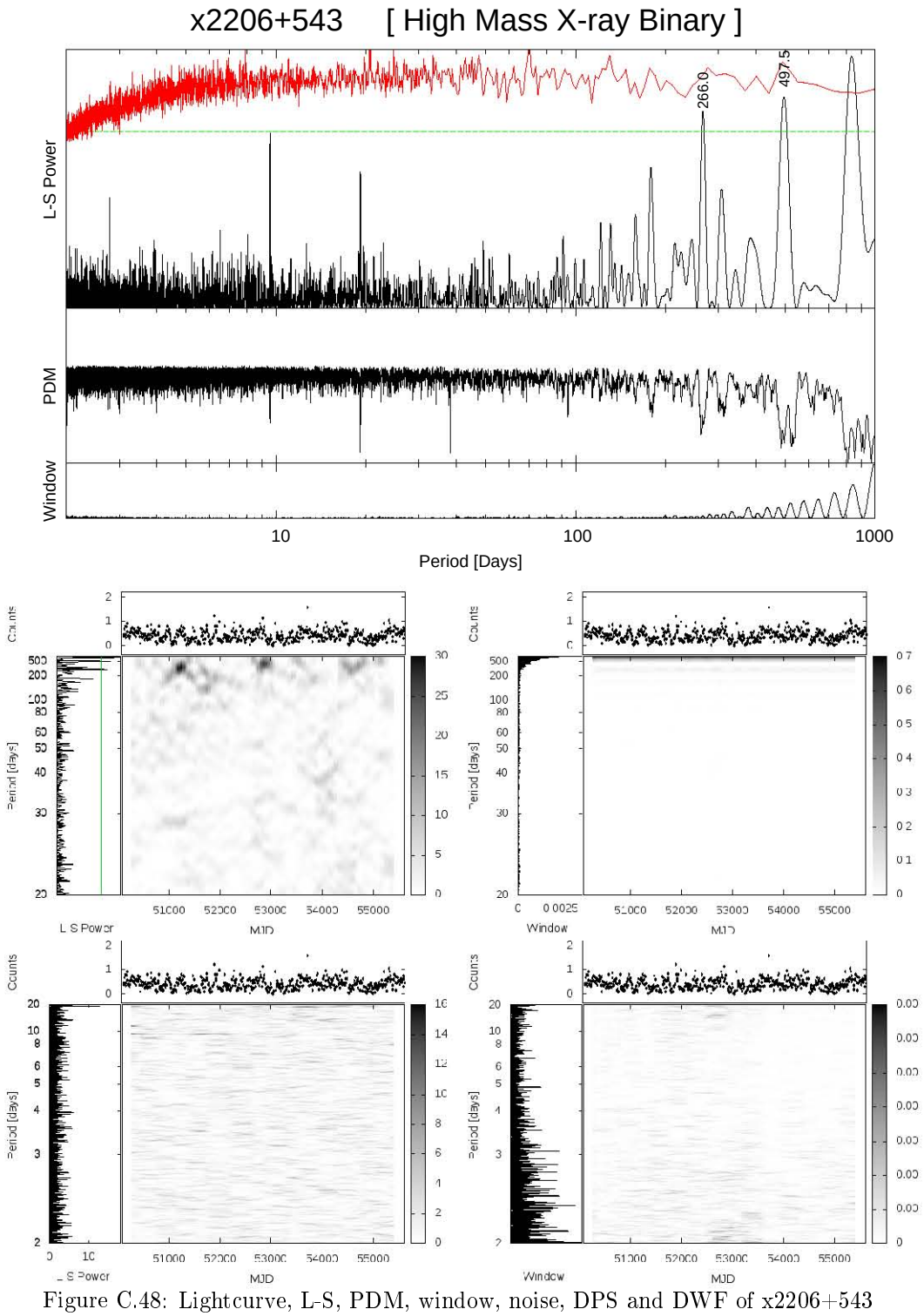

Figure C.48: Lightcurve, L-S, PDM, window, noise, DPS and DWF of x2206+543

Bibliography

Abell, G. O. & Margon, B. 1979, Natur, 279, 701

Abramowicz, M. A., Chen, X., Kato, S., Lasota, J.-P., & Regev, O. 1995, ApJ, 438, L37

Antonucci, R. 1993, ARA&A, 31, 473

Apparao, K. M. V. & Chitre, S. M. 1979, Ap&SS, 63, 125

Applegate, J. H. 1992, ApJ, 385, 621

Applegate, J. H. & Patterson, J. 1987, ApJ, 322, L99

Ash, T. D. C., Reynolds, A. P., Roche, P., Norton, A. J., Still, M. D., & Morales-Rueda, L. 1999, MNRAS, 307, 357

Ashok, N. M., Manchanda, R. K., Banerjee, D. P. K., Farrell, S., & Sood, R. K. 2006, AdSpR, 38, 2777

Bahcall, J. N. & Bahcall, N. A. 1972, ApJ, 178, L1

Balbus, S. A. & Hawley, J. F. 1991, ApJ, 376, 214

Baliunas, S. L. & Vaughan, A. H. 1985, ARA&A, 23, 379

Barnes, A. D., Casares, J., Charles, P. A., Clark, J. S., Cornelisse, R., Knigge, C., & Steeghs, D. 2006, MNRAS, 365, 296

Barret, D., Bouchet, L., Mandrou, P., Roques, J. P., Cordier, B., Laurent, P., Lebrun, F., Paul, J., Sunyaev, R., Churazov, E., Gilfanov, M., Diachkov, A., Khavenson, N., Novikov, B., Chulkov, I., & Kuznetsov, A. 1992, ApJ, 394, 615

Bassa, C. G., Jonker, P. G., Steeghs, D., & Torres, M. A. P. 2009, MNRAS, 399, 2055

Bath, G. T. & Pringle, J. E. 1982, MNRAS, 201, 345

Bayless, A. J., Robinson, E. L., Mason, P. A., & Robertson, P. 2011, ApJ, 730, 43

Becker, R. H., Smith, B. W., Swank, J. H., Boldt, E. A., Holt, S. S., Serlemitsos, P. J., & Pravdo, S. H. 1977, ApJ, 216, L101

Begelman, M. C., King, A. R., & Pringle, J. E. 2006, MNRAS, 370, 399

Bildsten, L., Chakrabarty, D., Chiu, J., Finger, M. H., Koh, D. T., Nelson, R. W., Prince, T. A., Rubin, B. C., Scott, D. M., Stollberg, M., Vaughan, B. A., Wilson, C. A., & Wilson, R. B. 1997, ApJS, 113, 367

Black, J. K., Brunton, A. N., Bannister, N. P., Deines-Jones, P., & Jahoda, K. 2003, NIMPA, 513, 123

Blanco, V. M. & Hiltner, W. A. 1977, IAUC, 3039, 3

Blundell, K. M., Bowler, M. G., & Schmidtobreick, L. 2007, A&A, 474, 903

—. 2008, ApJ, 678, L47

Boirin, L., Barret, D., Olive, J. F., Bloser, P. F., & Grindlay, J. E. 2000, A&A, 361, 121

Bolton, C. T. 1972a, Natur, 240, 124

—. 1972b, Natur, 235, 271

Bonnet-Bidaud, J. M., Motch, C., Beuermann, K., Pakull, M., Parmar, A. N., & van der Klis, M. 1989, A&A, 213, 97

Bradt, H. V. D., Ohashi, T., & Pounds, K. A. 1992, ARA&A, 30, 391

Brocksopp, C., Groot, P. J., & Wilms, J. 2001, MNRAS, 328, 139

Cackett, E. M., Wijnands, R., Linares, M., Miller, J. M., Homan, J., & Lewin, W. H. G. 2006, MNRAS, 372, 479

Callanan, P. J., Charles, P. A., van Paradijs, J., van der Klis, M., Pedersen, H., & Harlaftis, E. T. 1990, A&A, 240, 346

Capitanio, F., Giroletti, M., Molina, M., Bazzano, A., Tarana, A., Kennea, J., Dean, A. J., Hill, A. B., Tavani, M., & Ubertini, P. 2009, ApJ, 690, 1621

Casares, J., Charles, P. A., & Kuulkers, E. 1998, ApJ, 493, L39

Casares, J., Cornelisse, R., Steeghs, D., Charles, P. A., Hynes, R. I., O'Brien, K., & Strohmayer, T. E. 2006, MNRAS, 373, 1235

Casares, J., González Hernández, J. I., Israelian, G., & Rebolo, R. 2010, MNRAS, 401, 2517

Castor, J. I., Abbott, D. C., & Klein, R. I. 1975, ApJ, 195, 157

CDS. 2011, Website, `http://simbad.u-strasbg.fr/simbad/`

Charles, P., Clarkson, W., Cornelisse, R., & Shih, C. 2008, NewAR, 51, 768

Charles, P., Kotze, M., & Rajoelimanana, A. 2010, in AIPC, Vol. 1314, American Institute of Physics Conference Series, ed. V. Kologera & M. van der Sluys, 303–311

Chen, Y.-P., Zhang, S., Schurch, N., Wang, J.-M., Collmar, W., Li, T.-P., Qu, J.-L., & Zhang, C.-M. 2008, PASJ, 60, 1173

Chevalier, C. & Ilovaisky, S. A. 1977, A&A, 59, L9

Chodil, G., Mark, H., Rodrigues, R., Seward, F. D., & Swift, C. D. 1967, ApJ, 150, 57

Chou, Y. & Grindlay, J. E. 2001, ApJ, 563, 934

Chou, Y., Grindlay, J. E., & Bloser, P. F. 2001, ApJ, 549, 1135

Clark, D. H. & Murdin, P. 1978, Natur, 276, 44

Clarkson, W. I., Charles, P. A., Coe, M. J., & Laycock, S. 2003a, MNRAS, 343, 1213

Clarkson, W. I., Charles, P. A., Coe, M. J., Laycock, S., Tout, M. D., & Wilson, C. A. 2003b, MNRAS, 339, 447

Coe, M. J. 2000, in ASPC, Vol. 214, IAU Colloq. 175: The Be Phenomenon in Early-Type Stars, ed. M. A. Smith, H. F. Henrichs, & J. Fabregat, 656

Coe, M. J., Engel, A. R., & Quenby, J. J. 1976, Natur, 259, 544

Cook, M. C. & Page, C. G. 1987, MNRAS, 225, 381

Corbel, S., Nowak, M. A., Fender, R. P., Tzioumis, A. K., & Markoff, S. 2003, A&A, 400, 1007

Corbet, R. H. D. 2003, ApJ, 595, 1086

Corbet, R. H. D., Markwardt, C. B., & Tueller, J. 2007, ApJ, 655, 458

Cornelisse, R., Charles, P. A., & Robertson, C. 2006, MNRAS, 366, 918

Cornelisse, R., Steeghs, D., Casares, J., Charles, P. A., Barnes, A. D., Hynes, R. I., & O'Brien, K. 2007a, MNRAS, 380, 1219

Cornelisse, R., Steeghs, D., Casares, J., Charles, P. A., Shih, I. C., Hynes, R. I., & O'Brien, K. 2007b, MNRAS, 381, 194

Cowley, A. P. & Crampton, D. 1975, ApJ, 201, L65

Cowley, A. P., Crampton, D., & Hutchings, J. B. 1979, ApJ, 231, 539

Cowley, A. P., Crampton, D., Hutchings, J. B., Remillard, R., & Penfold, J. E. 1983, ApJ, 272, 118

Cowley, A. P., Schmidtke, P. C., Ebisawa, K., Makino, F., Remillard, R. A., Crampton, D., Hutchings, J. B., Kitamoto, S., & Treves, A. 1991, ApJ, 381, 526

Cox, N. L. J., Kaper, L., & Mokiem, M. R. 2005, A&A, 436, 661

Crampton, D., Cowley, A. P., & Hutchings, J. B. 1980, ApJ, 235, L131

Crampton, D., Cowley, A. P., Hutchings, J. B., & Kaat, C. 1976, ApJ, 207, 907

Crampton, D. & Hutchings, J. B. 1981, ApJ, 251, 604

Crampton, D., Hutchings, J. B., & Cowley, A. P. 1985, ApJ, 299, 839

Crampton, D., Hutchings, J. B., Cowley, A. P., Schmidtke, P. C., & Thompson, I. B. 1990, ApJ, 355, 496

Davidson, K. & Ostriker, J. P. 1973, ApJ, 179, 585

Deeter, J. E., Boynton, P. E., & Pravdo, S. H. 1981, ApJ, 247, 1003

Dower, R., Kelley, R., Margon, B., & Bradt, H. 1977, IAUC, 3144, 2

Doxsey, R., Bradt, H. V., Levine, A., Murthy, G. T., Rappaport, S., & Spada, G. 1973, ApJ, 182, L25

Dubus, G. 2003, in EAS Publications Series, Vol. 7, EAS Publications Series, ed. C. Motch & J.-M. Hameury, 283

Dubus, G., Lasota, J.-P., Hameury, J.-M., & Charles, P. 1999, MNRAS, 303, 139

Durant, M., Cornelisse, R., Remillard, R., & Levine, A. 2010, MNRAS, 401, 355

Epstein, A., Delvaille, J., Helmken, H., Murray, S., Schnopper, H. W., Doxsey, R., & Primini, F. 1977, ApJ, 216, 103

Esin, A. A., McClintock, J. E., & Narayan, R. 1997, ApJ, 489, 865

Fabbiano, G. & White, N. E. 2006, Compact stellar X-ray sources in normal galaxies, ed. Lewin, W. H. G. & van der Klis, M. (Cambridge University Press)

Fabian, A. C., Pringle, J. E., & Rees, M. J. 1975, MNRAS, 172, 15P

Falanga, M., Farinelli, R., Goldoni, P., Frontera, F., Goldwurm, A., & Stella, L. 2004, A&A, 426, 979

Farrell, S., Sood, R., & O'Neill, P. 2004, ATel, 283, 1

Farrell, S. A., Barret, D., & Skinner, G. K. 2009, MNRAS, 393, 139

Farrell, S. A., Sood, R. K., O'Neill, P. M., & Dieters, S. 2008, MNRAS, 389, 608

Fender, R. 2006, Jets from X-ray binaries, ed. Lewin, W. H. G. & van der Klis, M. (Cambridge University Press)

Fender, R. P., Belloni, T. M., & Gallo, E. 2004, MNRAS, 355, 1105

Fender, R. P., Spencer, R. E., Newell, S. J., & Tzioumis, A. K. 1997, MNRAS, 286, L29

Finley, J. P., Belloni, T., & Cassinelli, J. P. 1992, A&A, 262, L25

Finley, J. P., Taylor, M., & Belloni, T. 1994, ApJ, 429, 356

Fomalont, E. B., Geldzahler, B. J., & Bradshaw, C. F. 2001, ApJ, 558, 283

Forman, W., Jones, C., Cominsky, L., Julien, P., Murray, S., Peters, G., Tananbaum, H., & Giacconi, R. 1978, ApJS, 38, 357

Foulkes, S. B., Haswell, C. A., & Murray, J. R. 2010, MNRAS, 401, 1275

Fox, D. W., Lewin, W. H. G., Rutledge, R. E., Morgan, E. H., Guerriero, R., Bildsten, L., van der Klis, M., van Paradijs, J., Moore, C. B., Dotani, T., & Asai, K. 2001, MNRAS, 321, 776

Frank, J., King, A., & Raine, D. J. 2002, Accretion Power in Astrophysics: Third Edition, ed. Frank, J., King, A., & Raine, D. J. (Cambridge University Press)

Galloway, D. K., Chakrabarty, D., Muno, M. P., & Savov, P. 2001, ApJ, 549, L85

Galloway, D. K., Muno, M. P., Hartman, J. M., Psaltis, D., & Chakrabarty, D. 2008, ApJS, 179, 360

Galloway, D. K., Yao, Y., Marshall, H., Misanovic, Z., & Weinberg, N. 2010, ApJ, 724, 417

Ghosh, P. & Lamb, F. K. 1979a, ApJ, 232, 259

—. 1979b, ApJ, 234, 296

Giacconi, R., Gorenstein, P., Gursky, H., Usher, P. D., Waters, J. R., Sandage, A., Osmer, P., & Peach, J. V. 1967, ApJ, 148, L129

Giacconi, R., Gursky, H., Kellogg, E., Schreier, E., & Tananbaum, H. 1971, ApJ, 167, L67

Giacconi, R., Gursky, H., Paolini, F. R., & Rossi, B. B. 1962, PhRvL, 9, 439

Gibb, M. 2011, Website, `http://heasarc.gsfc.nasa.gov/docs/heasarc/missions.html`

Gies, D. R., McSwain, M. V., Riddle, R. L., Wang, Z., Wiita, P. J., & Wingert, D. W. 2002, ApJ, 566, 1069

Gilfanov, M. 2004, MNRAS, 349, 146

Gold, T. 1968, Natur, 218, 731

Gottlieb, E. W., Wright, E. L., & Liller, W. 1975, ApJ, 195, L33

Gottwald, M., Haberl, F., Parmar, A. N., & White, N. E. 1986, ApJ, 308, 213

Grebenev, S. A., Molkov, S. V., Revnivtsev, M. G., & Sunyaev, R. A. 2005a, ATel, 447, 1

Grebenev, S. A., Molkov, S. V., Revnivtsev, M. G., & Sunyaev, R. A. 2007, in ESASP, Vol. 622, ESA Special Publication, 373

Grebenev, S. A., Molkov, S. V., & Sunyaev, R. A. 2005b, ATel, 444, 1

Griffiths, R. E. & Seward, F. D. 1977, MNRAS, 180, 75P

Grimm, H.-J., Gilfanov, M., & Sunyaev, R. 2003, MNRAS, 339, 793

Grindlay, J., Gursky, H., Schnopper, H., Parsignault, D. R., Heise, J., Brinkman, A. C., & Schrijver, J. 1976, ApJ, 205, L127

Grindlay, J. E. 1979, ApJ, 232, L33

Grindlay, J. E., Bailyn, C. D., Cohn, H., Lugger, P. M., Thorstensen, J. R., & Wegner, G. 1988, ApJ, 334, L25

Grindlay, J. E. & Gursky, H. 1977, ApJ, 218, L117

Gruber, D. E. & Rothschild, R. E. 1984, ApJ, 283, 546

Grundstrom, E. D., Blair, J. L., Gies, D. R., Huang, W., McSwain, M. V., Raghavan, D., Riddle, R. L., Subasavage, J. P., Wingert, D. W., Levine, A. M., & Remillard, R. A. 2007, ApJ, 656, 431

Guerriero, R., Fox, D. W., Kommers, J., Lewin, W. H. G., Rutledge, R., Moore, C. B., Morgan, E., van Paradijs, J., van der Klis, M., Bildsten, L., & Dotani, T. 1999, MNRAS, 307, 179

Güver, T., Wroblewski, P., Camarota, L., & Özel, F. 2010, ApJ, 719, 1807

Hakala, P., Hjalmarsdotter, L., Hannikainen, D. C., & Muhli, P. 2009, MNRAS, 394, 892

Hakala, P., Ramsay, G., Muhli, P., Charles, P., Hannikainen, D., Mukai, K., & Vilhu, O. 2005, MNRAS, 356, 1133

Hakala, P. J., Chaytor, D. H., Vilhu, O., Piirola, V., Morris, S. L., & Muhli, P. 1998, A&A, 333, 540

Hakala, P. J., Muhli, P., & Dubus, G. 1999, MNRAS, 306, 701

Hall, D. S. 1991, ApJ, 380, L85

Harris, R. J., Levine, A. M., Durant, M., Kong, A. K. H., Charles, P., & Shahbaz, T. 2009, ApJ, 696, 1987

Hasinger, G., Langmeier, A., Sztajno, M., Truemper, J., & Lewin, W. H. G. 1986, Natur, 319, 469

Hasinger, G. & van der Klis, M. 1989, A&A, 225, 79

Heise, J. & in't Zand, J. 2006, Fast X-ray transients and X-ray flashes, ed. Lewin, W. H. G. & van der Klis, M. (Cambridge University Press)

Hellier, C. 2001, Cataclysmic Variable Stars, ed. Hellier, C. (Springer)

Herrero, A., Kudritzki, R. P., Gabler, R., Vilchez, J. M., & Gabler, A. 1995, A&A, 297, 556

Hewish, A., Bell, S. J., Pilkington, J. D. H., Scott, P. F., & Collins, R. A. 1968, Natur, 217, 709

Hills, J. G. 1976, MNRAS, 175, 1P

Hillwig, T. C. & Gies, D. R. 2008, ApJ, 676, L37

Hjellming, R. M. & Johnston, K. J. 1981, Natur, 290, 100

Hjellming, R. M., Stewart, R. T., White, G. L., Strom, R., Lewin, W. H. G., Hertz, P., Wood, K. S., Norris, J. P., Mitsuda, K., Penninx, W., & van Paradijs, J. 1990, ApJ, 365, 681

Hoffman, J. A., Lewin, W. H. G., & Doty, J. 1977, ApJ, 217, L23

Hoffman, J. A., Lewin, W. H. G., Doty, J., Hearn, D. R., Clark, G. W., Jernigan, G., & Li, F. K. 1976, ApJ, 210, L13

Holt, S. S., Boldt, E. A., Schwartz, D. A., Serlemitsos, P. J., & Bleach, R. D. 1971, ApJ, 166, L65

Holt, S. S., Boldt, E. A., Serlemitsos, P. J., & Kaluzienski, L. J. 1976, ApJ, 203, L63

Holt, S. S., Kaluzienski, L. J., Boldt, E. A., & Serlemitsos, P. A. 1979, ApJ, 227, 563

Homan, J., Jonker, P. G., Wijnands, R., van der Klis, M., & van Paradijs, J. 1999, ApJ, 516, L91

Homan, J. & van der Klis, M. 2000, ApJ, 539, 847

Homer, L., Charles, P. A., Hakala, P., Muhli, P., Shih, I.-C., Smale, A. P., & Ramsay, G. 2001, MNRAS, 322, 827

Hu, C.-P., Chou, Y., & Chung, Y.-Y. 2008, ApJ, 680, 1405

Hut, P., McMillan, S., Goodman, J., Mateo, M., Phinney, E. S., Pryor, C., Richer, H. B., Verbunt, F., & Weinberg, M. 1992, PASP, 104, 981

Hutchings, J. B. 1975, ApJ, 201, 413

Hutchings, J. B., Cowley, A. P., Osmer, P. S., & Crampton, D. 1977, ApJ, 217, 186

Hutchings, J. B., Crampton, D., & Cowley, A. P. 1978, ApJ, 225, 548

Hynes, R. I., Haswell, C. A., Chaty, S., Shrader, C. R., & Cui, W. 2002, MNRAS, 331, 169

Hynes, R. I., Robinson, E. L., & Jeffery, E. 2004, ApJ, 608, L101

Hynes, R. I., Steeghs, D., Casares, J., Charles, P. A., & O'Brien, K. 2003, ApJ, 583, L95

in't Zand, J. J. M., Baykal, A., & Strohmayer, T. E. 1998, ApJ, 496, 386

in't Zand, J. J. M., Bazzano, A., Cocchi, M., Cornelisse, R., Heise, J., Kuiper, L., Kuulkers, E., Markwardt, C. B., Muller, J. M., Natalucci, L., Smith, M. J. S., Strohmayer, T. E., Ubertini, P., & Verbunt, F. 2000, A&A, 355, 145

in't Zand, J. J. M., Hulleman, F., Markwardt, C. B., Méndez, M., Kuulkers, E., Cornelisse, R., Heise, J., Strohmayer, T. E., & Verbunt, F. 2003, A&A, 406, 233

Iorio, L. 2008, Ap&SS, 315, 335

Iping, R. C. & Petterson, J. A. 1990, A&A, 239, 221

Jernigan, J. G., Bradt, H. V., Doxsey, R. E., McClintock, J. E., & Apparao, K. M. V. 1977, Natur, 270, 321

Johnston, M. D., Bradt, H. V., & Doxsey, R. E. 1979, ApJ, 233, 514

Jonker, P. G., van der Klis, M., Kouveliotou, C., Méndez, M., Lewin, W. H. G., & Belloni, T. 2003, MNRAS, 346, 684

Kahabka, P. & van den Heuvel, E. P. J. 1997, ARA&A, 35, 69

Kahabka, P. & van der Heuvel, E. P. J. 2006, Super-soft sources, ed. Lewin, W. H. G. & van der Klis, M. (Cambridge University Press)

Kahn, S. M. & Grindlay, J. E. 1984, ApJ, 281, 826

Kaluzienski, L. J., Holt, S. S., Boldt, E. A., & Serlemitsos, P. J. 1976, in BAAS, Vol. 8, Bulletin of the American Astronomical Society, 541

Katz, J. I., Anderson, S. F., Grandi, S. A., & Margon, B. 1982, ApJ, 260, 780

Kelley, R. L., Jernigan, J. G., Levine, A., Petro, L. D., & Rappaport, S. 1983, ApJ, 264, 568

Kemp, J. C., Herman, L. C., & Barbour, M. S. 1978, AJ, 83, 962

Kennea, J. A., Burrows, D. N., Nousek, J. A., Chester, M., Barthelmy, S., Gehrels, N., Grebenev, S., & Beckmann, V. 2005, ATel, 476, 1

Khruzina, T. S. & Cherepashchuk, A. M. 1983, AZh, 60, 57

—. 1987, AZh, 64, 345

King, A. R. 2006, Accretion in compact binaries, ed. Lewin, W. H. G. & van der Klis, M. (Cambridge University Press)

King, A. R., Frank, J., Kolb, U., & Ritter, H. 1997, ApJ, 482, 919

King, A. R. & Ritter, H. 1998, MNRAS, 293, L42

Kitamoto, S., Egoshi, W., Miyamoto, S., Tsunemi, H., Ling, J. C., Wheaton, W. A., & Paul, B. 2000, ApJ, 531, 546

Koenigsberger, G., Swank, J. H., Szymkowiak, A. E., & White, N. E. 1983, ApJ, 268, 782

Kong, A. K. H., Charles, P. A., Homer, L., Kuulkers, E., & O'Donoghue, D. 2006, MNRAS, 368, 781

Kong, A. K. H., Charles, P. A., & Kuulkers, E. 1998, NewA, 3, 301

Kong, A. K. H., Charles, P. A., Kuulkers, E., & Kitamoto, S. 2002, MNRAS, 329, 588

Kotze, M. M. & Charles, P. A. 2010, MNRAS, 402, L16

—. 2012, MNRAS, 420, 1575

Kotze, M. M., Charles, P. A., & Crause, L. A. 2009, MNRAS, 395, 1579

Krzeminski, W. 1974, ApJ, 192, L135

Kubota, K., Ueda, Y., Fabrika, S., Medvedev, A., Barsukova, E. A., Sholukhova, O., & Goranskij, V. P. 2010, ApJ, 709, 1374

Kudryavtsev, M. I., Mamontova, N. A., Svertilov, S. I., & Tolstaya, E. D. 1989, PAZh, 15, 1072

Lachowicz, P., Zdziarski, A. A., Schwarzenberg-Czerny, A., Pooley, G. G., & Kitamoto, S. 2006, MNRAS, 368, 1025

Lamb, F. K., Shibazaki, N., Alpar, M. A., & Shaham, J. 1985, Natur, 317, 681

Lang, F. L., Levine, A. M., Bautz, M., Hauskins, S., Howe, S., Primini, F. A., Lewin, W. H. G., Baity, W. A., Knight, F. K., Rotschild, R. E., & Petterson, J. A. 1981, ApJ, 246, L21

Lasota, J.-P. 2001, NewAR, 45, 449

Leahy, D. A. & Dupuis, J. 2010, ApJ, 715, 897

Leahy, D. A. & Igna, C. D. 2010, ApJ, 713, 318

Leong, C., Kellogg, E., Gursky, H., Tananbaum, H., & Giacconi, R. 1971, ApJ, 170, L67

Levine, A. M., Bradt, H., Cui, W., Jernigan, J. G., Morgan, E. H., Remillard, R., Shirey, R. E., & Smith, D. A. 1996, ApJ, 469, L33

Levine, A. M., Bradt, H. V., Chakrabarty, D., Corbet, R. H. D., & Harris, R. J. 2011, ApJS, 196, 6

Levine, A. M., Rappaport, S. A., & Zojcheski, G. 2000, ApJ, 541, 194

Lewin, W. H. G. & Joss, P. C. 1977, Natur, 270, 211

Lewin, W. H. G. & van der Klis, M. 2006, Compact stellar X-ray sources, ed. Lewin, W. H. G. & van der Klis, M. (Cambridge University Press)

Lewin, W. H. G., van Paradijs, J., & Taam, R. E. 1993, SSRv, 62, 223

Li, F., Rappaport, S., & Epstein, A. 1978, Natur, 271, 37

Liller, W. 1973, ApJ, 184, L37

—. 1977, ApJ, 213, L21

Liu, Q. Z., van Paradijs, J., & van den Heuvel, E. P. J. 2006, A&A, 455, 1165

—. 2007, A&A, 469, 807

Lodato, G. & Price, D. J. 2010, MNRAS, 405, 1212

Lomb, N. R. 1976, Ap&SS, 39, 447

Loznikov, V. M. & Iamburenko, N. S. 1982, SvAL, 8, 255

Lucke, R., Yentis, D., Friedman, H., Fritz, G., & Shulman, S. 1976, ApJ, 206, L25

Makishima, K., Kawai, N., Koyama, K., Shibazaki, N., Nagase, F., & Nakagawa, M. 1984, PASJ, 36, 679

Makishima, K., Mihara, T., Nagase, F., & Tanaka, Y. 1999, ApJ, 525, 978

Margon, B. 1984, ARA&A, 22, 507

Margon, B., Thorstensen, J. R., & Bowyer, S. 1978, ApJ, 221, 907

Markert, T. H., Canizares, C. R., Clark, G. W., Lewin, W. H. G., Schnopper, H. W., & Sprott, G. F. 1973, ApJ, 184, L67

Markert, T. H., Laird, F. N., Clark, G. W., Hearn, D. R., Sprott, G. F., Li, F. K., Bradt, H. V., Lewin, W. H. G., Schnopper, H. W., & Winkler, P. F. 1979, ApJS, 39, 573

Marshall, H. L., Hoffman, J. A., Doty, J., Lewin, W. H. G., & Ulmer, M. P. 1979, ApJ, 227, 555

Marshall, N. & Ricketts, M. J. 1980, MNRAS, 193, 7P

Masetti, N. 2002, A&A, 381, L45

Mason, P. A., Robinson, E. L., Gray, C. L., & Hynes, R. I. 2008, ApJ, 685, 428

McClintock, J. E. & Remillard, R. A. 2006, Black hole binaries, ed. Lewin, W. H. G. & van der Klis, M. (Cambridge University Press)

McGowan, K. E., Charles, P. A., O'Donoghue, D., & Smale, A. P. 2003, MNRAS, 345, 1039

Meekins, J. F., Wood, K. S., Hedler, R. L., Byram, E. T., Yentis, D. J., Chubb, T. A., & Friedman, H. 1984, ApJ, 278, 288

Middleditch, J. & Nelson, J. 1976, ApJ, 208, 567

Migliari, S., Fender, R. P., Rupen, M., Jonker, P. G., Klein-Wolt, M., Hjellming, R. M., & van der Klis, M. 2003, MNRAS, 342, L67

Migliari, S., Fender, R. P., Rupen, M., Wachter, S., Jonker, P. G., Homan, J., & van der Klis, M. 2004, MNRAS, 351, 186

Mioduszewski, A. J. & Rupen, M. P. 2006, in AAS, Vol. 38, American Astronomical Society Meeting Abstracts, 954–+

Mirabel, I. F. 2007, in IAUS, Vol. 238, IAU Symposium, ed. V. Karas & G. Matt, 309–314

Mitchell, R. J., Culhane, J. L., Davison, P. J. N., & Ives, J. C. 1976, MNRAS, 175, 29P

Miyamoto, S. & Kitamoto, S. 1991, ApJ, 374, 741

Miyamoto, S. & Matsuoka, M. 1977, SSRv, 20, 687

Moore, C. B., Rutledge, R. E., Fox, D. W., Guerriero, R. A., Lewin, W. H. G., Fender, R., & van Paradijs, J. 2000, ApJ, 532, 1181

Morris, S. L., Liebert, J., Stocke, J. T., Gioia, I. M., Schild, R. E., & Wolter, A. 1990, ApJ, 365, 686

Motch, C., Chevalier, C., Ilovaisky, S. A., & Pakull, M. W. 1985, SSRv, 40, 239

Motch, C., Ricketts, M. J., Page, C. G., Ilovaisky, S. A., & Chevalier, C. 1983, A&A, 119, 171

Muñoz-Darias, T., Casares, J., & Martínez-Pais, I. G. 2008, MNRAS, 385, 2205

Muñoz-Darias, T., Casares, J., O'Brien, K., Steeghs, D., Martínez-Pais, I. G., Cornelisse, R., & Charles, P. A. 2009, MNRAS, 394, L136

Mudelsee, M. & Schulz, M. 2008, Website, `http://www.ncdc.noaa.gov/paleo/softlib/redfit/redfit.html`

Mukai, K., Smale, A. P., Stahle, C. K., Schlegel, E. M., & Wijnands, R. 2001, ApJ, 561, 938

Muno, M. P., Fox, D. W., Morgan, E. H., & Bildsten, L. 2000, ApJ, 542, 1016

Murdin, P., Jauncey, D. L., Lerche, I., Nicolson, G. D., Kaluzienski, L. J., Holt, S. S., & Haynes, R. F. 1980, A&A, 87, 292

Murray, J. R., Warner, B., & Wickramasinghe, D. T. 2000, MNRAS, 315, 707

Narayan, R. & Yi, I. 1994, ApJ, 428, L13

Narita, T., Palmieri, J. B., & Tow, E. S. 2009, ApJ, 690, 1145

Nowak, M. A., Juett, A., Homan, J., Yao, Y., Wilms, J., Schulz, N. S., & Canizares, C. R. 2008, ApJ, 689, 1199

Nowak, M. A. & Wilms, J. 1999, ApJ, 522, 476

Oda, M., Gorenstein, P., Gursky, H., Kellogg, E., Schreier, E., Tananbaum, H., & Giacconi, R. 1971, ApJ, 166, L1

O'Donoghue, D. & Charles, P. A. 1996, MNRAS, 282, 191

Ogilvie, G. I. & Dubus, G. 2001, MNRAS, 320, 485

Oppenheimer, J. R. & Volkoff, G. M. 1939, PhRv, 55, 374

Özdemir, S. 2010, AN, 331, 300

Özdemir, S. & Demircan, O. 2001, Ap&SS, 278, 319

Paczyński, B. 1971, ARA&A, 9, 183

Paczynski, B. 1983, ApJ, 273, L81

Pakull, M. 1978, IAUC, 3313, 1

Parmar, A. N., White, N. E., Giommi, P., & Gottwald, M. 1986, ApJ, 308, 199

Patterson, J. 1984, ApJS, 54, 443

Paul, B. & Kitamoto, S. 2002, JApA, 23, 33

Paul, B., Kitamoto, S., & Makino, F. 2000, ApJ, 528, 410

Pavlinsky, M. N., Grebenev, S. A., & Sunyaev, R. A. 1992, SvAL, 18, 88

—. 1994, ApJ, 425, 110

Pedersen, H., van Paradijs, J., & Lewin, W. H. G. 1981, Natur, 294, 725

Petterson, J. A. 1977, ApJ, 218, 783

Pietsch, W., Voges, W., Pakull, M., & Staubert, R. 1985, SSRv, 40, 371

Podsiadlowski, P., Rappaport, S., & Han, Z. 2003, MNRAS, 341, 385

Pooley, D., Lewin, W. H. G., Anderson, S. F., Baumgardt, H., Filippenko, A. V., Gaensler, B. M., Homer, L., Hut, P., Kaspi, V. M., Makino, J., Margon, B., McMillan, S., Portegies Zwart, S., van der Klis, M., & Verbunt, F. 2003, ApJ, 591, L131

Priedhorsky, W., Hasinger, G., Lewin, W. H. G., Middleditch, J., Parmar, A., Stella, L., & White, N. 1986, ApJ, 306, L91

Priedhorsky, W. & Terrell, J. 1983a, in BAAS, Vol. 15, Bulletin of the American Astronomical Society, 980

Priedhorsky, W. & Terrell, J. 1984a, ApJ, 284, L17

Priedhorsky, W. C. & Terrell, J. 1983b, ApJ, 273, 709

—. 1984b, ApJ, 280, 661

Priedhorsky, W. C., Terrell, J., & Holt, S. S. 1983, ApJ, 270, 233

Pringle, J. E. 1981, ARA&A, 19, 137

Pringle, J. E. & Wade, R. A. 1985, Interacting binary stars, ed. Pringle, J. E. & Wade, R. A. (Cambridge University Press)

Psaltis, D. 2006, Accreting neutron stars and black holes: a decade of discoveries, ed. Lewin, W. H. G. & van der Klis, M. (Cambridge University Press)

Raichur, H. & Paul, B. 2008, MNRAS, 387, 439

Rajoelimanana, A. F., Charles, P. A., & Udalski, A. 2011, MNRAS, 413, 1600

Rappaport, S. & Joss, P. C. 1984, ApJ, 283, 232

Rappaport, S., Ma, C. P., Joss, P. C., & Nelson, L. A. 1987, ApJ, 322, 842

Reig, P., Chakrabarty, D., Coe, M. J., Fabregat, J., Negueruela, I., Prince, T. A., Roche, P., & Steele, I. A. 1996, A&A, 311, 879

Retter, A., Chou, Y., Bedding, T. R., & Naylor, T. 2002, MNRAS, 330, L37

Revnivtsev, M. & Sunyaev, R. 2003, A&A, 399, 699

Reynolds, A. P., Quaintrell, H., Still, M. D., Roche, P., Chakrabarty, D., & Levine, S. E. 1997, MNRAS, 288, 43

Richman, H. R., Applegate, J. H., & Patterson, J. 1994, PASP, 106, 1075

Rico, J. 2008, ApJ, 683, L55

Robinson, C. R., Harmon, B. A., McCollough, M. L., Paciesas, W. S., Sahi, M., Scott, D. M., Wilson, C. A., Zhang, S. N., & Deal, K. J. 1997, in ESASP, Vol. 382, The Transparent Universe, ed. C. Winkler, T. J.-L. Courvoisier, & P. Durouchoux, 249

Samimi, J., Share, G. H., Wood, K., Yentis, D., Meekins, J., Evans, W. D., Shulman, S., Byram, E. T., Chubb, T. A., & Friedman, H. 1979, Natur, 278, 434

Sandage, A., Osmer, P., Giacconi, R., Gorenstein, P., Gursky, H., Waters, J., Bradt, H., Garmire, G., Sreekantan, B. V., Oda, M., Osawa, K., & Jugaku, J. 1966, ApJ, 146, 316

Sanduleak, N. & Philip, A. G. D. 1976, IAUC, 3023, 1

Scargle, J. D. 1982, ApJ, 263, 835

—. 1989, ApJ, 343, 874

Schmidtke, P. C. 1988, AJ, 95, 1528

Schreier, E., Giacconi, R., Gursky, H., Kellogg, E., & Tananbaum, H. 1972a, ApJ, 178, L71

Schreier, E., Gursky, H., Kellogg, E., Tananbaum, H., & Giacconi, R. 1971, ApJ, 170, L21

Schreier, E., Levinson, R., Gursky, H., Kellogg, E., Tananbaum, H., & Giacconi, R. 1972b, ApJ, 172, L79

Schrijver, C. J. & Zwaan, C. 1992, in ASPC, Vol. 26, Cool Stars, Stellar Systems, and the Sun, ed. M. S. Giampapa & J. A. Bookbinder, 370

Schwartz, D. A., Griffiths, R. E., Bowyer, S., Thorstensen, J. R., & Charles, P. A. 1980, AJ, 85, 549

Schwarzenberg-Czerny, A. 1991, MNRAS, 253, 198

Seetha, S., Ramadevi, M. C., Babu, V. C., Sharma, M. R., Murthy, N. S. R., Ashoka, B. N., Shyama, K. C., Kulkarni, R., Meena, G., & Sreekumar, P. 2006, AdSpR, 38, 2995

Seward, F. D. & Charles, P. A. 2010, Exploring the X-ray Universe, ed. Seward, F. D. & Charles, P. A. (Cambridge University Press)

Shakura, N. I. & Sunyaev, R. A. 1973, A&A, 24, 337

Shapiro, S. L., Lightman, A. P., & Eardley, D. M. 1976, ApJ, 204, 187

Shaposhnikov, N. & Titarchuk, L. 2007, ApJ, 663, 445

Shih, I. C., Bird, A. J., Charles, P. A., Cornelisse, R., & Tiramani, D. 2005, MNRAS, 361, 602

Shih, I. C., Charles, P. A., & Cornelisse, R. 2011, MNRAS, 412, 120

Skinner, G. K., Shulman, S., Share, G., Evans, W. D., McNutt, D., Meekins, J., Smathers, H., Wood, K., Yentis, D., Byram, E. T., Chubb, T. A., & Friedman, H. 1980, ApJ, 240, 619

Smale, A. P. & Kuulkers, E. 2000, ApJ, 528, 702

Smale, A. P. & Lochner, J. C. 1992, ApJ, 395, 582

Smale, A. P. & Mukai, K. 1988, MNRAS, 231, 663

Smale, A. P., Zhang, W., & White, N. E. 1997, ApJ, 483, L119

Smith, D. A., Morgan, E. H., & Bradt, H. 1997, ApJ, 479, L137

Spencer, R. E. 1979, Natur, 282, 483

Steeghs, D. & Casares, J. 2002, ApJ, 568, 273

Stella, L., Haberl, F., Lewin, W. H. G., Parmar, A. N., van Paradijs, J., & White, N. E. 1988, ApJ, 324, 379

Stella, L., Priedhorsky, W., & White, N. E. 1987, ApJ, 312, L17

Stellingwerf, R. F. 1978, ApJ, 224, 953

Stephenson, C. B. & Sanduleak, N. 1977, ApJS, 33, 459

Still, M., O'Brien, K., Horne, K., Boroson, B., Titarchuk, L. G., Engle, K., Vrtilek, S. D., Quaintrell, H., & Fiedler, H. 2001, ApJ, 554, 352

Strohmayer, T. & Bildsten, L. 2006, New views of thermonuclear bursts, ed. Lewin, W. H. G. & van der Klis, M. (Cambridge University Press)

Strohmayer, T. E. & Markwardt, C. B. 2002, ApJ, 577, 337

Strohmayer, T. E., Zhang, W., Swank, J. H., Smale, A., Titarchuk, L., Day, C., & Lee, U. 1996, ApJ, 469, L9

Sunyaev, R. & the Kvant Team. 1989, IAUC, 4839, 1

Tanaka, Y. & Tenma Team. 1983, IAUC, 3882, 1

Tananbaum, H., Gursky, H., Kellogg, E., Giacconi, R., & Jones, C. 1972a, ApJ, 177, L5

Tananbaum, H., Gursky, H., Kellogg, E. M., Levinson, R., Schreier, E., & Giacconi, R. 1972b, ApJ, 174, L143

Tarana, A., Bazzano, A., Ubertini, P., & Zdziarski, A. A. 2007, ApJ, 654, 494

Tauris, T. M. & van der Heuvel, E. P. J. 2006, Formation and evolution of compact stellar X-ray sources, ed. Lewin, W. H. G. & van der Klis, M. (Cambridge University Press)

Taylor, M., Finley, J. P., Kurt, C., & Koenigsberger, G. 1995, AJ, 109, 396

Thorstensen, J. R. 1987, ApJ, 312, 739

Trowbridge, S., Nowak, M. A., & Wilms, J. 2007, ApJ, 670, 624

Urry, C. M. & Padovani, P. 1995, PASP, 107, 803

Šimon, V. 2003, A&A, 405, 199

—. 2005, A&A, 436, 263

—. 2009, NewA, 14, 443

—. 2010, A&A, 513, A71

Val Baker, A. K. F., Norton, A. J., & Quaintrell, H. 2005, A&A, 441, 685

van der Klis, M. 2006, Rapid X-ray variability, ed. Lewin, W. H. G. & van der Klis, M. (Cambridge University Press)

van der Klis, M., Stella, L., White, N., Jansen, F., & Parmar, A. N. 1987, ApJ, 316, 411

van der Klis, M., Swank, J. H., Zhang, W., Jahoda, K., Morgan, E. H., Lewin, W. H. G., Vaughan, B., & van Paradijs, J. 1996, ApJ, 469, L1

van der Meer, A., Kaper, L., van Kerkwijk, M. H., Heemskerk, M. H. M., & van den Heuvel, E. P. J. 2007, A&A, 473, 523

van der Sluys, M. 2006, Website, `http://hemel.waarnemen.com/Informatie/Sterren/hoofdstuk6.html`

van Kerkwijk, M. H., van Oijen, J. G. J., & van den Heuvel, E. P. J. 1989, A&A, 209, 173

van Paradijs, J. 1996, ApJ, 464, L139

van Paradijs, J. & Zuiderwijk, E. 1977, A&A, 61, L19

Verbunt, F. & Hut, P. 1987, in IAUS, Vol. 125, The Origin and Evolution of Neutron Stars, ed. D. J. Helfand & J.-H. Huang, 187

Verbunt, F. & Lewin, W. H. G. 2006, Globular cluster X-ray sources, ed. Lewin, W. H. G. & van der Klis, M. (Cambridge University Press)

Villarreal, A. R. & Strohmayer, T. E. 2004, ApJ, 614, L121

Vrtilek, S. D., Quaintrell, H., Boroson, B., Still, M., Fiedler, H., O'Brien, K., & McCray, R. 2001a, ApJ, 549, 522

Vrtilek, S. D., Raymond, J. C., Boroson, B., Kallman, T., Quaintrell, H., & McCray, R. 2001b, ApJ, 563, L139

Wade, R. A., Quintana, H., Horne, K., & Marsh, T. R. 1985, PASP, 97, 1092

Wall, J. V. & Jenkins, C. R. 2003, Practical Statistics for Astronomers, ed. Wall, J. V. & Jenkins, C. R. (Cambridge University Press)

Walter, F. M., Mason, K. O., Clarke, J. T., Halpern, J., Grindlay, J. E., Bowyer, S., & Henry, J. P. 1982, ApJ, 253, L67

Wang, Z. & Chakrabarty, D. 2010, ApJ, 712, 653

Warner, B. 1988, Natur, 336, 129

—. 1995, Cataclysmic variable stars., ed. Warner, B. (Cambridge University Press)

Watson, M. G., Willingale, R., Grindlay, J. E., & Seward, F. D. 1983, ApJ, 273, 688

Webster, B. L. & Murdin, P. 1972, Natur, 235, 37

Wen, L., Levine, A. M., Corbet, R. H. D., & Bradt, H. V. 2006, ApJS, 163, 372

White, N. E. & Carpenter, G. F. 1978, MNRAS, 183, 11P

White, N. E. & Holt, S. S. 1982, ApJ, 257, 318

White, N. E. & Marshall, F. E. 1984, ApJ, 281, 354

White, N. E., Nagase, F., & Parmar, A. N. 1995, The properties of X-ray binaries., ed. W. H. G. Lewin, J. van Paradijs, & E. P. J. van den Heuvel (Cambridge University Press)

White, N. E. & Swank, J. H. 1982, ApJ, 253, L61

Whitehurst, R. & King, A. 1991, MNRAS, 249, 25

Wijers, R. A. M. J. & Pringle, J. E. 1999, MNRAS, 308, 207

Wijnands, R., Homan, J., van der Klis, M., Kuulkers, E., van Paradijs, J., Lewin, W. H. G., Lamb, F. K., Psaltis, D., & Vaughan, B. 1998, ApJ, 493, L87

Wijnands, R., Miller, J. M., Markwardt, C., Lewin, W. H. G., & van der Klis, M. 2001, ApJ, 560, L159

Wijnands, R., Miller, J. M., & van der Klis, M. 2002, MNRAS, 331, 60

Wijnands, R., van der Klis, M., & Rijkhorst, E.-J. 1999, ApJ, 512, L39

Wijnands, R. A. D., Kuulkers, E., & Smale, A. P. 1996, ApJ, 473, L45

Wijnands, R. A. D. & van der Klis, M. 1997, ApJ, 482, L65

Wilms, J., Nowak, M. A., Pottschmidt, K., Heindl, W. A., Dove, J. B., & Begelman, M. C. 2001, MNRAS, 320, 327

Wojdowski, P., Clark, G. W., Levine, A. M., Woo, J. W., & Zhang, S. N. 1998, ApJ, 502, 253

Woo, J. W., Clark, G. W., Levine, A. M., Corbet, R. H. D., & Nagase, F. 1996, ApJ, 467, 811

Yaqoob, T., Ebisawa, K., & Mitsuda, K. 1993, MNRAS, 264, 411

Zdziarski, A. A., Pooley, G. G., & Skinner, G. K. 2011, MNRAS, 412, 1985

Zdziarski, A. A., Wen, L., & Gierliński, M. 2007, MNRAS, 377, 1006

Zhang, S. N., Robinson, C. R., Wilson, R. B., Harmon, B. A., Scott, D. M., & Remillard, R. 1996, IAUC, 6468, 1